ASSESSMENT OF TRACE GAS OBSERVATIONS FROM THE TORONTO ATMOSPHERIC OBSERVATORY

by

Jeffrey R. Taylor

A thesis submitted in conformity with the requirements
for the degree of Doctor of Philosophy
Graduate Department of Physics
University of Toronto

Abstract

Assessment of Trace Gas Observations from the Toronto Atmospheric Observatory

Jeffrey R. Taylor
Doctor of Philosophy
Graduate Department of Physics
University of Toronto
2008

A high-resolution infrared Fourier Transform Spectrometer (FTS) has been operational at the Toronto Atmospheric Observatory (TAO) since May 2002. An optimal estimation retrieval technique is used to analyse the observed spectra and provide regular total and partial column measurements of trace gases in the troposphere and stratosphere as part of the Network for the Detection of Atmospheric Composition Change. The quality of these results were assessed through two ground-based validation campaigns, comparisons with three satellite instruments, and comparison with a three-dimensional chemical transport model.

The two ground-based campaigns involved two lower-resolution FTS instruments: the University of Toronto FTS and the Portable Atmospheric Research Interferometric Spectrometer for the Infrared. The first campaign took place over the course of four months and is the longest side-by-side intercomparison of ground-based FTS instruments, to date. The second campaign was more focused and involved all three instruments measuring over a two-week period. Simultaneous measurements of O_3, HCl, N_2O, and CH_4 were recorded and average total column differences were all $< 3.7\%$ in the extended campaign, and $< 4.5\%$ in the focused campaign.

Satellite-based comparisons were done with the SCanning and Imaging Absorption spectroMeter for Atmospheric CHartographY (SCIAMACHY), the Atmospheric Chemistry Experiment Fourier Transform Spectrometer (ACE-FTS), and the Optical Spectrograph and InfraRed Imager System (OSIRIS). Total column CO, CH_4, and N_2O compared with SCIAMACHY all had average differences $< 10\%$ with results from the TAO-FTS being as good as, or better, than that of other instruments. Validation with the ACE-FTS showed that average partial columns of O_3, NO_2, N_2O, CH_4, and HCl were within 10% while observations of CO and NO each had an average bias of about 25%. Comparisons of monthly average partial column O_3 and NO_2 with OSIRIS were highly correlated (R^2 = 0.82-0.97) with monthly mean differences of $< 3.1\%$ for O_3 and $< 2.6\%$ for NO_2.

Finally, comparisons with the GEOS-Chem chemical transport model revealed that the model consistently over-estimates tropospheric columns of CO and C_2H_6 observed at TAO. It was determined that the enhanced CO values were partially due to the North American emissions specified in the model, but more work must be done in the future if the source of this discrepancy is to be fully explained.

Dedication

For Jamie,

who showed me the way when she could not see,

who carried me when she could not stand,

and who gave me her pulse when she could not breathe.

Acknowledgements

I am deeply indebted to the many people who have helped provide their guidance and encouragement over the past 4.5 years. None of this work would be possible without their generous contributions and support.

I have been fortunate to receive funding from many different agencies and institutions in support of this work, including the University of Toronto, the Centre for Research in Earth and Space Technology, the Centre for Global Change Science, the Walter C. Sumner Foundation, and the Reginald Blyth Foundation. Funding for the Toronto Atmospheric Observatory was provided by the Natural Science and Engineering Research Council, the Canadian Space Agency, the Canadian Foundation for Climate and Atmospheric Science, ABB Bomem, the Canadian Foundation for Innovation, the Ontario Research and Development Challenge Fund, and the Premiers Research Excellent Award.

Collaborative laboratory work has been supported by many different technicians, undergraduate students and postdoctoral fellows, including P. Chen, S. Like, K. MacQuarrie, C. Midwinter, O. Mikhailov, C. Avis, B. Chugh, D. Edwards, G. Hassanpour, M. Jensen, R. Lindenmaier, R Saari, T. Kerzenmacher, M. Wolff, and D. Yashcov. My knowledge of Fourier transform spectroscopy stems almost entirely from the patient instruction of several friends and colleagues including, M. de Mazière, H. Fast, D. Fu, D. Griffith, F. Hase, N. Jones, R. Mittermeier, K. Sung, and S. Wood.

I owe much to the reliable support of my colleagues and life-long friends that I've made at the University of Toronto, in particular my fellow FTS group of Aldona Wiacek and Debra Wunch, and the TRIAD$^{\text{TM}}$: Annemarie Fraser and Matthew Toohey.

I have been very lucky to have Prof. Kimberly Strong, Prof. Dylan Jones, and Prof. Kaley Walker as my supervising committee. Their unending guidance and mentorship has been invaluable over the course of this project.

Finally, I must thank my family and Jamie Chan, without whom I wouldn't have had the inspiration to write any of this.

Contents

1 Introduction **1**

1.1 Motivation 1

1.2 Objectives 4

1.3 Contributions and Scope of the Project 7

2 Atmospheric Physics and Chemistry **10**

2.1 Atmospheric Composition and Structure 10

2.2 Stratospheric Ozone Depletion 12

2.3 Tropospheric Air Quality 15

2.4 Climate Change 18

3 Fourier Transform Spectroscopy **23**

3.1 Infrared Spectroscopy 23

  3.1.1 Molecular Energy States 23

  3.1.2 Spectral Line Broadening 30

  3.1.3 Atmospheric Radiative Transfer 35

3.2 Fourier Transform Spectrometry 37

  3.2.1 Optical Design of an Ideal FTS 37

  3.2.2 Mathematical Formulation 39

  3.2.3 Limitations of a Real FTS 43

  3.2.4 Advantages of an FTS 48

4 **Instrumentation** **51**

4.1 Toronto Atmospheric Observatory 51

4.2 Bomem DA8 Fourier Transform Spectrometer 55

5 **Observations and Data Analysis** **63**

5.1 Interferograms and Spectral Acquisition 63

5.2 Retrievals 67

5.3 Error Estimates 79

5.4 Information Content Analysis 90

5.5 Trace Gas Concentrations and Submission to the NDACC Archive 95

6 **Ground-Based Data Validation** **112**

6.1 Extended FTS Intercomparison 115

6.1.1 U of T FTS 115

6.1.2 Intercomparison Strategy 116

6.1.3 Data Analysis 118

6.1.4 Tropospheric Species Intercomparison 124

6.1.5 Stratospheric Species Intercomparison 126

6.1.6 Summary of Extended Ground-Based Intercomparison 136

6.2 Focused FTS Intercomparison 139

6.2.1 PARIS-IR 140

6.2.2 Observations and Analysis Strategy 141

6.2.3 Influence of Instrument Line Shape 143

6.2.4 Influence of Instrument Resolution 149

6.2.5 Results from the Focused Intercomparison 155

6.2.6 Summary of Focused Ground-Based Intercomparison 161

7 **Satellite-Based Data Validation** **164**

7.1 Comparisons with SCIAMACHY and ACE 165

7.2 Comparisons with OSIRIS 170

7.2.1 The Optical Spectrograph and Infrared Imager System 171

7.2.2 Stratospheric NO_2 Cross-Validation 174

7.2.3 Stratospheric O_3 Cross-Validation 181

7.2.4 Summary of TAO-OSIRIS Comparisons 188

8 Model-Based Validation 195

8.1 Measurements of Pollutants in Toronto 196

8.2 GEOS-Chem Chemical Transport Model 200

8.3 Tropospheric C_2H_6 Cross-Validation 204

8.4 Tropospheric CO Cross-Validation 208

8.5 Summary and Future Work on Model-Based Validation of Tropospheric Gases 215

9 Conclusions 218

9.1 Summary of Results 218

9.2 Future Work 223

Appendix A 225

Bibliography 244

List of Tables

2.1 2000-2050 projected global pollution emission trends based on chemical transport model calculations driven by a global circulation model (data taken from Wu et al. [2008]). 21

4.1 Spectral coverage of the TAO-FTS filter set. 58

5.1 Number of days on which the TAO-FTS was observing per calendar year. 67

5.2 Summary of the TAO-FTS 2005-2006 data submitted to the NDACC archive. The degrees of freedom for signal were calculated using Equation 5.40. 96

5.3 Summary of the mean percentage error of the species retrieved from TAO-FTS 2005-2006 data submitted to the NDACC archive. All values are composed of the smoothing error and retrieval noise error combined in quadrature. 97

5.4 Summary of the mean degrees of freedom for signal of the species retrieved from TAO-FTS 2005-2006 data submitted to the NDACC archive. All values were calculated using Equation 5.40. 98

5.5 Results from the first stage of quality control for the TAO-FTS 2005-2006 data submitted to the NDACC archive. 99

5.6 Results from the second stage of quality control for the TAO-FTS 2005-2006 data submitted to the NDACC archive. 104

6.1 Instrument parameters from the ground-based, extended FTS intercomparison campaign. 117

6.2 Spectral microwindows used for the retrieval of each trace gas as well as interfering species that were fitted simultaneously in the ground-based, extended FTS intercomparison campaign. Both CH_4 and O_3 (2775) were globally fitted with three simultaneous band-passes. 120

6.3 Median total column differences: 200*(U of T - TAO)/(U of T + TAO), standard deviation of total column differences, theoretical slopes of linear trends, fitted slopes of linear trends, R^2 value of the fits, and the total number of data points for each of the four species investigated. 140

6.4 Instrument parameters from the ground-based, focused FTS intercomparison campaign. 143

6.5 Spectral parameters from the ground-based, focused FTS intercomparison campaign. The signal-to-noise ratio is the mean value determined from the noise in the residual of the spectral fit. 151

6.6 Mean total column differences calculated between the instruments (see Wunch et al. [2007] for details). Bold-faced values are significantly different at the 95% confidence level as derived from the t-test. 162

7.1 Summary of (SCIAMACHY-TAO)/(TAO) comparisons. The first row indicates the % mean difference (with standard error of the mean) between TAO and SCIAMACHY determined for a specific gas, from each algorithm, as well as the scatter associated with the same comparison. The second row shows the same quantities calculated for the average of all 11 ground-based sites. The third row indicates the upper and lower extreme differences for each species. All values are from Dils et al. [2006]. 166

7.2 Summary of TAO-ACE partial column comparisons. The first column indicates mean TAO % differences for each species and standard deviation. The second column indicates the upper and lower difference bounds (with standard deviation) for each species, that is, the minimum and maximum difference of all the ground-based FTS sites involved in the comparison. The CO comparisons used two different smoothing techniques to compare the data products, as such, there is a range of values. All values are from Clerbaux et al. [2008], Mazière et al. [2008], Dupuy et al. [2008], Kerzenmacher et al. [2008], Mahieu et al. [2008], Strong et al. [2008]. . . 169

7.3 Statistics of OSIRIS−TAO monthly mean column amounts. The comparison denoted in the first column gives the two retrieval methods being compared (the first minus the second). The second column gives the number of months compared: n. The third column gives the calculated correlation coefficient: R^2. The fourth column gives the mean percent difference in monthly mean columns: $\overline{\delta}$. The fifth column gives the standard deviation of the mean percent difference in monthly mean columns: σ_δ. The sixth column gives the calculated slope of the linear weighted-least-squares fit to the scatter plots of the first retrieval versus the second retrieval. The seventh column gives the value of the strongest statistical mode present in the histogram of the percent differences. 194

8.1 Spectral microwindows used for the retrieval of C_2H_6 and CO, as well as interfering species that were fitted simultaneously, the mean SNR, and mean total column degrees of freedom for signal (d_s). Both species were retrieved by globally fitting multiple bandpasses. 202

A.1 Spectral microwindows used for the retrieval of each trace gas as well as interfering species that were fitted simultaneously for the 2005-2006 NDACC archival. CH_4 was globally fitted with three simultaneous bandpasses. 226

A.2 Parameterization of *a priori* error covariance and typical measurement error covariance (expressed as SNR) used in the retrieval of gases for the 2005-2006 NDACC archival. 227

List of Figures

2.1 Sample pressure and temperature profiles over Toronto taken from the National Centers for Environmental Prediction (NCEP) analysis for 1 March 2006 (`hyperion.gsfc.nasa.gov/data_services/automailer/index`). . 11

2.2 Estimated changes in natural and anthropogenic contributions to radiative forcing of the climate from 1750-2005 [IPCC, 2007]. LOSU - Level Of Scientific Understanding. 20

3.1 Simulated transmittance spectrum of the ν_2 fundamental vibrational mode of HCN. The rotational lines of the P branch are on the left, those of the Q branch are in the centre, and the R branch on the right. This simulation was performed using spectral line parameters from the HITRAN 2000 database. 30

3.2 Simulations of the Lorentz, Doppler, and Voigt lineshapes. The half-widths at half-maximum were set to 1 for all three calculations. 34

3.3 Schematic representation of a Michelson Interferometer. The amplitude of the source beam is divided at the beamsplitter, travels along the paths z_1 and z_2 to be reflected off the stationary and scan mirrors, respectively, and is then recombined at the beam splitter and sent to the detector. . . 38

3.4 (a) Sinc function; (b) Fourier Transform of a boxcar function (blue) and of a triangle function (red); (c) Ideal ILS (blue) compared with that of a modelled instrument with a 40% modulation loss (red); (d) Empirically determined asymmetric ILS generated with a phase error. 45

3.5 Ray tracing schematic for the field-of-view of a typical FTS. M1 and M2 represent the stationary and moving arms of the interferometer, separated by an OPD of $x/2$. The divergent rays impinge on the mirrors at an angle α from the normal. This effectively decreases the OPD by the distance travelled from A-B-C = $x \cos(\alpha)$. 46

4.1 The Heliostat installed on the roof of the Toronto Atmospheric Observatory directs infrared solar radiation into the laboratory (photo courtesy of A. Wiacek). 53

4.2 The Brewer Spectrophotometer was installed on the roof of the Toronto Atmospheric Observatory in 2005. It records atmospheric observations of UV-Visible solar radiation. 54

4.3 The primary and complementary stations of the Network for the Detection of Atmospheric Composition Change (taken from `www.ndsc.ncep.noaa.gov/`). 57

4.4 FTS and suntracker installation at TAO. The mirrors M1, M2, and M3 serve to couple the heliostat optics to the DA8 FTS. A removable 45° mirror (M4) can be used to couple the FTS to a blackbody source or to direct radiation from the heliostat to other instruments. (Figure courtesy of ABB Bomem) 59

4.5 The DA8 FTS modified Michelson Interferometer. A moving folding mirror selects between the emission port used for solar absorption measurements, and internal sources (shown in the faded portion at top right) used for instrument line shape testing. (Figure courtesy of ABB Bomem) . . . 61

5.1 Measurements made by the TAO-FTS from 2002-2007, distributed by filter (see Table 4.1). 68

5.2 Infrared absorption spectrum recorded by the TAO-FTS on 17 June 2003 (Filter 3 region). 75

5.3 Example fit and residual for the ozone infrared absorption spectral microwindow in the 3045 cm^{-1} region (Filter 3). This microwindow is from the spectrum shown in Figure 5.2, which was recorded on 17 June 2003. The observed spectrum is shown in blue and the forward modelled values are shown in red. The RMS value of the residual is 0.18%. 76

5.4 Example weighting function matrix calculated for the ozone infrared absorption spectral microwindow in the 3045 cm^{-1} region. This was calculated for the spectrum shown in Figure 5.2, which was recorded on 17 June 2003. 77

5.5 Example averaging kernel matrix calculated for the ozone retrieval of the infrared absorption spectral microwindow in the 3045 cm^{-1} region. This was calculated for the spectrum shown in Figure 5.2, which was recorded on 17 June 2003. 78

5.6 Example rows of the averaging kernel matrix calculated for the ozone infrared absorption spectral microwindow in the 3045 cm^{-1} region. Each curve represents a different value on the vertical grid – the corresponding altitude (in km) is indicated in the legend. This was calculated for the spectrum shown in Figure 5.2, which was recorded on 17 June 2003. . . . 79

5.7 *A priori* profile (black) and retrieved profile (blue) from the ozone features in the 3045 cm^{-1} region. This was calculated from the spectrum shown in Figure 5.2, which was recorded on 17 June 2003. The volume mixing ratio is expressed in parts per volume. 80

5.8 Ozone *a priori* covariance matrix contours, $\mathbf{S_a}$, used for retrievals with the TAO-FTS. For each layer, the error is given as 20%, that is $\sigma^2 = (0.2)^2 = 0.04$. 82

5.9 Ozone smoothing error covariance matrix contours, $\mathbf{S_s}$, calculated for the retrieval using the spectrum shown in Figure 5.2, which was recorded on 17 June 2003. 83

5.10 Ozone retrieval noise covariance matrix contours, $\mathbf{S_m}$, calculated for the retrieval using the spectrum shown in Figure 5.2, which was recorded on 17 June 2003. 85

5.11 Ozone state space interference error covariance matrix contours, $\mathbf{S_p}$, calculated for the retrieval using the spectrum shown in Figure 5.2, which was recorded on 17 June 2003. 87

5.12 Ozone total retrieval error covariance matrix contours, $\mathbf{S_t}$, calculated for the retrieval using the spectrum shown in Figure 5.2, which was recorded on 17 June 2003. 88

5.13 Ozone retrieval variances (σ^2) derived for the retrieval of the spectrum shown in Figure 5.2, which was recorded on 17 June 2003. The total error (black) is determined by adding the retrieval noise (red), the state space parameter interference error (purple), the smoothing error (green), and the forward model error (cyan), in quadrature. The *a priori* error is shown in blue. All values are expressed in parts per volume. 89

5.14 N_2O retrieval variances (σ^2) derived for the retrieval of the spectrum shown in Figure 5.2, which was recorded on 17 June 2003. The total error (black) is determined by adding the retrieval noise (red), the state space parameter interference error (purple), the smoothing error (green), and the forward model error (cyan), in quadrature. The *a priori* error is shown in blue. All values are expressed in parts per volume. 91

5.15 Ozone leading singular vectors and the associated degree of freedom for signal per vector calculated from their singular values for the retrieval using the spectrum shown in Figure 5.2, which was recorded on 17 June 2003. The total degrees of freedom for signal for the retrieval is 1.67. . . 95

5.16 The second stage of the quality control process applied to retrievals of HCl. Accepted profiles have solid lines, while rejected profiles have dashed lines. The volume mixing ratio is expressed in parts per volume. 102

5.17 Results from the second stage of the quality control process applied to retrievals of HCl. Total columns of HCl are shown as blue dots, with rejected column values circled in red. The rejected columns were represented by the profiles with the dashed lines in Figure 5.16. 103

5.18 HCl total columns, stratospheric columns, and tropospheric columns submitted to the NDACC archive. Error bars represent smoothing error and retrieval noise added together in quadrature. 105

5.19 HF total columns, stratospheric columns, and tropospheric columns submitted to the NDACC archive. Error bars represent smoothing error and retrieval noise added together in quadrature. 106

5.20 O_3 total columns, stratospheric columns, and tropospheric columns submitted to the NDACC archive. Error bars represent smoothing error and retrieval noise added together in quadrature. 107

5.21 N_2O total columns, stratospheric columns, and tropospheric columns submitted to the NDACC archive. Error bars represent smoothing error and retrieval noise added together in quadrature. 108

5.22 CH_4 total columns, stratospheric columns, and tropospheric columns submitted to the NDACC archive. Error bars represent smoothing error and retrieval noise added together in quadrature. 109

5.23 NO total columns, stratospheric columns, and tropospheric columns submitted to the NDACC archive. Error bars represent smoothing error and retrieval noise added together in quadrature. 110

5.24 NO_2 total columns, stratospheric columns, and tropospheric columns submitted to the NDACC archive. Error bars represent smoothing error and retrieval noise added together in quadrature. 111

6.1 Time series of coincident CH_4 total column observations. Blue circles represent the U of T FTS columns, while red squares represent the TAO FTS columns. Error bars are a combination of retrieval noise, smoothing error, and state space parameter interference error. 125

6.2 Scatter plot and fit of coincident CH_4 total column observations. Measurements made on different days are represented by different symbols. Error bars are as for Figure 6.1. 126

6.3 Time series of coincident N_2O total column observations. Blue circles represent the U of T FTS columns, while red squares represent the TAO FTS columns. Error bars are a combination of retrieval noise, smoothing error, and state space parameter interference error. 127

6.4 Scatter plot and fit of coincident N_2O total column observations. Measurements made on different days are represented by different symbols. Error bars are as for Figure 6.1. 128

6.5 Time series of coincident O_3 total column observations retrieved from the 3040 cm^{-1} microwindow. Blue circles represent the U of T FTS columns, while red squares represent the TAO FTS columns. Error bars are a combination of retrieval noise, smoothing error, and state space parameter interference error. 129

6.6 Time series of coincident O_3 total column observations retrieved from the 2775 cm^{-1} microwindow. Blue circles represent the U of T FTS columns, while red squares represent the TAO FTS columns. Error bars are a combination of retrieval noise, smoothing error, and state space parameter interference error. 130

6.7 Scatter plot and linear fit of coincident O_3 total column observations retrieved from the 3040 cm^{-1} microwindow. Measurements made on different days are represented by different symbols. Error bars are as for Figure 6.1. 131

6.8 Scatter plot and linear fit of coincident O_3 total column observations retrieved from the 2775 cm^{-1} microwindow. Measurements made on different days are represented by different symbols. Error bars are as for Figure 6.1. 132

6.9 O_3 averaging kernels for the 3040 cm^{-1} microwindow retrieval: (a) total column averaging kernels, (b) density-weighted total column averaging kernels, and (c) ratio of the U of T FTS total column averaging kernel to that of the TAO-FTS. Blue circles represent the U of T FTS, red squares represent the TAO FTS, and black triangles represent U of T FTS to TAO FTS ratio. 133

6.10 O_3 averaging kernels for the 2775 cm^{-1} microwindow retrieval: (a) total column averaging kernels, (b) density-weighted total column averaging kernels, and (c) ratio of the U of T FTS total column averaging kernel to that of the TAO-FTS. Blue circles represent the U of T FTS, red squares represent the TAO FTS, and black triangles represent U of T FTS to TAO FTS ratio. 134

6.11 Time series of coincident HCl total column observations. Blue circles represent the U of T FTS columns, while red squares represent the TAO FTS columns. Error bars are a combination of retrieval noise, smoothing error, and state space parameter interference error. 136

6.12 Scatter plot and linear fit of coincident HCl total column observations. Measurements made on different days are represented by different symbols. Error bars are as for Figure 6.1. 137

6.13 HCl averaging kernels retrieved from the 2859 cm^{-1} microwindow: (a) total column averaging kernels, (b) density-weighted total column averaging kernels, and (c) ratio of the U of T FTS total column averaging kernel to that of the TAO-FTS. Blue circles represent the U of T FTS, red squares represent the TAO FTS, and black triangles represent U of T FTS to TAO FTS ratio. 138

6.14 Experimental configuration of the TAO-FTS, U of T FTS, and PARIS-IR for the focused intercomparison. (Figure courtesy of D. Fu). 142

6.15 Modulation efficiency and phase error for the TAO-FTS (left), U of T FTS (centre), and PARIS-IR (right) measured during the focused intercomparison campaign. The black curves with dots were determined from gas cell measurements analysed using LINEFIT v.9.0 and v.11.0 [Hase et al., 1999]. The blue curves represent the calculated EAP and EPHS parameters derived from SFIT2 fits. The monotonic decrease in modulation efficiency observed by all instruments indicates that the intensity of the interferogram signal decreases with OPD, as expected. (Figure courtesy of D. Wunch). 145

6.16 Mean columns from data recorded on 2 September 2005, using the EPHS/EAP retrieval (blue), the standard retrieval (red) and the ILS input retrieval (black). The thick black horizontal line indicates the TAO-FTS column means on the same day and the grey shading represents the standard deviation of the TAO-FTS retrieved values. The error bars indicate the standard deviation of the retrieved values. (Figure courtesy of D. Wunch). 148

6.17 Simulated retrievals of ozone columns in the 3040 cm^{-1} microwindow as a function of OPD (assumed SNR = 250). Mean column amounts are shown with the 2σ standard deviation error bars derived from the ensemble of the two sets of retrievals: one that retrieves third-order polynomial coefficients for the EPHS and EAP functions from the microwindow itself (blue circles, labelled as "EPHS/EAP retrieved"), and one that does not retrieve coefficients (red squares, labelled as "standard retrieval"). The *a priori* column value is shown as a black dotted line and the "truth" is shown as a black solid line, where "truth" is the column amount that was used to generate the model spectra. 152

6.18 Same as Figure 6.17 but for simulations of ozone in the 2775 cm^{-1} microwindow. 153

6.19 Same as Figure 6.17 but for simulations of HCl. 154

6.20 Same as Figure 6.17 but for simulations of N_2O. 155

6.21 Same as Figure 6.17 but for simulations of CH_4. 156

6.22 Ozone total columns retrieved from the 3040 cm^{-1} microwindow, co-added to 20-minute integration times so as to be consistent with that of the TAO-FTS. Columns from all three instruments are plotted against the coincident TAO columns, with PARIS-IR denoted by blue circles, the U of T FTS denoted by red squares, and the TAO-FTS denoted by a black 1:1 line (TAO vs TAO). Error bars represent state space parameter interference error, retrieval noise, and smoothing error added in quadrature. 157

6.23 Same as Figure 6.22 but for ozone retrieved from the 2775 cm^{-1} microwindow. 158

6.24 Same as Figure 6.22 but for HCl retrievals. 159

6.25 Same as Figure 6.22 but for N_2O retrievals. 160

6.26 Same as Figure 6.22 but for CH_4 retrievals. 161

7.1 “Virtual coincidence” correction of NO_2 partial columns measured at TAO on 1 Sept. 2005 (shown as blue circles). The slope was fixed for each day at 1.02 $\times 10^{14}$ molecules/cm^2/hr and only the vertical offset was fitted to the columns (shown as the red solid line). The “coincidences” are extrapolated from the slope so as to coincide with the times of the OSIRIS overpass (shown as red squares). 176

7.2 Monthly observation frequency of AM and PM measurements recorded by the TAO-FTS (red) and OSIRIS (blue) from May 2002 to December 2006. The dashed line represents the minimum statistical limit of five measurements; any month in which either instrument has fewer measurements is not used for this comparison. 177

7.3 NO_2 partial column averaging kernel for the TAO-FTS. This represents the altitude sensitivity of the measurement to atmospheric volume mixing ratios between 16-50 km. 178

7.4 Timeseries of monthly mean NO_2 partial columns for each month in which there are more than five measurements. Blue triangles represent the DOAS-based retrievals from OSIRIS, red circles represent the MART-based retrievals from OSIRIS, and gray squares represent the values derived from the TAO-FTS. Error bars show one standard deviation. 179

7.5 NO_2 monthly means derived from TAO-FTS observations plotted against monthly means derived from OSIRIS-MART retrievals. Error-bars represent one standard deviation. The solid line shows the 1:1 line and the dashed line shows a weighted-least-squares linear fit to the data. 180

7.6 Histogram of the differences between NO_2 monthly mean partial columns: 100*2*(MART - TAO)/(MART + TAO). 181

7.7 NO_2 monthly means derived from TAO-FTS observations plotted against monthly means derived from OSIRIS-DOAS retrievals. Error bars represent one standard deviation. The solid line shows the 1:1 line and the dashed line shows a weighted-least-squares linear fit to the data. 182

7.8 Histogram of the differences between NO_2 monthly mean partial columns: 100*2*(DOAS - TAO)/(DOAS + TAO). 183

7.9 NO_2 monthly means derived from OSIRIS-MART observations plotted against monthly means derived from OSIRIS-DOAS retrievals. Error bars represent one standard deviation. The solid line shows the 1:1 line and the dashed line shows a weighted-least-squares linear fit to the data. . . . 184

7.10 Histogram of the differences between NO_2 monthly mean partial columns: 100*2*(DOAS - MART)/(DOAS + MART). 185

7.11 Timeseries of monthly mean O_3 partial columns for each month in which there are more than five measurements. Blue triangles represent the DOAS-based retrievals from OSIRIS, red circles represent the MART-based retrievals from OSIRIS, and gray squares represent the values derived from the TAO-FTS. Error bars show one standard deviation. 186

7.12 O_3 partial column averaging kernel for the TAO-FTS. This represents the altitude sensitivity of the measurement to atmospheric volume mixing ratios between 16-50 km. 187

7.13 O_3 monthly means derived from TAO-FTS observations plotted against monthly means derived from OSIRIS-MART retrievals. Error bars represent one standard deviation. The solid line shows the 1:1 line and the dashed line shows a weighted-least-squares linear fit to the data. 188

7.14 Histogram of the differences between O_3 monthly mean partial columns: 100*2*(MART - TAO)/(MART + TAO). 189

7.15 O_3 monthly means derived from TAO-FTS observations plotted against monthly means derived from OSIRIS-Triplet retrievals. Error bars represent one standard deviation. The solid line shows the 1:1 line and the dashed line shows a weighted-least-squares linear fit to the data. 190

7.16 Histogram of the differences between O_3 monthly mean partial columns: 100*2*(Trip. - TAO)/(Trip. + TAO). 191

7.17 O_3 monthly means derived from OSIRIS-Triplet observations plotted against monthly means derived from OSIRIS-MART retrievals. Error bars represent one standard deviation. The solid line shows the 1:1 line and the dashed line shows a weighted-least-squares linear fit to the data. 192

7.18 Histogram of the differences between O_3 monthly mean partial columns: 100*2*(Triplet - MART)/(Triplet + MART). 193

8.1 Timeseries of CO total columns measured by ground-based FTS sites in Europe. Measurements are shown from Ny Ålesund (black), Kiruna (red), Harestua (green), Zugspitze (blue), Jungfraujoch (cyan), and Izaña (pink), (courtesy of UFTIR group; Principal Investigator: M de Mazière; http://www.nilu.no/uftir/). 197

8.2 Top: Timeseries of C_2H_6 total columns observed by ground-based FTS sites in Europe. Top: measurements from Ny Ålesund (red circles), Kiruna (triangles), and Harestua (green circles). Bottom: measurements from Zugspitze (orange circles), Jungfraujoch (triangles), and Izaña (green circles), (courtesy of UFTIR group; Principal Investigator: M de Mazière; http://www.nilu.no/uftir/). 198

8.3 2005 Daily mean surface CO concentrations observed by the Air Quality Ontario observing network site in downtown Toronto. Error bars represent 1 standard deviation, the orange line (30 ppm) represents the level above which CO concentrations are considered *poor*, the red line (50 ppm) represents the level above which CO concentrations are considered *extremely poor*, and the black vertical lines denote days upon which an air quality advisory was publicly issued. (Data obtained from `http://www.airqualityontario.ca/`). 201

8.4 Daily mean surface CO concentrations observed by the Air Quality Ontario monitoring network site in downtown Toronto in 2005 (blue squares) compared with like daily means generated by GEOS-Chem (red circles). The GEOS-Chem values are from the lowest layer output for the grid-box encompassing Toronto (974.07 hPa). 203

8.5 Typical horizontal measurement smearing that occurs during an observation in the summer by the TAO-FTS. Differing colours represent different altitudes along the line-of-sight during a 20-minute observation. This example was calculated for 17 August 2007 using geometric assumptions. (Figure courtesy of F. Kolonjari). 205

8.6 Same as Figure 8.5 but representative of winter observing conditions. This example was calculated for 17 January 2008 using geometric assumptions. (Figure courtesy of F. Kolonjari). 206

8.7 Sample C_2H_6 profile over Toronto generated by the GEOS-Chem model (red) and the same C_2H_6 profile smoothed with the TAO-FTS averaging kernel and *a priori* profile (blue). VMR is expressed in parts per volume. 207

8.8 All C_2H_6 profiles over Toronto generated by the GEOS-Chem model in 2005. The raw profiles output from the model are shown on the left panel, while the right panel shows the same profiles after smoothing with the TAO-FTS averaging kernel and *a priori* profile. The black, horizontal line at 3-km altitude represents the lower boundary of the partial column calculation. VMR is expressed in parts per volume. 208

8.9 Timeseries of C_2H_6 3-12 km partial column retrievals from the TAO-FTS. The median partial column error is $\approx$ 1.3% and is composed of state space parameter interference error and retrieval noise added together in quadrature. For clarity, the error bars are not shown. 209

8.10 Timeseries of C_2H_6 3-12 km partial column daily means retrieved from the TAO-FTS (red) and the GEOS-Chem model (blue). Error bars represent 1 standard deviation (for the days upon which there is only one measurement, the error bars are set to 0). 210

8.11 All CO profiles over Toronto generated by the GEOS-Chem model in 2005. The raw profiles output from the model are shown on the left, while the right shows the same profiles after smoothing with the TAO-FTS averaging kernel and *a priori* profile. The black, horizontal line at 3 km altitude represents the lower boundary of the partial column calculation. VMR is expressed in parts per volume. 211

8.12 Sample CO profile over Toronto generated by the GEOS-Chem model (red) and the same CO profile smoothed with the TAO-FTS averaging kernel and *a priori* profile (blue). VMR is expressed in parts per volume. 212

8.13 Timeseries of CO 3-12 km partial column retrievals from the TAO-FTS. The median partial column error is less than 1% and is composed of state space parameter interference error and retrieval noise added together in quadrature. For clarity, the error bars are not shown. 213

8.14 Timeseries of CO 3-12 km partial column daily means retrieved from the TAO-FTS (red) and the GEOS-Chem model (blue). Error bars represent 1 standard deviation (for the days upon which there is only one measurement, the error bars are set to 0). 214

8.15 Timeseries of CO 3-12 km partial column daily means retrieved from the TAO-FTS (red) and the GEOS-Chem model with a North American emission reduction of 60% (blue). Error bars represent 1 standard deviation (for the days upon which there is only one measurement, the error bars are set to 0). 215

A.1 Fit and residual for the HCl infrared absorption spectral microwindow in the 2925 cm^{-1} region (Filter 3) from an observation taken on 10 Aug 2005. The observed spectrum is shown in blue and the forward modelled values are shown in red. 228

A.2 Averaging kernel matrix calculated for the HCl infrared absorption spectral microwindow shown in Figure A.1. 229

A.3 Fit and residual for the HF infrared absorption spectral microwindow in the 4039 cm^{-1} region (Filter 1) from an observation taken on 6 Jan 2006. The observed spectrum is shown in blue and the forward modelled values are shown in red. 230

A.4 Averaging kernel matrix calculated for the HF infrared absorption spectral microwindow shown in Figure A.3. 231

A.5 Fit and residual for the N_2O infrared absorption spectral microwindow in the 2482 cm^{-1} region (Filter 3) from an observation taken on 6 Nov 2006. The observed spectrum is shown in blue and the forward modelled values are shown in red. 232

A.6 Typical averaging kernel matrix calculated for the N_2O infrared absorption spectral microwindow shown in Figure A.5. 233

A.7 Typical fit and residual for the NO_2 infrared absorption spectral microwindow in the 2914 cm^{-1} region (Filter 3) from an observation taken on 26 Jan 2006. The observed spectrum is shown in blue and the forward modelled values are shown in red. 234

A.8 Typical averaging kernel matrix calculated for the NO_2 infrared absorption spectral microwindow shown in Figure A.7. 235

A.9 Typical fit and residual for the NO infrared absorption spectral microwindow in the 1900 cm^{-1} region (Filter 5) from an observation taken on 31 Aug 2006. The observed spectrum is shown in blue and the forward modelled values are shown in red. 236

A.10 Typical averaging kernel matrix calculated for the NO infrared absorption spectral microwindow shown in Figure A.9. 237

A.11 Typical fit and residual for the O_3 infrared absorption spectral microwindow in the 3045 cm^{-1} region (Filter 3) from an observation taken on 14 June 2006. The observed spectrum is shown in blue and the forward modelled values are shown in red. 238

A.12 Typical averaging kernel matrix calculated for the O_3 infrared absorption spectral microwindow shown in Figure A.11. 239

A.13 Typical fit and residual for the CH_4 infrared absorption spectral microwindow in the 2651 cm^{-1} region (Filter 3) from an observation taken on 24 Nov 2006. The observed spectrum is shown in blue and the forward modelled values are shown in red. 240

A.14 Typical fit and residual for the CH_4 infrared absorption spectral microwindow in the 2667 cm^{-1} region (Filter 3) from an observation taken on 24 Nov 2006. The observed spectrum is shown in blue and the forward modelled values are shown in red. 241

A.15 Typical fit and residual for the CH_4 infrared absorption spectral microwindow in the 2674 cm^{-1} region (Filter 3) from an observation taken on 24 Nov 2006. The observed spectrum is shown in blue and the forward modelled values are shown in red. 242

A.16 Typical averaging kernel matrix calculated for all three CH_4 infrared absorption spectral microwindows shown in Figures A.13–A.15. 243

List of Acronyms

ACE	Atmospheric Chemistry Experiment
AQHI	Air Quality Health Index
AQI	Air Quality Index
CFC	ChloroFluoroCarbon
CNRS	Centre National de la Recherche Scientifique
CTM	Chemical Transport Model
DFT	Discrete Fourier Transform
DOAS	Differential Optical Absorption Spectroscopy
EAP	Effective Apodization Parameters
EOS	Earth Observing System
EPA	Environmental Protection Agency
EPHS	Effective PHaSe error parameters
FFT	Fast Fourier Transform
FOV	Field-Of-View
FTIR	Fourier Transform InfraRed spectroscopy

FTS	Fourier Transform Spectrometer
GHG	GreenHouse Gas
GLO	Ground Level Ozone
GMAO	Global Modeling and Assimilation Office
HALOE	HALogen Occultation Experiment
HCFC	HydroChloroFluoroCarbon
HITRAN	HIgh-resolution TRANsmission molecular absorption database
ICARTT	International Consortium for Atmospheric Research on Transport and Transformation
ILS	Instrument Line Shape
IMAP	Iterative Maximum A Posteriori method
IMLM	Iterative Maximum Likelihood Method
IPCC	Intergovernmental Panel on Climate Change
IRWG	InfraRed Working Group
LOSU	Level Of Scientific Understanding
LTE	Local Thermodynamic Equilibrium
MAESTRO	Measurements of Aerosol Extinction in the Stratosphere and Troposphere Retrieved by Occultation
MANTRA	Middle Atmosphere Nitrogen TRend Assessment
MAP	Maximum A Posteriori

MART	Multiplicative Algebraic Reconstruction Technique
MCT	Mercury Cadmium Tellurium
MIPAS	Michelson Interferometer for Passive Atmospheric Sounding
MOPITT	Measurements Of Pollution In The Troposphere
MLS	Microwave Limb Sounder
NASA	National Aeronautics and Space Administration
NCEP	National Centers for Environmental Prediction
NDACC	Network for the Detection of Atmospheric Composition Change
NEI	National Emissions Inventory
NMHC	Non-Methane HydroCarbon
NMVOC	Non-Methane Volatile Organic Compounds
OEM	Optimal Estimation Method
OPD	Optical Path Difference
OMI	Ozone Monitoring Experiment
OSIRIS	Optical Spectrograph and InfraRed Imaging Spectrometer
PARIS-IR	Portable Atmospheric Research Interferometric Spectrometer for the InfraRed
PDF	Probability Density Function
PM	Particulate Matter
RMS	Root-Mean-Square

SAOZ	Système D'Analyse par Observations Zénithales
SCIAMACHY	SCanning and Imaging Absorption SpectroMeter for Atmospheric CHartographY
SMR	Sub-Millimetre Radiometer
SNR	Signal-to-Noise Ratio
SPHS	Simple PHaSe error parameter
SPS	Sun Photo Spectrometer
SSE	Sum of the Squared Error
SST	Sum of the Squared Total error
SZA	Solar Zenith Angle
TAO	Toronto Atmospheric Observatory
TEAP	Technology and Economic Assessment Panel
TES	Tropospheric Emission Spectrometer
U of T	University of Toronto
UFTIR	timeseries of Upper free troposphere observations by Fourier Transform InfraRed spectroscopy
UV	UltraViolet
VMR	Volume Mixing Ratio
VOC	Volatile Organic Compound
WFM	Weighting Function Modified method

WHO	World Health Organization
ZPD	Zero Path Difference

Chapter 1

Introduction

1.1 Motivation

Environmental change is one of the most important global issues facing society. Air quality, ozone depletion, and climate change are all issues that receive considerable exposure in both the social and political arenas. The potential impact of atmospheric change on the economy and health of Canadians is dramatic. Scientific research into the causes, consequences, and mitigation of such changes is essential for informed policy-making.

The changing chemical composition of the atmosphere impacts life on Earth in many direct and indirect ways. In turn, the feedbacks associated with these changes also influence the atmosphere, resulting in numerous nonlinear interactions. It is now accepted that human activity has resulted in perturbing the natural geochemical cycles of the Earth and atmosphere, including the carbon cycle, the oxygen cycle, and the nitrogen cycle [IPCC, 1995]. Anthropogenic emissions of synthetic chemical compounds have resulted in changes to atmospheric composition which, in turn, have negatively influenced human health [WHO, 2003]. There are also many negative indirect effects of the changing atmosphere, including decreased global crop yield [Tebaldi and Lobell, 2008], destruction of marine life through ocean acidification [Orr et al., 2005], and enhanced natural destruction through increased severe weather [Emanuel, 2005], to name a few. The continued monitoring of atmospheric composition is necessary to develop a better understanding of these interactions and impacts, as well as to aid in forecasting future atmospheric trends.

Poor air quality has been linked to respiratory and cardiovascular diseases as well as subclinical and symptomatic events that do not immediately warrant medical treatment and can often go unreported. It has been found that minor increases in the ambient concentrations of trace pollutants can result in significant health complications. An increase of 12.5% in the ground-level concentration of nitrogen dioxide (NO_2) and 8.6% in the ground-level concentration of particulate matter (PM) is significantly correlated (to the 95% confidence level) with an increase in the risk of emergency myocardial infarction [Zanobetti and Schwartz, 2006]. It is known that exposure to increased concentrations of ozone (O_3), NO_2, and PM all result in decreased lung function, an increase in chronic obstructive pulmonary disease, and a consequent decrease in life expectancy [WHO, 2004]. When mean O_3 levels in ambient air are over 100 μg/m^3 in an eight-hour period, 1-2% of all deaths that occur during this time can be attributed to this increase in pollution [WHO, 2005]. The US Environmental Protection Agency (EPA) states that O_3 can aggravate asthma as well as inflame and damage the lining of the lung [EPA, 1999]. In the two-week period immediately following an increased pollutant event in an urban centre, it was found that the total cardiopulmonary mortality increased by as much as 2.9% [Neubergera et al., 2007]. Carbon monoxide gas (CO) is another important pollutant that can enter the bloodstream and inhibit oxygen uptake by human organs and tissues [Ontario Ministry of the Environment, 2007]. A study involving levels of five pollutants in 13 of Canada's largest cities revealed that mortality doubles from 10.6 to 20.9 deaths/10^5 population/day when their concentrations are highest [Stieb et al., 2002]. The maximum concentrations for PM, NO_2, and CO recorded in this study were all found in Canada's largest urban centre: Toronto. It is estimated that in the City of Toronto, approximately 6000 hospital admissions and 1700 deaths each year are due to exposure to outdoor air pollution [Toronto Public Health, 2004].

Many of the trace gases that contribute to poor air quality are also related to climate forcing. The primary greenhouse gases that perturb the radiative balance of the atmosphere are methane (CH_4), nitrous oxide (N_2O), carbon dioxide (CO_2), and halocarbons (carbonaceous compounds that contain fluorine, chlorine, and bromine) [IPCC, 2007]. CO_2 emissions from global annual combined fossil fuel combustion and cement manufacture have increased by 70% over the last 30 years [Marland et al., 2006], while measurements of CO_2 concentrations have indicated an average increase of 1.4 ppm/yr in the past 45 years [Keeling and Whorf, 2005]. Observations of CH_4 have shown that its global concentration has increased by 30% in the 25 years prior to 1988 [Blake and Rowland, 1988], though its growth rate has slowed to almost zero in the past 15 years [Dlugokencky et al., 2003]. The reasons for the recent decrease in the CH_4 growth rate are not well understood, nor are implications for future changes [IPCC, 2001]. For the past three decades, concentrations of N_2O have been increasing at a rate of 0.26%/yr [Thompson et al., 2004]. The increases in concentrations of these three gases since the pre-industrial era are responsible for a radiative forcing perturbation of more than 2 W/m^2 [IPCC, 2007]. This increased radiative forcing can potentially increase the global surface temperature of the Earth, resulting in agricultural perturbations [Parry et al., 2004], decreased biodiversity in ecosystems [Root et al., 2003], and equilibrium changes in global biogeochemical cycles [Friedlingstein et al., 2003]. In the past five years in Toronto alone, the record for the frequency of *hot days* (days for which the air temperature is above 30°C) has been broken twice, with 23 days in 2002 and 27 days in 2005 [Ontario Ministry of the Environment, 2004].

Many greenhouse gases have long chemical lifetimes which allow them to be transported into the stratosphere, where they can result in perturbations to the O_3 layer. Average springtime O_3 concentrations in the stratosphere have decreased by 37% in Antarctic regions compared to (1970-1982) mean values [WMO, 2007]. These decreases have been caused by catalytic loss cycles associated with halogenated compounds (see Section 2.2). By reducing the amount of O_3 in the stratosphere, high-energy, ultra-violet, *erythemal* radiation emitted by the Sun is able to reach the Earth's surface more efficiently [Bernhard et al., 2006]. From 1979-1998, the amount of erythemal radiation incident on the Earth's surface has increased by as much as 8% in some parts of the globe, with a growth rate of 2-9% at Toronto's latitude [Tarasick et al., 2003]. The estimated increase in instances of skin cancer due to exposure to erythemal radiation caused by reduced stratospheric O_3 by 2050 is 7.5-35% [Slaper et al., 1996]. In Ontario, it is estimated that one-in-three of all cancer diagnoses are skin cancer, while one-in-seven Canadians will contract some form of skin cancer [Cancer Care Ontario, 2005].

In order to provide insight and to aid in informing policy surrounding these issues, it is necessary to continually monitor concentrations of the aforementioned trace gases and to understand how and why they are changing. The Toronto Atmospheric Observatory provides adequate instrumentation for the long-term monitoring of these, and other, trace gases.

1.2 Objectives

The Toronto Atmospheric Observatory (TAO) houses a suite of instruments that are dedicated to monitoring concentrations of various trace gases in the lower and middle atmosphere over downtown Toronto. The principal instrument is a Fourier Transform Spectrometer (FTS) that measures high-resolution infrared signatures of over 20 species at different altitudes (see Section 4.2). TAO has been certified by the Network for the Detection of Atmospheric Composition Change (NDACC) as a complementary station. This ensures that the TAO-FTS adheres to an internationally recognized standard of observations and analysis. The initial research that was done to establish and demonstrate the observational capability of the TAO-FTS is described by Wiacek et al. [2007].

These measurements of trace gases provide quasi-instantaneous temporal sampling of the atmosphere above Toronto. By utilizing the modern remote sensing analysis technique of Optimal Estimation, the vertical distribution of trace gases and their associated errors can be determined [Wiacek, 2006]. The concentrations of these compounds over a range of altitudes can be determined and can provide more information than surface measurements; the ability to detect trace gases at altitudes as high as ≈100 km with the TAO-FTS has already been demonstrated [Wiacek et al., 2006]. To ensure that these retrieved values are representative of the true state of the atmosphere, they are validated against similar observations from other ground-based and satellite-based instruments. However it should be noted that because of the difficulties associated with making altitude-resolved observations of gases, rigorous validation is not always possible.

As a complementary instrument of the NDACC, it is required that retrieved columns of trace gases monitored by the TAO-FTS be archived in the NDACC database. The first such submission was completed in June 2005 [Wiacek, 2006], and the second submission was completed in September 2007 as part of this project. This work strives to provide the first rigorous validation of the TAO-FTS observations through comparison with other measurements. The capability and precision of the TAO-FTS will be shown by analysing the quality of the derived columns for submission to the NDACC database, including all error calculations and quality assurance procedures. Following this, the TAO-FTS data products will be validated against ground-based and satellite-based measurements and model output.

Two ground-based campaigns involving two additional, lower-resolution FTS instruments were undertaken. One of these campaigns provides the longest, continual, side-by-side intercomparison of FTS measurements to date and was used to identify small systematic and multiplicative biases between the instruments' observations of O_3, CH_4, N_2O, and hydrogen chloride (HCl).

The satellite-based validation assesses TAO-FTS observations from the first four years of operation. The TAO-FTS observations of N_2O, O_3, HCl, CH_4, nitrogen oxide (NO), nitrogen dioxide (NO_2), and carbon monoxide (CO) were compared with like observations from Atmospheric Chemistry Experiment Fourier Transform Spectrometer (ACE-FTS) satellite instrument [Strong et al., 2008, Dupuy et al., 2008, Mahieu et al., 2008, Mazière et al., 2008, Kerzenmacher et al., 2008, Clerbaux et al., 2008]. Observations of CH_4, N_2O and CO were further compared with measurements from the SCanning and Imaging Absorption spectroMeter for Atmospheric CartograpHY (SCIAMACHY) satellite instrument [Dils et al., 2006]. All of these comparisons consisted of binning the TAO-FTS observations with many other ground-based observations so as to best validate the satellite data products. A dedicated assessment of the O_3 and NO_2 observing capability of the TAO-FTS was carried out by statistically comparing observations of these gases with measurements from the Optical Spectrograph and InraRed Imaging Spectrometer (OSIRIS).

The final assessment focused on preliminary comparisons of concentrations of CO and ethane (C_2H_6) observed by the TAO-FTS with like estimates generated by the GEOS-Chem three-dimensional, global, chemical transport model. Comparisons with the model output did not focus on identifying quantitative differences but rather on understanding how well these species are represented in the model fields over Toronto.

The results from these various validation efforts provide the first quantitative assessment of trace gas measurements made at the Toronto Atmospheric Observatory and show that the TAO-FTS can provide data that is invaluable for addressing scientific questions related to atmospheric climate change, tropospheric air quality, and stratospheric O_3 depletion.

1.3 Contributions and Scope of the Project

As this project endeavors to validate the large set of data recorded by the TAO-FTS against several other data sets, it involved collaborative work with many research groups. Every effort has been made to ensure that the work documented here has been done solely for this project and, where necessary, contributions from others are properly acknowledged.

The Fourier transform spectroscopy that is performed at the Toronto Atmospheric Observatory (Chapters 3 and 4) was a collaborative effort. The initial work that was done in establishing TAO and its standard operations was in conjunction with a fellow PhD student (Aldona Wiacek) and her contributions to this project are documented in her thesis [Wiacek, 2006]. She also aided in developing the nominal data analysis routines (see Chapter 5), however all of the TAO-FTS results shown in this work were generated entirely as part of this project. Throughout this work, every effort has been made to acknowledge the work of Wiacek [2006] and ensure that no results have been improperly duplicated. The instrument line shape characterization and maintenance protocol of the TAO-FTS were developed during an MSc project [Taylor, 2003]. While the day-to-day operations of TAO, including regular observations and maintenance of instruments, were overseen as part of this project, there was operational help from 10 different undergraduate students and technicians.

The ground-based validation work described in Chapter 6 was a collaboration between the University of Toronto and the University of Waterloo. All observations and results from the U of T FTS were provided by former PhD student Debra Wunch and technician Clive Midwinter from Toronto. Observations and results from the Portable Atmospheric Research Interferometric Spectrometer for the Infrared (PARIS-IR) instrument were provided by former PhD student Dejian Fu from Waterloo. Results from the comparisons shown here were all generated as part of this project unless otherwise identified as contributions from Wunch et al. [2007].

Chapter 7 discusses satellite-based validation that consists of contributions that have been made to larger validation efforts for the ACE-FTS instrument and the SCIAMACHY instrument, as well as comparisons with the OSIRIS instrument that were done solely as part of this project. All of the TAO-FTS results that were used in these comparisons were generated as part of this project with the exception of the CO columns used in ACE-FTS validation [Clerbaux et al., 2008]. Results that were submitted to validation efforts carried out for SCIAMACHY were analysed at the Belgian Institute for Space Aeronomy by former PhD student Bart Dils. TAO-FTS data products that were submitted for comparison with ACE-FTS observations were analysed by several different research groups: O_3, N_2O, NO, and NO_2 data were validated by fellow colleagues in our research group at the University of Toronto, HCl results were analysed by Dr. Emmanuel Mahieu at the Université de Liège, and CH_4 results were analysed by Dr. Martine de Mazière at the Belgian Institute for Space Aeronomy.

OSIRIS O_3 and NO_2 results generated by the Multiplicative Algebraic Reconstruction

Technique (MART) retrieval technique were provided by Prof. Douglas Degenstein's research group at the University of Saskatchewan. OSIRIS results generated by the triplet retrieval algorithm and by the DOAS algorithm were provided by PhD student Craig Haley at York University. Chemical box-modelling of nitrogenous compounds was contributed by Dr. Chris McLinden of Environment Canada.

The TAO-FTS comparisons with the GEOS-Chem model outlined in Chapter 8 were all performed as part of this project. The GEOS-Chem data were provided by Prof. Dylan Jones from the University of Toronto.

All of the work undertaken in this project is summarized in Chapter 9. Potential research questions stemming from these results and recommended areas of future work are also identified.

Chapter 2

Atmospheric Physics and Chemistry

Atmospheric science is a vast field composed of many sub-disciplines that are fundamentally rooted in the traditional fields of physics and chemistry. Emerging from these sciences are the modern disciplines of meteorology, climatology, biogeochemistry, earth science, and numerous interdisciplinary studies. The mere fact that the study of the atmosphere cannot be categorically defined in terms of traditional approaches to science makes it not only very complicated, but also very interesting. In order to understand the complexities associated with atmospheric physics and chemistry, it is necessary to have a basic appreciation of the structure of the atmosphere.

2.1 Atmospheric Composition and Structure

The dry atmosphere at sea level is primarily composed of 78% nitrogen gas (N_2), 21% oxygen gas (O_2), and 0.93% argon gas (Ar) [Jacob, 1999]. Depending on the location and meteorological conditions at any given time, there can also be a significant amount of water vapour (H_2O) in the atmosphere: as much as 1% of the local composition. The atmosphere is composed of many other gases but in extremely low concentrations – these species are referred to as trace gases. Although these compounds appear to have insignificant concentrations relative to the primary species, perturbative changes, such as anthropogenic emissions, can significantly impact radiative balance and air quality. This is one of the reasons why it is particularly important to monitor the concentrations of trace gases.

It is common practice to consider the atmosphere as partitioned into several layers that are vertically stacked. For the purposes of this project, consideration will only be given to the two lowermost layers: the *troposphere* and the *stratosphere*. Figure 2.1 shows sample pressure and temperature profiles over Toronto on 1 March 2006. It can be seen that the temperature monotonically decreases with altitude from the surface until approximately 15 km. This region of the atmosphere is known as the troposphere and the height at which the temperature ceases to decrease with altitude is known as the *tropopause*.

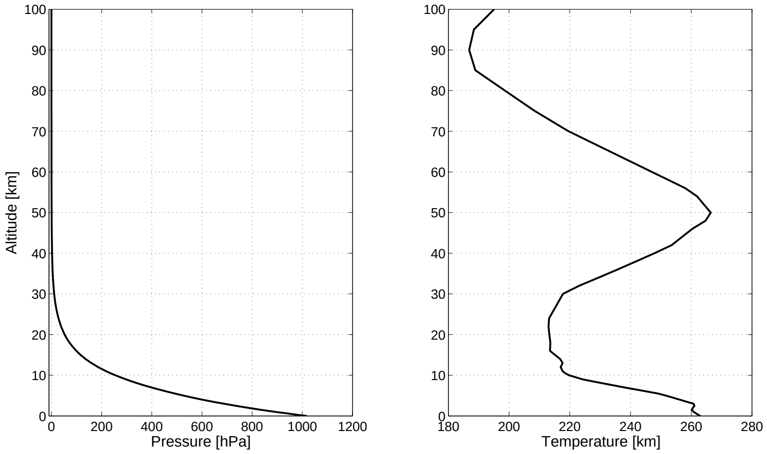

Figure 2.1: Sample pressure and temperature profiles over Toronto taken from the National Centers for Environmental Prediction (NCEP) analysis for 1 March 2006 (`hyperion.gsfc.nasa.gov/data_services/automailer/index`).

Above the tropopause, the atmospheric temperature begins to increase with altitude, defining the layer of the atmosphere known as the stratosphere. The temperature peaks at the *stratopause*, the upper boundary of the stratosphere, which is typically near 50 km altitude. The temperature above the stratosphere defines other regions of the atmosphere known as the *mesosphere* and *thermosphere*. Although these regions of the upper atmosphere are scientifically interesting in their own right, the work presented here is only pertinent to the troposphere and stratosphere. Because of the exponential decrease in atmospheric pressure with altitude, the troposphere and stratosphere account for more than 99% of the total atmospheric mass [Jacob, 1999]. In a general sense, the scientific questions surrounding trace gases in these two regions can be divided into three categories: ozone depletion in the stratosphere, air quality and pollution in the troposphere, and climate change.

2.2 Stratospheric Ozone Depletion

Ozone is naturally generated and destroyed in the stratosphere by the Chapman mechanism [Chapman, 1930]:

$$\begin{aligned} O_2 + h\nu &\rightarrow O + O \\ O + O_2 + M &\rightarrow O_3 + M \\ O_3 + h\nu &\rightarrow O_2 + O\left(^1D\right) \\ O_3 + O &\rightarrow 2O_2, \end{aligned} \tag{2.1}$$

where hν represents a photon of ultraviolet light, and M represents a generic bath gas molecule. According to this mechanism, O_3 should naturally have a chemical equilibrium concentration that is approximately a factor of two greater than the observed value [Jacob, 1999]. A more complete description requires stratospheric dynamics which redistributes O_3 from the tropics, where it is formed, to the mid-latitude and polar regions [Dobson, 1956]. The chemical destruction of stratospheric ozone through chemical loss cycles is also an important process. As the presence of ozone in the stratosphere is not only responsible for driving the radiative processes that regulate temperature but also for blocking incident ultraviolet radiation from the Earth's surface, it is important that changes to its concentration be understood [WMO, 2007].

Hydrogen oxide radicals (HO_x = OH + HO_2) were determined to play a role in stratospheric O_3 loss in the 1960s [Hunt, 1966]. Hydroxyl radicals are produced in the stratosphere by oxidation of water and subsequently destroy O_3:

$$\begin{aligned} H_2O + O &\rightarrow 2OH \\ OH + O_3 &\rightarrow HO_2 + O_2 \\ O_3 + HO_2 &\rightarrow OH + 2O_2. \end{aligned} \tag{2.2}$$

This mechanism of O_3 loss is often referred to as HO_x catalysis and is the main O_3 sink above 40 km. Equations 2.2 are also critical for other catalytic loss cycles as they govern the partitioning of the hydroxyl radical. This is pertinent to the stratospheric loss cycle governed by nitrogen oxide radicals (NO_x):

$$\begin{aligned} NO + O_3 &\rightarrow NO_2 + O_2 \\ O + NO_2 &\rightarrow NO + O_2. \end{aligned} \tag{2.3}$$

This catalytic loss cycle is referred to as NO_x (NO + NO_2) catalysis and is the dominant loss mechanism between 25-40 km [Crutzen, 1970, 1971, WMO, 2007]. The primary source of NO_x in the stratosphere is the breakdown of N_2O. N_2O, which is also an important greenhouse gas, is biogenically produced by oceans and tropical forests, while anthropogenic emissions primarily come from cultivated soil, cattle, and biomass burning [IPCC, 2001]. The concentrations of stratospheric NO_x radicals are controlled through conversion to reservoir species by reactions with OH. As a result, Equations 2.2 and 2.3 are intrinsically dependent upon one another.

The final important stratospheric O_3 loss mechanism is that of halogen catalysis. Through the production of synthetic industrial compounds, such as chlorofluorocarbons (CFCs), hydrochlorofluorocarbons (HCFCs), and halons, many halogenated molecules have been transported to the stratosphere. These catalytically consume O_3 as:

$$\begin{aligned} X + O_3 &\rightarrow XO + O_2 \\ O + XO &\rightarrow X + O_2. \end{aligned} \tag{2.4}$$

where X is a halogen atom (in the stratosphere, reactive halogens are predominantly composed of chlorine and bromine) [Molina and Rowland, 1974]. There are also other cycles that incorporate more than one halogenated compound (such as BrO and ClO). In addition to halogenated catalytic loss through gas-phase chemistry, heterogeneous chemistry can also occur in the presence of aerosols. Heterogeneous chemistry is particularly efficient in the polar regions when stratospheric temperatures become low enough to form polar stratospheric clouds [Kreidenweis et al., 1999]. Consequently, chlorine-catalyzed O_3 loss through heterogeneous chemistry in the Antarctic is estimated to be responsible for over 70% of the O_3 hole [Molina et al., 1987]. Due to their high O_3-depleting potential, the production of halogenated compounds is highly regulated.

Although there is significant scientific concern about the loss of O_3 in the stratosphere, the converse is true in the troposphere. At lower altitudes, O_3 is not only active as a greenhouse gas, but also plays a significant role in the production of smog and related pollutants.

2.3 Tropospheric Air Quality

Clean air for breathing is considered to be a basic necessity of human health. As such, the United Nations has identified four major pollutants that are globally widespread and internationally recognized as being primarily correlated with adverse health consequences: O_3, NO_x, sulphur dioxide (SO_2), and particulate matter (PM, both 2.5 μm and 10 μm diameter) [WHO, 2005]. In addition to these four pollutants, Health Canada has recognized that there is fifth trace gas, CO, that negatively impacts the health of the population [Health Canada, 2003]. CO is generated as a by-product of fossil fuel combustion and is an important component of smog generation.

Poor air quality is characterized by high concentrations of any or all of these five *criteria pollutants*. The direct health concern is related to concentrations of Ground Level Ozone (GLO) as it is a strong oxidizing agent that is known to be toxic to humans and vegetation [WHO, 2004]. The exact concentrations of GLO that constitute a "poor air quality event" depend on the location and policy-derived standard. The Canada Wide Standard for O_3 reduction is set to be 65 ppb over an 8-hour average by the year 2010 [Ontario Ministry of the Environment, 2004]. The average GLO concentration recorded in Toronto over 2004-2006 was 75 ppb [Ontario Ministry of the Environment, 2007].

O_3 is produced in the troposphere through oxidation of CO, CH_4, and other Non-Methane Volatile Organic Compounds (NMVOCs) in the presence of NO_x. Production of tropospheric O_3 via the Chapman Mechanism is inhibited because the stratospheric O_3 layer blocks UV radiation at wavelengths lower than $\approx$290 nm and, thus, the initial reaction in Equation 2.1 cannot happen. There is, however, nitrogen oxide cycling that occurs via Equation 2.3. Although this reaction is responsible for the destruction of O_3 in the stratosphere, it is a precursor to O_3 production in the troposphere. Combined with CO, NO_x facilitates the production of O_3:

$$\begin{aligned} CO + OH &\rightarrow CO_2 + H \\ H + O_2 + M &\rightarrow HO_2 + M \\ HO_2 + NO &\rightarrow OH + NO_2 \\ NO_2 + h\nu &\rightarrow NO + O \\ O + O_2 + M &\rightarrow O_3 + M, \end{aligned} \tag{2.5}$$

resulting in a net reaction of:

$$CO + 2O_2 \rightarrow CO_2 + O_3. \tag{2.6}$$

The oxidation of CO by OH accounts for 90-95% of total CO destruction [Logan et al., 1981] and approximately 75% of tropospheric OH removal [Thompson, 1992]. The initial reaction of CO in Equation 2.5 can be replaced with a similar oxidation reaction of CH_4 or NMVOCs, yielding the net reaction:

$$RH + 4O_2 + 2h\nu \rightarrow RCHO + H_2O + 2O_3, \tag{2.7}$$

where RH denotes a generic hydrocarbon (such as CH_4 or NMHC) and the carbonyl group, RCHO, denotes its generic oxidized product. Equation 2.7 actually ends with the reaction pathway in Equation 2.5. Therefore, it is possible to consider the oxidation of all organic compounds as ultimately ending with the production of CO that further oxidizes to produce O_3. As both the oxidation of CH_4 and NMVOCs still depend on the NO_x radicals shown in Equation 2.5, the efficiency of these reactions is based on the relative abundance of these molecules [Penkett et al., 2003]. As in the stratosphere, there are also more complex reaction schemes that develop when combinations of hydrocarbons and nitrogenous compounds combine to form reservoir species.

Tropospheric NO_x is primarily produced through anthropogenic combustion of fossil fuels and biomass burning, although there is some small production from natural sources. In addition to CH_4 and NMVOC oxidation, CO is produced through anthropogenic emissions in industrial processes and biomass burning. CH_4 is the most abundant organic compound and has a tropospheric concentration of approximately three times that of all other NMVOCs (see Table 2.1). About 20% of CH_4 is generated through natural emissions, while the remaining 80% come from human-induced agricultural emissions, biomass burning, and natural gas leakage [Bergamaschi et al., 2005].

The two other criteria pollutants, SO_2 and PM, are not only hazardous to human health in their own right, but are important for the production of photochemical smog [Brasseur et al., 2003]. Smog is formed when these two pollutants combine in a smoke-like form in which the SO_2 nucleates on the PM to form sulphuric acid [Hobbs, 2000]. When this suspension is combined with a mixture of GLO and its precursors, it is commonly referred to as *photochemical smog* and is associated with numerous negative health effects [WHO, 2005].

It is clear that the improvement of air quality will require continued monitoring of criteria pollutants and their associated trace gases to ensure that anthropogenic emission reduction targets are met. However, it is also important to note that the future changes in concentrations of these gases will also be influenced by changes in climate conditions. The changing climate will also have an impact on the changing O_3 concentrations in the stratosphere. To understand the feedbacks between these processes, it is necessary to understand how trace gases and climate influence each other.

2.4 Climate Change

The chemical composition of the Earth's atmosphere directly influences the Earth's climate in a number of different ways. The most direct link is through the greenhouse effect. The phenomenon of the greenhouse effect was first proposed by Fourier in the 1820's [Pierrehumbert, 2004] with the first quantitative work done in the late 19th century by Arrhenius [1896].

Approximately 70% of the visible and near-infrared radiation that is incident on the Earth's surface is absorbed, while the remaining 30% is reflected. This extent to which radiation is reflected is known as the Earth's *albedo*. In a simple radiative equilibrium model for the Earth-Sun system in which both the Earth and Sun are assumed to be blackbodies (see Section 3.1.3), it can be shown that the equilibrium temperature of the Earth, T_E is given by [Jacob, 1999, for example]:

$$T_E = \left(\frac{F_S \left(1 - A\right)}{4\sigma} \right)^{1/4} = 255K, \tag{2.8}$$

where A is the Earth's albedo, F_S is the *solar constant*, that is, the Sun's irradiance incident on the top of the Earth's atmosphere (which is $\approx$1370 W/m^2), and σ is the Stefan-Boltzmann constant [$5.6704 \cdot 10^{-8}$ W/m^{2}K^4]. However, the Earth's average surface temperature is approximately 288 K: over 30 K warmer than the expected equilibrium temperature. This enhancement is due to the greenhouse effect.

Although the solar radiation incident on the Earth's surface peaks in the visible region near 500 nm, the terrestrial radiation emitted back out to space peaks in the mid-infrared near 10 μm. There are many trace gases in the troposphere and stratosphere that efficiently absorb infrared radiation (see Section 3.1), allowing it to be re-emitted toward the Earth's surface – this is known as the atmospheric greenhouse effect. The greenhouse effect is what acts to increase the mean surface temperature of the Earth to 288 K.

As not all chemical compounds actively absorb infrared radiation (see Section 3.1.1), only some trace gases are considered to be GreenHouse Gases (GHGs). The GHGs with the most significant radiative forcing are H_2O, CO_2, CH_4, N_2O, O_3 – all of which have been shown to be involved in air quality and/or stratospheric O_3 depletion.

The most obvious relationship between these trace gases and climate is through the greenhouse effect; if the concentrations of these gases increase, they will contribute more infrared radiative forcing to the surface of the Earth and ultimately cause an increase in atmospheric temperature [IPCC, 2007]. However, due to the complex nonlinear feedbacks between the dynamics, thermodynamics, and chemistry of the atmosphere, quantifying the impacts of enhanced GHGs on climate change is difficult. The total net anthropogenic radiative forcing on the Earth is currently estimated to be from 0.6-2.4 W/m^2, with almost all of the positive forcing coming from GHGs (see Figure 2.2). The Earth's mean surface temperature has increased by 0.75% ($\approx$1.5 K) since 1860 and it is now very likely (at the 90% confidence level) that the Earth's warming in the past 50 years is due to increases in greenhouse gases [IPCC, 2007].

An increase in surface temperature will, in turn, have feedbacks upon the processes governing both air quality and stratospheric O_3 depletion. Many chemical reaction rate coefficients are temperature dependent, resulting in a shift in equilibrium chemical concentrations. Because enhanced concentrations of GHGs absorb outgoing infrared radiation near the surface of the Earth, they inhibit this radiation from reaching gases higher in the atmosphere and ultimately cause the stratosphere to become cooler. The depletion of stratospheric O_3 also results in a cooling effect; this results in an indirect cooling effect for GHGs that are also O_3-depleting substances (*e.g.*, CFCs). This potential de-

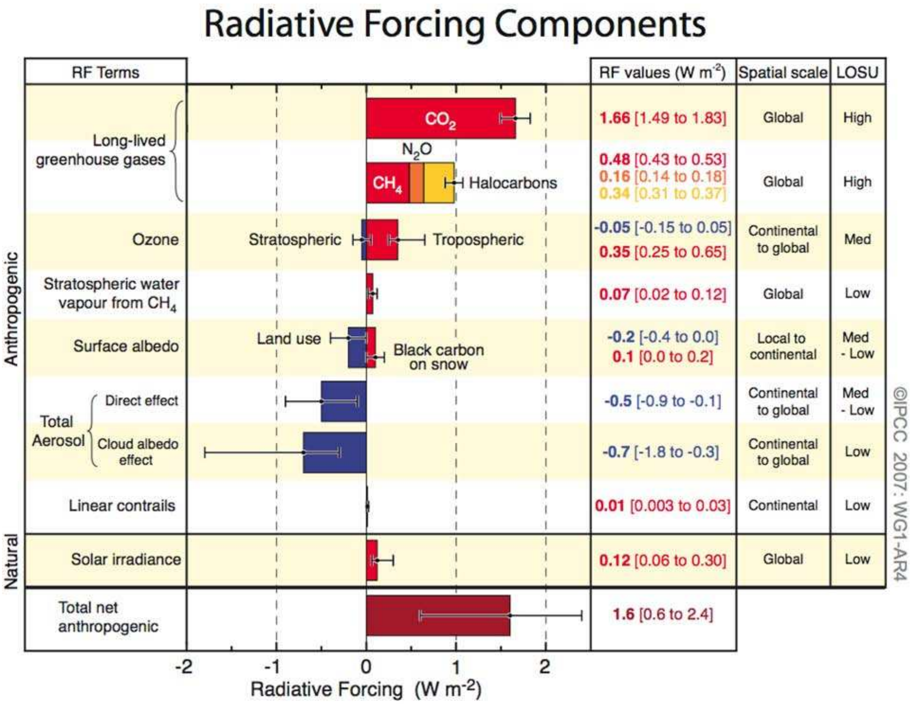

Figure 2.2: Estimated changes in natural and anthropogenic contributions to radiative forcing of the climate from 1750-2005 [IPCC, 2007]. LOSU - Level Of Scientific Understanding.

crease in stratospheric temperature could result in an increase in the formation of polar stratospheric clouds in polar regions. These clouds promote the heterogeneous chemical reactions which efficiently destroy O_3 in the stratosphere. As a result, one of the effects of climate change may be to exacerbate O_3 depletion at the poles [WMO, 2007]. However, the cooling of stratospheric temperatures in the non-polar regions results in a slowing of O_3 depleting reactions and ultimately results in a reduction in global O_3 depletion [IPCC/TEAP, 2005].

The influence of climate change on tropospheric air quality is even more pronounced, with concentrations of pollutants expected to increase in the next 50 years (see Table

2.1). Wu et al. [2008] used the GEOS-Chem chemical transport model driven by a global circulation model to demonstrate that the coupled effects of climate change and surface emissions are expected to enhance the production of tropospheric O_3 by ≈17%. The largest relative increase is for NMVOCs (such as C_2H_6) which are predicted to change by over +150% by the year 2050.

Table 2.1: 2000-2050 projected global pollution emission trends based on chemical transport model calculations driven by a global circulation model (data taken from Wu et al. [2008]).

Chemical Species	2000 Emissions	% Change 2000-2050
NO_x [Tg N y^{-1}]		
Anthropogenic	34	+71%
Biogenic	11	+13%
Non-methane VOCs [Tg C y^{-1}]		
Anthropogenic	43	+130%
Biogenic	610	+ 23%
CO [Tg y^{-1}]	1020	+25%
CH_4 [ppbv]	1750	+37%

Although it is apparent that concentrations of tropospheric and stratospheric trace gases are changing, the scientific understanding of precisely how this will influence the atmosphere has not yet been established. With health concerns associated with diminishing concentrations of O_3 in the stratosphere and increased concentrations of toxic pollutants in the troposphere, it is essential that long-term monitoring of trace gases be maintained. Ground-based Fourier transform spectroscopy is an opportune technique for providing such a data record and instruments like the TAO-FTS are an integral part of furthering our knowledge of atmospheric composition and its changes over time. The theory behind infrared Fourier transform spectroscopy is addressed in the next chapter.

Chapter 3

Fourier Transform Spectroscopy

3.1 Infrared Spectroscopy

In order to adequately address the interaction between infrared radiation and atmospheric trace gases, it is necessary to understand how the fundamental properties of molecules on the microscopic level manifest themselves on the macroscopic level. An explanation of how the transitions between energy states of molecules give rise to well-defined infrared spectroscopic features is given here. Additionally, the relationship between these small-scale processes and the global-scale transfer of infrared radiation through the atmosphere is developed.

3.1.1 Molecular Energy States

Following the development of Bernath [2005], a simple description for the interaction of electromagnetic radiation with matter can be given by a semi-classical approach. This model relies on the classical description of radiation, but uses a quantum mechanical description of molecules. The energy of a molecule is described by solutions of the time-independent Schrödinger Equation:

$$\widehat{H}\psi_n = E_n\psi_n \tag{3.1}$$

where $\widehat{H}$ is the time-independent Hamiltonian Operator, ψ_n is the nth quantum state of the molecule, and E_n is the energy of the nth state. The complete Hamiltonian of this system is given by:

$$\widehat{H} = \widehat{T}_N + \widehat{T}_e + \widehat{V}_{NN}\left(\mathbf{R}\right) + \widehat{V}_{ee}\left(\mathbf{r}\right) + \widehat{V}_{eN}\left(\mathbf{r},\mathbf{R}\right) \tag{3.2}$$

where $\widehat{T}_N$ and $\widehat{T}_e$ denote the nuclear and electron kinetic energy operators, respectively, and $\widehat{V}_{NN}\left(\mathbf{R}\right)$, $\widehat{V}_{ee}\left(\mathbf{r}\right)$, and $\widehat{V}_{eN}\left(\mathbf{r},\mathbf{R}\right)$ represent the nuclear-nuclear, electron-electron, and electron-nuclear interaction potential operators as functions of the nuclear coordinates, $\mathbf{R}$, and electronic coordinates, $\mathbf{r}$, respectively. Exact solutions to Equation 3.1 with the Hamiltonian Operator given in Equation 3.2 are not possible. In order to find solutions, certain approximations must be made.

The Born-Oppenheimer approximation simplifies the Hamiltonian in Equation 3.2 by assuming that the large difference between the masses of nuclei and electrons allows for a separation of variables. Consequently, the quantum states become the product of the electronic and nuclear states, and the Hamiltonian can be separated into its electronic and nuclear parts:

$$\widehat{H_e} = \widehat{T}_e + \widehat{V}_{ee}\left(\mathbf{r}\right) + \widehat{V}_{eN}\left(\mathbf{r},\mathbf{R}\right), \text{ and} \tag{3.3}$$

$$\widehat{H_N} = \widehat{T}_N + \widehat{V}_{NN}\left(\mathbf{R}\right). \tag{3.4}$$

By using the separation of variables given by Equations 3.3 and 3.4, Equation 3.1 can be solved for a particular nuclear geometry, allowing for the energy of a molecule to be expressed as the sum of the electronic energy and the nuclear energy for a given orientation. Implicit in this approximation is the assumption that the electrons and the nuclei interact adiabatically, which is often only true for simple molecules.

The energy associated with electronic motion is on the order of $10^4 - 10^6$ cm^{-1} and is found in the visible/ultraviolet part of the spectrum. The energy due to nuclear motion of a molecule is manifested as vibrational-rotational movement and radiates primarily in the microwave/infrared portion of the spectrum ($\approx 10 - 10^4$ cm^{-1}). As the primary interest here is the interaction of infrared radiation with matter, the remainder of this chapter will deal exclusively with vibrational-rotational motion of molecules.

In order for a molecule to interact with electromagnetic radiation, it is necessary for the molecule to couple with the electric field. This is generally facilitated though the molecule's electric dipole or quadrupole moment, whether permanent or induced, and can also include magnetic moment interaction. The most abundant gases in the atmosphere, O_2 and N_2, are linear and symmetrically charged, resulting in the absence of dipole moments, and therefore can only interact with infrared radiation through weak quadrupole moments. Molecules that have more complex charge orientations, such as H_2O, O_3, and CO_2, have dipole moments that allow for the absorption and emission of infrared radiation. Because the geometry of a molecule plays an integral role in this interaction, it is necessary to model the changes in energy of a molecule in terms of its structure and motion.

For a simple diatomic molecule allowed to rotate about its centre of mass, a rigid rotor model is adequate to describe its energy [Herzberg, 1950]. In this case, the Hamiltonian Operator (Equation 3.2) corresponds to the kinetic energy of the molecule, resulting in solutions to Equation 3.1 given by:

$$E_J = BJ\left(J+1\right),\; J \in \{0,1,2,...\} \tag{3.5}$$

where B is the rotational constant and J is known as the *rotational quantum number*. B is expressed in units of wavenumbers and is composed of:

$$B = \frac{h^2}{8\pi^2 Ic} \tag{3.6}$$

where h is Planck's Constant, I is the moment of inertia of the molecule, and c is the speed of light. Classically, radiation of any frequency could be absorbed or emitted by a molecule with a dipole moment, however, quantum theory restricts the energy levels of the molecule to be only those described by Equation 3.5. Furthermore, Planck's relation shows that changes between two adjacent energy levels, M and N, give rise to distinct frequencies of radiation, ν:

$$E_M - E_N = h\nu. \tag{3.7}$$

This means that a purely rotational spectrum for a simple diatomic molecule would consist of lines equidistantly spaced at $2B\ cm^{-1}$ from one another. The transitions between states are governed by quantum mechanical selection rules, resulting in only $\Delta J = \pm 1$ being *allowed* for this model (refer to Herzberg [1950] for a detailed derivation of selection rules). For a slightly more complicated model in which the diatomic molecule is not assumed to be rigid, (*i.e.*, the non-rigid rotor), a centrifugal distortion constant must be considered, which results in the lines of the rotational spectrum no longer being evenly spaced, but slightly skewed toward lower wavenumber values for higher rotational quantum numbers:

$$E_J = \quad BJ\left(J+1\right) - DJ^2\left(J+1\right) \tag{3.8}$$

where the constant, D, accounts for the centrifugal distortion.

For more complicated polyatomic molecules, the changes in the rotational energy states are constrained by the different moments of inertia. For linear molecules, the rotational spectral lines are the same as those of simple diatomic molecules, although the spacing between lines is different. However, for molecules that have two different axes about which they can rotate, two different moments of inertia must be considered and, therefore, a second quantum number, K, must be introduced. Depending on the geometry of the molecule, different values of J and K are *allowed* and, for the purposes of this discussion, need not be considered in detail. Polyatomic molecules that have three axes of rotation are obviously the most complicated, and general analytical expressions for their energy states cannot be made.

By using similar simplifications to solve Equation 3.1, the spectra of vibrational energy states can be determined. For the simple model of a diatomic molecule, this time not permitted to rotate, but free to vibrate in various modes, the harmonic oscillator model can be used for the Hamiltonian Operator (Equation 3.2). This yields the following solutions to Equation 3.1:

$$E_v = \omega_{osc}\left(v + \frac{1}{2}\right),\ v \in \{0, 1, 2, ...\} \tag{3.9}$$

where ω_{osc} is the oscillation frequency, and v is the *vibrational quantum number*. The oscillation frequency is given in units of wavenumbers by:

$$\omega_{osc} = \frac{1}{2\pi c}\sqrt{\frac{k}{\mu}} \tag{3.10}$$

where k is the classical spring force constant, μ is the reduced mass of the molecule, and c is the speed of light. As with molecular rotational energy, it is important to note that transitions between different states of molecular vibrational energy are restricted by the selection rule $\Delta v = \pm 1$ (see Herzberg [1950] for a derivation). By considering Equations 3.9 and 3.10, this selection rule restricts the *allowable* transitions to all have the same energy, ω_{osc}. This means that there will be only one spectral line that corresponds to transitions between all vibrational energy states.

Obviously real molecules do not vibrate with simple harmonic motion, and this model is limited in its description of spectral features. A more precise description is found from the anharmonic oscillator model in which the Morse Potential is used in Equation 3.2. The Morse Potential accounts for the anharmonic motion of real molecular bonds and allows for overtone and combination vibrational modes [Morse, 1929]. Using this to solve Equation 3.1 results in vibrational energy states given by:

$$E_v = \omega_e \left(v + \frac{1}{2} \right) - \omega_e x_e \left(v + \frac{1}{2} \right)^2 \tag{3.11}$$

where ω_e and $\omega_e x_e$ are the equilibrium oscillation frequency and anharmonicity constant, respectively derived from the Morse Potential Function. Using this model, the quantum mechanical selection rules for the *vibrational quantum number* are found to be:

$$\Delta v = \pm 1, \pm 2, \pm 3, ... \tag{3.12}$$

that is, transitions between all vibrational energy states are *allowed*. For a given molecule, its fundamental modes (*i.e.*, its $\Delta v = \pm 1$ states) are dependent on its geometric construction, and in most cases, there are several different modes with different energies.

As rotational-vibrational energy transitions of molecules are due to interaction with infrared radiation, it is necessary to have a model that considers each of these effects simultaneously. For a simple diatomic molecule, vibrations and rotations can be decoupled, allowing the vibrational-rotational energy states to be expressed as the sum of the two terms:

$$\begin{aligned} E_{J,v} &= E_J + E_v \\ &= BJ\left(J+1\right) - DJ^2\left(J+1\right) \\ &\quad +\omega_e\left(v+\frac{1}{2}\right) - \omega_e x_e\left(v+\frac{1}{2}\right)^2, \end{aligned} \tag{3.13}$$

The quantum mechanical selection rules for these energy states are a combination of the previous rules:

$$\Delta v = \pm 1, \pm 2, \pm 3, ... ; \quad \Delta J = \pm 1. \tag{3.14}$$

Therefore, for each value of v (*i.e.*, for each vibrational band), there are a large number of rotational lines that correspond to various J numbers. Figure 3.1 shows the spectral lines that correspond to the fundamental vibrational mode (ν_2) of HCN. Two distinct branches of lines are apparent; the P branch on the left side of the spectrum, and the R branch on the right side, with respect to wavenumber. These branches of rotational lines correspond to the energy transitions between the different *allowable* states. The lines in the P branch are for all $\Delta J = -1$ transitions, while those of the R branch represent the $\Delta J = +1$ transitions. Similarly structured P and R branches are found for all the other vibrational modes of HCN.

For polyatomic molecules, the simplifying assumption of vibration and rotation being decoupled no longer holds true, and extra cross-terms must be added to Equation 3.13. There are numerous results that arise from this coupling, but this discussion will only focus on one related change in the selection rules (see Banwell [1983] for a discussion of further results). Because the geometry of more complex molecules allows for dipole moments to be induced not just parallel to the intranuclear axis, but also perpendicular to it, there can be rotational transitions induced in the energy of the molecule without any vibrational energy change. As a result, the $\Delta J = 0$ transition can be *allowed*. Transitions

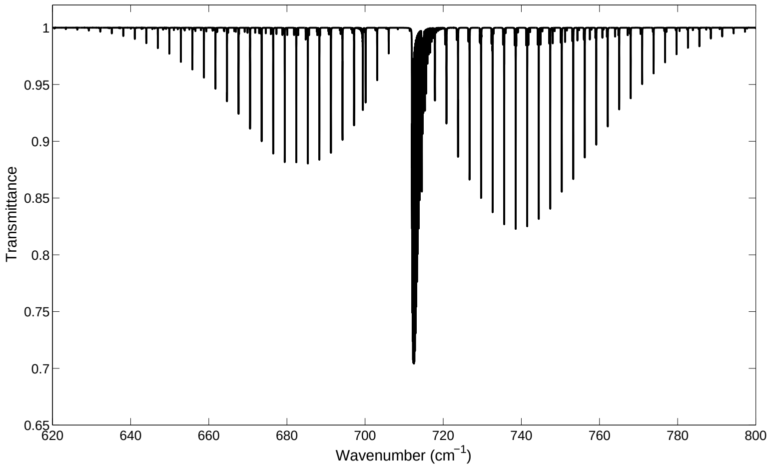

Figure 3.1: Simulated transmittance spectrum of the ν_2 fundamental vibrational mode of HCN. The rotational lines of the P branch are on the left, those of the Q branch are in the centre, and the R branch on the right. This simulation was performed using spectral line parameters from the HITRAN 2000 database.

that correspond to this value are represented as very narrowly spaced lines at the centre of the vibrational band, known as the Q branch (see Figure 3.1). For large, polyatomic molecules, there can be other rotational transitions that result in other branches, but for this study only the P, Q, and R branches are considered.

3.1.2 Spectral Line Broadening

A knowledge of the interaction between electromagnetic radiation and molecules is necessary for understanding the existence of lines in the infrared spectrum. However, in order to extract specific molecular information from spectral lines, it is important to understand how the shapes of these lines are influenced. According to the previously given semi-classical description of energy state transitions, a spectral line should correspond to one unique energy value. According to Equation 3.7, it follows that this energy value would give rise to a monochromatic spectral line of infinitesimal width. In practice, monochromatic spectral lines are never observed, as there is always some slight change in energy levels during transitions. This section addresses the shapes of spectral lines and the three primary causes of line broadening in the infrared. The actual act of observing a spectral line can also cause broadening (*i.e.*, instrument broadening), however, that will be addressed in Section 4.2.

A spectral line due to an isolated, stationary molecule will exhibit *natural broadening* because the transition between two energy states is never perfectly defined. All excited energy states have a natural, finite lifetime after which they will spontaneously decay to lower energy states. The relationship between the energy of a state, E, and its natural lifetime, Δt, is governed by the Heisenberg Uncertainty Principle [Heisenberg, 1927]:

$$\Delta E \Delta t \geq \frac{h}{2\pi}, \tag{3.15}$$

where h once again represents Planck's constant. By combining this expression with Equation 3.7, the frequency of emitted radiation associated with a transition of a specific energy is found to be:

$$\Delta \nu \geq \frac{1}{2\pi \Delta t}. \tag{3.16}$$

Therefore, the emitted radiation can never be monochromatic. The half-width at half-maximum for natural line broadening, α_N, is simply:

$$\alpha_N \approx \frac{1}{4\pi \Delta t}. \tag{3.17}$$

Typically, for an isolated molecule, this natural lifetime is about 10^{-8} seconds, resulting in a half-width of only $\approx 8 \times 10^6$ Hz or $\approx 2.7 \times 10^{-4}$ cm^{-1} [Banwell, 1983]. In comparison to other sources of line broadening, this value is small enough to be negligible.

Because gaseous molecules are in continual motion, there are frequent collisions between molecules. These collisions result in a temporary deformation of the molecule and hence change its vibrational-rotational energy. For a molecule emitting infrared radiation, a collision with another molecule would result in a shift in the frequency of this radiation. Lorentz [1906] showed that the distribution of time between collisions behaves according to Poisson's Law and ultimately gives rise to the *Lorentz lineshape*:

$$f_L\left(\nu - \nu_0\right) = \frac{1}{\pi}\frac{\alpha_L}{\left(\nu - \nu_0\right)^2 + \alpha_L^2}\ , \tag{3.18}$$

where ν_0 is the frequency of the line centre, and the half-width at half-maximum, α_L, is determined by the temperature and pressure:

$$\alpha_L = \alpha_0 \left(\frac{p}{p_0}\right)\left(\frac{T_0}{T}\right)^{\frac{1}{2}}\ . \tag{3.19}$$

At standard temperature and pressure, T_0 and p_0, respectively, the half-width at half-maximum is denoted as α_0 and is typically $\approx 3 \times 10^9$ Hz or ≈ 0.1 cm^{-1}. Lorentz line broadening can be significant in the wings of the spectral line and is almost always orders of magnitude greater than natural broadening.

In a highly rarefied gas, there are limited collisions between molecules and the pressure-induced Lorentz broadening becomes less important. However, as the molecules in the gas still have velocity, it is necessary to consider spectral line broadening due to the Doppler effect [Liou, 2002]. If a molecule with velocity, v, emits infrared radiation at frequency, ν_0, an observer will observe a shift along the line of sight of the molecule. The Doppler-shifted frequency is given by:

$$\nu = \nu_0\left(1 + \frac{v}{c}\right)\ . \tag{3.20}$$

For a gas in Local Thermodynamic Equilibrium (LTE), kinetic theory describes the distribution of molecular velocities with the Maxwell-Boltzmann distribution (see Liou

[2002] for details). By combining this distribution with Equation 3.20, the *Doppler lineshape* is found to be:

$$f_D(\nu - \nu_0) = \frac{1}{\alpha_D \sqrt{\pi}} \exp\left[-\left(\frac{\nu - \nu_0}{\alpha_D} \right)^2 \right], \tag{3.21}$$

where α_D is the *e-folding width* given by:

$$\alpha_D = \nu_0 \left(\frac{2KT}{mc^2} \right)^{\frac{1}{2}}, \tag{3.22}$$

where m is the mass of the molecule, T is temperature, c is the speed of light, and K is the Boltzmann constant (the e-folding width is commonly used for mathematical convenience, however the half-width at half-maximum is simply $\alpha_D\sqrt{\ln 2}$). Compared to the Lorentz lineshape, the Doppler lineshape is stronger in the centre of the line and weaker in the wings (see Figure 3.2). Due to the fact that there is no explicit pressure dependence, the Doppler lineshape is of greater importance for molecules radiating at lower pressures, when the Lorentz lineshape is no longer dominant.

As the pressure in the atmosphere changes by orders of magnitude from the troposphere to the mesosphere, infrared lineshapes can be described by either of these two functions. Lorentz broadening is dominant below roughly 20 km, while Doppler broadening is the main mechanism above 50 km. For the atmosphere between these two regions, both processes play an integral role in determining the effective lineshape. Consequently, it is advantageous to use a lineshape that combines these two effects by convolving the Lorentz and Doppler lineshapes to yield the *Voigt lineshape* [Huang and Yung, 2004]:

$$\begin{aligned} f_V(\nu - \nu_0) &= f_L(\nu - \nu_0) \star f_D(\nu - \nu_0) \\ &= \frac{1}{\pi^{\frac{3}{2}}} \frac{\alpha_L}{\alpha_D} \int_{-\infty}^{\infty} \frac{1}{(\nu' - \nu_0)^2 + \alpha_L^2} \exp\left[\frac{-(\nu' - \nu_0)^2}{\alpha_D^2} \right] d\nu'. \end{aligned} \tag{3.23}$$

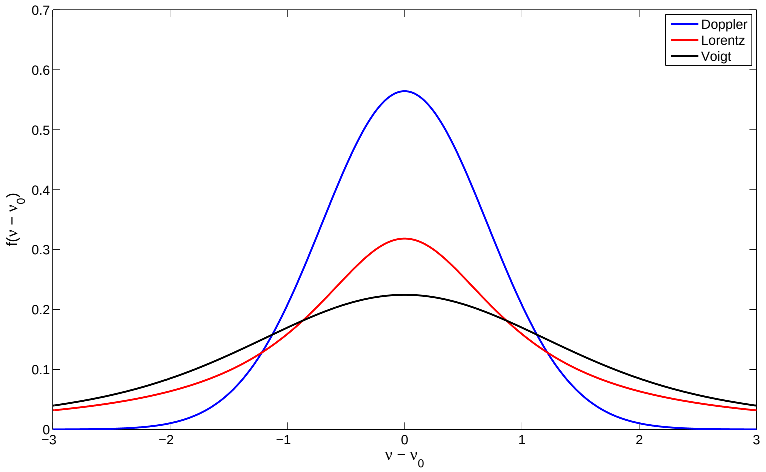

Figure 3.2: Simulations of the Lorentz, Doppler, and Voigt lineshapes. The half-widths at half-maximum were set to 1 for all three calculations.

Figure 3.2 shows that the Voigt lineshape has, in fact, the broadest width of the three. This is a direct result of convolving the two other lineshapes and consequently captures the effects of broadening in both the wings and the core of the spectral line.

In addition to the shape and frequency of an infrared spectral line, there is a third component known as line strength, S. This is actually one of the most important features for remote sensing, as the line strength is directly related to the absorption coefficient, k_ν:

$$S = \int_{-\infty}^{\infty} k_\nu d\nu, \tag{3.24}$$

(*n.b.*, for Equation 3.24 to be true, the absorption coefficient must be normalized). This fact will later be exploited as it shows that the strength of the infrared spectral line depends on the amount of absorber. If this is employed in the inverse sense, a spectral line can be analysed to determine the concentration of absorber present, that is, an instrument measuring infrared spectra can remotely sense the concentrations of gaseous chemicals in the atmosphere. Before these notions can be further developed, it is necessary to briefly outline some basic principles of atmospheric radiative transfer.

3.1.3 Atmospheric Radiative Transfer

In order to quantify radiative absorption and emission processes in the atmosphere, the laws of blackbody radiation must be used. A *blackbody* is simply a material in which the absorption and emission of radiation occur in complete equilibrium; this phenomenon is described by Planck's Law [Planck, 1901]. Planck postulated that atoms behave like small electromagnetic oscillators that each have a characteristic frequency of oscillation. Since changes in energy are related to these frequencies by Equation 3.7, the average energy emitted per oscillator is described as a function of temperature, T, by the Planck function:

$$B_{\nu}(T) = \frac{2h\nu^3}{c^2\left(e^{\frac{h\nu}{KT}} - 1\right)}, \tag{3.25}$$

where, again, c is the speed of light, h is Planck's constant, and K is the Boltzmann constant. Therefore, the rate at which a blackbody emits radiation is a function of temperature and frequency as long as it maintains thermodynamic equilibrium. For molecules within a localized volume of the Earth's atmosphere below 60-70 km, to a good approximation, the temperature can be considered uniform and the radiation field can be considered isotropic, resulting in local thermodynamic equilibrium (LTE) conditions [Liou, 2002].

When electromagnetic radiation interacts with matter, the intensity of the radiation will be decreased by an amount, dI, for each specific frequency, ν:

$$dI_\nu = -k_\nu \rho I_\nu dx, \tag{3.26}$$

where ρ is the density of the material, k_ν is the absorption coefficient, I_ν is the initial intensity incident on the material, and dx is the thickness of the material. By integrating Equation 3.26, an expression for the decrease in radiation due to this interaction with a homogeneous medium is found to be:

$$I_\nu\left(x\right) = I_\nu\left(0\right) e^{-\int k_\nu \rho dx}. \tag{3.27}$$

This is commonly known as the Beer-Bouguer-Lambert Law or, simply, Beer's Law [Bouguer, 1729, Perrin, 1948]. Because this formulation has implicitly assumed that the removal process is dependent on the absorption coefficient (see Equation 3.24), it is not accounting for other removal processes, such as scattering. Although direct scattering of radiation by molecules does take place in the atmosphere in the form of Rayleigh Scattering [Rayleigh, 1871], this interaction accounts for less than 1% of extinguished infrared radiation in a vertical column of the atmosphere [Houghton, 2002]. Mie Scattering influences infrared radiation in the atmosphere very efficiently [Mie, 1908], however, it does not occur at the molecular level, rather, it occurs for larger scattering bodies, such as clouds and aerosols [Liou, 2002]. Hence, for the study of infrared radiative transfer in a cloud-free atmosphere, the assumption of a nonscattering medium can be made.

A beam of radiation can also have its intensity augmented by emission. Since, it has been assumed that the atmosphere is in a state of local thermodynamic equilibrium, it follows that the source of this emission can be described by the Planck function for a blackbody (see Equation 3.25). This changes Equation 3.26 to become:

$$\frac{dI_\nu}{dx} = -k_\nu \rho I_\nu + k_\nu \rho B_\nu\left(T\right), \tag{3.28}$$

where the first term on the right hand side accounts for the extinction of infrared radiation and the second term on the right hand side accounts for the source of infrared radiation. Equation 3.28 is known as Schwarzschild's Equation [Schwarzschild, 1914] and describes all monochromatic infrared radiative transfer in the atmosphere below 60-70 km.

Before the underlying theory of measuring the interaction of infrared radiation with matter can be fully developed, a basic description of Fourier transform spectrometry must be given.

3.2 Fourier Transform Spectrometry

There are many instruments and techniques that can be used to measure infrared radiation in the laboratory and in the atmosphere. In the strictest sense, Fourier transform spectroscopy is a technique that can be applied to any instrument that samples radiation in a time-domain, and relies on the temporal coherence of the radiative source, regardless of wavelength [Davis et al., 2001]. The design and theory described here will be that of a traditional infrared Fourier Transform Spectrometer (FTS) following from the original design work of Jacquinot and Dufour [1948] and Fellgett [1951], and the theoretical development of Connes [1958]. The basic optical design of an ideal instrument, as well as the mathematical description of how the infrared radiation is measured will be given. Additionally, the common advantages and disadvantages associated with this technique will briefly be outlined.

3.2.1 Optical Design of an Ideal FTS

The principal optical component of an FTS is a Michelson Interferometer [Michelson, 1887]. This is a two-beam interferometer that consists of one stationary arm, one moving arm, and a beamsplitter (Figure 3.3). Each arm consists of two mutually perpendicular mirrors, one of which is stationary, and the other of which moves along an axis perpendicular to its plane. Incoming radiation first interacts with the beamsplitter that lies between these two mirrors, which is ideally 50% reflective and 50% transmissive. The amplitude of the radiation is then divided into two equal portions and sent along each of the two arms of the interferometer where it is reflected by the mirrors. The two beams of light then recombine at the beamsplitter and interfere with each other according to the difference in optical paths travelled. The recombined beam is collected and sent to a detector where the interference signal may be processed.

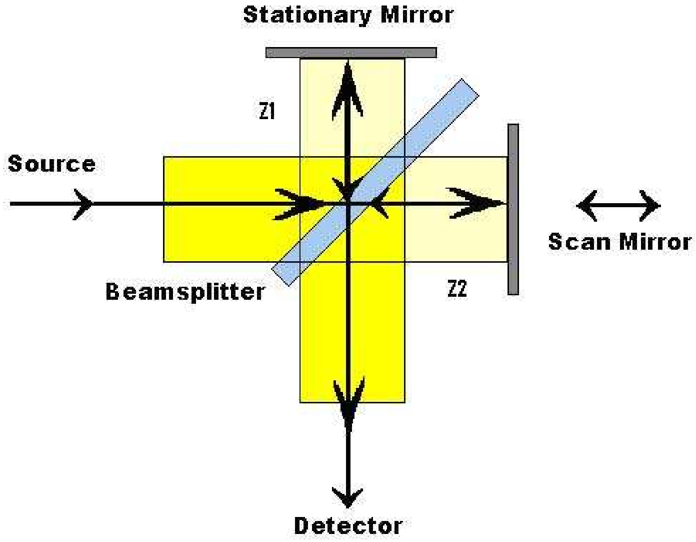

Figure 3.3: Schematic representation of a Michelson Interferometer. The amplitude of the source beam is divided at the beamsplitter, travels along the paths z_1 and z_2 to be reflected off the stationary and scan mirrors, respectively, and is then recombined at the beam splitter and sent to the detector.

The Optical Path Difference (OPD) of the two beams of light is simply introduced by the different distances the light travels along each arm. As the electromagnetic waves are recombined at the beamsplitter, their amplitudes will add according to their relative phase differences. If the two beams recombine when their phase difference is an integer multiple of their wavelength, then they will interfere constructively and the amplitude will ideally be the same as that of the source radiation. As the mirror of the scanning arm is moved along its axis, and the optical path difference changes, the phase difference of the two waves will change and periodically move through a pattern of constructive and destructive interference. This pattern of alternating bright and dark fringes is known as an interferogram and forms the basis of Fourier transform spectroscopy. The mathematical interpretation of an interferogram is established in the next section.

3.2.2 Mathematical Formulation

The formalism used to describe the mathematical theory of Fourier transform spectroscopy can be developed in a number of ways. The derivations adopted here combine the work of several authors, including Bell [1972], Chamberlain [1979], Griffiths and de Haseth [1986], Davis et al. [2001], and Kauppinen and Partanen [2001].

The initial beam of light that enters into the Michelson Interferometer is most easily described by a plane wave:

$$\Psi = A_{\circ} e^{i(\omega t - \mathbf{k}\cdot\mathbf{x})}, \tag{3.29}$$

where $A_{\circ}$ is the amplitude of the wave, t is time, ω is the angular frequency of the wave, **x** is the position of the wave and **k** is the wavenumber vector described by:

$$\mathbf{k} = \frac{2\pi}{\lambda}\hat{k} = 2\pi\sigma\hat{k}, \tag{3.30}$$

where λ denotes the wavelength of the wave in the $\hat{k}$ direction or, alternatively, the reciprocal of wavelength, σ can be used to denote the magnitude of the wavenumber in the $\hat{k}$ direction. When the incident wave of light is partitioned by the beamsplitter, two separate beams of light are produced; Ψ_r is the reflected beam and Ψ_t is the transmitted beam given by:

$$\Psi_r = |r|\, A_\circ e^{i(\omega t - kz_1 + 2\pi\phi_r)}, \tag{3.31}$$

$$\Psi_t = |t|\, A_\circ e^{i(\omega t - kz_2 + 2\pi\phi_t)}, \tag{3.32}$$

where z$_i$ denotes the optical path, $|r|$ denotes the reflection coefficient, $|t|$ denotes the transmission coefficient, and ϕ_r and ϕ_t represent the phase shifts induced by reflection and transmission, respectively. When the beams of light travel along the arms of the interferometer and reflect off of the stationary and scanning mirrors, respectively, they return to the beamsplitter where the reflected beam gets transmitted toward the detector and the transmitted beam gets reflected toward the detector, causing Equations 3.31 and 3.32 to become:

$$\Psi_r = |r|\,|t|\, A_\circ e^{i(\omega t - 2kz_1 + 2\pi\phi_r + 2\pi\phi_t)}, \tag{3.33}$$

$$\Psi_t = |t|\,|r|\, A_\circ e^{i(\omega t - 2kz_2 + 2\pi\phi_t + 2\pi\phi_r)}, \tag{3.34}$$

respectively. The final, recombined beam of light that is received at the detector must be a sum of these two waves:

$$\begin{aligned}\Psi_{tot} &= \Psi_r + \Psi_t \\ &= |r|\,|t|\, A_\circ e^{i(\omega t + 2\pi\phi_t + 2\pi\phi_r)} \left[e^{2ikz_1} + e^{2ikz_2}\right].\end{aligned} \tag{3.35}$$

Ideally, the beamsplitter divides the beam evenly, so the transmission and reflection coefficients are assumed to be:

$$|r|^2 = |t|^2 = 1/2. \tag{3.36}$$

It can also be assumed that the beamsplitter is constructed in a way that compensates for any phase-induced changes upon reflection and transmission, such that:

$$\phi_r = \phi_t = 0. \tag{3.37}$$

The optical path difference, δx, described in Section 3.2 is defined by the difference in the optical path lengths of the arms of the interferometer:

$$\delta x = z_2 - z_1. \tag{3.38}$$

By substituting Equations 3.36, 3.37, and 3.38 into Equation 3.35, the beam of light incident on the detector is described as:

$$\Psi_{tot} = \frac{A_\circ}{2} e^{i(\omega t)} e^{2ikz_1} \left[e^{2ik\delta x} + 1 \right]. \tag{3.39}$$

The corresponding intensity, I, of the incident wave can be found by taking the square modulus:

$$\begin{aligned} I &= \Psi_{tot} \Psi_{tot}^* \\ &= \frac{A_\circ^2}{2} \left[1 + \cos\left(2k\delta x \right) \right]. \end{aligned} \tag{3.40}$$

In these terms, it is conventional to express the interferogram recorded at the detector as a function of the OPD, (hereafter, referred to as x, rather than $2\delta x$), and express the associated component of the wavenumber vector, k, by Equation 3.30:

$$I\left(x\right) = \frac{I_\circ}{2} \left[1 + \cos\left(2\pi\sigma x \right) \right], \tag{3.41}$$

where $I_\circ$ is the square amplitude of the light wave and σ is simply the *linear wavenumber* given by the reciprocal of the wavelength. The interferogram, that is, the signal recorded at the detector that varies as a function of OPD, will always be superimposed on a constant background signal of $I_\circ/2$.

For the construction of a conventional FTS, the arms of the Michelson Interferometer are set to be of equal optical path lengths at the initiation of a scan: known as Zero Path Difference (ZPD). As the scanning arm moves through a distance, x, the OPD changes and the interferogram can be recorded as a function of the scanning mirror position (that is, the OPD is directly coupled to the position of the scan mirror). For a polychromatic light source, at each position, x, the intensity, I, consists of all wave frequencies superposed and integrated together. It follows that the amplitude, $I_\circ$, is actually composed of spectral intensities that depend on all wavenumbers, $B(\sigma)$. Therefore, the integrated interferogram for a polychromatic light source can be expressed in terms of spectral intensity:

$$I(x) = \frac{1}{2}\int_0^\infty B(\sigma)\cos(2\pi\sigma x)\,d\sigma, \tag{3.42}$$

where the constant background term has been left out for simplicity. Since this signal is a superposition of waves, it is implicit that the interferogram's signal is additive and continuous and can therefore undergo Fourier decomposition to extract the spectral intensity as a function of wavenumber, $B(\sigma)$ [Pinkus and Zafrany, 1999]:

$$B(\sigma) = 2\int_0^\infty I(x)\cos(2\pi\sigma x)\,dx. \tag{3.43}$$

Equation 3.43 is the spectrum that is derived from the Fourier transform of the interferogram: the defining characteristic of a Fourier transform spectrometer. The following sections will outline the limitations and advantages of using this process.

3.2.3 Limitations of a Real FTS

The preceding derivation of the equations for the interferogram and spectrum was based on ideal conditions and implicitly assumed that there were no computational limitations. In reality, there are a number of constraints that cause recorded interferograms and spectra to be less than perfect. The issues of finite optical path length, finite field-of-view, and potential phase errors are all reflected by the Instrument Line Shape (ILS) of the instrument. Ultimately, this will influence important instrument factors such as spectral resolution and Signal-to-Noise Ratio (SNR).

To calculate the spectrum from Equation 3.43, it is necessary to integrate over the entire optical path difference. Realistically, the OPD cannot be an infinite quantity and will, therefore, need to be limited in this integral. The simplest way to address this is by incorporating an apodization factor that will impose the limits of the scan mirror on the Fourier transform [Davis et al., 2001]. The simplest choice of apodizing function, D, is the *boxcar function* in which the value is 1 for the values over which the OPD is defined, and 0 elsewhere (sometimes, spectra derived using this factor are referred to as "unapodized"):

$$\begin{aligned} D(x) &= 1, \quad 0 \leq x \leq max(x) \\ D(x) &= 0, \quad x < 0, \; x > max(x)\,. \end{aligned} \tag{3.44}$$

By multiplying Equation 3.42 by this apodization factor, the spectrum is modified by the Fourier transform of the boxcar function:

$$\begin{aligned} F\left[D\left(x\right)\right] &= \int_{0}^{\infty} D\left(x\right) dx. \\ &= \frac{\sin\left(2\pi\sigma L\right)}{\pi\sigma} \\ &= \frac{2L\sin\left(2\pi\sigma L\right)}{2\pi\sigma L} \\ &= 2L\mathrm{sinc}\left(2\pi\sigma L\right), \end{aligned} \tag{3.45}$$

where L represents the maximum OPD and the *sinc function* is defined as:

$$\mathrm{sinc}\left(x\right) = \frac{\sin\left(x\right)}{x}. \tag{3.46}$$

Figure 3.4a shows the graphical representation of the sinc function. As the sinc function inherently introduces ringing into the spectrum, it may be advantageous to use a different apodization factor, such as a triangle function (see Figure 3.4b), Hamming function, etc. Because the apodizing factor is effectively convolved with the spectrum, it determines the instrumental broadening of the spectral lines and, therefore, acts to define the resolution of the instrument. Using the full-width at half-maximum of the sinc function derived from boxcar apodization, the resolution is calculated to be $0.6/L$, while the Rayleigh criterion of two such sinc functions defines the resolution to be $0.5/L$. Using a triangular apodization function to reduce the amount of ringing in the spectrum will cause the sinc function to broaden, causing the same two definitions of resolution to result in values of $0.9/L$ and $1/L$, respectively. Therefore, when choosing an apodization factor, it is necessary to balance the desired resolution of the measurement with the noise that will necessarily be introduced. Furthermore, because the resolution of the spectrum depends on the chosen apodization factor, it is common practice to refer to an *instrument's resolution* in terms of its maximum OPD, thus avoiding confusion (see Bell [1972] for details and examples).

The Field-Of-View (FOV) of an FTS is defined by the solid angle at the collimating optical component subtended by the entrance aperture:

$$FOV = \frac{\theta}{2L}, \tag{3.47}$$

where θ is the diameter of the instrument entrance aperture, and L is the focal length of the collimator. For the ideal case, the entrance aperture is infinitely small and located at the focus of the collimator, causing the FOV to be zero. In actuality, the entrance aperture is a finite, extended source that will allow divergent rays of light to enter into the spectrometer (see Figure 3.5).

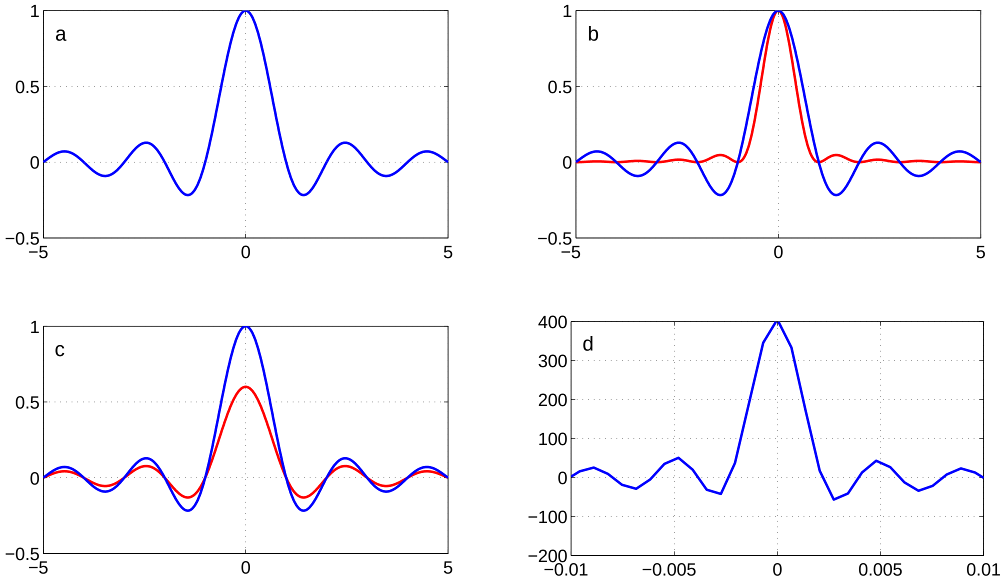

Figure 3.4: (a) Sinc function; (b) Fourier Transform of a boxcar function (blue) and of a triangle function (red); (c) Ideal ILS (blue) compared with that of a modelled instrument with a 40% modulation loss (red); (d) Empirically determined asymmetric ILS generated with a phase error.

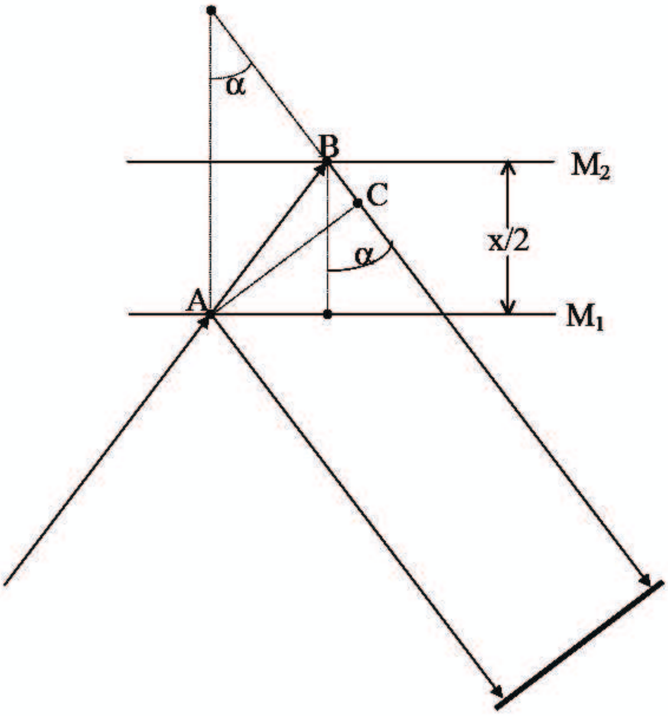

Figure 3.5: Ray tracing schematic for the field-of-view of a typical FTS. M1 and M2 represent the stationary and moving arms of the interferometer, separated by an OPD of $x/2$. The divergent rays impinge on the mirrors at an angle α from the normal. This effectively decreases the OPD by the distance travelled from A-B-C $= x\cos(\alpha)$.

If these divergent rays enter the instrument at an angle, α, defined by the distance from the optical axis, d, and the focal length of the collimator, L:

$$\alpha = \frac{d}{L}, \tag{3.48}$$

then an *effective optical path difference*, x_{eff}, can be defined (assuming that α is small):

$$x_{eff} = x\cos(\alpha) \approx x\left(1 - \frac{\alpha^2}{2}\right). \tag{3.49}$$

This implies that divergent rays will effectively be shifted to values of lower OPD. In terms of the size of the entrance aperture, the effective OPD will be greatest for the rays that enter at the edge of the aperture, that is, when $\alpha = \theta/2$:

$$x_{eff} = x\left(1 - \frac{1}{2}\left(\frac{d}{L}\right)^2\right) = x\left(1 - \frac{\theta^2}{8L^2}\right). \tag{3.50}$$

Thus, the combination of light rays entering through the aperture will result in a broadening of spectral lines over the effective OPD and an ultimate reduction in resolution. By combining Equations 3.47 and 3.50, the width, w, of the broadening over the effective OPD as a function of FOV can be found:

$$w = -\frac{x\theta^2}{8L^2} = \frac{x}{2}FOV^2. \tag{3.51}$$

Therefore, in order to properly convert the interferogram in Equation 3.42 to the spectrum in Equation 3.43, the FOV must be known so that this correction can be incorporated into the calculation. The resultant broadening of the spectral lines is reflected by a broadening of the features in the sinc function that arrives from the finite OPD.

Throughout the derivation of the equations describing the interferogram and spectrum in Section 3.2.2, it was assumed that any phase changes induced by the optical components of the instrument were perfectly compensated prior to reaching the detector. In reality, this is never realized and phase errors do commonly occur. Equation 3.42 shows that an ideal interferogram is a real and symmetric function. If a small phase error, ϵ is introduced into the equation:

$$I\left(x\right) = \frac{1}{2}\int_0^\infty B\left(\sigma\right)\cos\left(2\pi\sigma x + \epsilon\right)d\sigma, \tag{3.52}$$

part of the interferogram will get mapped into the imaginary plane by the Fourier transform. This phase error manifests itself as an asymmetry in the aforementioned sinc function. Similarly, any decrease in the intensity of the signal throughout the measurement will, consequently affect the efficiency with which the instrument modulates the phase of the reflected and transmitted beams and ultimately be manifested as a decrease in the amplitude of the sinc function. This is further addressed in Section 5.1.

As the combination of all of these effects ultimately influences the shape and behaviour of the sinc function that results from the Fourier transformed boxcar function, the instrument's inherent sinc function is known as the Instrument Line Shape (ILS). Figure 3.4 shows examples of how the ILS is influenced by phase errors and poor modulation efficiency due to misaligned optics.
As it is impossible to have a perfect sinc function as the ILS, it is imperative that the ILS of all Fourier transform spectrometers be monitored regularly to ensure that any limiting effects are taken into consideration during analysis.

3.2.4 Advantages of an FTS

In comparison to other spectroscopic techniques, Fourier transform spectroscopy offers several principal advantages that are traditionally referred to as the Jacquinot Advantage, the Fellgett Advantage, the Connes Advantage, and the Michelson Advantage [Connes, 1987].

The Michelson Advantage, or resolving power advantage, is probably the simplest and most intrinsic to the optical design as it basically allows the spectrometer to attain very fine resolution measurements [Michelson, 1887, Connes, 1987]. Because the spectral resolution, $\delta\sigma$ is directly related to the reciprocal of the maximum optical path difference, $\max(x)$, it can be increased indefinitely. This is because instrumental line broadening is only limited by the ILS and can be reduced to a negligible amount in comparison to Doppler line broadening (Equation 3.22).

The Connes Advantage, or calibration advantage, is due to the highly accurate wavenumber sampling of an FTS [Erickson, 1979, Connes, 1970]. Unlike conventional grating or prism spectrometers, the accurate sampling of the FTS provides spectral information without interpolation or wavenumber calibration. This also increases the stability of the instrument over a long time period.

The more commonly known traditional advantages are those of Fellgett [Fellgett, 1951] and Jacquinot [Jacquinot and Dufour, 1948]. The Fellgett Advantage, or multiplexing advantage, is based on the principle that all spectral elements are measured simultaneously by the interferogram. That is, each element of the interferogram contributes to every element of the spectrum. This means that a spectrum can be measured relatively quickly in comparison to traditional dispersive spectroscopy with scanning detectors, and multiple scans can be co-added together in a short period of time. However, there is also a potential disadvantage associated with this. If there is an acute instance of elevated noise recorded in the interferogram, it will increase the noise over the entire spectrum. For this reason, it is often best to have noise limited by the detector rather than the source.

The Jacquinot Advantage, or throughput advantage, is due to the conserved étendue of the instrument's optical design [Jacquinot and Dufour, 1948]. The étendue, G, is the property of an optical system that represents how dispersed the beam of radiation becomes. It is most simply defined in terms of the cross sectional area of the incoming radiation, A, and the solid angle subtended by the entrance aperture, Ω:

$$G = A \cdot \Omega. \tag{3.53}$$

Because all of the radiation incident on the input aperture is collimated and sent through the interferometer before being refocused onto the detector, there is, ideally, no loss of radiation. That is, the axis of symmetry in the spectrometer ensures that there is no loss of information during the measurement and the signal arriving at the detector is as strong as the source. In reality, no FTS is perfectly efficient and there is always some loss that occurs during the motion of the scanning mirror. This will ultimately be reflected by the modulation efficiency captured by the ILS (see Figure 3.4c).

The practical implementation of this theory and the development of empirical techniques with a Fourier transform spectrometer are discussed in the following chapter.

Chapter 4

Instrumentation

4.1 Toronto Atmospheric Observatory

The Toronto Atmospheric Observatory (TAO) was established in October 2001 on the roof of the McLennan Physical Laboratories of the University of Toronto (43.66N, 79.40W, 174 m above sea level). TAO was established to acquire high-quality long-term measurements of trace gases for the purpose of understanding chemical and dynamical processes in the atmosphere and to validate models and satellite measurements of atmospheric constituents. The geographic position of TAO makes it well suited for measurements of mid-latitude stratospheric ozone, related species, and greenhouse gases, while its urban setting enables measurements of tropospheric pollutants. The primary scientific objectives of the work at TAO are:

- To make daily measurements (weather permitting) of the vertical columns and partial columns of tropospheric and stratospheric gases.

- To identify and quantify the sources and sinks of atmospheric pollutants, and to better understand the interactions between tropospheric trace gases that control urban air quality.

- To investigate chemical and physical processes that control the mid-latitude stratospheric ozone budget.
- To combine these data with space-based atmospheric measurements made by space-based missions such as EOS-Terra (MOPITT), Odin (OSIRIS and SMR), SCISAT-1 (ACE-FTS and MAESTRO), ENVISAT (SCIAMACHY and MIPAS), and EOS-Aura (OMI, TES, and MLS) both for satellite validation and for correlative studies.

The work presented here primarily seeks to address the first and fourth objectives while indirectly addressing the second and third objectives.

To accomplish these objectives, a suite of instruments has been installed at TAO. The primary instrument at TAO is a high-resolution DA8 Fourier Transform Spectrometer manufactured by ABB Analytical Business PRU Québec, Canada. All of the results presented in this study are based on data collected by this instrument (see Section 4.2 for a discussion of the instrument and Section 5.1 for a discussion of the data collection). A Heliostat manufactured by Aim Control Ltd (California, USA) captures the solar radiation for the DA8 FTS and occasionally for some guest instruments (see Chapter 6). It is mounted on the roof and follows the sun during the day, reflecting solar radiation into the lab through an opening in the ceiling (see Figure 4.1). Once the radiation enters the lab, a series of mirrors are used to focus, split and direct the radiation beam into the instruments.

A Brewer MkIV spectrophotometer was installed at TAO in March 2005 (see Figure 4.2). This instrument is on loan from Environment Canada and is one of over 80 Brewer spectrophotometers that are used worldwide to monitor stratospheric and total ozone levels. It makes automated measurements of UV-visible radiation that ultimately yield daily total ozone columns as well as information on aerosol optical depth, sulphur dioxide, and

Figure 4.1: The Heliostat installed on the roof of the Toronto Atmospheric Observatory directs infrared solar radiation into the laboratory (photo courtesy of A. Wiacek).

nitrogen dioxide [Kerr et al., 1985].

The University of Toronto UV-visible grating spectrometer was assembled in 1998, and has been deployed on the MANTRA balloon campaigns in Vanscoy, Saskatchewan [Bassford et al., 2005] and on Arctic springtime campaigns at Eureka, Nunavut since 1999 [Melo et al., 2004]. When it is not acquiring measurements in the field, this instrument is maintained at TAO, where Differential Optical Absorption Spectroscopy (DOAS) is utilized to retrieve vertical columns of O_3, NO_2, and BrO. From 2006 to 2007, a companion ground-based UV-visible spectrometer known as Système D'Analyse par Observations Zénithales (SAOZ) instrument [Pommereau and Goutail, 1988] was on loan from the Centre National de la Recherche Scientifique (CNRS), France.

Figure 4.2: The Brewer Spectrophotometer was installed on the roof of the Toronto Atmospheric Observatory in 2005. It records atmospheric observations of UV-Visible solar radiation.

In addition to these instruments, there are a number of smaller complementary instruments that require very little maintenance. A Davis Vantage Pro weather station is used to record local meteorological parameters, such as temperature, humidity, wind speed and direction, precipitation and solar irradiance. As well, a Sun Photo Spectrometer (SPS) [McElroy, 1995] recorded UV-visible solar radiation spectra intermittently from 2002-2004. There have also been instruments resident at TAO for dedicated campaigns at various times throughout the past six years (see Chapter 6 for details).

Although these instruments are/were automated, they still require maintenance and infrastructure monitoring that was routinely done as part of this project. It should be noted that the data management and analysis was completed by other personnel as part of their projects, so only minimal attention was required for all of the secondary instruments. For this reason, the technical details given in Section 4.2 are only for the principal instrument: the Fourier transform spectrometer.

4.2 Bomem DA8 Fourier Transform Spectrometer

The Network for the Detection of Atmospheric Composition Change was officially founded in 1991 (then under the name of the Network for the Detection of Stratospheric Change) [Kurylo and Zander, 2000]. The network now consists of over 70 operational ground-based remote sensing research stations distributed all over the world. The science goals of TAO overlap well with those of the NDACC. According to Kurylo and Zander [2000], they are:

- To study the spatial and temporal variability of atmospheric composition and structure in order to provide early detection and subsequent long-term monitoring of changes in the physical and chemical state of the [atmosphere], as well as ancillary data to discern and understand the causes of such things.

- To establish the links between changes in stratospheric ozone, UV radiation at the ground, and climate.
- To contribute independent validation and calibration data for space-based sensors of the atmosphere and to make complementary measurements; also to support field campaigns focusing on specific processes occurring at various latitudes, altitudes, and seasons.
- To produce verified data sets of geophysical parameters for testing and improving multi-dimensional chemistry and transport models of both the stratosphere and the troposphere.

In accordance with the two mutual sets of science goals, the Toronto Atmospheric Observatory Fourier Transform Spectrometer (TAO-FTS) fills a mid-latitude coverage gap within the NDACC (see Figure 4.3). Infrared spectra recorded at NDACC stations by FTSs have provided long-term time series of ozone columns and ozone profiles [Pougatchev et al., 1995, Barret et al., 2002, Schneider et al., 2005b] and related chemical species [Zander et al., 1994, Rinsland et al., 2002a, 2003, Schneider et al., 2005a]. In addition, the urban location of TAO allows for enhanced monitoring of pollutants that are typically only above detectable limits in urban locations [Molina and Molina, 2004] and, as a result, can provide relatively unique monitoring of species that are not commonly archived as part of the NDACC protocol.

In 2001, the Bomem DA8 Fourier Transform Spectrometer was installed at the Toronto Atmospheric Observatory and, following a commissioning phase (see Wiacek [2006]), became fully operational in May 2002. After demonstrating that the instrument met all of the requisite technical requirements to join the NDACC, a retrieval algorithm certification exercise was completed to show that the data quality and capability of the operating

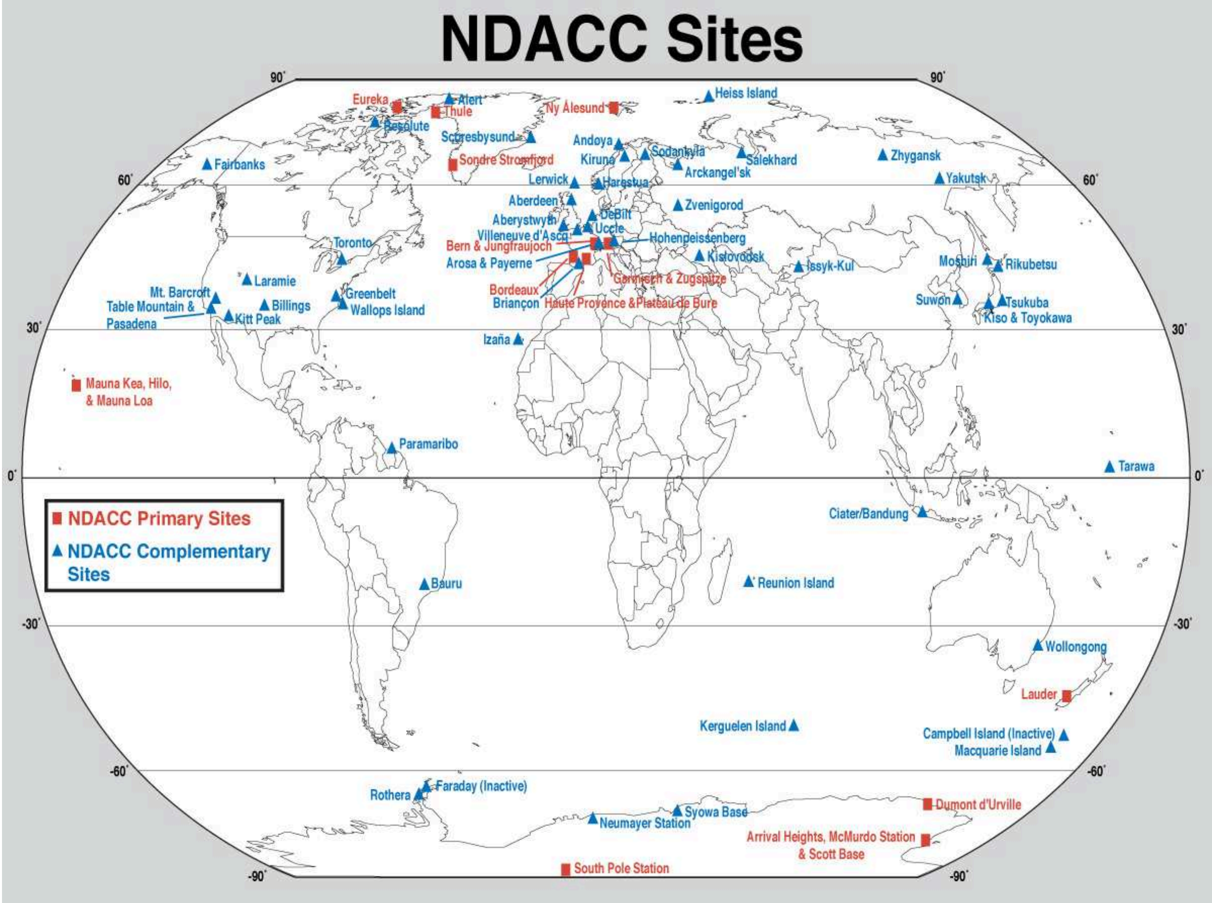

Figure 4.3: The primary and complementary stations of the Network for the Detection of Atmospheric Composition Change (taken from `www.ndsc.ncep.noaa.gov/`).

personnel met all standards (see Wiacek et al. [2007] for details). TAO was granted official status as a complementary site of the NDACC in March 2004. This status not only reflects the high precision of the data collected by the TAO-FTS, but also requires that this data be archived regularly on the NDACC's international database (see Section 5.5 for details).

The TAO-FTS is coupled to the heliostat by several input mirrors (labelled as M1-M3 in Figure 4.4). Mirrors M1 and M2 collect the beam of collimated infrared solar radiation and direct it to an off-axis parabolic mirror (M3) which then focuses the beam through an optical filter and onto an input aperture (labelled as the “Emission Port/Iris” in Figure 4.4). The focal length of this parabolic mirror is 325.12 mm and the radius of the aperture is 0.5 mm, yielding a half-angle field-of-view of 1.54×10^{-3} sr.

The optical filters are housed in an electro-mechanically operated wheel that is used for automatically selecting filters during measurements. These six optical interference filters limit the infrared spectral range of the incoming solar beam and are commonly employed by instruments within the NDACC’s InfraRed Working Group (IRWG). Table 4.1 shows the spectral ranges of the filters (assuming a nominal instrument configuration used at TAO) as well as the principal atmospheric trace gases that absorb in these regions.

Table 4.1: Spectral coverage of the TAO-FTS filter set.

Filter Number	Wavenumber (cm^{-1})	Wavelength (μm)	Principal Species
1	4000−4300	2.3−2.5	HF, CO
2	2900−3500	2.6−3.3	H_2O, C_2H_2, HCN
3	2400−3100	3.3−4.1	O_3, HCl, N_2O, CH_4, NO_2, C_2H_6, H_2O, CO_2
4	2000−2700	3.9−5.0	CO, OCS, N_2
5	1500−2200	4.7−6.3	CO, NO, COF_2
6	750−1350	7.4−14	O_3, $ClONO_2$, HNO_3, N_2O, CH_4, C_2H_2, C_2H_4, CFCs

Once the focused beam of infrared radiation has passed through the aperture, it gets re-collimated by a complementary off-axis parabolic mirror and directed into a vertically oriented Michelson Interferometer (see Section 3.2.1) to generate the phase interference.

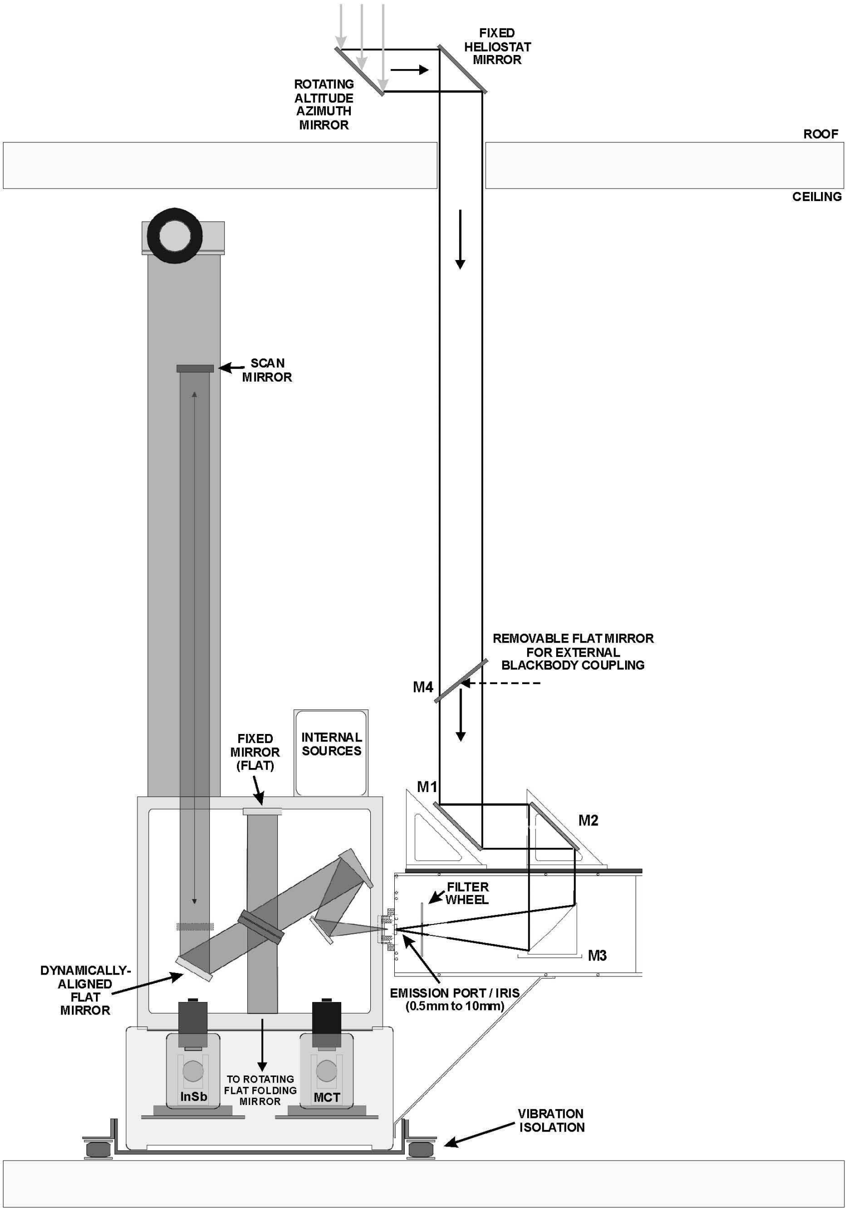

Figure 4.4: FTS and suntracker installation at TAO. The mirrors M1, M2, and M3 serve to couple the heliostat optics to the DA8 FTS. A removable 45° mirror (M4) can be used to couple the FTS to a blackbody source or to direct radiation from the heliostat to other instruments. (Figure courtesy of ABB Bomem)

The moving arm of the interferometer can generate a maximum optical path difference of 250 cm (that is, a maximum spectral resolution of 0.004 cm^{-1}). Previous designs of Fourier transform spectrometers manufactured by Bomem used a dynamic alignment configuration in which the position of the fixed mirror of the interferometer was adjusted to compensate for alignment deviations generated by the moving mirror (see Figure 4.5). In the new design, the fixed mirror is permanently mounted and an adjustable flat mirror has been added to connect the beam to the moving arm of the interferometer. It is this connecting mirror that now provides dynamic alignment and compensates for any irregular motion of the moving mirror during a scan. At the same time, the dynamic alignment circuitry and actuation are kept stationary at the connecting mirror. This arrangement results in a fixed optical axis through the beamsplitter (and a fixed focal point on the detector) as well as a more stable modulation efficiency. It should be noted that, due to the way in which this design is implemented, the DA8 is unable to record interferograms while the scanning mirror is moving backward and, therefore, can only record single-sided interferograms. While there have been other DA8 spectrometers retrofitted with this dynamic alignment configuration, the TAO-FTS represents the first commercial implementation of this design on the high-resolution model.

After the infrared beam of radiation has passed through the interferometer, it is recombined at the beamsplitter and directed toward the detectors. All nominal solar measurements done with the TAO-FTS use a KBr beamsplitter that has a spectral range of approximately 500-4500 cm^{-1}, restricting radiation to the mid-infrared region of the spectrum. The two detectors can be used alternately, with the InSb detector (1500-5000 cm^{-1}) used for measurements with Filters 1-5, and the HgCdTe (MCT) detector (700-4500 cm^{-1}) dedicated to Filter 6 measurements. To maintain consistent measurement conditions, the entire system is vibration isolated and is kept under vacuum to a constant pressure of approximately 13 Pa.

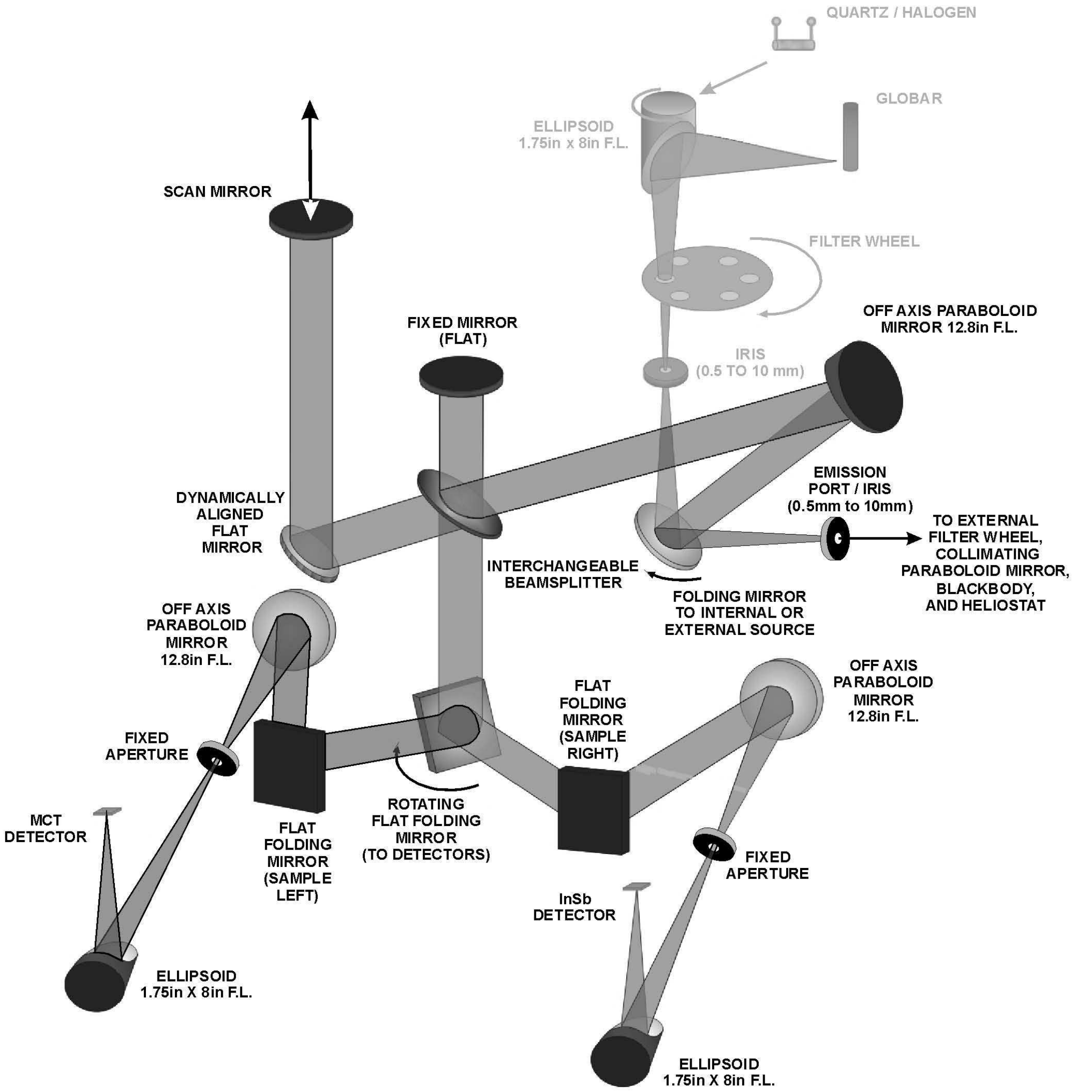

Figure 4.5: The DA8 FTS modified Michelson Interferometer. A moving folding mirror selects between the emission port used for solar absorption measurements, and internal sources (shown in the faded portion at top right) used for instrument line shape testing. (Figure courtesy of ABB Bomem)

To maximize resolution, input apertures were chosen to be as small as possible while still allowing for an adequate SNR value. Additionally, a fixed aperture of 1.3 mm radius is placed before the MCT detector (see Figure 4.5) to ensure that there are no signal contributions arising from self-emission of the instrument. As such, the nominal input aperture radius of 0.5 mm is increased to 2.5 mm to ensure that the fixed aperture is completely filled with the interferogram signal. The resulting half-angle field-of-view for all MCT spectra is 4.61×10^{-3} sr.

To ensure that the instrument is performing in a consistent fashion, the instrument line shape must be continually monitored (see Section 3.2). This is done by making regular measurements with a calibrated gas cell of hydrogen bromide (HBr) [Coffey et al., 1998] and analyzing these data with the LINEFIT version 9.0 analysis routine [Hase et al., 1999]. The details of how this is done can be found in Taylor [2003] and recent results are shown in Wiacek et al. [2007]. Based on the results of these cell tests, the TAO-FTS may be re-aligned so as to ensure that an optimal ILS is maintained. This ensures that observations can be recorded with minimal instrument error.

The details of how the interferograms recorded by the instrument detectors are processed into spectra, as well as how all of the trace gas concentrations are retrieved from these data, are discussed in the next chapter.

Chapter 5

Observations and Data Analysis

Since the TAO-FTS became operational in October 2001 and began nominal measurements in May 2002, interferograms have been regularly recorded under clear-sky conditions. These measurements constitute the raw data, or *Level 0* data product, produced by the TAO-FTS. These interferograms are then converted into infrared spectra by Equation 3.43: the *Level 1* data product. The details of how this procedure is done for observations made by the TAO-FTS is explored in Section 5.1. The *Level 2* product is derived from these spectra by inverting them to determine the atmospheric concentrations of trace gases. This retrieval process is discussed in Section 5.2. The retrieved quantities are then analysed to determine their respective information content as well as their associated uncertainty. These calculations are explained in Sections 5.3 and 5.4, respectively. As TAO is a complementary NDACC site, the final products must be scrutinized for quality and ultimately submitted to an international data archive. This procedure is outlined in Section 5.5.

5.1 Interferograms and Spectral Acquisition

High-resolution, infrared, atmospheric interferograms are nominally recorded by the TAO-FTS year-round, under clear-sky conditions. To ensure that the resolution of the spectra is sufficient to obtain adequate trace gas information, a maximum OPD of 250 cm is used (this corresponds to a spectral resolution of 0.004 cm^{-1} and is consistent with the standards outlined by the NDACC Infrared Working Group). Approximately 5 minutes is required to complete a single scan and an additional 30 seconds is necessary to return the scanning arm of the interferometer to the original position (Zero Path Difference). To reduce the noise in a given observation, four interferograms are co-added together to yield one spectrum over a period of approximately 22 minutes. This reduces the random error in each spectrum while still minimizing the airmass smearing that occurs due to the continuously changing solar zenith angle.

As the interferogram signal is sampled digitally by the detectors, Equation 3.42 becomes a Discrete Fourier Transform (DFT):

$$I\left(m\Delta x\right) = \frac{\Delta\sigma}{2}\sum_{n=0}^{N-1} B\left(n\Delta\sigma\right) e^{\frac{i2\pi mn}{N}}, \tag{5.1}$$

where m and n index the points sampled in the interferogram and spectra, respectively, and N represents the total number of points. The analogous DFT of the spectrum (Equation 3.43) is given by:

$$B\left(n\Delta\sigma\right) = \frac{\Delta x}{2}\sum_{m=0}^{N-1} I\left(n\Delta x\right) e^{\frac{-i2\pi mn}{N}}. \tag{5.2}$$

For computational ease, the Fast Fourier Transform (FFT) is employed at TAO for these calculations [Cooley and Tukey, 1965]. It should be noted that the FFT algorithm normally requires that the number of points involved in the DFT be an integer power of two. If this is not the case, then the interferogram will be padded with zeros until N is of such a value. This produces an interpolation effect and will cause the final spectrum to have more points than the resolution of the instrument. The details of the digital processing associated with these calculations can be found in Wiacek [2006].

The design of the TAO-FTS requires that all interferograms be recorded as single-sided (see Figure 4.4). This implies that all measurements are, by construction, asymmetric and a phase error correction is required in all cases. In addition to phase errors, it is also possible to have two other types of errors in the recorded interferogram: *intensity errors* and *additive errors*. Intensity errors generally arise from changing signal intensity over the duration of the scan. This was earlier related to the modulation loss of the interferometer and was seen to manifest itself as a decrease in the strength of the ILS (see Figure 3.4c). This can be reduced by regularly monitoring and optimizing the optical alignment of the interferometer. The dynamic alignment system of the TAO-FTS ensures that intensity error is minimized (or, at least, kept constant) during measurements. Additive errors are due to periodic inhomogeneities in the interferogram signal. Multiple reflections between parallel optical components (commonly referred to *etaloning*, or *channeling*) are a common source of these errors. During post-processing, filtering techniques may be used to fit the frequencies associated with this effect. The TAO-FTS employs wedged optical elements to ensure that channeling is minimized. Regular monitoring of instrument performance has yet to indicate that there are any noticeable additive errors present in the interferograms.

As was discussed in Section 3.2.2, phase errors generate asymmetric measurements and ultimately cause some of the information in the interferogram to be mapped into the imaginary part of the spectrum. This is not only caused by recording one-sided interferograms, but can also arise from misaligned optics, digital sampling errors, and/or detector electronics. Mathematically, this error can be easily corrected by calculating the phase angle, ϕ and subtracting it out of the spectrum:

$$\phi\left(\sigma\right) = \arctan\left(\frac{B_I\left(\sigma\right)}{B_R\left(\sigma\right)}\right), \tag{5.3}$$

where B_I and B_R denote the imaginary and real parts of the spectrum, respectively. This calculation implicitly assumes that the interferogram is double-sided and has no intensity errors. For the single-sided interferograms recorded by the TAO-FTS, it is necessary to apply the Mertz phase correction [Mertz, 1967]. This technique involves recording a very-low-resolution double-sided interferogram on either side of ZPD at the beginning of a measurement. A spectrum is calculated from this interferogram and interpolated to the full resolution of the measured spectrum to determine the shift arising from phase error. This assumes that the phase error is stationary and a smooth function over all wavenumbers. The square modulus is then calculated from this full-resolution interpolated spectrum and the measured spectrum derived from the full-resolution, single-sided interferogram. This should result in moving all information from the imaginary part of the spectrum into the real part of the spectrum. Regular monitoring of the ILS can reveal the presence of uncorrected phase errors (see Figure 3.4d).

It should be noted that all of the calculations that are performed in converting that TAO-FTS interferograms into spectra are done with licensed *PCDA software.* This is proprietary software that has been developed by the FTS manufacturers, ABB Bomem. The details of how these calculations are programed in the software are considered their intellectual property.

The actual measurements are carried out using an automated scheduler that maximizes the number of observations on a given day. Table 5.1 shows the total number of days upon which measurements were made by the TAO-FTS in a given year. The mean number of observing days is 84.75/year for 2003-2006. This average is consistent with observations made by FTSs at other mid-latitude NDACC stations.

As the TAO-FTS uses six different filters to observe spectral bands, at least six measurements are necessary to have one complete set of observations (see Table 4.1). This

Table 5.1: Number of days on which the TAO-FTS was observing per calendar year.

2002	2003	2004	2005	2006
73	89	63	99	88

requires over two hours of cloud-free weather conditions in a given day and, as such, does not always happen. Figure 5.1 shows the distribution of measurements by filter from 2002-2007. In general, the climate in Toronto consists of increased incidences of clear-sky conditions in the summer months while the winter months are often characterized by cloudy days. There have also been some periods of extended maintenance, such as Fall 2004, which have resulted in a loss of observations. Currently, the TAO-FTS is performing well and it is expected to continue to do so.

The analytical techniques used to calculate trace gas concentrations from atmospheric spectra are explored in the next section.

5.2 Retrievals

As was discussed in Section 3.1.3, it is possible to use Schwarzchild's Equation to describe the interaction of infrared radiation with atmospheric constituents (see Equation 3.28). Ultimately, the spectrum recorded by the TAO-FTS can be exploited to yield the concentration of specific absorbers in the atmosphere. However, in practice, this problem is complicated to solve because the atmosphere is not a controlled environment. Therefore, to prevent this problem from being ill-posed, it is necessary to optimize the amount of information by combining the observations with known quantities. The derivation of this process is based on the mathematical formalism outlined by Rodgers [2000], in which a more rigorous treatment of this subject can be found.

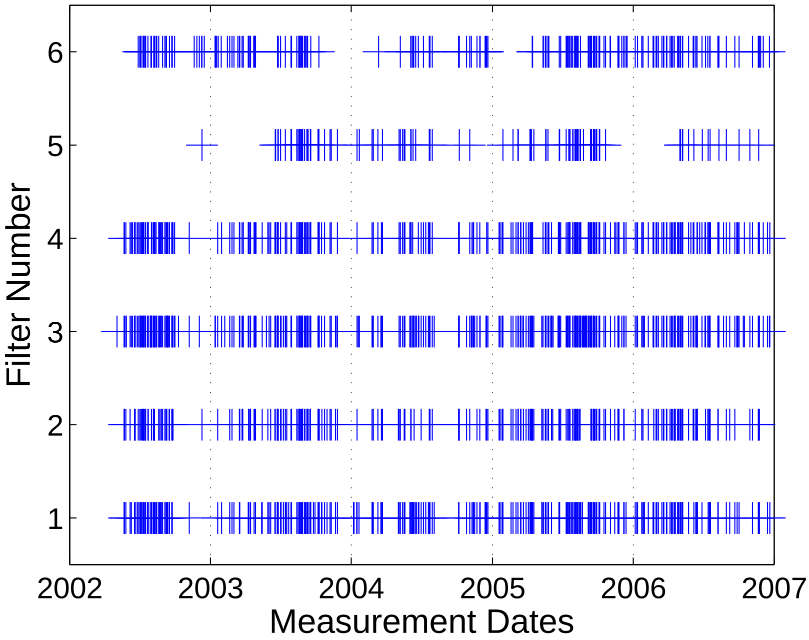

Figure 5.1: Measurements made by the TAO-FTS from 2002-2007, distributed by filter (see Table 4.1).

The technique of combining observations with known information is ideally implemented with a forward function, $\mathbf{f}$. The forward function describes all of the physics necessary to relate the atmospheric state and the measured state. Realistically, this can never be perfectly defined and can only be approximated by a forward model, $\mathbf{F}$. Computationally, the forward model maps the true atmospheric state, $\mathbf{x}$, into the measurement space, $\mathbf{y}$:

$$\mathbf{y} = \mathbf{F}\left(\mathbf{x}, \mathbf{b}\right) + \boldsymbol{\epsilon}, \tag{5.4}$$

where $\mathbf{b}$ represents the vector of ancillary model parameters that are necessary for the calculation and $\boldsymbol{\epsilon}$ represents the error. For the analysis of the TAO-FTS observations, the measurement vector, $\mathbf{y}$, contains the intensities of the infrared spectrum and the atmospheric state vector, $\mathbf{x}$, represents the volume mixing ratio of the trace gases.

If it is assumed that the forward function is invertible, then there exists an inverse function, **R**, that maps values from the measurement state space into the atmospheric state space:

$$\begin{aligned}\hat{\mathbf{x}} &= \mathbf{R}\left(\mathbf{y}, \mathbf{b}, \mathbf{x}, \mathbf{c}\right) \\ &= \mathbf{R}\left(\mathbf{F}\left(\mathbf{x}, \mathbf{b}\right) + \boldsymbol{\epsilon}, \mathbf{b}, \mathbf{x}, \mathbf{c}\right), \qquad (5.5)\end{aligned}$$

where **c** represents the vector of additional ancillary model parameters that may be required for the inverse calculation. In practice, none of these quantities are known with infinite precision and it is therefore necessary to use a prior estimate of the true atmospheric state, $\mathbf{x_a}$, and a best estimate of model parameters, $\hat{\mathbf{b}}$. A Taylor Series expansion about these estimates causes the forward model in Equation 5.4 to become:

$$\mathbf{F}\left(\mathbf{x}, \mathbf{b}\right) = \mathbf{F}\left(\mathbf{x_a}, \hat{\mathbf{b}}\right) + \frac{\partial \mathbf{F}}{\partial \mathbf{x}}\left(\mathbf{x} - \mathbf{x_a}\right) + \frac{\partial \mathbf{F}}{\partial \mathbf{b}}\left(\mathbf{b} - \hat{\mathbf{b}}\right) + ... + \boldsymbol{\epsilon}. \qquad (5.6)$$

It is assumed that the forward model and the inverse model are linear over the range of the *a priori* state space and the true state space, allowing higher order terms to be dropped from Equation 5.6. By substituting Equation 5.6 into Equation 5.5:

$$\hat{\mathbf{x}} = \mathbf{R}\left(\mathbf{F}\left(\mathbf{x_a}, \hat{\mathbf{b}}\right) + \mathbf{K}\left(\mathbf{x} - \mathbf{x_a}\right) + \mathbf{K_b}\left(\mathbf{b} - \hat{\mathbf{b}}\right) + \boldsymbol{\epsilon}, \hat{\mathbf{b}}, \hat{\mathbf{x}}, \mathbf{c}\right), \qquad (5.7)$$

where **K** is known as the weighting function matrix, $\mathbf{K_b}$ is known as the parameter space weighting function matrix, and $\hat{\mathbf{x}}$ represents the retrieved best estimate of the true atmospheric state. The respective weighting function matrices represent the sensitivity of the forward model to the true atmospheric state and true model parameter space, respectively. By defining $\mathbf{y}_\circ$ as:

$$\mathbf{y}_{\circ} = \mathbf{F}\left(\mathbf{x_a}, \hat{\mathbf{b}}\right), \tag{5.8}$$

the same Taylor Series expansion of the inverse model in Equation 5.7 can be performed with respect to $\mathbf{y}_{\circ}$:

$$\begin{aligned}
\hat{\mathbf{x}} &= \mathbf{R}\left(\mathbf{F}\left(\mathbf{x_a}, \hat{\mathbf{b}}\right), \hat{\mathbf{b}}, \mathbf{x_a}, \mathbf{c}\right) + \frac{\partial \mathbf{R}}{\partial \mathbf{y}}\left(\mathbf{K}\left(\mathbf{x} - \mathbf{x_a}\right) + \mathbf{K_b}\left(\mathbf{b} - \hat{\mathbf{b}}\right) + \boldsymbol{\epsilon}\right) \\
\hat{\mathbf{x}} &= \mathbf{x_a} + \mathbf{GK}\left(\mathbf{x} - \mathbf{x_a}\right) + \mathbf{GK_b}\left(\mathbf{b} - \hat{\mathbf{b}}\right) + \mathbf{G}\boldsymbol{\epsilon},
\end{aligned} \tag{5.9}$$

where $\mathbf{G}$ is referred to as the gain matrix. This matrix represents the sensitivity of the retrieved state to the measurements. Equation 5.9 is commonly simplified to emphasize the atmospheric state space:

$$\hat{\mathbf{x}} = \mathbf{x_a} + \mathbf{A}\left(\mathbf{x} - \mathbf{x_a}\right) + \epsilon_{\mathbf{x}}, \tag{5.10}$$

where the final terms are collected into one error term known as $\epsilon_{\mathbf{x}}$ and $\mathbf{A}$ is called the averaging kernel matrix. As the averaging kernel matrix is the product of the gain matrix and the weighting function matrix, it represents the sensitivity of the retrieved state to the true atmospheric state:

$$\begin{aligned}
\mathbf{A} &= \mathbf{GK} \\
&= \frac{\partial \hat{\mathbf{x}}}{\partial \mathbf{y}} \cdot \frac{\partial \mathbf{y}}{\partial \mathbf{x}} \\
&= \frac{\partial \hat{\mathbf{x}}}{\partial \mathbf{x}}.
\end{aligned} \tag{5.11}$$

From Equation 5.10, it can be seen that the best estimate of the atmospheric state is based on a combination of the true state and the *a priori* state. To determine the exact way in which the retrieval weights this combination, it is necessary to choose an approach based on statistical methods. For the retrieval calculations performed at TAO, Bayesian

Inference is used to determine a *Maximum A Posteriori* (MAP) estimator.

According to Bayes's Theorem [Bayes, 1763]:

$$P\left(\mathbf{x}|\mathbf{y}\right) = \frac{P\left(\mathbf{y}|\mathbf{x}\right) P\left(\mathbf{x}\right)}{P\left(\mathbf{y}\right)}, \tag{5.12}$$

where $P\left(\mathbf{x}\right)$ is the prior Probability Density Function (PDF) of the state $\mathbf{x}$, $P\left(\mathbf{y}\right)$ is the prior PDF of the state $\mathbf{y}$, $P\left(\mathbf{y}|\mathbf{x}\right)$ is the conditional PDF of $\mathbf{y}$ given $\mathbf{x}$, and $P\left(\mathbf{x}|\mathbf{y}\right)$ is the conditional PDF of $\mathbf{x}$ given $\mathbf{y}$. As $P\left(\mathbf{x}|\mathbf{y}\right)$ is the posterior PDF determined from combining *a priori* estimates of the state space with the observations in the measurement space, it is referred to as the *a posteriori* estimate. This approach is suitable for atmospheric remote sensing as it allows for both the prior expectation of a given quantity and for the distribution of potential values arising from error.

For simplicity, it is commonly assumed that these PDFs follow a Gaussian Distribution, such that:

$$\begin{aligned} P\left(\mathbf{y}\right) &= \frac{1}{\left(2\pi\right)^{n/2}\left|\mathbf{S_y}\right|^{1/2}} e^{-\frac{1}{2}\left(\mathbf{y}-\overline{\mathbf{y}}\right)^T \mathbf{S_y}^{-1}\left(\mathbf{y}-\overline{\mathbf{y}}\right)} \\ \Rightarrow -2\ln\left[P\left(\mathbf{y}\right)\right] &= \left(\mathbf{y}-\overline{\mathbf{y}}\right)^T \mathbf{S_y}^{-1}\left(\mathbf{y}-\overline{\mathbf{y}}\right) + \mathbf{C}, \end{aligned} \tag{5.13}$$

where $\overline{\mathbf{y}}$ denotes the mean value of the observation vector, $\mathbf{y}$, $\mathbf{S_y}$ denotes the measurement error covariance matrix, n is the number of elements in the vector, and $\mathbf{C}$ is the constant term defined by:

$$\mathbf{C} = 2\ln\left[\left(2\pi\right)^{n/2}\left|\mathbf{S_y}\right|^{1/2}\right]. \tag{5.14}$$

Similarly, $P\left(\mathbf{x}\right)$ and $P\left(\mathbf{y}|\mathbf{x}\right)$ can be expressed as:

$$\begin{aligned} -2\ln\left[P\left(\mathbf{x}\right)\right] &= \left(\mathbf{x}-\mathbf{x_a}\right)^T\mathbf{S_a}^{-1}\left(\mathbf{x}-\mathbf{x_a}\right)+\mathbf{C_x}, && (5.15)\\ -2\ln\left[P\left(\mathbf{y}|\mathbf{x}\right)\right] &= \left(\mathbf{y}-\mathbf{F}\left(\mathbf{x},\mathbf{b}\right)\right)^T\mathbf{S}_\epsilon{}^{-1}\left(\mathbf{y}-\mathbf{F}\left(\mathbf{x},\mathbf{b}\right)\right)+\mathbf{C_{yx}}, && (5.16)\end{aligned}$$

where $\mathbf{C_x}$ and $\mathbf{C_{yx}}$ denote constants that depend on the respective error covariance matrices, as shown in Equation 5.14.

In practice, $P\left(\mathbf{y}\right)$ is just a normalizing factor and can be neglected in the calculation of $P\left(\mathbf{x}|\mathbf{y}\right)$. To attain the MAP estimator, the derivative of Equation 5.12 is set to zero to obtain:

$$\begin{aligned} &\nabla_x\left[P\left(\mathbf{x}|\mathbf{y}\right)\right] = \\ &\qquad \nabla_x\left[\left(\mathbf{y}-\mathbf{F}\left(\mathbf{x},\mathbf{b}\right)\right)^T\mathbf{S}_\epsilon{}^{-1}\left(\mathbf{y}-\mathbf{F}\left(\mathbf{x},\mathbf{b}\right)\right)\right]+...\\ &\qquad \nabla_x\left[\left(\mathbf{x}-\mathbf{x_a}\right)^T\mathbf{S_a}^{-1}\left(\mathbf{x}-\mathbf{x_a}\right)\right]\\ &\quad = \; 0, && (5.17)\end{aligned}$$

where $\mathbf{S}_\epsilon$ is the total observation error covariance matrix, the $\mathbf{S_a}$ is the *a priori* error covariance matrix, and it is implicitly assumed that the forward model estimates generated by Equation 5.4 and the *a priori* estimates of the state space are representative of the mean observations and mean true state, respectively. Equation 5.17 can be further simplified to yield the derivative of the cost function, $\mathbf{g}\left(\mathbf{x}\right)$:

$$\mathbf{g}\left(\mathbf{x}\right) = -\mathbf{K}^T\mathbf{S}_\epsilon{}^{-1}\left(\mathbf{y}-\mathbf{F}\left(\mathbf{x},\mathbf{b}\right)\right)+\mathbf{S_a}^{-1}\left(\mathbf{x}-\mathbf{x_a}\right). \qquad (5.18)$$

As this derivation has been done in the framework of a moderately linear problem, the solution to this cost function can be found using Newtonian iteration:

$$\mathbf{x_{i+1}} = \mathbf{x_i}-\left[\nabla_x\left(\mathbf{g}\left(\mathbf{x_i}\right)\right)\right]^{-1}\mathbf{g}\left(\mathbf{x_i}\right), \qquad (5.19)$$

where $\mathbf{g}$ denotes the cost function defined by Equation 5.18. Therefore, by substituting Equation 5.18 into Equation 5.19 and using the *a priori* state as the initial guess, the optimal solution to Equation 5.17 with Newtonian Iteration is given by:

$$\mathbf{\hat{x}_{i+1}} \quad = \quad \mathbf{x_a} + \left(\mathbf{S_a}^{-1} + \mathbf{K_i}^T\mathbf{S}_{\boldsymbol{\epsilon}}^{-1}\mathbf{K_i}\right)^{-1}\mathbf{K_i}^T\mathbf{S}_{\boldsymbol{\epsilon}}^{-1}\left[\left(\mathbf{y} - \mathbf{F}\left(\mathbf{x_i}\right)\right) - \mathbf{K_i}\left(\mathbf{x_a} - \mathbf{x_i}\right)\right], \tag{5.20}$$

where $\mathbf{K_i}$ denotes $\mathbf{K}$ evaluated at the state retrieved in the previous iteration, $\mathbf{x_i}$. This technique is commonly referred to as the Optimal Estimation Method (OEM). By equating coefficients with Equation 5.10, it can be seen that the gain matrix is given by:

$$\mathbf{G} \quad = \quad \left(\mathbf{S_a}^{-1} + \mathbf{K}^T\mathbf{S}_{\boldsymbol{\epsilon}}^{-1}\mathbf{K}\right)^{-1}\mathbf{K}^T\mathbf{S}_{\boldsymbol{\epsilon}}^{-1}, \tag{5.21}$$

and the expression for the averaging kernel matrix in Equation 5.11 becomes:

$$\mathbf{A} \quad = \quad \left(\mathbf{S_a}^{-1} + \mathbf{K}^T\mathbf{S}_{\boldsymbol{\epsilon}}^{-1}\mathbf{K}\right)^{-1}\mathbf{K}^T\mathbf{S}_{\boldsymbol{\epsilon}}^{-1}\mathbf{K}, \tag{5.22}$$

This analysis is implemented at TAO with the SFIT2 optimal estimation retrieval algorithm [Rinsland et al., 1982, 1998]. This algorithm is widely employed at NDACC FTS stations. The forward model is based on ray-tracing code that was originally developed by Gallery et al. [1983] with recent improvements made specifically for use with SFIT2 [Meier et al., 2004]. The required ancillary model parameters include altitude profiles of pressure and temperature, infrared spectroscopic line parameters, and *a priori* state estimates of trace gas Volume Mixing Ratio (VMR) profiles. The pressure and temperature profiles are obtained from NCEP analyses provided by the NASA Goddard Space Flight Centre automailer (`hyperion.gsfc.nasa.gov/data_services/automailer/index.html`). Spectroscopic absorption line parameters and their temperature and pressure dependencies are taken from the HITRAN 2004 spectral database [Rothman et al., 2005] and are used by SFIT2 for calculating absorption features with a Voigt line shape (see Equation 3.23).

The *a priori* estimates of trace gas VMR profiles were constructed by Wiacek [2006] from a combination of climatological estimates of HALOE v.19 satellite data [Russell et al., 1994] and mid-latitude daytime 2001 MIPAS reference profiles [Carli et al., 2004].

The TAO-FTS retrievals are performed on a 38-layer, pressure-weighted, altitude retrieval grid that ranges from the surface to 100 km. To convert this VMR profile into column concentrations, a *column operator*, $\boldsymbol{\rho}$, composed of the air density estimated by the forward model, is multiplied by $\hat{\mathbf{x}}$:

$$\hat{c} = \sum_i \boldsymbol{\rho}_i \hat{\mathbf{x}}_i, \tag{5.23}$$

where $\hat{c}$ represents the column concentration in molecules/cm^2 and i is the index that spans the elements of the altitude range over which this column is calculated.

In addition to the principal gas VMR profile on the 38-layer grid, there are other parameters that are typically retrieved in the state space. For a given region of the spectrum, this includes total column concentrations of species with spectral features that interfere with the principal gas, and basic fitting parameters, such as spectral baseline offset and curvature. To demonstrate the complexity of a typical infrared spectrum recorded at TAO, Figure 5.2 shows an observation made with Filter 3.

To minimize computational cost, the retrievals are fit in small regions of the spectrum, known as spectral microwindows. Figure 5.3 shows a typical fit for O_3 in the 3045 cm^{-1} region. This particular microwindow contains 235 spectral points; the length of the observation vector, $\mathbf{y}$.

From the forward modelled value of the spectrum, the weighting function matrix, $\mathbf{K}$, can be determined. Figure 5.4 shows the weighting function matrix for the fit in Figure 5.3.

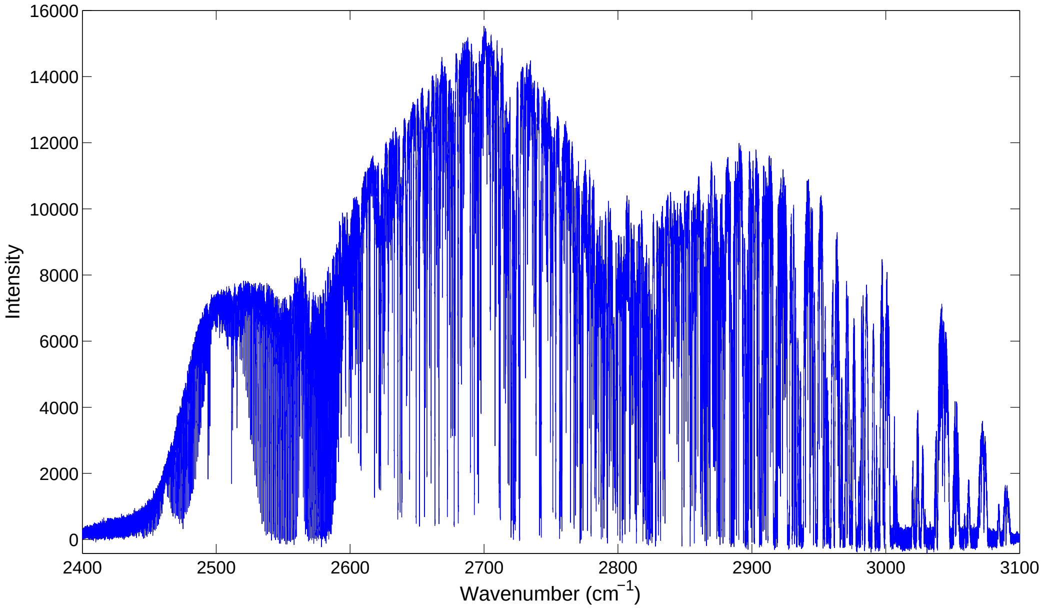

Figure 5.2: Infrared absorption spectrum recorded by the TAO-FTS on 17 June 2003 (Filter 3 region).

The relative strength of the contours indicates what part of the spectral lines weight the retrieval – as it is an absorption spectrum, the magnitudes are negative. Because ozone is predominantly a stratospheric gas (see Chapter 2), the strongest weighting occurs for altitudes between 20 and 40 km. This is further indicated by the fact that the weighting occurs, almost exclusively, from the core of the spectral lines. As the Voigt line shape is used in the forward model (see Equation 3.23), central line features associated with the lower pressure of the stratosphere have the strongest weight while higher-pressure tropospheric features associated with the wings of the spectral lines are not emphasized.

By Equation 5.22, the weighting function matrix, combined with error covariance matrices, yields the averaging kernel matrix (see Figure 5.5). This represents the sensitivity

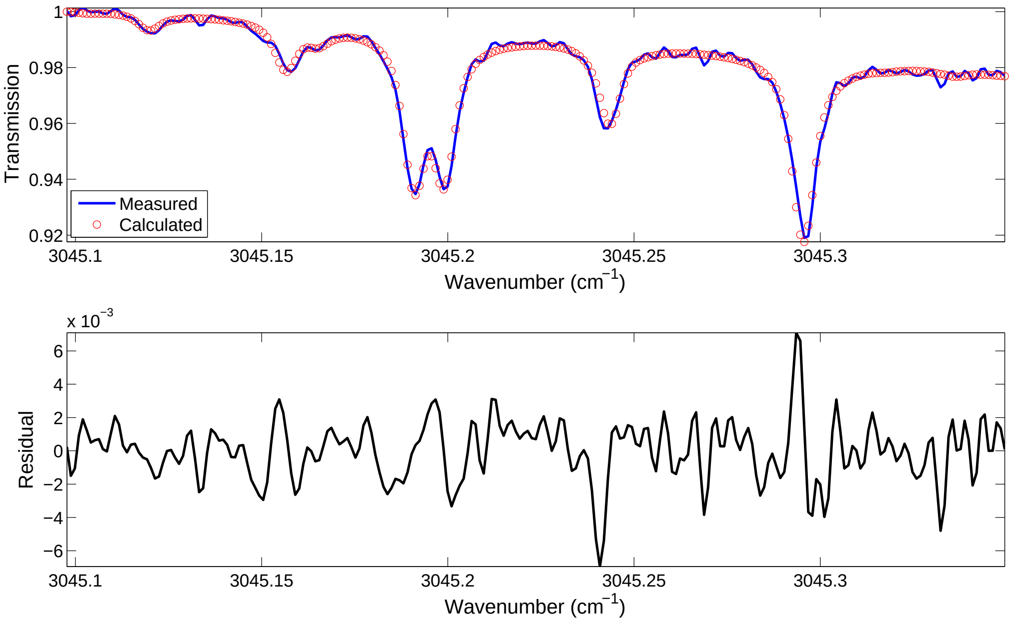

Figure 5.3: Example fit and residual for the ozone infrared absorption spectral microwindow in the 3045 cm^{-1} region (Filter 3). This microwindow is from the spectrum shown in Figure 5.2, which was recorded on 17 June 2003. The observed spectrum is shown in blue and the forward modelled values are shown in red. The RMS value of the residual is 0.18%.

of the retrieval to the underlying true state. As was initially indicated by the weighting function matrix, the primary source of information is in the stratosphere, between 20 and 40 km. The symmetry of the contours indicates that the weighting functions are well correlated in the stratosphere, that is, perturbations to the true stratospheric ozone VMR will be captured by this retrieval. Asymmetric averaging kernel matrices indicate that information is being skewed, that is, unequal contributions are being made from above and below the nominal altitude. Consequently, changes in the truth may manifest themselves as apparent changes at incorrect altitudes in the retrieval.

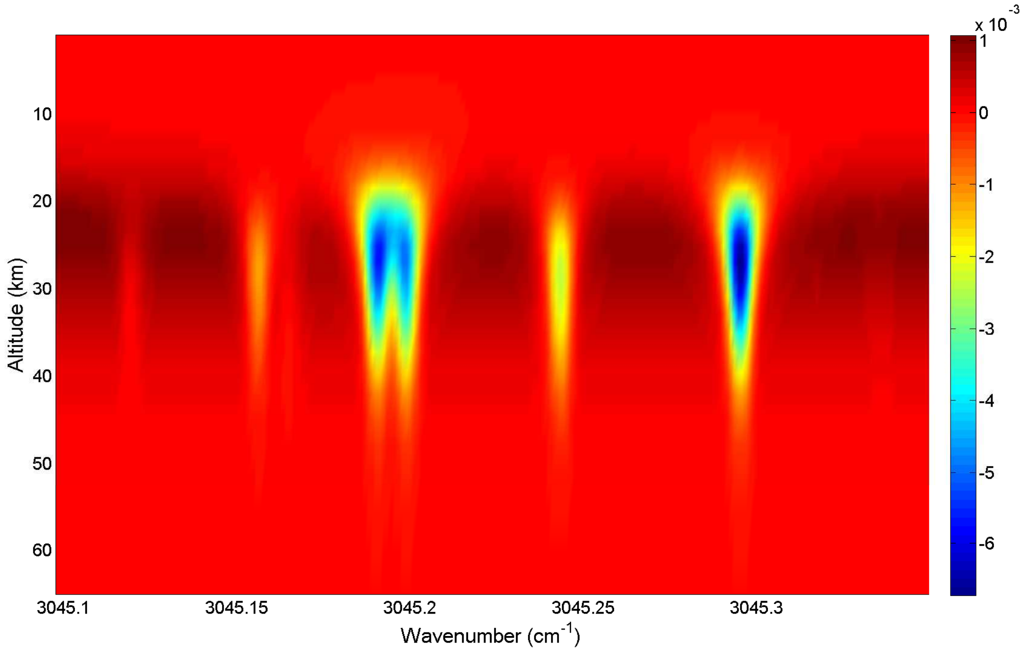

Figure 5.4: Example weighting function matrix calculated for the ozone infrared absorption spectral microwindow in the 3045 cm^{-1} region. This was calculated for the spectrum shown in Figure 5.2, which was recorded on 17 June 2003.

Although the contour plot of the averaging kernel matrix is informative, it is necessary to consider the rows of the matrix, that is the actual averaging kernels, in order to gain full insight into the behaviour of the retrieval. Figure 5.6 shows sample rows of the averaging kernel matrix for different altitudes. As suspected, the strongest signals are present in the rows that represent the altitudes covering 20-40 km. However, it should also be noted that there are some strong negative signals present in these kernels. This implies that there is some smoothing that not only results in poor altitude resolution, but also in artificial subsidence. Upon integrating into stratospheric or total columns, the smoothing seen here is not a concern, but it is important to realize that this limits

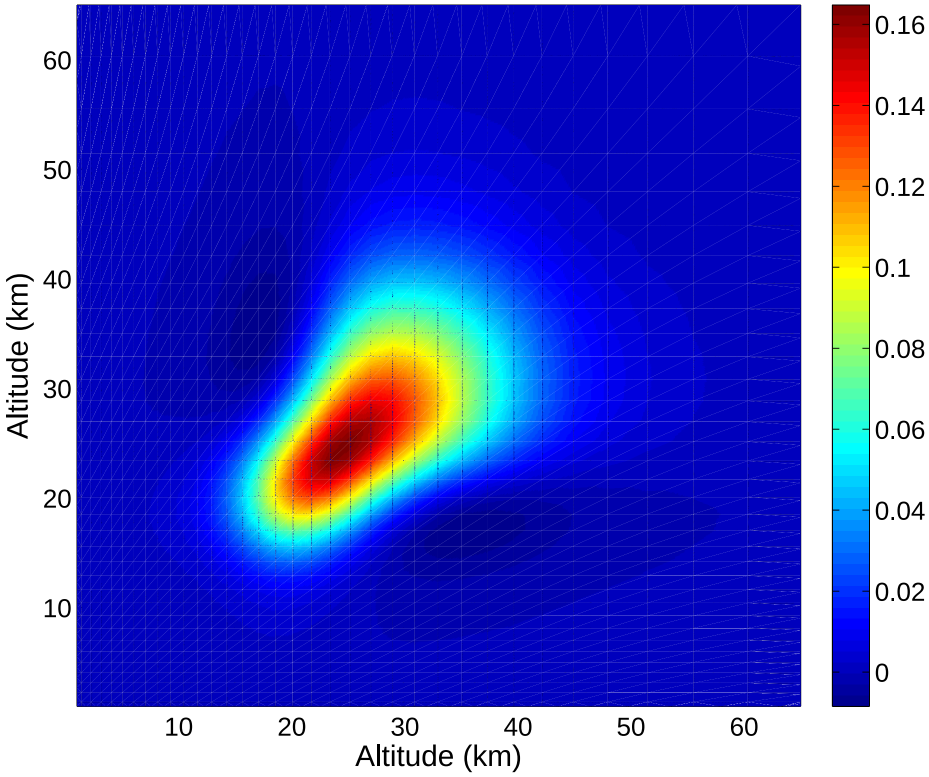

Figure 5.5: Example averaging kernel matrix calculated for the ozone retrieval of the infrared absorption spectral microwindow in the 3045 cm^{-1} region. This was calculated for the spectrum shown in Figure 5.2, which was recorded on 17 June 2003.

the vertical resolution of the instrument. Consequently, the retrieved profiles generated by Equation 5.20 must be considered carefully. This is further explored in Section 5.4.

The final retrieved profile is shown in Figure 5.7. It can be seen that the retrieved profile only differs from the *a priori* profile over the stratospheric region. This confirms what was suggested by both the averaging kernel matrix and the weighting function matrix. The final column products are derived from Equation 5.23 by integrating this profile over

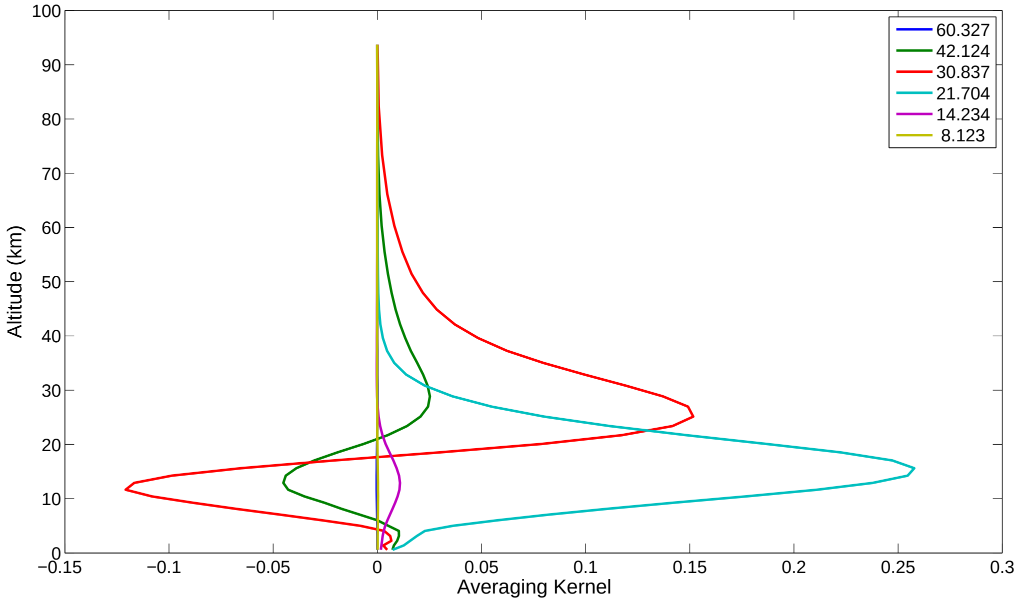

Figure 5.6: Example rows of the averaging kernel matrix calculated for the ozone infrared absorption spectral microwindow in the 3045 cm^{-1} region. Each curve represents a different value on the vertical grid – the corresponding altitude (in km) is indicated in the legend. This was calculated for the spectrum shown in Figure 5.2, which was recorded on 17 June 2003.

the appropriate altitude ranges. The exact range of altitudes over which this integration is appropriate is discussed in Section 5.4.

5.3 Error Estimates

As the mathematical derivations of the analytical error expressions follow the same formalism outlined in the previous section, the approach shown here will again be based on that of Rodgers [2000]. The error expressions associated with the quantities retrieved in the state space are most easily derived by subtracting the true state from the retrieved

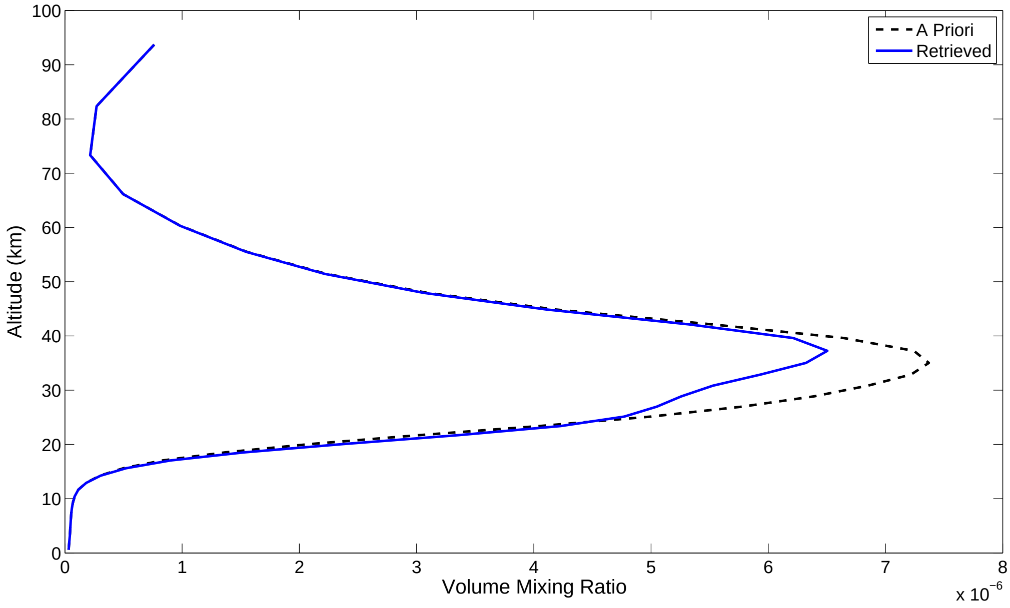

Figure 5.7: *A priori* profile (black) and retrieved profile (blue) from the ozone features in the 3045 cm^{-1} region. This was calculated from the spectrum shown in Figure 5.2, which was recorded on 17 June 2003. The volume mixing ratio is expressed in parts per volume.

state in Equation 5.9:

$$\hat{\mathbf{x}} - \mathbf{x} = (\mathbf{A} - \mathbf{I})(\mathbf{x} - \mathbf{x_a}) + \mathbf{G}\mathbf{K_b}\left(\mathbf{b} - \hat{\mathbf{b}}\right) + \mathbf{G}\boldsymbol{\epsilon}. \tag{5.24}$$

Each term in Equation 5.24 represents a different source of error. The first term represents the smoothing error that is introduced by interpolating the true profile onto a 38-layer grid. The statistical description of this error, $\mathbf{S_s}$, is given by the expectation value:

$$\begin{aligned} \mathbf{S_s} &= \left\langle (\mathbf{A} - \mathbf{I})(\mathbf{x} - \mathbf{x_a})(\mathbf{x} - \mathbf{x_a})^T (\mathbf{A} - \mathbf{I})^T \right\rangle \\ &= (\mathbf{A} - \mathbf{I})\,\mathbf{S_e}\,(\mathbf{A} - \mathbf{I})^T . \end{aligned} \tag{5.25}$$

Unfortunately, as the true state can never actually be known, the calculation of the true state covariance matrix, $\mathbf{S_e}$, cannot actually be performed. Rather, an estimate of this covariance must be made from climatological observations. At TAO, the *a priori* error covariance matrix, $\mathbf{S_a}$, is already an estimate based on climatological observations (see Section 5.2). Consequently, all smoothing error estimates shown here are based on the pertinent *a priori* error covariance matrix; this is commonly referred to as the *ad-hoc* formulation.

An *a priori* error covariance matrix used for TAO ozone retrievals and smoothing error calculations is given in Figure 5.8. An example of a smoothing error covariance matrix for an ozone observation made by the TAO-FTS is given in Figure 5.9. To avoid numerical instabilities generated by the inversions in Equation 5.20, the *a priori* covariance error was chosen to be 20% (*i.e.*, $\sigma = 0.2$) for each level and diagonal over the entire altitude range (typically, a value of 30% is used). For this example, it was assumed that all of the layers were independent and uncorrelated (an unrealistic assumption but, nonetheless, numerically stable). It is also interesting to note that in the stratosphere, the region where the sensitivity of the retrieval was the greatest, the smoothing error is larger than the *a priori* error. This potentially indicates two things: 1. that the ad-hoc choice of using the *a priori* error in the calculation of the smoothing error has artificially inflated the error [Rodgers, 2000], or 2. that the error in the retrieved quantity is actually greater than the *a priori* error and the measurement does not contribute any information beyond that which was known *a priori*. In practice, these problems can be avoided by smoothing like observations with the same averaging kernels so as to ensure that observation platform bias is minimized (see Chapters 7 and 8).

The second term in Equation 5.24 represents the forward model parameter error, $\mathbf{S_f}$. This arises from improper estimates of model parameters and can be statistically described in

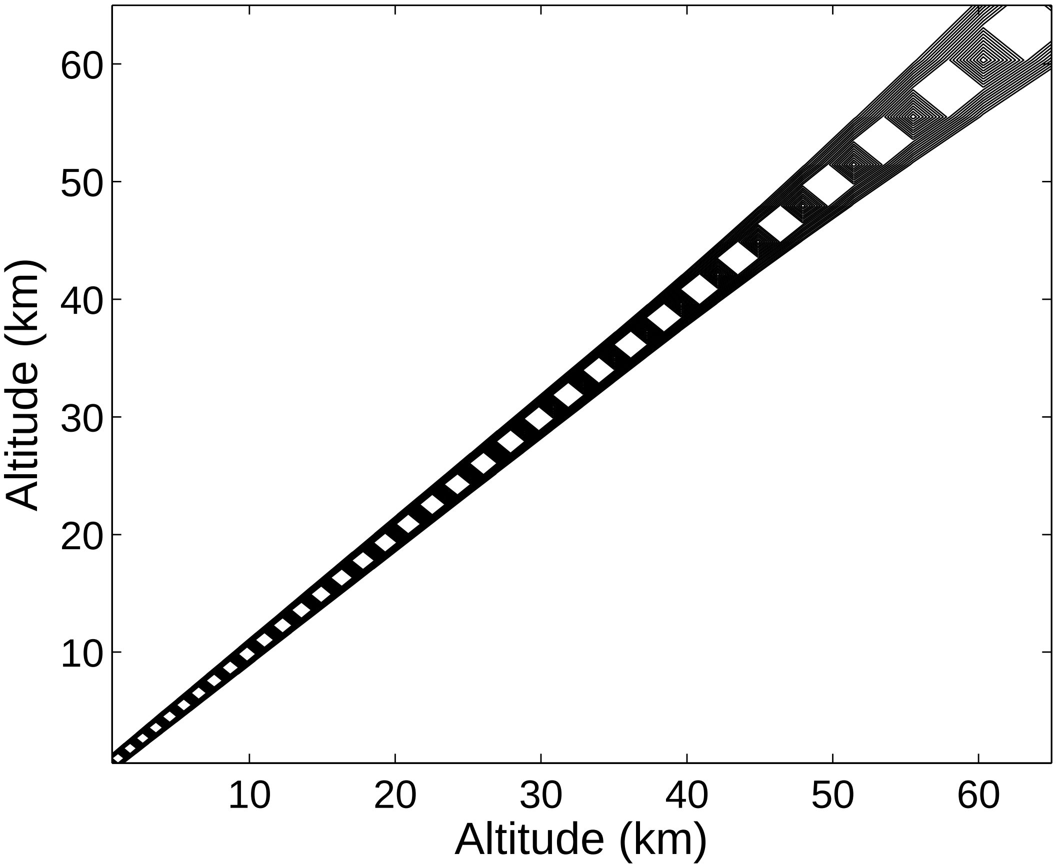

Figure 5.8: Ozone *a priori* covariance matrix contours, $\mathbf{S_a}$, used for retrievals with the TAO-FTS. For each layer, the error is given as 20%, that is $\sigma^2 = (0.2)^2 = 0.04$.

the same fashion as smoothing error:

$$\begin{aligned} \mathbf{S_f} &= \left\langle \mathbf{G K_b} \left(\mathbf{b} - \hat{\mathbf{b}}\right) \left(\mathbf{b} - \hat{\mathbf{b}}\right)^T \mathbf{K_b}^T \mathbf{G}^T \right\rangle \\ &= \mathbf{G K_b S_b K_b}^T \mathbf{G}^T. \end{aligned} \tag{5.26}$$

As with the $\mathbf{S_e}$ matrix, the $\mathbf{S_b}$ matrix cannot be precisely determined, as knowledge of the true forward model parameters is needed. Estimating these quantities for each retrieval calculation is computationally expensive and therefore they have been assumed to be

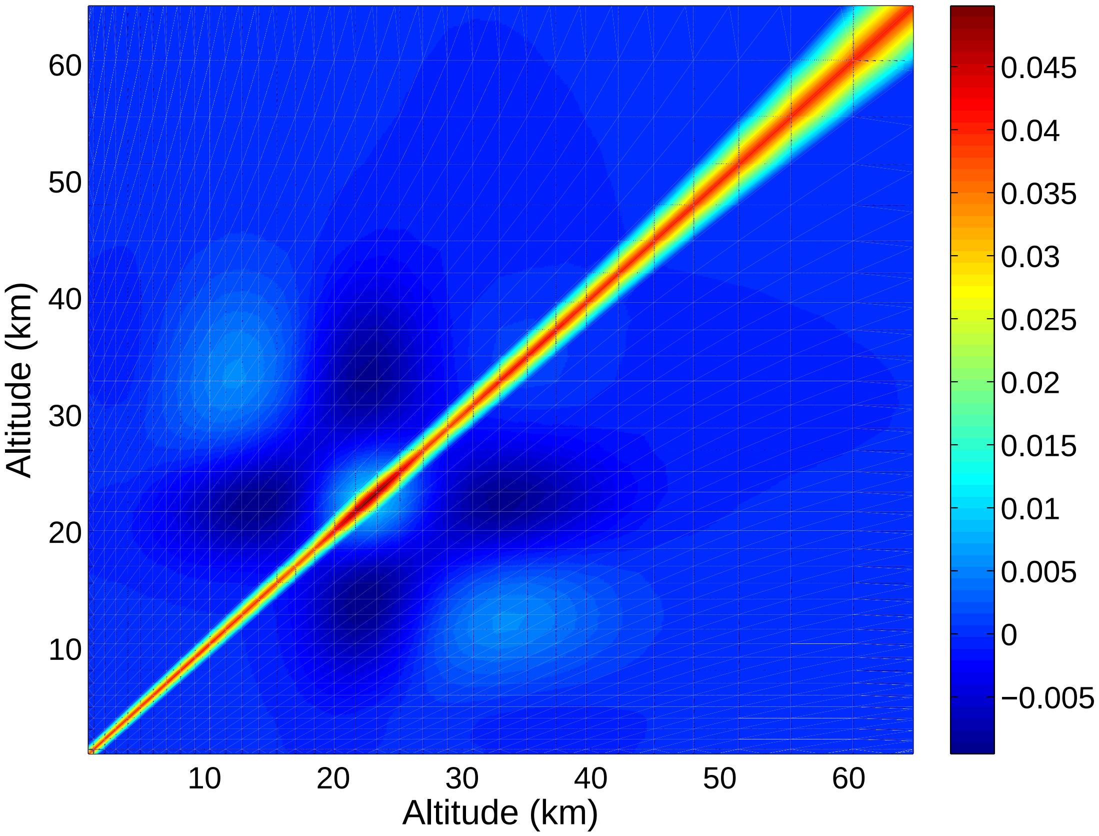

Figure 5.9: Ozone smoothing error covariance matrix contours, $\mathbf{S_s}$, calculated for the retrieval using the spectrum shown in Figure 5.2, which was recorded on 17 June 2003.

systematic and constant for each trace gas. Previous work has shown that errors arising from forward model ray-tracing with FSCATM and SFIT2 are less than 1% [Schneider et al., 2005b]. Errors arising from inaccurate spectroscopic line parameterization are manifested as artificial line broadening/narrowing which will reflect artificial subsidence of the trace gas, but do not impact the precision of columns or properly defined partial columns [Schneider et al., 2005b]. For this reason, estimates of spectroscopic errors are neglected. The principal component of forward model error is temperature error. This was explored at length by Wiacek [2006] and has been found to contribute up to 10%

error in the total column for some species.

The third term in Equation 5.24 represents the retrieval noise, $\mathbf{S_m}$. This is essentially the mapping of the spectral measurement noise into the state space, and is expressed as:

$$\begin{aligned} \mathbf{S_m} &= \left\langle \mathbf{G} \boldsymbol{\epsilon} \boldsymbol{\epsilon}^T \mathbf{G}^T \right\rangle \\ &= \mathbf{G} \mathbf{S}_{\boldsymbol{\epsilon}} \mathbf{G}^T. \end{aligned} \tag{5.27}$$

The $\mathbf{S}_{\boldsymbol{\epsilon}}$ matrix represents the covariance of the measurement noise in a given spectral microwindow. As this error is random and irregular, it must be estimated for each observation. To ease the computational burden associated with these calculations, the covariance matrix is chosen to be diagonal and uncorrelated. The elements of the matrix represent each of the spectral elements in the microwindow and are estimated from the noise in the residual of the fit:

$$\mathbf{S}_{\boldsymbol{\epsilon}} = \sigma^2_{RMS} \cdot \mathbf{I}, \tag{5.28}$$

where RMS denotes the root-mean-square value of the residual. Figure 5.10 shows the retrieval noise covariance matrix for the sample measurement of ozone taken on 17 June 2003. This error shows some anti-correlation, with off-diagonal elements in the stratosphere. However, in comparison to other sources of error, the magnitude of this error is actually very small and is often negligible.

There is one final error quantity that arises from having a state space that includes more than just one retrieved quantity. As the averaging kernel matrix is a complicated combination of weighting function matrices and error covariance matrices (see Equation 5.22), it usually contains off-diagonal elements that represent unphysical correlations:

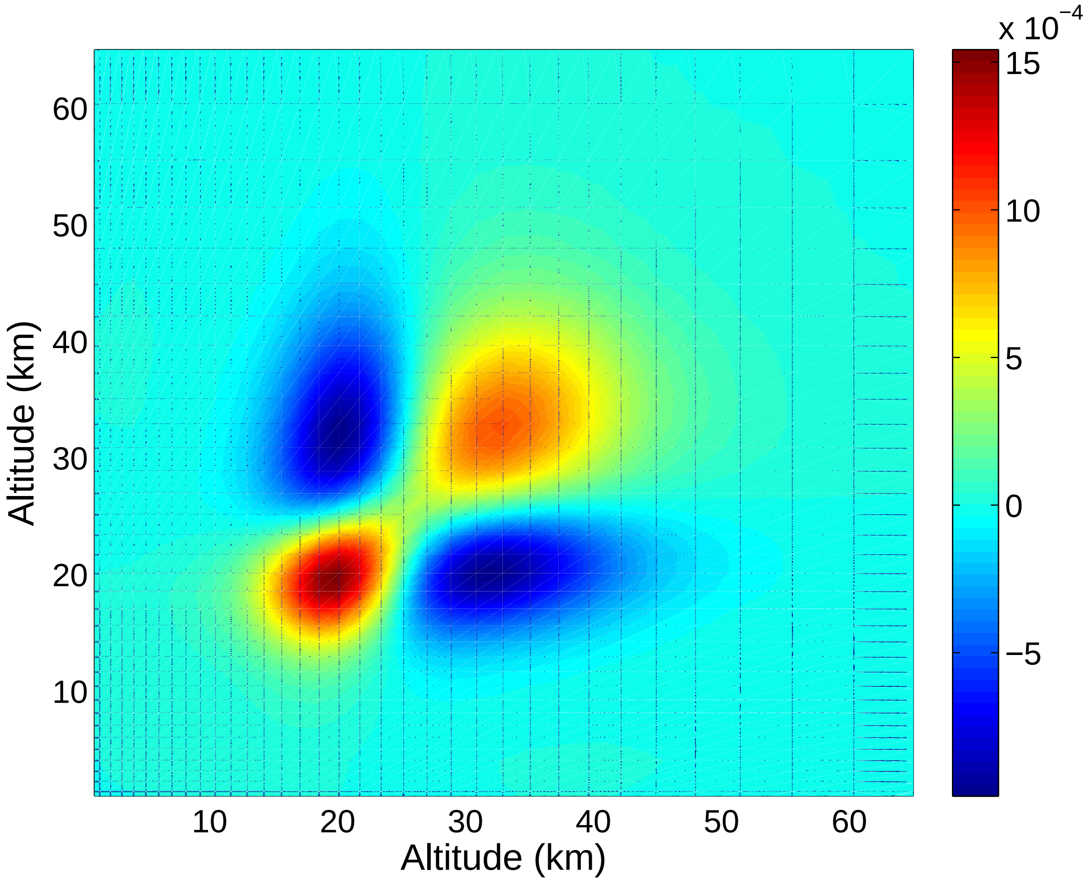

Figure 5.10: Ozone retrieval noise covariance matrix contours, $\mathbf{S_m}$, calculated for the retrieval using the spectrum shown in Figure 5.2, which was recorded on 17 June 2003.

$$\mathbf{A} = \begin{bmatrix} \mathbf{A_{pp}A_{px}A_{pi}} \\ \mathbf{A_{xp}A_{xx}A_{xi}} \\ \mathbf{A_{ip}A_{ix}A_{ii}} \end{bmatrix}, \tag{5.29}$$

where the subscript p denotes elements of the state space that represent fitting parameters, the subscript x denotes elements of the state space that represent the principal trace gas profile, and the subscript i denotes elements of the state space that represent interfering species. Following the approach of Rodgers and Connor [2003], this error is referred to as state space interference error, $\mathbf{S_p}$, and can be estimated as:

$$\mathbf{S_p} = \mathbf{A_{px}}\mathbf{S_{ap}}\mathbf{A}_{\mathbf{px}}^{T} + \mathbf{A_{xi}}\mathbf{S_{ai}}\mathbf{A}_{\mathbf{xi}}^{T} \tag{5.30}$$

where $\mathbf{S_{ap}}$ and $\mathbf{S_{ai}}$ are the *a priori* covariance matrices for the fitting parameters and interfering species, respectively (for all the retrievals presented here, these matrices are assumed to be diagonal with 100% covariance). Figure 5.11 shows the state space interference error calculated for the sample measurement of ozone taken on 17 June, 2003. As with the retrieval noise covariance matrix, this matrix shows pronounced anti-correlated values in the stratosphere. It also has a very small magnitude and ultimately contributes little to the total error covariance.

There is one other potential source of error that is not considered here. As was mentioned in Section 5.2, the forward model described by Equation 5.4 is actually an approximation to the true physics represented by the forward function. As knowledge of the physics of the atmosphere is already represented as precisely as possible in the forward model, it is difficult to estimate how this deviates from the truth given by the forward function. For this reason, modelling bias is often neglected in the estimate of retrieval uncertainty [Rodgers, 2000].

Total error covariance, $\mathbf{S_t}$, associated with the final retrieved quantities can be estimated by adding all of the source error terms together:

$$\mathbf{S_t} = \mathbf{S_s} + \mathbf{S_f} + \mathbf{S_m} + \mathbf{S_p}. \tag{5.31}$$

Figure 5.12 shows the total error covariance matrix for the sample ozone retrieval from 17 June 2003. It may be seen that the dominant source of error comes from a combination

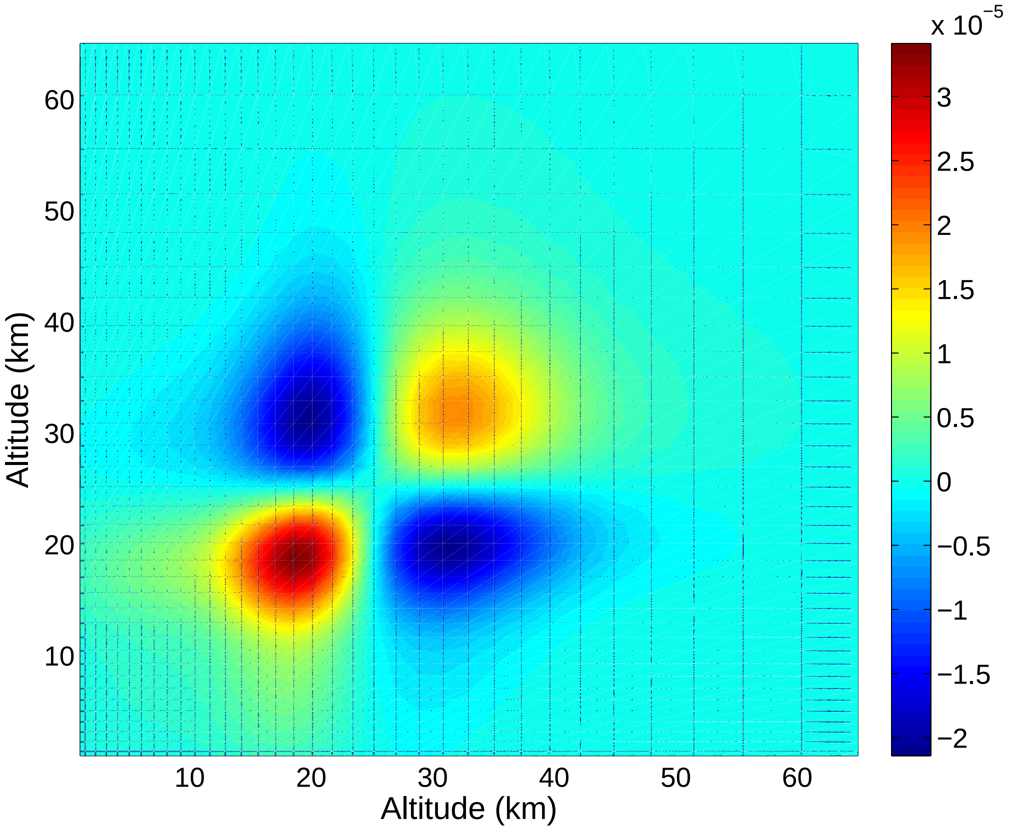

Figure 5.11: Ozone state space interference error covariance matrix contours, $\mathbf{S_p}$, calculated for the retrieval using the spectrum shown in Figure 5.2, which was recorded on 17 June 2003.

of the smoothing error and the forward model error due to temperature error (here, it was assumed that the temperature error was constant at 9% for all layers).

As the final, retrieved products of the TAO-FTS are total and partial column concentrations, there is a recurring question about how to represent the total retrieval error for these lone quantities. A 38 by 38 dimensional covariance matrix cannot be reduced to one number without losing some information. The practice currently in use at TAO is to assume that the diagonal elements of the covariance matrix (that is, the variance of each

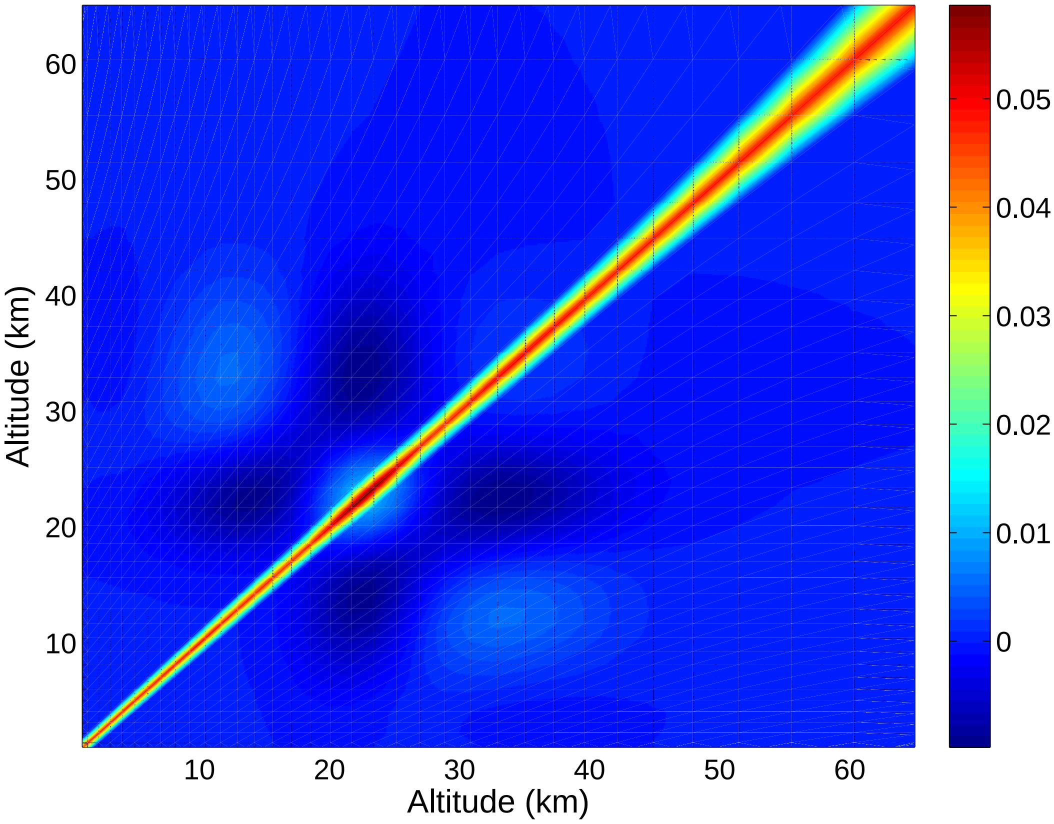

Figure 5.12: Ozone total retrieval error covariance matrix contours, $\mathbf{S_t}$, calculated for the retrieval using the spectrum shown in Figure 5.2, which was recorded on 17 June 2003.

profile element) are independent and can be added together in quadrature for a given column. Therefore, for a column concentration calculated from Equation 5.23, the total retrieval error, $\delta\hat{\mathbf{c}}$ is estimated as:

$$\delta\hat{\mathbf{c}} = \sqrt{\sum_i \mathbf{S_{t_{ii}}}}, \tag{5.32}$$

where i spans the elements for the altitude range over which the column is calculated. To understand how the relative sources of error contribute to this total estimate, Figure

5.13 shows the breakdown of the individual variances. All error estimates for columns shown in the following sections will be based on Equation 5.32, unless otherwise stated.

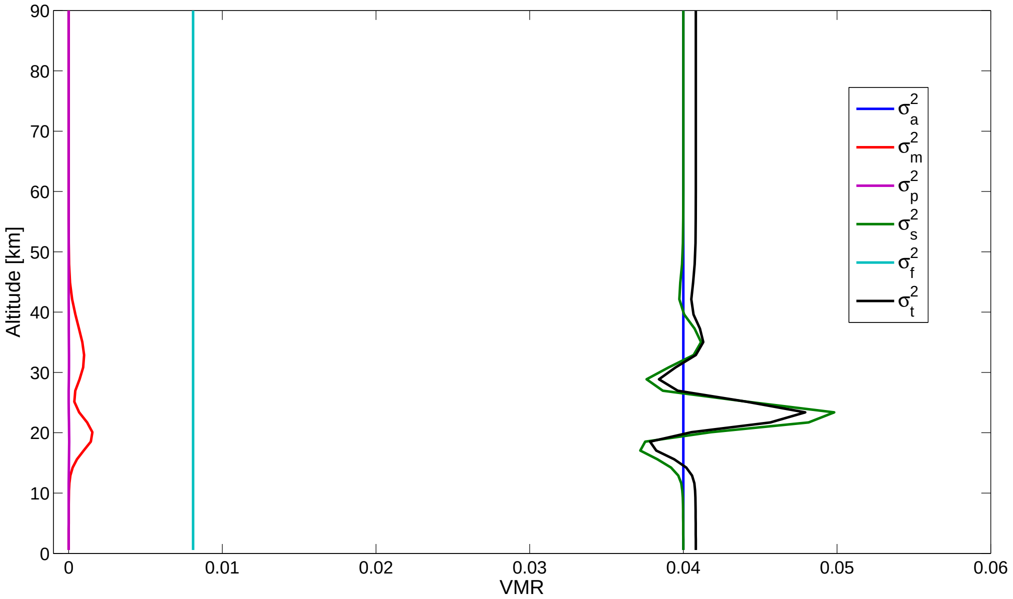

Figure 5.13: Ozone retrieval variances (σ^2) derived for the retrieval of the spectrum shown in Figure 5.2, which was recorded on 17 June 2003. The total error (black) is determined by adding the retrieval noise (red), the state space parameter interference error (purple), the smoothing error (green), and the forward model error (cyan), in quadrature. The *a priori* error is shown in blue. All values are expressed in parts per volume.

The example retrieval errors shown in Figure 5.13 indicate that this retrieval is not useful as the total error exceeds the *a priori* error (that is, the measurement does not contribute to the knowledge of the true state). As was pointed out earlier, this is primarily due to the fact that the smoothing error for this particular retrieval is greater than the *a priori* error. This example was shown here to specifically demonstrate the influence of blindly choosing an ad-hoc *a priori* error covariance matrix: although it provided numerical stability, it did not provide useful results.

However, when the same *a priori* error covariance matrix is used to retrieve N_2O from the exact same spectrum, the error variance shows that this retrieval is much more useful. Figure 5.14 shows that the total error only exceeds the *a priori* error above approximately 40 km, where retrievals are insensitive to volume mixing ratios of N_2O. In the troposphere, where N_2O is primarily located, the error terms are all less than the *a priori* error, indicating that this retrieval is contributing to the knowledge of the true state. This emphasizes the subtle point that although results from some retrievals may indicate the actual measurement is not useful, results from other retrievals can demonstrate the exact opposite. It is for this reason that results from all retrievals must be carefully scrutinized before they can be considered reliable.

5.4 Information Content Analysis

As was discussed in the previous two sections, retrieving VMR profiles on a 38-layer altitude grid does not imply that there are 38 independent pieces of information in each measurement. The vertical resolution, rather, is much coarser than this and requires that partial columns be calculated with Equation 5.23. To determine the altitudes over which these partial columns can be derived, it is necessary to consider the information content of a given measurement. To continue with the same formalism that has already been developed, the derivations in this section will be based on the work of Rodgers [2000].

As the weighting function matrix, $\mathbf{K}$, is responsible for relating the true state of the atmosphere to the observation, it is necessary to scrutinize this matrix in detail. The observation does not provide enough information to represent the truth on a 38-layer altitude profile. Only part of the truth will be captured by the signal in the observation,

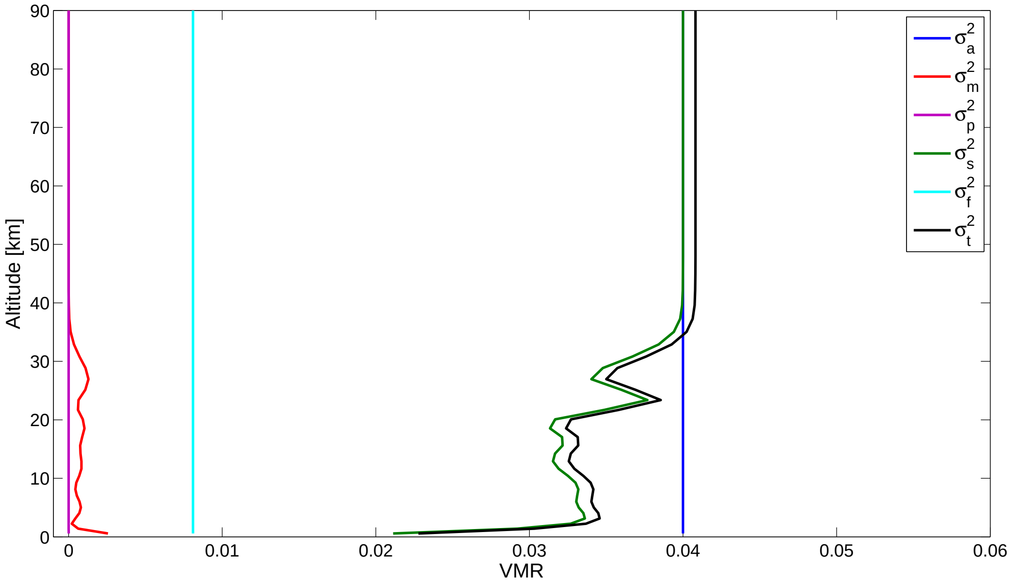

Figure 5.14: N_2O retrieval variances (σ^2) derived for the retrieval of the spectrum shown in Figure 5.2, which was recorded on 17 June 2003. The total error (black) is determined by adding the retrieval noise (red), the state space parameter interference error (purple), the smoothing error (green), and the forward model error (cyan), in quadrature. The *a priori* error is shown in blue. All values are expressed in parts per volume.

while the rest of the truth will be indistinguishable from the noise. To determine how the weighting function matrix maps between the observations and the truth, the state vectors must first be rotated and normalized.

To ensure that the weighting function matrix has independent layers with no off-diagonal elements, the state vectors must be *pre-whitened*. Let

$$\begin{aligned}\tilde{\mathbf{x}} &= \mathbf{S_a}^{-\frac{1}{2}}\mathbf{x},\\ \tilde{\mathbf{y}} &= \mathbf{S}_{\boldsymbol{\epsilon}}^{-\frac{1}{2}}\mathbf{y}.\end{aligned} \tag{5.33}$$

This transforms the relationship between the observed state space and the true state space to:

$$\begin{aligned}\mathbf{y} &= \mathbf{Kx} + \boldsymbol{\epsilon}\\ \Rightarrow \mathbf{S}_{\boldsymbol{\epsilon}}^{\frac{1}{2}}\tilde{\mathbf{y}} &= \mathbf{KS_a}^{\frac{1}{2}}\tilde{\mathbf{x}} + \boldsymbol{\epsilon}\\ \Rightarrow \tilde{\mathbf{y}} &= \mathbf{S}_{\boldsymbol{\epsilon}}^{-\frac{1}{2}}\mathbf{KS_a}^{\frac{1}{2}}\tilde{\mathbf{x}} + \mathbf{S}_{\boldsymbol{\epsilon}}^{-\frac{1}{2}}\boldsymbol{\epsilon}\\ &= \tilde{\mathbf{K}}\tilde{\mathbf{x}} + \tilde{\boldsymbol{\epsilon}},\end{aligned} \tag{5.34}$$

The measurement covariance in this new coordinate space becomes:

$$\begin{aligned}\mathbf{S}_{\tilde{\mathbf{y}}} &= \left\langle \left(\tilde{\mathbf{K}}\tilde{\mathbf{x}} + \tilde{\boldsymbol{\epsilon}}\right)\left(\tilde{\mathbf{K}}\tilde{\mathbf{x}} + \tilde{\boldsymbol{\epsilon}}\right)^T \right\rangle\\ &= \tilde{\mathbf{K}}\mathbf{I_n}\tilde{\mathbf{K}}^T + \mathbf{I_m}\\ &= \tilde{\mathbf{K}}\tilde{\mathbf{K}}^T + \mathbf{I_m},\end{aligned} \tag{5.35}$$

where $\mathbf{I_n}$ and $\mathbf{I_m}$ denote the identity matrices that are generated from the $\tilde{\mathbf{x}}$ and $\tilde{\boldsymbol{\epsilon}}$ unit matrices, respectively. The n-dimension represents the true state (38 layers, at TAO) and the m-dimension represents the observed state (that is, the number of spectral elements in a given microwindow). Since $\mathbf{I_m}$ is the component of the covariance matrix that arises from the measurement noise, it follows that $\tilde{\mathbf{K}}\tilde{\mathbf{K}}^T$ must represent the variability of the true state that is captured by the measurement. To ensure that the product $\tilde{\mathbf{K}}\tilde{\mathbf{K}}^T$ is diagonal and therefore comparable to $\mathbf{I_m}$, Singular Value Decomposition is performed on $\tilde{\mathbf{K}}$:

$$\tilde{\mathbf{K}} = \mathbf{U}\boldsymbol{\Lambda}\mathbf{V}^T, \tag{5.36}$$

where $\mathbf{U}$ is an m by m orthogonal matrix, $\mathbf{V}$ is an n by n orthogonal matrix, such that $\mathbf{U}^T\mathbf{U} = \mathbf{V}^T\mathbf{V} = \mathbf{I}$ and $\mathbf{\Lambda}$ is the diagonal matrix of singular values. If another coordinate space is defined as:

$$\begin{aligned} \acute{\mathbf{x}} &= \mathbf{V}^T\tilde{\mathbf{x}}, \\ \acute{\mathbf{y}} &= \mathbf{U}^T\tilde{\mathbf{y}}, \end{aligned} \tag{5.37}$$

then Equation 5.34 can be re-written as:

$$\begin{aligned} \tilde{\mathbf{y}} &= \tilde{\mathbf{K}}\tilde{\mathbf{x}} + \tilde{\boldsymbol{\epsilon}} \\ \Rightarrow \mathbf{U}\acute{\mathbf{y}} &= \mathbf{U}\mathbf{\Lambda}\mathbf{V}^T\mathbf{V}\acute{\mathbf{x}} + \tilde{\boldsymbol{\epsilon}} \\ \Rightarrow \acute{\mathbf{y}} &= \mathbf{U}^T\mathbf{U}\mathbf{\Lambda}\mathbf{V}^T\mathbf{V}\acute{\mathbf{x}} + \mathbf{U}^T\tilde{\boldsymbol{\epsilon}} \\ &= \mathbf{\Lambda}\acute{\mathbf{x}} + \acute{\boldsymbol{\epsilon}}. \end{aligned} \tag{5.38}$$

Since $\acute{\boldsymbol{\epsilon}}$ is white, its covariance matrix is the identity matrix and substituting this result into Equation 5.35 shows that $\tilde{\mathbf{K}}\tilde{\mathbf{K}}^T = \mathbf{\Lambda}^2$. Therefore, each singular value, λ_i, that is greater than about 1 will be represented by the observation better than the noise. From this, the number of independent pieces of information that can be derived from a given measurement is reflected in the singular values of the $\tilde{\mathbf{K}}$ matrix.

Following directly from this derivation is the concept of *degrees of freedom for signal*. As the initial formulation of the retrieval equation used here was based on Gaussian statistics (see Section 5.2), the most probable state is represented by a χ^2 distribution in which the total degrees of freedom are equal to the number of measurements. These degrees of freedom will be partitioned into two categories: the degrees of freedom for signal, d_s, is attributable to the state vector, and the degrees of freedom for noise, d_n, is attributable to the error. The degrees of freedom for signal can be derived from:

$$d_s = \left\langle \left(\hat{\mathbf{x}} - \mathbf{x_a}\right)^T \mathbf{S_a}^{-1} \left(\hat{\mathbf{x}} - \mathbf{x_a}\right) \right\rangle . \tag{5.39}$$

In terms of the coordinate transformations in Equations 5.33 and 5.37, this can be simplified to:

$$\begin{aligned} d_s &= tr\left[\mathbf{\Lambda}^2 \left(\mathbf{\Lambda}^2 + \mathbf{I_m}\right)^{-1}\right] \\ &= \sum_{i=1}^{m} \frac{\lambda_i^2}{1+\lambda_i^2}. \end{aligned} \tag{5.40}$$

Figure 5.15 shows singular vectors and their associated degree of freedom for signal per vector calculated from their singular values for a sample ozone observation made by the TAO-FTS. The total degrees of freedom for signal of this retrieval is 1.67. This indicates that there are less than two independent pieces of information contained in the retrieved state vector, $\hat{\mathbf{x}}$. Realistically, this limits the retrieval to only one partial column. The singular vector that has the degree of freedom equal to almost 1 is most strongly represented in the retrieval. The full width at half maximum of this singular vector can be used to guide the altitudes over which the partial column can be integrated. In this case, the indicated altitudes range is 20-36 km. The portions of the retrieved ozone profile beyond this altitude range are represented by the *a priori* profile as the true state space over these altitudes was lost in the measurement noise. This is consistent with Figures 5.4, 5.5, 5.6, and 5.7 from Section 5.2 which indicate that the retrieval is most sensitive over a similar altitude range.

As the ozone retrieved from the spectrum obtained on 17 June 2003 was shown to have limited vertical information content, it is necessary to consider how the quality of results from the TAO-FTS can be optimized. This is addressed in the next section.

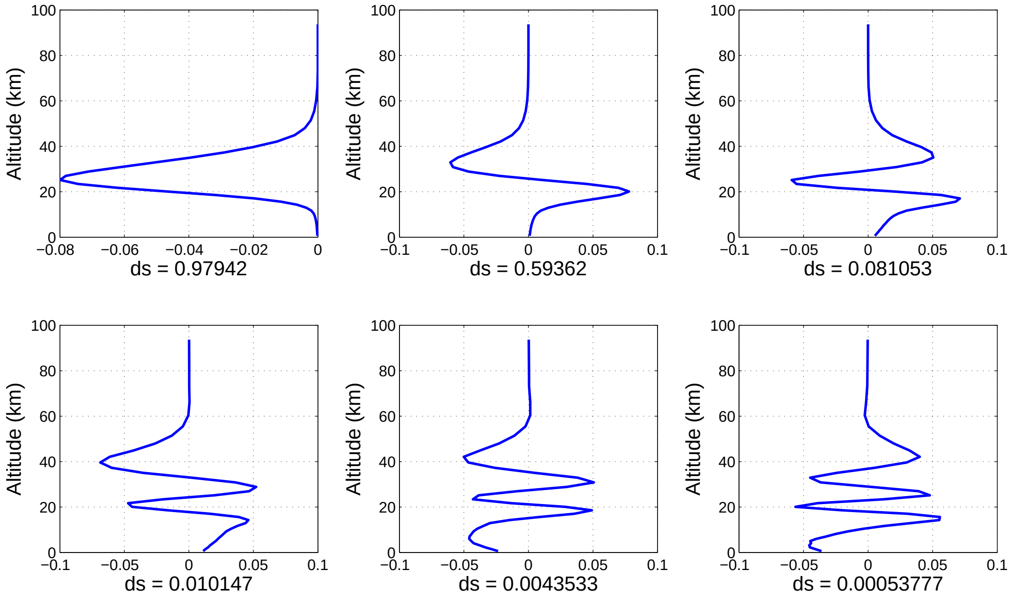

Figure 5.15: Ozone leading singular vectors and the associated degree of freedom for signal per vector calculated from their singular values for the retrieval using the spectrum shown in Figure 5.2, which was recorded on 17 June 2003. The total degrees of freedom for signal for the retrieval is 1.67.

5.5 Trace Gas Concentrations and Submission to the NDACC Archive

As the Toronto Atmospheric Observatory is a complementary station of the Network for the Detection of Atmospheric Composition Change, it is an obligation that data from the TAO-FTS be submitted to the NDACC. For the purposes of the NDACC, there are seven trace gases measured by the TAO-FTS that are currently archived: HCl, HF, N_2O, NO_2, NO, O_3, and CH_4. For each of these gases, total column values, stratospheric partial columns, tropospheric partial columns, and all of their respective errors are calculated and submitted. The first such submission took place in June 2005, and included all TAO-FTS data until the end of 2004 [Wiacek, 2006]. The second submission, which was performed as part of this project, took place in September 2007 and was composed of all the data collected by the TAO-FTS in 2005-2006. The details of the individual retrievals (including microwindow fits) can be found in Appendix A. The retrievals, errors, and information content details are summarized in Tables 5.2, 5.3 and 5.4, respectively.

Table 5.2: Summary of the TAO-FTS 2005-2006 data submitted to the NDACC archive. The degrees of freedom for signal were calculated using Equation 5.40.

Trace Gas	Total Number of Spectra	2005 Mean d_s	2005 Std. Dev. d_s	2006 Mean d_s	2006 Std. Dev. d_s
HCl	381	3.32	0.170	3.36	0.212
HF	170	2.27	0.194	2.36	0.172
N_2O	403	3.00	0.161	3.15	0.088
NO_2	392	2.62	0.170	2.62	0.173
NO	70	1.10	0.244	1.14	0.142
O_3	405	1.93	0.188	2.07	0.118
CH_4	429	3.18	0.141	3.23	0.132

As there is so much data to manage, it is necessary to establish and maintain a regular quality control scheme by which these data can be scrutinized. To facilitate this, a two-stage quality control plan was developed.

The first stage applies to the spectral measurements (i.e., the Level 1 data product). As each spectrum is recorded over a duration of approximately 20 minutes, it is possible that there is interference in the infrared radiation due to transient clouds. This source of

Table 5.3: Summary of the mean percentage error of the species retrieved from TAO-FTS 2005-2006 data submitted to the NDACC archive. All values are composed of the smoothing error and retrieval noise error combined in quadrature.

Trace Gas	2005 0-100 km	2005 0-15 km	2005 15-50 km	2006 0-100 km	2006 0-15 km	2006 15-50 km
HCl	0.7	16	1.8	0.7	16	1.7
HF	1.4	30	2.0	1.2	29	1.9
N_2O	0.3	0.6	4.2	0.2	0.5	4.1
NO_2	4.8	7.2	4.9	5.0	7.2	5.1
NO	5.2	20	6.9	4.7	20	6.3
O_3	2.2	9.2	2.3	2.0	9.3	2.0
CH_4	0.5	0.7	3.8	0.4	0.7	3.8

error is manifested in the spectrum as a net decrease in radiant intensity and, ultimately, a lower than normal signal-to-noise ratio. As was mentioned in Section 5.3, consideration is made for this in the calculation of measurement error, however, there must be a limit at which the measurement error becomes so large that the spectrum is no longer reliable as a high-precision observation. Imposing rigid numerical quality control boundaries for each spectrum is not feasible as each trace gas retrieval comes from a different part of the spectrum and, therefore, will include lines of various strengths and microwindows of various SNR. Consequently, SNR boundaries must be imposed for each individual trace gas retrieval.

To determine what the “normal” SNR value for a given microwindow is, an ensemble of retrievals in that microwindow must be scrutinized. After collecting data in a one year period at TAO, the SNR values for all of the fitted spectra in each microwindow

Table 5.4: Summary of the mean degrees of freedom for signal of the species retrieved from TAO-FTS 2005-2006 data submitted to the NDACC archive. All values were calculated using Equation 5.40.

Trace Gas	2005 0-100 km	2005 0-15 km	2005 15-50 km	2006 0-100 km	2006 0-15 km	2006 15-50 km
HCl	3.32	0.625	2.69	3.36	0.643	2.70
HF	2.27	0.312	1.96	2.36	0.342	2.02
N_2O	3.00	1.46	1.54	3.15	1.51	1.64
NO_2	2.62	0.412	2.21	2.62	0.421	2.20
NO	1.10	0.018	1.00	1.14	0.014	1.05
O_3	1.93	0.148	1.78	2.07	0.172	1.90
CH_4	3.18	1.52	1.66	3.23	1.54	1.69

are statistically analysed. The residual of the spectral fit in a microwindow is used to determine the SNR:

$$SNR = \frac{1}{\sigma_{RMS}}. \tag{5.41}$$

The median SNR value is then calculated from the ensemble of retrievals for a given year. The cutoff value for spectra that are considered too noisy is taken to be

$$1.2 * \langle SNR \rangle , \tag{5.42}$$

where $\langle SNR \rangle$ denotes the median signal-to-noise ratio. This cutoff value of 20% above the median was determined from a systematic study carried out by Wiacek [2006] for a previous submission of TAO-FTS data to the NDACC archive, and is used for all gases.

Because Equation 5.41 is directly related to the measurement error (Equation 5.28), this is, in effect, equivalent to defining the quality control in terms of the observation errors. However, it is thought that the SNR is a more readily interpretable quantity for determining the quality of a spectrum and was therefore used instead. A listing of all SNR cutoffs used for each of the gases submitted to the NDACC archive for the years 2005 and 2006 is shown in Table 5.5.

Table 5.5: Results from the first stage of quality control for the TAO-FTS 2005-2006 data submitted to the NDACC archive.

Trace Gas	Number of Spectra	SNR Cutoff	Number Rejected	Number Accepted
HCl	558	772	177	381
HF	281	261	111	170
N_2O	567	471	164	403
NO_2	544	1035	152	392
NO	115	159	45	70
O_3	555	363	150	405
CH_4	562	719	133	429

This first stage of the quality control process is designed to ensure that there are no sub-standard measurements being considered in any scientific studies. However, it is still possible that the retrieved atmospheric trace gas concentrations are unreliable due to poor-quality retrievals. The second stage of the quality control process should ensure that this does not happen.

This second stage applies to the retrieved VMR profiles (i.e., the Level 2 data product). Although the altitude resolution of trace gas profiles retrieved from ground-based, solar absorption spectra is limited (see Section 5.4), it is still helpful to scrutinize retrieved profiles to ensure that the integrated column amounts are reliable.

It directly follows from the retrieval theory outlined in Section 5.2 that the retrieved profiles are expected to deviate from the *a priori* profile, but this deviation should be within the *a priori* error. Since the *a priori* error is based on the natural variability of the trace gas profile, deviations beyond this value are exceptional and are most likely unphysical values due to numerical instability that arises from matrix ill-conditioning in Equation 5.10 [Hase et al., 2004]. Therefore, quality control should consider the extreme values of the retrieved profiles. The most direct way of doing this, is to simply impose the following criterion:

$$\hat{\mathbf{x}} \in \left[\mathbf{x_a} - 2\sqrt{\mathbf{S_{a_{ii}}}},\ \ \mathbf{x_a} + 2\sqrt{\mathbf{S_{a_{ii}}}}\right]. \tag{5.43}$$

This implies that the retrieved profile should lie within ±2σ of the *a priori* profile. This selection criterion is useful for most of the species of interest (HF, N_2O, NO, NO_2, and O_3), but not necessarily all of them. Because this criterion implicitly assumes that the retrieved state is linearly related to the *a priori* state, it does not always allow for true atmospheric variability which can span orders of magnitude due to the exponential nature of atmospheric pressure (see Figure 2.1). For CH_4 this was easily rectified by allowing an additional 20% variability. That is:

$$\hat{\mathbf{x}}_{\mathbf{CH4}} \in \left[\mathbf{x_a} - 2.2\sqrt{\mathbf{S_{a_{ii}}}},\ \ \mathbf{x_a} + 2.2\sqrt{\mathbf{S_{a_{ii}}}}\right]. \tag{5.44}$$

This relaxation in the criteria for CH_4 is not unreasonable as the variability of methane has previously been identified as problematic for both satellite-based FTS retrievals [Worden et al., 2004] and ground-based FTS retrievals [Dils et al., 2006].

For retrievals of HCl, this issue was more complicated as the *a priori* profile spanned several decades (from 10^{-9} to 10^{-12} parts per volume). Because of this large range in the state space, the retrieved trace gas profile frequently had oscillations that were negative and, therefore, unphysical. This problem has been previously identified at TAO [Wiacek, 2006] and in other retrieval data sets [Hase et al., 2004]. Although the negative profile values are unphysical, these values frequently occur in the troposphere and contribute little to the integrated column amounts (see Figure 5.16). Because these retrieved profiles are known to not be accurate representations of the troposphere (see the degrees of freedom for signal given in Table 5.4), allowance for negative profile oscillations was added to the quality control of HCl (the final timeseries of columns is shown in Figure 5.17):

$$\hat{\mathbf{x}}_{\mathbf{HCl}} \in \left[-\mathbf{x_a} + 2\sqrt{\mathbf{S_{a_{ii}}}},\ \ \mathbf{x_a} + 2\sqrt{\mathbf{S_{a_{ii}}}}\right]. \tag{5.45}$$

By allowing both HCl and CH_4 to have tailored quality control criteria on their respective retrieved profiles, the number of accepted and rejected observations from the second stage of the quality control is consistent with those of the other trace gases (see Table 5.6).

Figures 5.18-5.22 show the resulting 2005-2006 timeseries of retrieved columns submitted to the NDACC archive. For consistency, total columns (0-100 km), stratospheric columns (15-50 km), and tropospheric columns (0-15 km) are calculated for every species regardless of whether the averaging kernels and degrees of freedom for signal support such concentrations (see Table 5.4). Errors are derived from combining the corresponding smoothing error and retrieval noise in quadrature, for each species (see Table 5.3).

The HCl columns shown in Figure 5.18 once again demonstrate the importance of considering the altitude sensitivity of the measurements and the related degrees of freedom for signal. As HCl is predominantly found in the stratosphere, the total columns are almost equivalent to the stratospheric columns. The tropospheric columns are comparatively

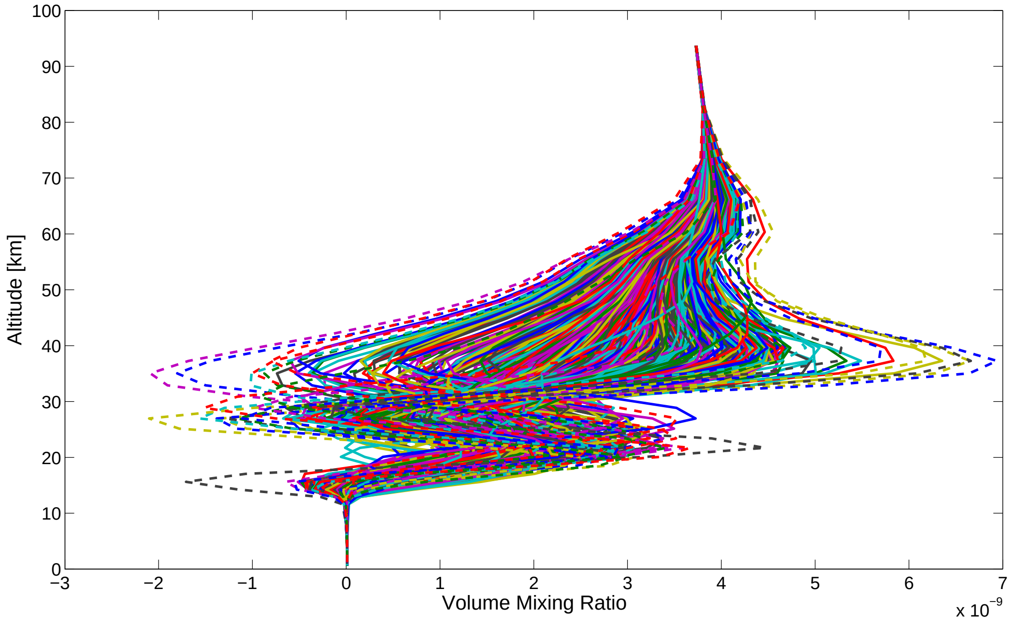

Figure 5.16: The second stage of the quality control process applied to retrievals of HCl. Accepted profiles have solid lines, while rejected profiles have dashed lines. The volume mixing ratio is expressed in parts per volume.

very small and significant uncertainty is associated with them. The mean degrees of freedom for signal of the total HCl columns are ≈3.3 while those of the tropospheric and stratospheric columns are ≈0.6 and ≈2.7, respectively. This further indicates that the bulk of the information gained by the measurement is present in the stratosphere and the values in the troposphere are composed almost entirely of the *a priori* values.

Similar to HCl, both HF (see Figure 5.19) and O_3 (see Figure 5.20) are gases which have a predominantly stratospheric signal. In both cases, the total columns and stratospheric columns virtually overlap while the tropospheric columns are close to zero. The mean degrees of freedom for signal of total column HF are ≈2.3 while those of the HF strato-

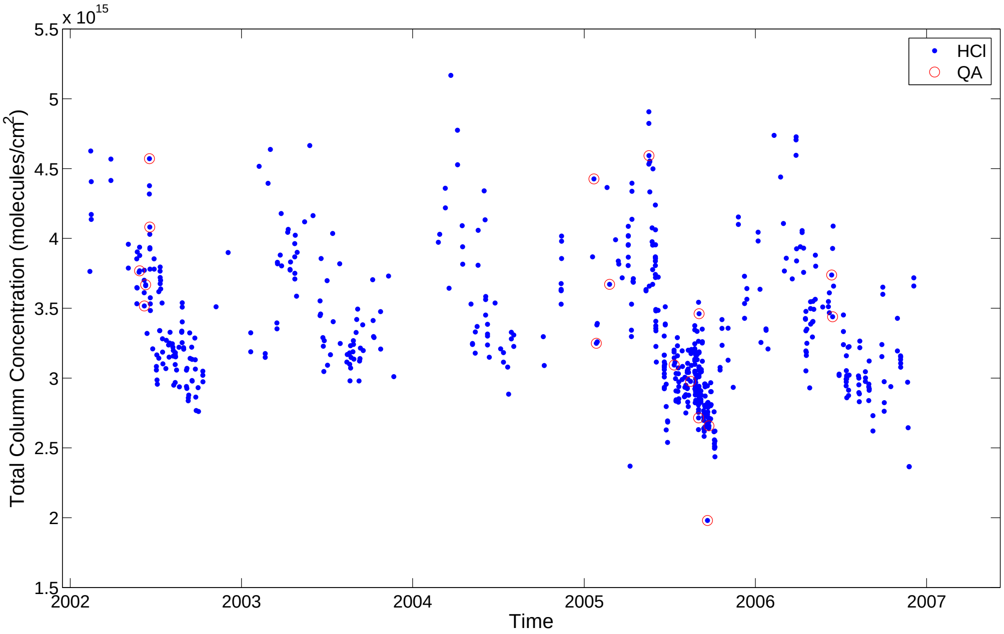

Figure 5.17: Results from the second stage of the quality control process applied to retrievals of HCl. Total columns of HCl are shown as blue dots, with rejected column values circled in red. The rejected columns were represented by the profiles with the dashed lines in Figure 5.16.

spheric columns are ≈2.0 and HF tropospheric columns are ≈0.3. The same distribution of information in the measurements is seen in the O_3 retrievals as the mean total column degrees of freedom for signal are ≈2.0, while those of the stratosphere and troposphere are ≈1.8 and ≈0.2, respectively.

N_2O results display the opposite effect as it is predominantly located in the troposphere and, as such, its total column values are primarily comprised of its tropospheric column (see Figure 5.21). It is important to note that although the N_2O stratospheric columns are comparatively small, they still contain useful information. For this gas, both the

Table 5.6: Results from the second stage of quality control for the TAO-FTS 2005-2006 data submitted to the NDACC archive.

Trace Gas	Number of Profiles	Number Rejected	Number Accepted
HCl	381	10	371
HF	170	19	151
N_2O	403	197	206
NO_2	392	17	375
NO	70	9	61
O_3	405	4	401
CH_4	429	64	365

tropospheric and stratospheric column mean degrees of freedom for signal are $\approx$1.5, indicating that the information contained in the measurement is evenly distributed between these two regions of the atmosphere. The mean total column N_2O degrees of freedom for signal are $\approx$3.0. Therefore, unlike HCl, HF, and O_3, retrievals of N_2O have vertical sensitivity over the entire 0-50 km range.

The CH_4 retrievals are similar to those of N_2O as they have with vertical sensitivity in both the troposphere and stratosphere (see Figure 5.22). The mean total column degrees of freedom for CH_4 are $\approx$3.2 while those of the stratosphere and troposphere are $\approx$1.5 and $\approx$1.7, respectively. Therefore, CH_4 can also be measured well over the entire 0-50 km range.

NO and NO_2 retrievals are marked by their relatively large column uncertainty (see Figures 5.23 and 5.24, respectively). NO tropospheric columns appear to be relatively large, but this is almost entirely due to the *a priori* values as the mean degrees of freedom for

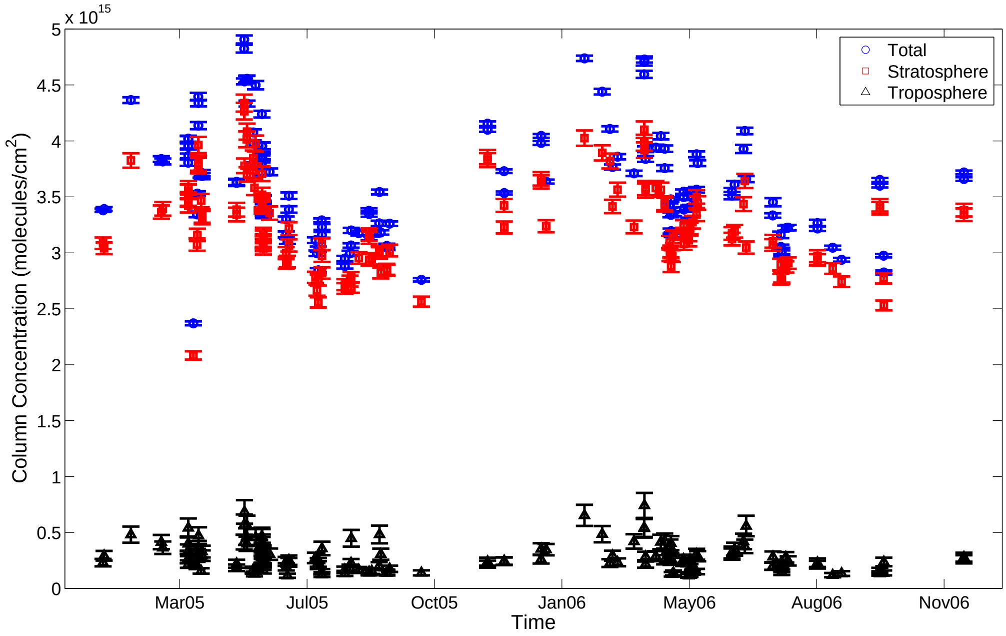

Figure 5.18: HCl total columns, stratospheric columns, and tropospheric columns submitted to the NDACC archive. Error bars represent smoothing error and retrieval noise added together in quadrature.

signal in the troposphere is close to 0. Almost all of the information in the NO retrievals is found in the stratospheric column as the mean total and stratospheric degrees of freedom for signal are ≈1.1 and ≈1.0, respectively.

The NO_2 retrievals are similar in that almost all of the information is contained in the stratospheric column. The mean total column degrees of freedom for signal are 2.6 while those of the stratospheric and tropospheric columns are ≈2.2 and ≈0.4 respectively.

The assessment of the quality of these retrieved quantities through cross-validation with other ground-based measurements is addressed in the next chapter.

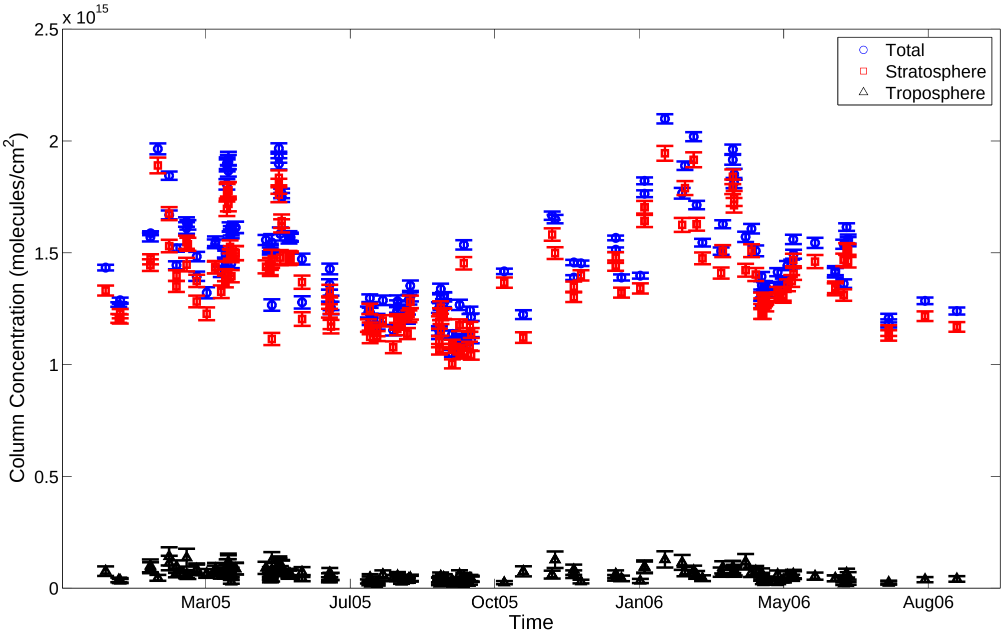

Figure 5.19: HF total columns, stratospheric columns, and tropospheric columns submitted to the NDACC archive. Error bars represent smoothing error and retrieval noise added together in quadrature.

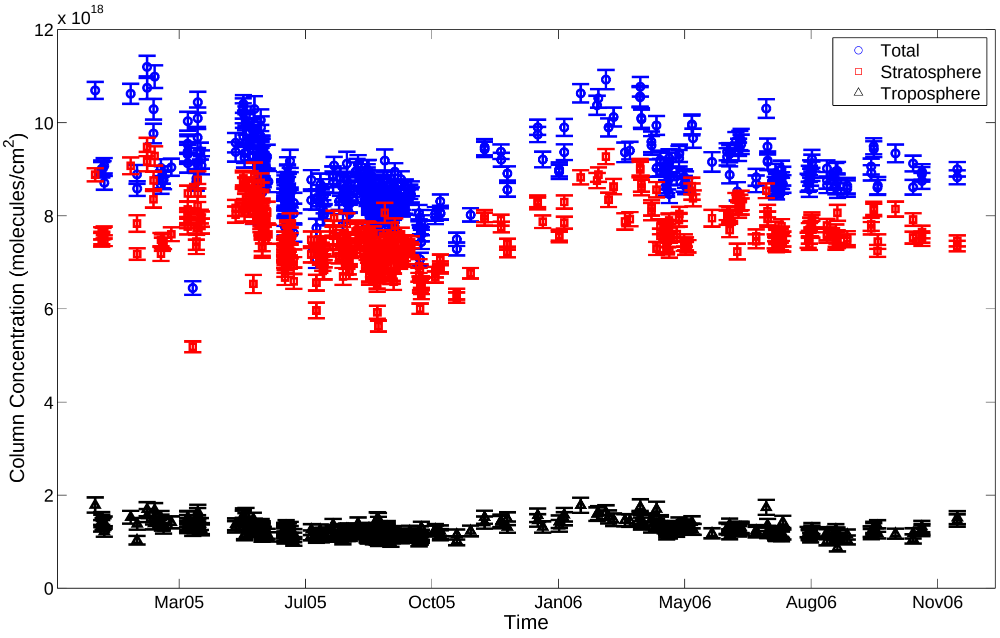

Figure 5.20: O_3 total columns, stratospheric columns, and tropospheric columns submitted to the NDACC archive. Error bars represent smoothing error and retrieval noise added together in quadrature.

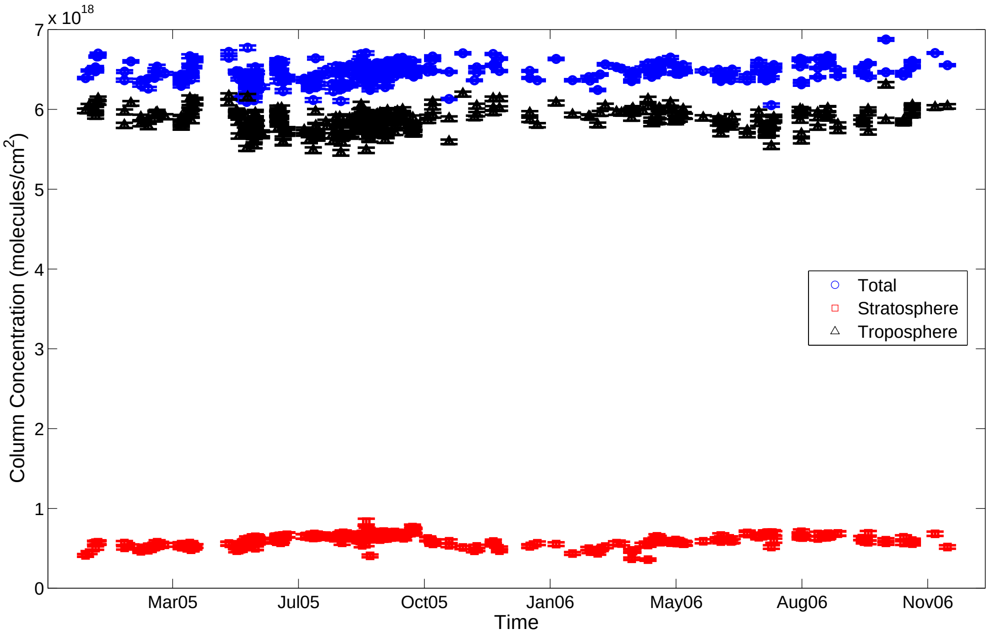

Figure 5.21: N_2O total columns, stratospheric columns, and tropospheric columns submitted to the NDACC archive. Error bars represent smoothing error and retrieval noise added together in quadrature.

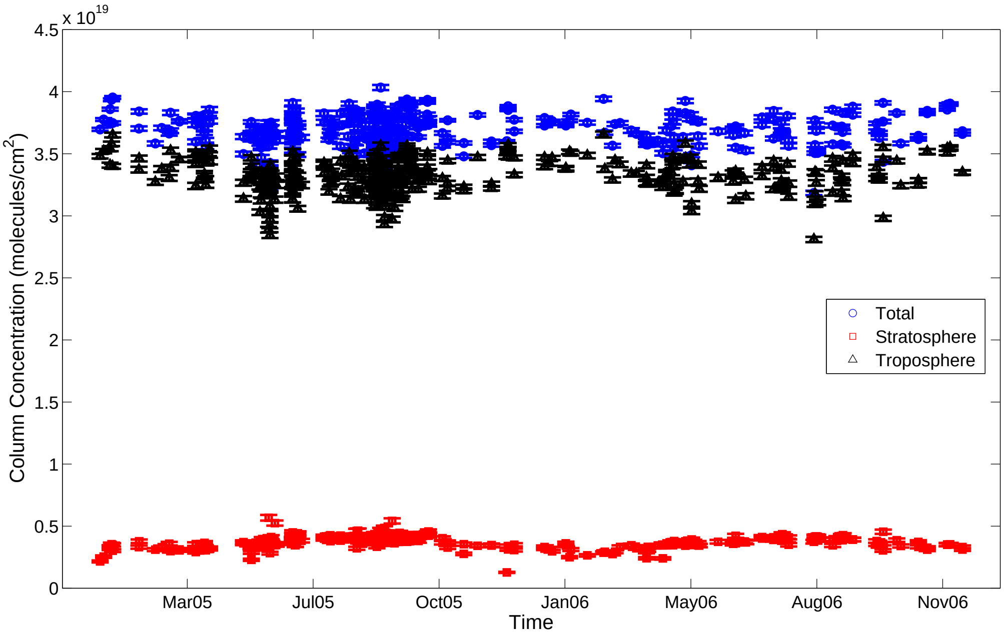

Figure 5.22: CH_4 total columns, stratospheric columns, and tropospheric columns submitted to the NDACC archive. Error bars represent smoothing error and retrieval noise added together in quadrature.

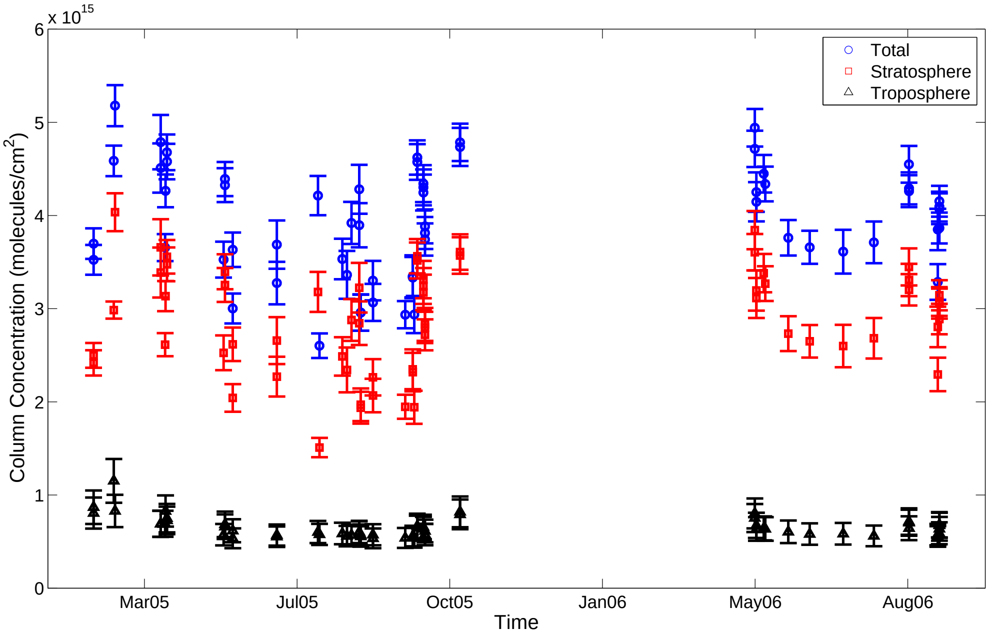

Figure 5.23: NO total columns, stratospheric columns, and tropospheric columns submitted to the NDACC archive. Error bars represent smoothing error and retrieval noise added together in quadrature.

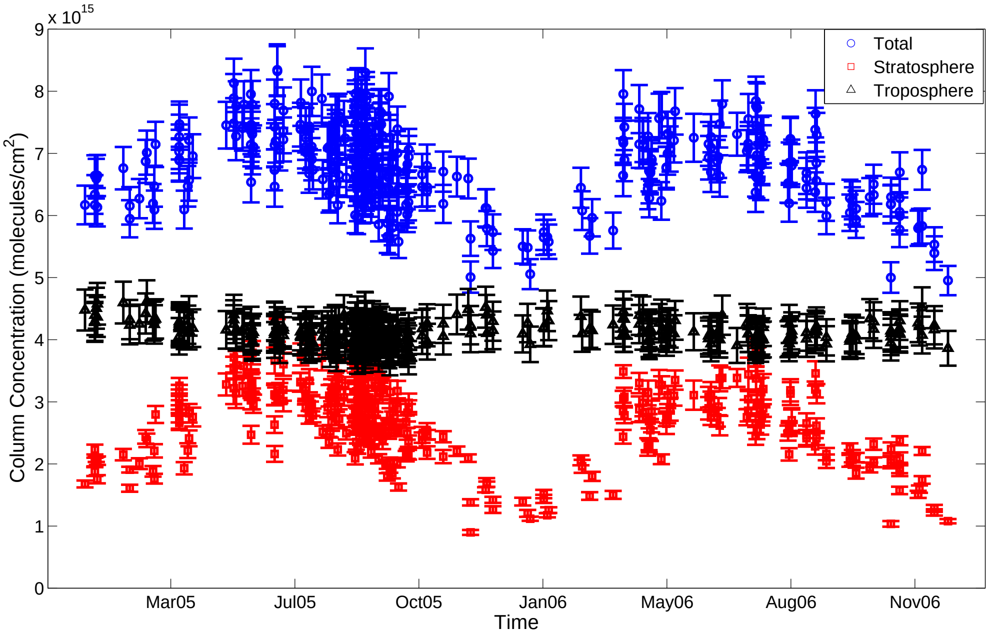

Figure 5.24: NO_2 total columns, stratospheric columns, and tropospheric columns submitted to the NDACC archive. Error bars represent smoothing error and retrieval noise added together in quadrature.

Chapter 6

Ground-Based Data Validation

As atmospheric remote sensing relies on the observation of one variable to yield insight into the state of another variable, an inversion of the function relating these two variables must be performed to retrieve the final data product of interest (see Section 5.2). The relationship between the measured quantity and the proxy variable is often complicated and requires many *a priori* estimates [Rodgers and Connor, 2003]. An integral part of scrutinizing the quality of the data collected by an instrument is to validate the retrieved values by comparing them with a *standard* data set. Ideally, this *standard* data set would adequately reflect the true state of the atmosphere; however, if the true state were actually known, there would be little need to make further measurements. As such, the process of instrument validation is concerned with detecting any potential bias between the data products of two instruments as well as to aid in characterizing the precision of the measurements. As a *standard* data set is not always available, it is often necessary to compare like observations from one or more instruments that have not previously been validated. This provides equally valuable insight into the characterization of the instrument and is commonly referred to as "cross validation" [von Clarmann, 2006].

Traditionally, all instruments must go through a validation and certification process prior to gaining official status as an NDACC affiliated instrument [Kurylo and Zander, 2000]. As Fourier transform spectrometers are typically large instruments that have limited mobility, it is often impractical to validate an instrument with side-by-side intercomparison campaigns [Griffith et al., 2003]. To certify TAO as a complementary site of the NDACC, a retrieval intercomparison was performed in which the data recorded by the TAO-FTS and the expertise of the operating personnel was scrutinized (for details, see Wiacek et al. [2007]). Following the NDACC certification of TAO in 2004, arrangements were made to have a side-by-side instrument intercomparison campaign with a second FTS known as the University of Toronto Fourier Transform Spectrometer (U of T FTS), immediately followed by a shorter focused campaign involving a third FTS: the Portable Atmospheric Research Interferometric Spectrometer for the Infrared (PARIS-IR).

Previous intercomparisons of ground-based FTS observations have primarily focused upon the agreement of quantities retrieved with different analysis algorithms or addressed how the individual instrument performance impacts the retrieved vertical column concentrations [Paton-Walsh et al., 1997, Goldman et al., 1999, Griffith et al., 2003, Meier et al., 2005, Hase et al., 2004]. Similarly, this intercomparison sought to address the question of agreement between the instruments' measurements, but because they were both located at the University of Toronto, extensive simultaneous measurements could be made over a duration of four months. These relatively large data sets allowed for a more detailed statistical comparison than previous ground-based campaigns. By employing the vertical profile retrieval technique technique in use at TAO, analytical calculations of averaging kernels could be made, allowing for a better characterization of the agreement between altitude sensitivity of the individual measurements. Consequently, the differences between the measurements were considered in terms of systematic biases, both additive and multiplicative.

The study is presented here in two parts; the first addresses the long timeseries of coincident observations between the TAO-FTS and the aforementioned U of T FTS [Taylor et al., 2008], while the second is a focused campaign which compared these two instruments with a third, lower-resolution FTS using data acquired over a two-week period [Wunch et al., 2007]. While both comparisons were necessarily collaborative in nature, it should be noted that the focused comparison was included in the work of another PhD project and, as such, every effort has been made to ensure that the work presented here is representative of the work done for this project. Both intercomparisons focused on the same four gases: O_3, HCl, N_2O, and CH_4. In addition to testing the repeatability of whether spectral resolution impacts the retrievals of all four gases, the cause of the differences between O_3 and HCl was determined by analysing differences between the instruments' total column averaging kernels.

These four trace gases were chosen for the comparison data set as they are a scientifically important cross-sectional sample from both the troposphere and stratosphere. Stratospheric O_3 is known to be important not only in the context of the ozone layer, but also as a greenhouse gas (see Section 2.4). HCl is related to stratospheric ozone depletion because it acts as a reservoir species for reactive chlorine that catalyzes ozone loss (see Equation 2.4). Both of these gases are predominantly found in the stratosphere and, as such, test the instruments' abilities to precisely detect stratospheric species. The other trace gases, CH_4 and N_2O, are two of the most important greenhouse gases (see Figure 2.2). As well, CH_4 is an important precursor of ground level ozone (see Equation 2.7), and N_2O is the source of stratospheric NO_x (see Section 2.2). As these two species are predominantly tropospheric, they provide an adequate test of the instruments' tropospheric sensitivities.

6.1 Extended FTS Intercomparison

This intercomparison campaign was held from 26 May - 2 September 2005 with a lower-resolution instrument known as the U of T FTS. To date, this campaign represents the longest intercomparison of ground-based observations between Fourier transform spectrometers and, therefore, provides a timeseries of side-by-side observations larger than any previous cross-validation exercises (see Taylor et al. [2008] for details).

6.1.1 U of T FTS

The University of Toronto's Fourier Transform Spectrometer is an ABB Analytical DA5 instrument with a 50-cm maximum OPD that records single-sided interferograms along a linear mirror path. The instrument measures with two photovoltaic detectors (InSb and MCT) simultaneously through the use of a beamsplitter. The U of T FTS has a spectral range spanning 1200–5000 cm^{-1} that is constrained by the detectors, a CaF_2 beamsplitter and a germanium solar filter.

The instrument has had new electronics and software installed so that it can be used both on high-altitude balloon platforms and on the ground. It has taken part in the Middle Atmosphere Nitrogen TRend Assessment (MANTRA) mission high-altitude balloon flights, flown biennially in 1998-2004 from Vanscoy, Saskatchewan, Canada (52° 01′ N, 107° 02′ W, 511.0 m) [Strong et al., 2005]. The modifications include control software that allows automated measurements and access to housekeeping data (voltages, temperatures, etc.). The U of T FTS has also been fitted with a sun tracker that has a small tracking range (±10° in both zenith and azimuth). It is used on the balloon to track the Sun during sunrise or sunset, where it performs fine azimuth pointing to complement the payload's main pointing system. The tracker for this intercomparison is used to align the U of T FTS with the TAO sun tracker. A more detailed description of the U of T FTS can be found in Wunch et al. [2006].

For the purpose of this intercomparison campaign, only data from the MCT detector are shown. At two points during the summer of 2005, the detector alignment system for the InSb detector was upgraded (without affecting the MCT detector alignment), hence, a time series based on InSb observations would add uncertainty to the results. The spectral ranges of the two detectors overlap in all regions of interest for this study.

6.1.2 Intercomparison Strategy

The observation strategy for this intercomparison campaign was designed to determine the influence of the instruments on retrieved vertical column amounts by minimizing the impact of other factors. By using co-located, ground-based instruments, many of the challenges associated with instrument intercomparisons can be eliminated. Because the instruments were simultaneously measuring solar absorption, they were, in effect, both sampling the same infrared spectra. Consequently, there is no need to consider the effects of temporal and/or spatial sampling heterogeneity. Additionally, the retrievals performed on the recorded spectra utilized the same constraints by measuring in the same spectral range, using identical retrieval methods, *a priori* information, line parameters, and model atmospheres. This ultimately provided observation systems that were so similar, there was no need to consider the differences in data products in the fashion recommended by Rodgers and Connor [2003]; rather, the differences arising from this intercomparison can be directly related to the instruments.

To measure the same atmospheric path simultaneously with both instruments, the solar beam from the TAO sun tracker was shared by using a small pick-off mirror to deflect a portion of the light into the U of T FTS. Every effort was made to ensure that the TAO-FTS incurred a minimal loss of signal (the mean SNR decrease was less than 5%

in comparison to the nominal SNR), while still providing sufficient signal for the U of T FTS. This arrangement ensured that the atmospheric conditions were identical for each instrument throughout the measurements. To further ensure simultaneity, the U of T FTS co-added interferograms to match the recording periods of the TAO instrument, which has a longer scan time. While the TAO-FTS co-adds four interferograms to record one spectrum in approximately 20 minutes, the U of T FTS only requires 50 seconds to record an interferogram. Consequently, 15–20 scans from the U of T FTS were co-added to generate a spectrum that was coincident in time with that of the TAO-FTS. See Table 6.1 for more details.

Table 6.1: Instrument parameters from the ground-based, extended FTS intercomparison campaign.

Parameters	U of T FTS	TAO-FTS
Maximum Optical Path Difference (cm)	50	250
Time per scan (s)	50	300
Interferograms per Spectrum	15-20	4
Spectral Range (cm^{-1})	1200–5000	F3 (2400–3100)
Measurement Period	26 May–12 Sept.	Year-round

As this comparison uses measured solar absorption of O_3, HCl, CH_4, and N_2O in the same spectral region, TAO-FTS measurements used in the intercomparison were carried out solely with NDACC Filter 3, which spans 2400–3100 cm^{-1}. This was chosen for two reasons: first, the Filter 3 region has the strongest signal, and so the slight loss from the pick-off mirror used to feed the U of T FTS was of little consequence to the SNR of the TAO-FTS observations, and second, filter 3 contains informative spectral features for all four of the species of interest.

As was mentioned previously, these four gases were chosen as they represent species that are predominantly located within the stratosphere (O_3 and HCl) as well as species that are predominantly tropospheric (CH_4 and N_2O). By making this choice, the differences in the pressure broadening of spectral lines observed by the lower and higher-resolution instruments could be investigated. Additionally, all of these compounds are of scientific interest and, therefore, require precise measurements. Vertical profile retrievals of O_3 from ground-based FTS spectra were first retrieved by Pougatchev et al. [1995], while the first ground-based FTS measurements of HCl were recorded by Goldman et al. [1986]. N_2O and CH_4 have both been routinely observed by ground-based FTIR since 1979 [Zander et al., 1989, Wallace and Livingston, 1990a,b, Zander et al., 1994].

6.1.3 Data Analysis

As is standard protocol for data analysis at TAO, the SFIT2 algorithm was used for retrieving results from both the TAO-FTS and the U of T FTS. This employs the Optimal Estimation Method (OEM) that was outlined in Section 5.2. Previous ground-based intercomparison campaigns have relied on the SFIT1 algorithm [Rinsland et al., 1982], which treated all quantities in the state space as scaling factors for VMR profiles, and utilized a nonlinear least squares fitting routine as opposed to the OEM technique. Column concentrations retrieved with SFIT2 from ground-based spectra have been compared with like results from other retrieval algorithms and have been found to agree within 1% for matched retrieval constraints [Hase et al., 2004].

The nonlinear forward model of the SFIT2 algorithm also uses *FSCATM* v2.03, which relies on *a priori* knowledge of pressure, temperature, and VMR profiles to perform refractive ray tracing and calculations of the air mass distribution for a model atmosphere. The TAO-FTS standard operating parameters were used for this (see Section 5.2) so as to eliminate any differences in the parameterization of the retrieval.

To reduce the computational burden, retrievals have traditionally been carried out in small "microwindow" intervals which contain the spectral absorption features of interest. Table 6.2 shows the microwindows used for all of the retrievals in this intercomparison as well as the interfering gases fitted. The selection of the range and parameters of these microwindows was based upon previous intercomparison campaigns [Meier et al., 2005] and on the available spectral range of the instruments. For each of the target gases, the *a priori* covariance matrices were constructed to represent 30% standard deviation in all 38 layers of the state space without any off-diagonal correlations so as to provide the most numerically stable retrievals [Rodgers and Connor, 2003]. The measurement covariance matrices were constructed using the SNRs of the spectral microwindows and were also chosen to be uncorrelated.

Most instrument intercomparison and validation campaigns often encounter the problem of only having a brief period of time in which to gather coincident data, thus limiting the number of measurements available for comparison. Previous campaigns have provided statistical comparisons of such data sets, but were constrained to comparing mean values [Goldman et al., 1999, Griffith et al., 2003] or considering systematic biases [Paton-Walsh et al., 1997, Meier et al., 2005]. As well, previous campaigns have been restricted to using column retrieval algorithms in which the altitude information is folded into the data products.

The advantage of having a relatively long-term intercomparison of coincident observations by two instruments is the opportunity not only to gather a large quantity of good data, but also to develop a more rigorous statistical analysis of the differences between the data sets. Furthermore, by having two observing systems make simultaneous observations with identical viewing geometry, similar instrumentation, and the same retrieval algorithms and constraints, many of the barriers that inhibit the direct comparison of

Table 6.2: Spectral microwindows used for the retrieval of each trace gas as well as interfering species that were fitted simultaneously in the ground-based, extended FTS intercomparison campaign. Both CH_4 and O_3 (2775) were globally fitted with three simultaneous band-passes.

Target Gas	Microwindow(s) (cm^{-1})	Interfering Gases	Typical SNR (TAO-FTS)	Typical SNR (U of T FTS)
O_3	3039.90-3040.60	H_2O, CH_4	205	365
O_3	2775.68-2776.30	CH_4, CO_2, HCl, N_2O	410	915
	2778.85-2779.20	CH_4, HDO, N_2O		
	2781.57-2782.06	CH_4, HDO, N_2O, CO_2		
HCl	2925.75-2926.05	H_2O, CH_4, NO_2, O_3	685	760
N_2O	2481.30-2482.60	CO_2, CH_4, O_3	465	610
CH_4	2859.83-2860.21	H_2O, HCl, O_3	420	350
	2898.32-2898.98	(same as above)		
	2903.60-2904.16	(same as above)		

observations, such as different smoothing error covariances [Rodgers and Connor, 2003], *a priori* states [von Clarmann and Grabowski, 2007], or different altitude grids [Calisesi et al., 2005], can be neglected. By utilizing the SFIT2 profile retrieval algorithm, an analysis of the vertical sensitivity of the observations can aid in better quantifying the cause of the differences. For this reason, initial comparisons were made between the two data sets by using statistical approaches that incorporate both additive and multiplicative biases [Dunn, 2004].

If it is assumed that two vectors of multiple measurements of a variable quantity, $\mathbf{y_1}$ and $\mathbf{y_2}$, made by the two instruments are each linear representations of a true quantity, $\boldsymbol{\tau}$, then the two data sets can be expressed as:

$$\begin{aligned} \mathbf{y_1} &= \alpha + \beta\boldsymbol{\tau} + \mathbf{e_1}, \\ \mathbf{y_2} &= \gamma + \delta\boldsymbol{\tau} + \mathbf{e_2}. \end{aligned} \tag{6.1}$$

The slopes of the equations, β and δ, represent the multiplicative biases for the first and second data set, respectively. Physically, this characterizes how sensitive an instrument is to changes in the truth. The intercepts of the equations, α and γ, represent the additive biases for the first and second data sets, respectively. Physically, this accounts for any consistent bias between the observations and the truth. The vectors $\mathbf{e_1}$ and $\mathbf{e_2}$ represent the errors in $\mathbf{y_1}$ and $\mathbf{y_2}$, respectively.

By substituting for the true quantity, $\boldsymbol{\tau}$, a single equation relating the two data sets can be derived:

$$\mathbf{y_2} = \frac{\delta}{\beta}\mathbf{y_1} + \left[\gamma + \mathbf{e_2} - \frac{\delta}{\beta}\left(\alpha + \mathbf{e_1}\right)\right]. \tag{6.2}$$

Therefore, by plotting data sets of coincident observations against each other and solving for the line of best fit, the slope will yield the ratio of the relative multiplicative biases of the two instruments, while the intercept will be a combination of the multiplicative biases, additive biases, and errors.

It is important to note that this reasoning is predicated on our initial assumption of linearity. While this is not necessarily true, it is often necessary to assume that the problem is nearly linear – that is, the problem is linear to the accuracy of the measurements within the normal range of variation of the truth, $\boldsymbol{\tau}$ [Rodgers, 2000]. Because of this, it is possible that some of the variance of the data will be due to nonlinearity. Furthermore, these data sets should be treated as heteroskedastic (i.e. the data may have differing variances). Consequently, a weighted least squares approach outlined by York et al. [2004] was used to fit the data to Equation 6.2.

By substituting the retrieved values from Equation 5.10 into Equation 6.2, a linear relation between the retrieved sets of data from each instrument is derived. Thus, the line of best fit of a scatter plot of the two data sets can be expressed in terms of averaging kernels, *a priori* states, and errors as:

$$\hat{\mathbf{x}}_\mathbf{2} = \left(\mathbf{A_2 A_1^{-1}}\right)\hat{\mathbf{x}}_\mathbf{1} + \left(\mathbf{I} - \mathbf{A_2 A_1^{-1}}\right)\mathbf{x_a} - \mathbf{A_2 A_1^{-1}}\boldsymbol{\epsilon}_\mathbf{1} + \boldsymbol{\epsilon}_\mathbf{2}. \tag{6.3}$$

Therefore, by plotting the retrieved results from each instrument against each other, the slope of the best fit represents the multiplicative biases in terms of the averaging kernels. For this comparison, the focus has been placed on total columns, which involves multiplying Equation 5.10 by a total column operator, $\boldsymbol{\rho}$, composed of the air density profile. As with Equation 6.3, the line of best fit for the resulting total columns, $\hat{c}_1$ and $\hat{c}_2$, can be expressed in terms of averaging kernels, *a priori* states, and errors as:

$$\hat{c}_2 = \left(\boldsymbol{\rho}\mathbf{A_2 A_1^{-1}}\boldsymbol{\rho}^{-\mathbf{1}}\right)\hat{c}_1 + \boldsymbol{\rho}\left(\mathbf{I} - \mathbf{A_2 A_1^{-1}}\right)\mathbf{x_a} - \boldsymbol{\rho}\mathbf{A_2 A_1^{-1}}\boldsymbol{\epsilon}_\mathbf{1} + \boldsymbol{\rho}\boldsymbol{\epsilon}_\mathbf{2}. \tag{6.4}$$

By comparing Equations 6.4 and 6.2, the corresponding coefficients result in the slope of the total column scatter plots being given by:

$$\mathit{slope} = \frac{\delta}{\beta} = \boldsymbol{\rho}\mathbf{A_2}\left(\boldsymbol{\rho}\mathbf{A_1}\right)^{-1}. \tag{6.5}$$

The quality of the spectra was determined by examining the signals of all recorded interferograms as well as the root-mean-square of the fit residuals in a given microwindow. As the RMS of the fit residual is related to the SNR of the spectrum (in the absence of serious systematic fitting errors), this screening technique filtered any spectra that had an excessive amount of noise (details and examples of this procedure are shown in Section

5.5). The fits were quantitatively scrutinized by setting a threshold RMS value above which all fits were discarded, thus eliminating the likelihood of using cloud-contaminated data. To ensure a high standard for this comparison, the threshold value was set to be 20% greater than the median value for a given microwindow.

Because spectra from both instruments were retrieved with the same algorithm and constraints, errors arising from systematic errors in the forward model or in the forward model parameters can be neglected. Likewise, errors associated with cloud contamination and/or day-to-day sub-visible solar variability need not be considered, as both spectrometers were measuring the collimated solar beam simultaneously. Total column errors were estimated from three sources: retrieval noise, smoothing error, and state space parameter interference error [Rodgers, 2000] (see Section 5.3). The error bars on all column amounts shown in figures represent these three errors combined together in quadrature.

The retrieval noise is an estimate of how the measurement error gets mapped onto the retrieved state space. The measurement error was estimated from the RMS noise of the fit residual for a given microwindow. For computational ease, it was assumed that the noise was uncorrelated.

In order to estimate the smoothing error, an ensemble of states that adequately represents the true state of the atmosphere must be chosen. Since the *a priori* states used in the retrievals were already constructed from climatologies derived from ensembles of observations, these same states were used for estimating the smoothing error. Once again, the standard deviations of these values were assumed to be uncorrelated between atmospheric layers. It is important to note that an *a priori* covariance of 30% over all layers was used for each gas so as to ensure numerical stability during the retrieval calculations.

For CH_4 and N_2O, this choice is higher than the expected variability of these gases in the troposphere, which may create larger than realistic error estimates.

Parameter interference error arises from retrieving a number of non-VMR elements in the state space. Not only is a volume mixing ratio profile being retrieved, but other parameters that are secondary to the comparison are also retrieved (such as wavenumber calibration, baseline curvature, etc.) Invariably, the retrieved VMR state has some correlation with all of these parameters and this must be considered by utilizing the averaging kernels [Rodgers and Connor, 2003].

6.1.4 Tropospheric Species Intercomparison

Measuring CH_4 columns in the infrared has previously been identified as problematic for both ground-based [Mazière et al., 2004] and satellite-based measurements [Worden et al., 2004]. These problems are primarily rooted in the current lack of accurate knowledge of the spectroscopic line parameters. However, for the purposes of this comparison, these do not contribute to any discrepancy between the retrieved columns. The retrieved CH_4 total columns have a median difference ($200 \times (UofT - TAO) \, / \, (UofT + TAO) \pm \sigma$) of 3.7±2.5%, with the U of T FTS observations showing consistently elevated values compared to those of the TAO-FTS (see Figure 6.1). However, the scatter plot of the columns (Figure 6.2) shows that the R^2 goodness of fit estimator is negative for the line of best fit. This estimate is calculated by using the standard formula: $R^2 = 1 - SSE/SST$, where SSE and SST are the sum of the squared error and total sum of squares respectively. Therefore, a negative value indicates that this fit does not adequately represent the data (it is actually worse than fitting a horizontal line), and should be discarded. This is not unexpected for this well-mixed gas as the observations sample a very small range of the methane parameter space, resulting in a plot with no discernable slope. In the focused comparison discussed in Section 6.2, the instruments' column values yielded a mean difference of 2.3%. Although this extended comparison incorporates 63 paired data points (compared to only 19 in the focused comparison), it appears that this disagreement is enhanced.

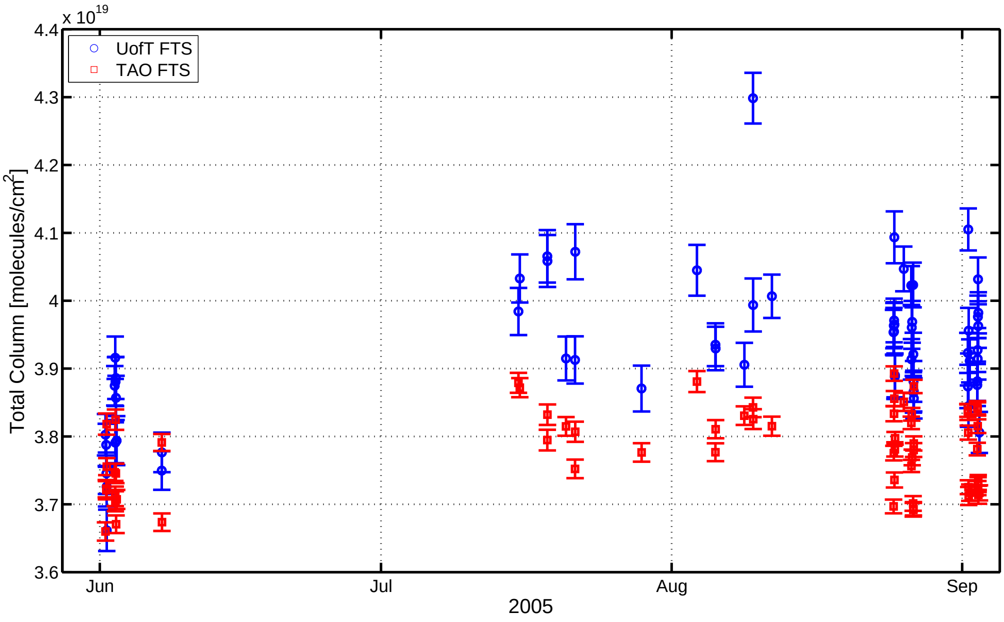

Figure 6.1: Time series of coincident CH_4 total column observations. Blue circles represent the U of T FTS columns, while red squares represent the TAO FTS columns. Error bars are a combination of retrieval noise, smoothing error, and state space parameter interference error.

The N_2O observations are in better agreement, with a median total column difference of less than 0.4±1.8% (see Figure 6.3). Unlike the CH_4 observations, there appears to be no significant additive bias between the two instruments. However, similar to CH_4, there is very little variation in the day-to-day values of N_2O, resulting in a scatter plot of concentrated data (see Figure 6.4). Consequently, fitting with the linear model again results in a negative R^2 value and does not adequately represent the data. The focused

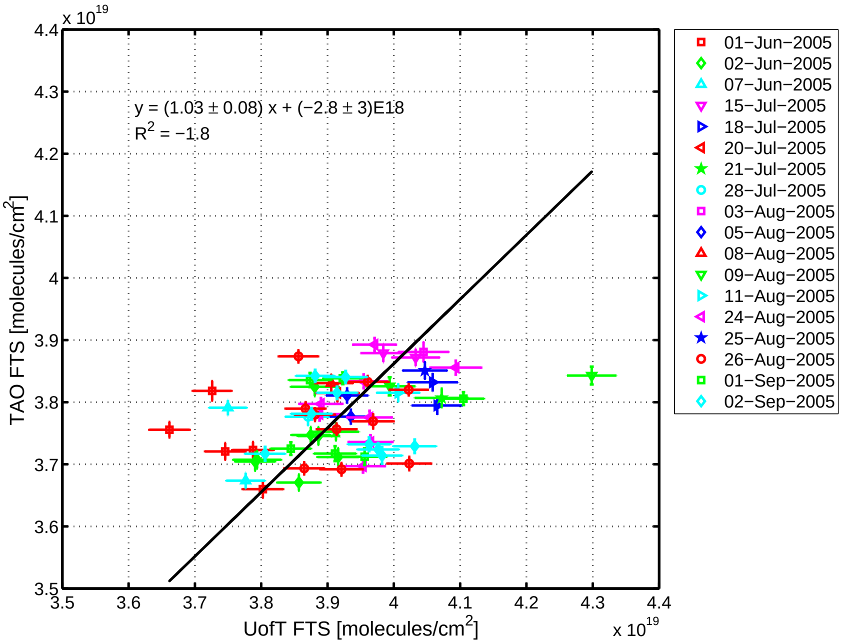

Figure 6.2: Scatter plot and fit of coincident CH_4 total column observations. Measurements made on different days are represented by different symbols. Error bars are as for Figure 6.1.

intercomparison of N_2O total column values showed the same level of agreement (0.4%) (see Section 6.2). This suggests that the broadened line features of N_2O are readily recorded in the lower-resolution spectra of the U of T FTS and the results compare well with those of the TAO-FTS.

6.1.5 Stratospheric Species Intercomparison

As it is expected that the narrow spectral features of stratospheric lines will generate the largest disagreement, emphasis has been placed on understanding how well the O_3 and HCl columns agree. In order to compare results from microwindows with different height sensitivities, two different O_3 retrievals were carried out in the vicinity of 3000 cm^{-1}

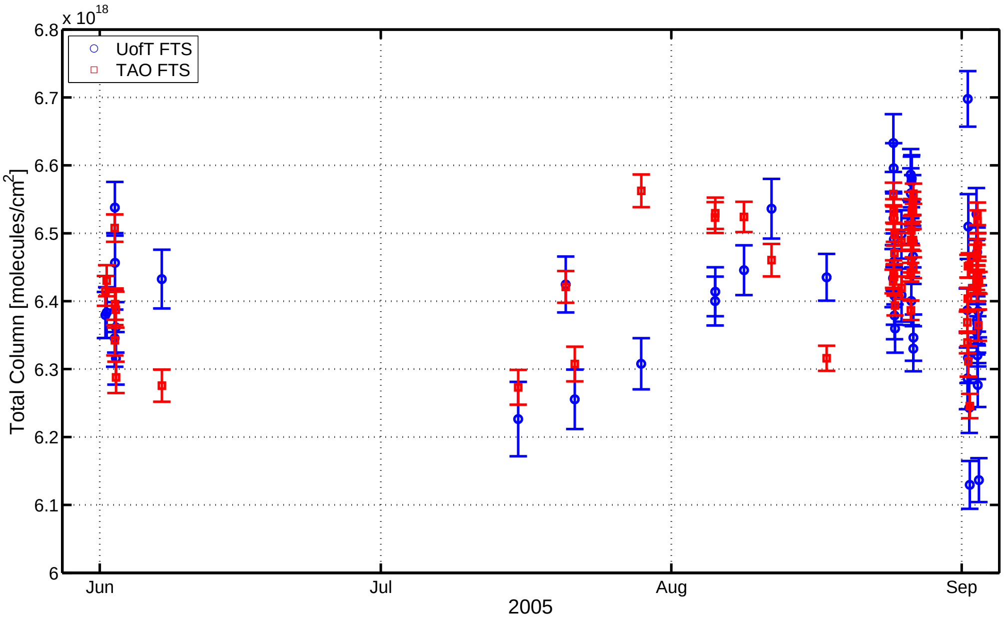

Figure 6.3: Time series of coincident N_2O total column observations. Blue circles represent the U of T FTS columns, while red squares represent the TAO FTS columns. Error bars are a combination of retrieval noise, smoothing error, and state space parameter interference error.

(see Table 6.2). Figures 6.5 and 6.6 show the time series of the retrieved total column O_3 observed by each instrument from the $3\nu_3$ band (3040 cm^{-1}) and the $2\nu_1 + \nu_2$ band (2775 cm^{-1}) microwindows, respectively. The overall qualitative agreement between the O_3 observations is better for the 2775 cm^{-1} microwindow, with a median difference of -1.7±3.7%. The 3040 cm^{-1} microwindow columns have a median difference of 2.7±3.7%. These findings are consistent with those of the focused intercomparison, which found that the 2775 cm^{-1} microwindow had a difference of 0.7% and the 3040 cm^{-1} microwindow had a difference of 3.3% (see Section 6.2).

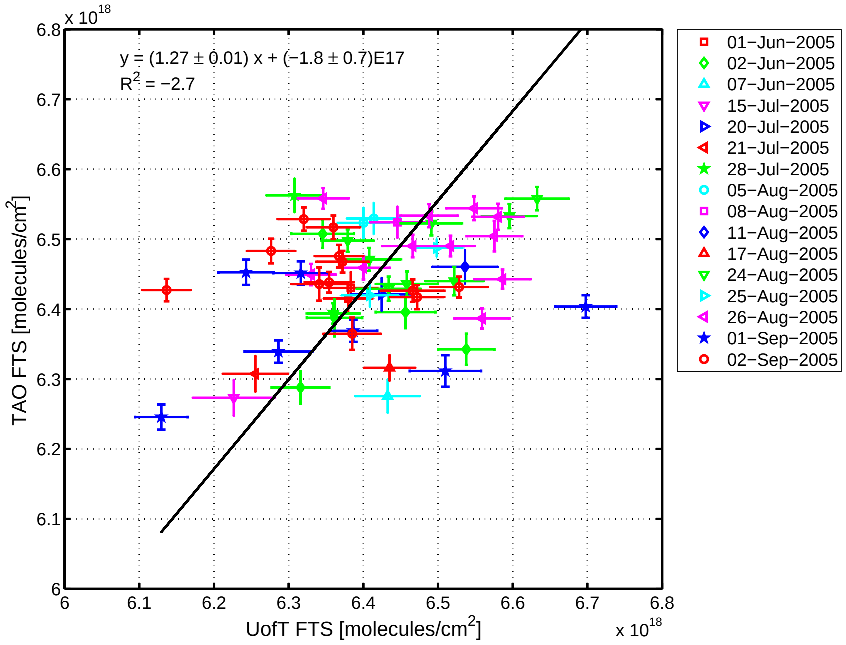

Figure 6.4: Scatter plot and fit of coincident N_2O total column observations. Measurements made on different days are represented by different symbols. Error bars are as for Figure 6.1.

Analyzing the differences in the retrieved column concentrations is the traditional way in which to quantify an intercomparison of this nature [Paton-Walsh et al., 1997, Goldman et al., 1999, Griffith et al., 2003, Meier et al., 2005]. However, by merely considering the average column difference, only the additive differences in the retrieved values are being investigated. A simple result from this comparison would be inconclusive as it would show that the O_3 values observed by the TAO-FTS are generally greater than those of the U of T FTS when retrieving from the 2775 cm^{-1} microwindow, while the opposite trend is found when retrieving from the 3040 cm^{-1} microwindow. Hence, it is necessary to consider other factors.

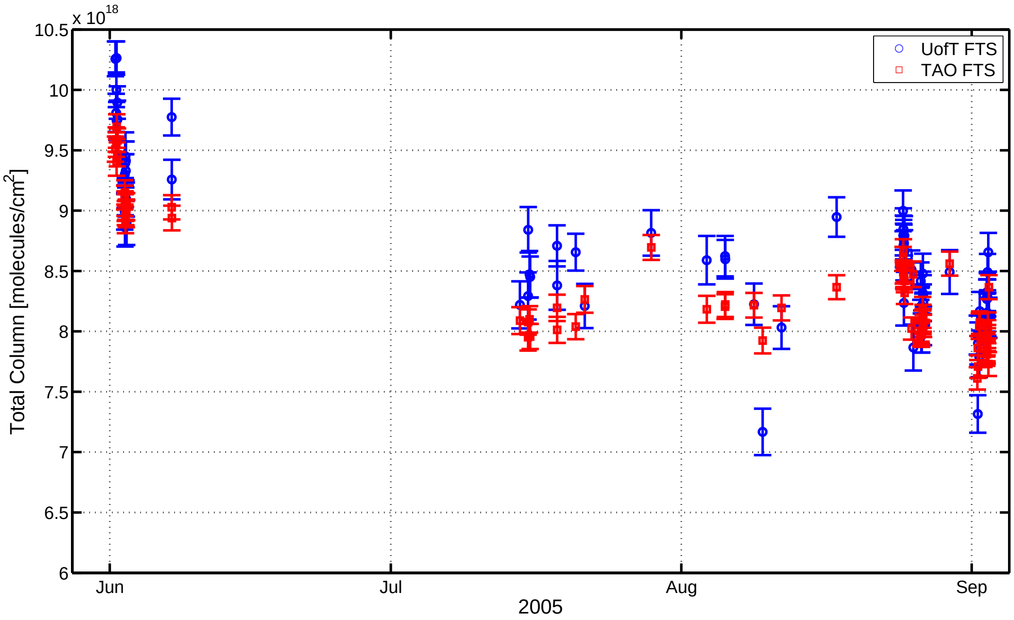

Figure 6.5: Time series of coincident O_3 total column observations retrieved from the 3040 cm^{-1} microwindow. Blue circles represent the U of T FTS columns, while red squares represent the TAO FTS columns. Error bars are a combination of retrieval noise, smoothing error, and state space parameter interference error.

From the assumed linear relation between the observation and the truth (Equation 6.1), it can be seen that it is important to also consider the influence of the multiplicative biases. This is of particular concern for the extended campaign results, as the relatively long time period over which measurements were recorded captures some seasonal variation in total column concentrations (particularly for the stratospheric gases). As average comparisons aimed at identifying additive differences will have a large variance, agreement between instruments must also be assessed in terms of multiplicative bias. By using the weighted least squares approach outlined in Section 6.1.3, these data can be fit and the ratio of the multiplicative biases given by Equation 6.2 can be found.

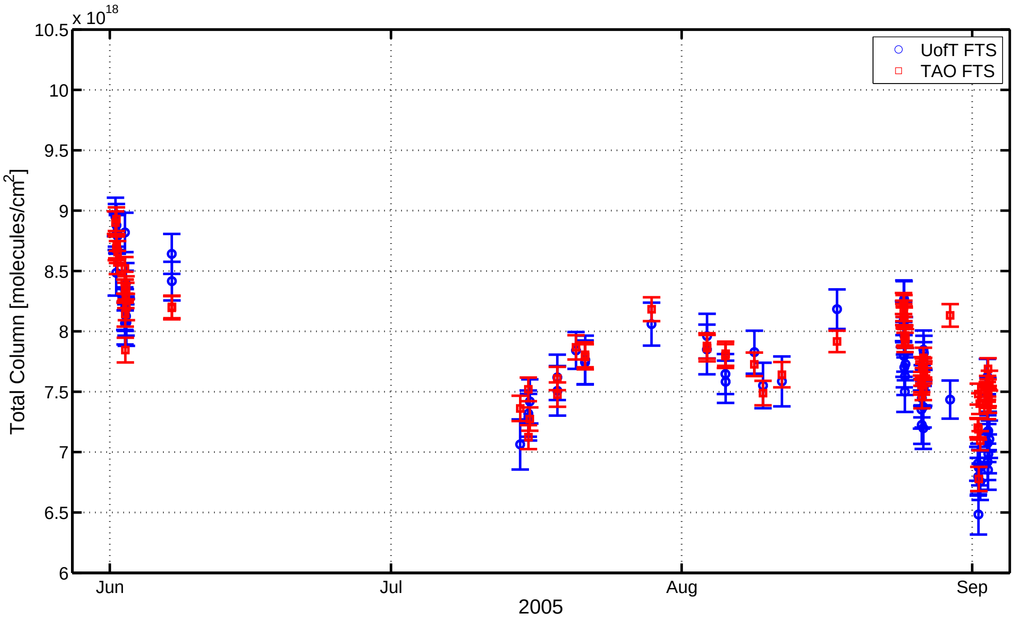

Figure 6.6: Time series of coincident O_3 total column observations retrieved from the 2775 cm^{-1} microwindow. Blue circles represent the U of T FTS columns, while red squares represent the TAO FTS columns. Error bars are a combination of retrieval noise, smoothing error, and state space parameter interference error.

Figures 6.7 and 6.8 show the scatter plots for the retrievals from the 3040 cm^{-1} and 2775 cm^{-1} microwindows, respectively. The slopes of the lines of best fit ($TAO = m \times UofT + b$) are both less than 1 (0.89 and 0.78, respectively), indicating that there is a definite difference in multiplicative bias between the instruments, with the U of T FTS having a larger bias.

As the averaging kernels of both of these microwindows are well conditioned and invertible, it is possible to directly calculate the expected value of these slopes. Using Equation 6.5, the calculated value of the slope for the 3040 cm^{-1} microwindow is 0.94, and the

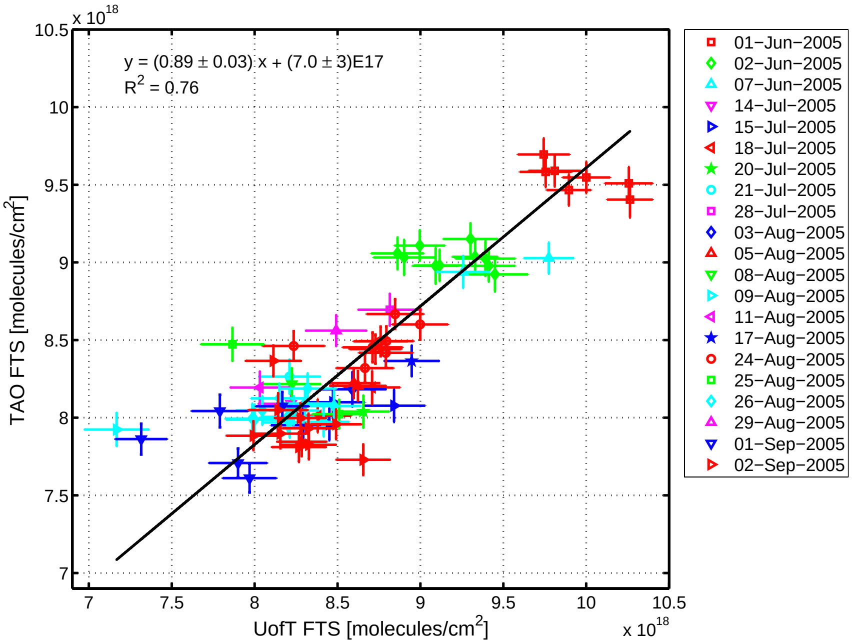

Figure 6.7: Scatter plot and linear fit of coincident O_3 total column observations retrieved from the 3040 cm^{-1} microwindow. Measurements made on different days are represented by different symbols. Error bars are as for Figure 6.1.

slope for the 2775 cm^{-1} microwindow is 0.79. The latter value agrees with the empirically fitted slope (0.78±0.03), while the 3040 cm^{-1} calculation is slightly larger than the fitted slope (0.89±0.03).

Although both the theory and the results indicate that the multiplicative bias of the U of T FTS is greater than that of the TAO FTS for O_3 observations, it is not directly obvious how this is manifested in the total column comparison. The median differences indicate that the TAO-FTS recorded generally higher concentrations from the 2775 cm^{-1} microwindow, while the U of T FTS recorded generally higher concentrations from the 3040 cm^{-1} microwindow. If one were to rely entirely on the multiplicative biases, it

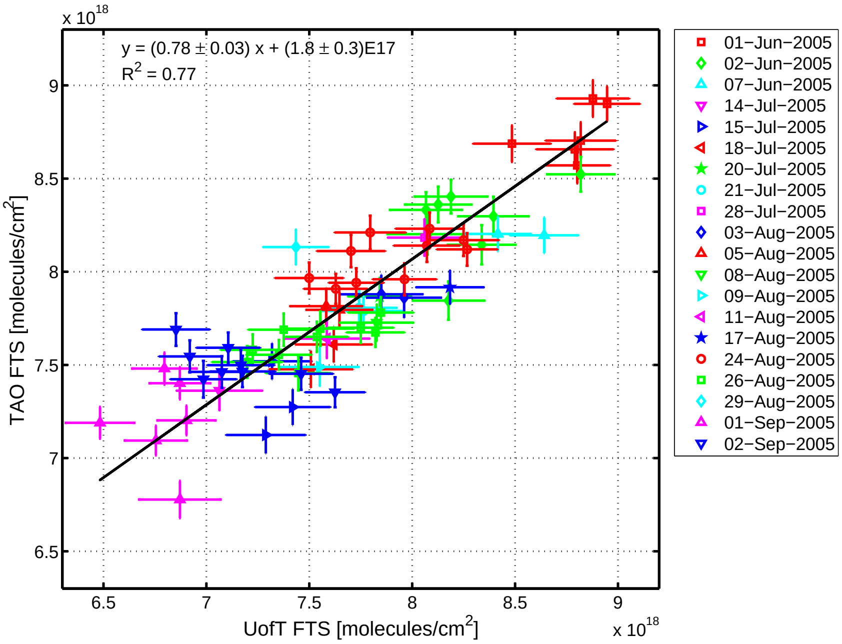

Figure 6.8: Scatter plot and linear fit of coincident O_3 total column observations retrieved from the 2775 cm^{-1} microwindow. Measurements made on different days are represented by different symbols. Error bars are as for Figure 6.1.

would be expected that the U of T FTS should report higher column amounts from both microwindows. The reason for this discrepancy is that the altitude dependence of these columns is not reflected in the total column values.

By considering the averaging kernels (see Equation 5.11), this apparent difference in retrieved total columns can be explained. Figures 6.9 and 6.10 show the instruments' total column averaging kernels for the 3040 cm^{-1} and 2775 cm^{-1} microwindows, respectively, as well as the ratio of the U of T FTS total column averaging kernel to that of the TAO-FTS, for each. It is interesting to note that the U of T FTS shows a consistent increase in sensitivity below 20 km relative to the TAO-FTS, however, it is markedly different in magnitude for each microwindow.

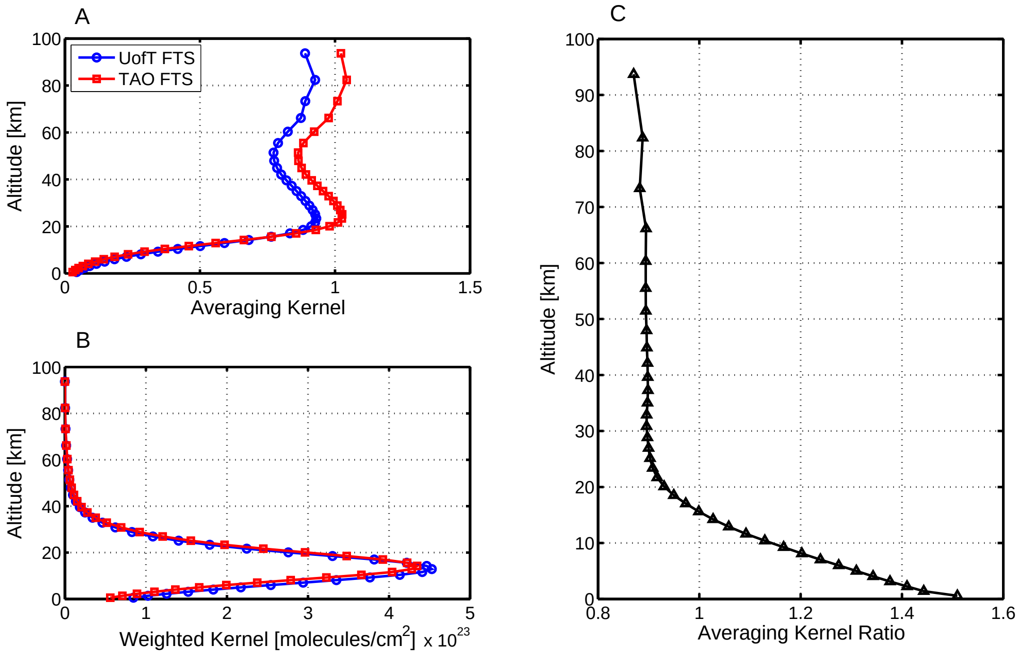

Figure 6.9: O_3 averaging kernels for the 3040 cm^{-1} microwindow retrieval: (a) total column averaging kernels, (b) density-weighted total column averaging kernels, and (c) ratio of the U of T FTS total column averaging kernel to that of the TAO-FTS. Blue circles represent the U of T FTS, red squares represent the TAO FTS, and black triangles represent U of T FTS to TAO FTS ratio.

For the 3040 cm^{-1} microwindow, the sensitivity of the U of T FTS retrieval constantly increases relative to that of the TAO-FTS retrieval from about 0.9 times that of the TAO-FTS at 20 km to about 1.5 times that of the TAO-FTS at the surface. Above 20 km, the U of T FTS shows a constant deficit of 10% relative to the TAO-FTS sensitivity. Since the median O_3 concentration in the atmosphere peaks near 25 km at the latitude of Toronto [Brasseur and Solomon, 2005], it is likely that the U of T FTS is essentially

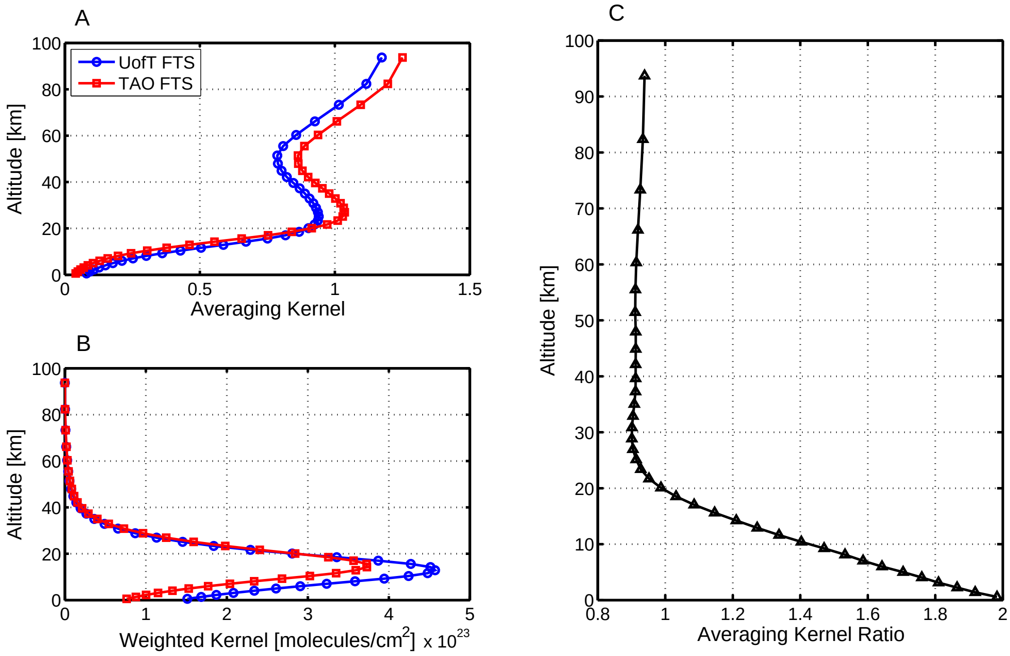

Figure 6.10: O_3 averaging kernels for the 2775 cm^{-1} microwindow retrieval: (a) total column averaging kernels, (b) density-weighted total column averaging kernels, and (c) ratio of the U of T FTS total column averaging kernel to that of the TAO-FTS. Blue circles represent the U of T FTS, red squares represent the TAO FTS, and black triangles represent U of T FTS to TAO FTS ratio.

underestimating the O_3 observations above 20 km compared to the TAO-FTS, and overestimating below 20 km compared to the TAO-FTS, yielding total columns that are in relatively close agreement. As the overestimation below 20 km is more pronounced, it is responsible for the derived multiplicative bias enhancement for the U of T FTS O_3 columns. This difference in altitude sensitivity is most likely a direct consequence of apparent broadening of the spectral lines due to the differences in spectral resolution of the instruments and related differences in SNR.

The total column averaging kernels from the 2775 cm^{-1} microwindow show similar behaviour, although the U of T FTS averaging kernel sensitivity is more pronounced at altitudes below 20 km, attaining double the sensitivity of the TAO-FTS averaging kernel at the surface. The same decrease in sensitivity above 20 km is present as in the 3040 cm^{-1} microwindow, resulting in the TAO-FTS being approximately 10% more sensitive at higher altitudes. Although this microwindow shows a more extreme difference in lower altitude sensitivities, the total column values are still in relatively close agreement between the two instruments. This large difference at lower altitudes causes the U of T FTS to have a larger multiplicative bias value, but because there is a relatively small amount of O_3 in this portion of the total column, it does not cause the retrieved values to differ significantly. Without the use of a profile retrieval algorithm and the subsequently derived averaging kernels, the multiplicative bias ratios (from Figures 6.7 and 6.8) would have incorrectly indicated that the U of T FTS total columns should have been more sensitive to the truth.

Following from this, the same comparison was carried out for HCl retrievals. The coincident HCl total column observations for each instrument are shown in Figure 6.11. The median total column difference is $+2.2\pm4.8\%$, which is consistent with the 2.6% difference found in the focused intercomparison. The scatter plot of the columns shows that the multiplicative bias of the TAO-FTS is about 18% larger than that of the U of T FTS (see Figure 6.12). This is explained by the averaging kernels shown in Figure 6.13. The TAO-FTS retrieval appears to be more sensitive to HCl concentrations for all altitudes, with the largest difference being about 22% near 12 km. As with O_3, HCl is predominantly a stratospheric species and any enhanced sensitivity to concentrations below about 20 km will have a negligible impact on the total column concentration. Consequently, the total columns remain in relatively close agreement between the two instruments. The fitted slope value of 1.18 ± 0.05 agrees well with the theoretically derived value of 1.22.

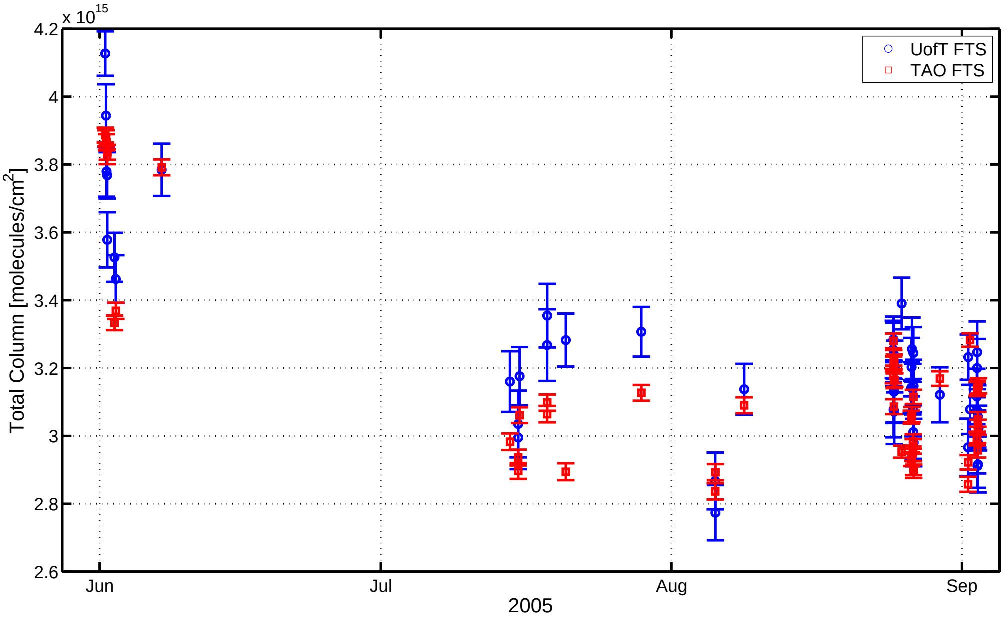

Figure 6.11: Time series of coincident HCl total column observations. Blue circles represent the U of T FTS columns, while red squares represent the TAO FTS columns. Error bars are a combination of retrieval noise, smoothing error, and state space parameter interference error.

6.1.6 Summary of Extended Ground-Based Intercomparison

Simultaneous measurements of O_3, HCl, N_2O, and CH_4 were recorded by two infrared Fourier transform spectrometers of differing resolution (0.004 cm^{-1} and 0.02 cm^{-1}) over a period of four months in the summer of 2005. Comparisons between the retrievals of stratospheric species (O_3 and HCl) do not show a consistent multiplicative bias between instruments. O_3 retrievals in two microwindows have shown that the lower-resolution observations by the U of T FTS are more sensitive to changes in the lower atmosphere, although this has little impact on the total column comparison. The difference in total column O_3 retrieved in each microwindow is also noticeable. On average, O_3 columns

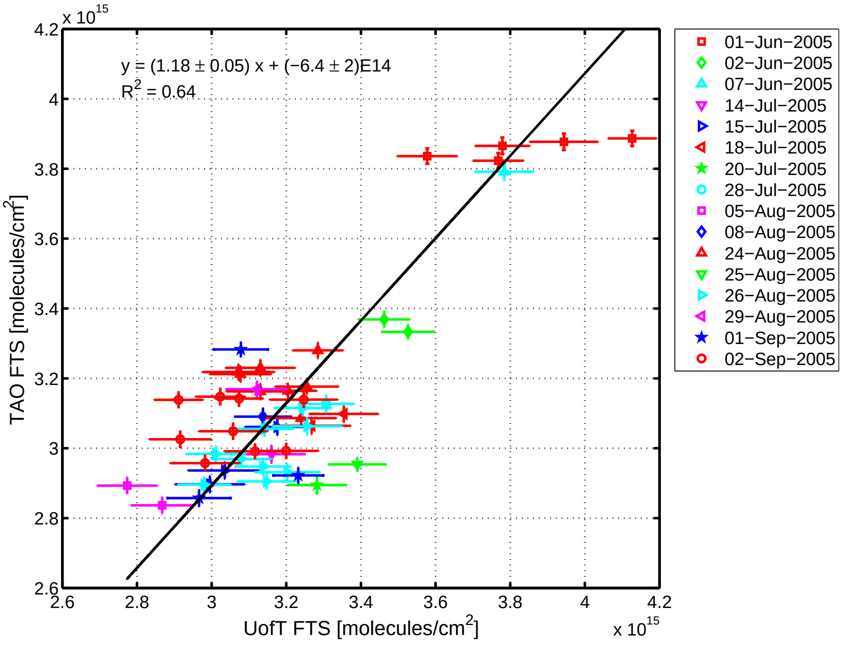

Figure 6.12: Scatter plot and linear fit of coincident HCl total column observations. Measurements made on different days are represented by different symbols. Error bars are as for Figure 6.1.

retrieved in the 3040 cm^{-1} microwindow are 5% higher than those from the 2775 cm^{-1} microwindow, for both instruments. By considering the density-weighted averaging kernels for each microwindow, it may be seen that there is enhanced sensitivity to O_3 concentrations near 20 km for both instruments in the 3040 cm^{-1} microwindow (although it is much more pronounced for the TAO-FTS). For both microwindows, the U of T FTS has a fitted multiplicative bias of 0.89±0.03 and 0.78±0.03 times that of the TAO-FTS for the 3040 cm^{-1} and 2775 cm^{-1} microwindows, respectively. The median column differences (UofT - TAO) were 2.7±3.7% and -1.7±3.7% for the 3040 cm^{-1} and 2775 cm^{-1} microwindows, respectively. These results are summarized in Table 6.3.

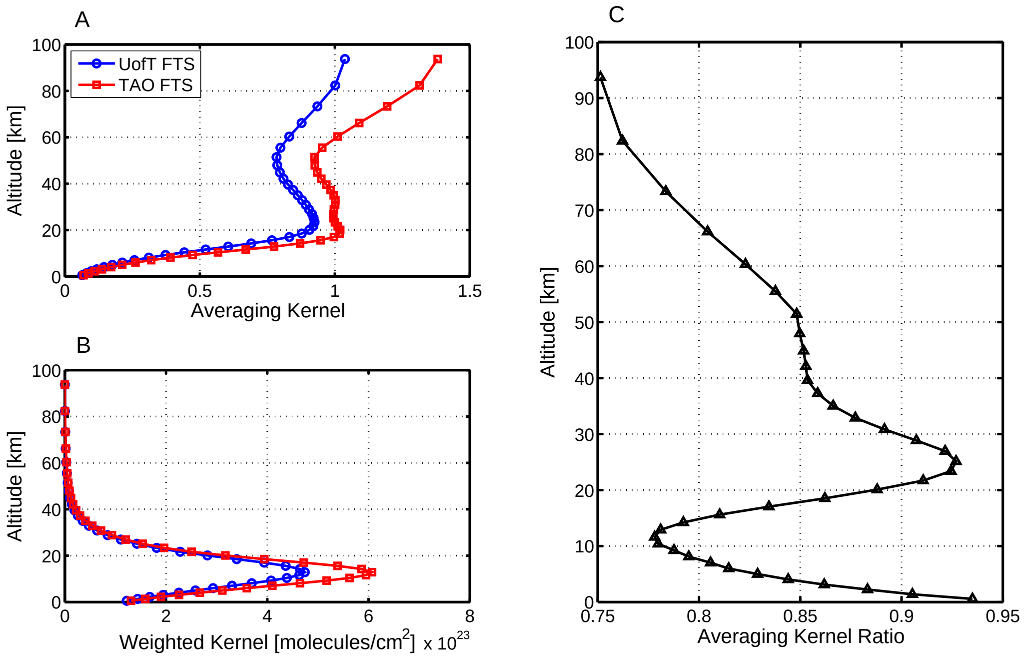

Figure 6.13: HCl averaging kernels retrieved from the 2859 cm^{-1} microwindow: (a) total column averaging kernels, (b) density-weighted total column averaging kernels, and (c) ratio of the U of T FTS total column averaging kernel to that of the TAO-FTS. Blue circles represent the U of T FTS, red squares represent the TAO FTS, and black triangles represent U of T FTS to TAO FTS ratio.

The TAO-FTS observations are 5 to 25% more sensitive to HCl concentrations than the U of T FTS, resulting in a total column multiplicative bias ratio of 1.18±0.05. This resulting median difference in column measurements was 2.2±4.8%. Compared to the tropospheric retrievals, the stratospheric species show qualitatively less scatter from the linear fit and are better correlated. The difference in multiplicative bias between the two instruments arises from the lack of sensitivity to pressure broadening for HCl (as well as for O_3) by the U of T FTS, resulting from narrower spectroscopic features that are not easily captured by lower-resolution instruments. This highlights the need to be aware of instrument biases in total column measurements arising from lower-resolution infrared observations and their averaging kernels.

The tropospheric species did not allow for as detailed a comparison as the stratospheric gases. The median total column differences were 3.7±2.5% and 0.36±1.8% for CH_4 and N_2O, respectively. The pressure-induced line broadening of these tropospheric species generates broader spectroscopic features that are captured by both the low and high-resolution instruments. Consequently, the averaging kernels for both CH_4 and N_2O contain information throughout the troposphere and, as a result, are non-invertible. This inhibits the calculation of multiplicative and additive biases. Unfortunately, the scatter plots for each of these species don't show representative linear relationships that can elucidate these biases further. A campaign of longer duration, albeit unpractical, would better capture the seasonal variation of the tropospheric gases and allow for better comparison of the scatter plotted data. The time series of data acquired in this study indicate that both the low-resolution and high-resolution FTS are capable of retrieving the same total columns of predominantly tropospheric species.

6.2 Focused FTS Intercomparison

Following immediately after the extended FTS campaign, a third FTS was added to the instrument suite and simultaneous measurements were made for four days over the course of a two-week period. The third FTS was the Portable Atmospheric Research Interferometric Spectrometer for the Infrared (PARIS-IR), which has a spectral resolution corresponding to 25 cm OPD. Like the U of T FTS, PARIS-IR participated in the MANTRA 2004 high-altitude balloon campaign, albeit in a different configuration [Strong et al., 2005]. The goals of this intercomparison were to retrieve total column amounts of the same four species, O_3, HCl, N_2O, and CH_4, from the data recorded si-

Table 6.3: Median total column differences: 200*(U of T - TAO)/(U of T + TAO), standard deviation of total column differences, theoretical slopes of linear trends, fitted slopes of linear trends, R^2 value of the fits, and the total number of data points for each of the four species investigated.

Target Gas and Micro-window (cm^{-1})	Median % Diff.	% Std. Dev.	Expected Slope	Fitted Slope	R^2	N
O_3 - 3040	2.7	3.7	0.94	0.89 ± 0.03	0.76	75
O_3 - 2775	-1.7	3.7	0.79	0.78 ± 0.03	0.77	70
HCl - 2925	2.2	4.8	1.22	1.18 ± 0.05	0.64	50
N_2O - 2482	-0.36	1.8	1.02	1.27 ± 0.01	-2.7	58
CH_4 - 2859	3.7	2.5	1.02	1.03 ± 0.08	-1.8	63

multaneously by these three instruments, to determine which retrieval parameters most affect the retrieved column amounts for the lower-resolution instruments, and to determine the causes of any remaining discrepancies. A complete description of this campaign and the associated results can be found in Wunch et al. [2007].

6.2.1 PARIS-IR

The Atmospheric Chemistry Experiment Fourier Transform Spectrometer (ACE-FTS) is the primary instrument on the Canadian scientific satellite mission SCISAT-1, which was launched by NASA on 12 August 2003 [Bernath et al., 2005]. PARIS-IR is a new, compact, portable FTS built by ABB Bomem for the Waterloo Atmospheric Observatory (43.47°N, 80.55°W, 319.0 m a.s.l.) [Fu et al., 2007]. PARIS-IR was primarily constructed from spare flight components that were manufactured for the ACE-FTS and consequently has a very similar optical design, producing double-sided interferograms with the same maximum OPD (25 cm) and spectral range (750-4400 cm^{-1}). The sandwich detectors are composed of a photovoltaic InSb detector and a photoconductive MCT detector, which is corrected for detector nonlinearity. The data presented here, however, are only from the InSb detector. To obtain a sufficiently long optical path difference within a compact volume, ABB Bomem used a double pendulum interferometer and also used an entrance mirror to pass radiation through the interferometer twice. In addition to the MANTRA campaign in August 2004, PARIS-IR has participated in five ground-based ACE validation campaigns in the Canadian high Arctic at Eureka, Nunavut [Kerzenmacher et al., 2005, Sung et al., 2007, Fu et al., 2008]. The instrument is also operated at the Waterloo Atmospheric Observatory (WAO) for recording ground-based atmospheric absorption spectra.

6.2.2 Observations and Analysis Strategy

The observation strategy for the campaign was constructed to focus on the effects of the instrument resolution on the retrieved column amounts. This was achieved by measuring simultaneously from the same location, in the same spectral range, and using similar retrieval methods with identical *a priori* information, line parameters and forward model. All three instruments were located at TAO for the duration of the campaign. The data presented here were recorded on 24 August, 26 August, 1 September and 2 September 2005, with at least 14 spectra recorded by the TAO-FTS on each day.

To measure the same atmospheric path simultaneously with all three instruments, two small pick-off mirrors were placed in the TAO sun tracker's solar beam to deflect a portion of the light into the U of T FTS and PARIS-IR (see Figure 6.14). Every attempt was made to ensure that the TAO FTS incurred a minimal loss of signal, and as a result, its signal-to-noise ratio was reduced by less than 10%. As was mentioned in Section 6.1, the TAO-FTS requires 5 minutes to record one interferogram and ≈ 20 minutes for a spectrum derived from four co-added interferograms. To further ensure simultaneity, the U of T FTS and PARIS-IR co-added individual spectra that were recorded during the 20-min interval required to produce one TAO-FTS spectrum. The PARIS-IR instrument measures the largest number of spectra per unit time, with a 20 second scan time, whereas the U of T FTS measures one interferogram in 50 s. Table 6.4 summarizes the instrument details.

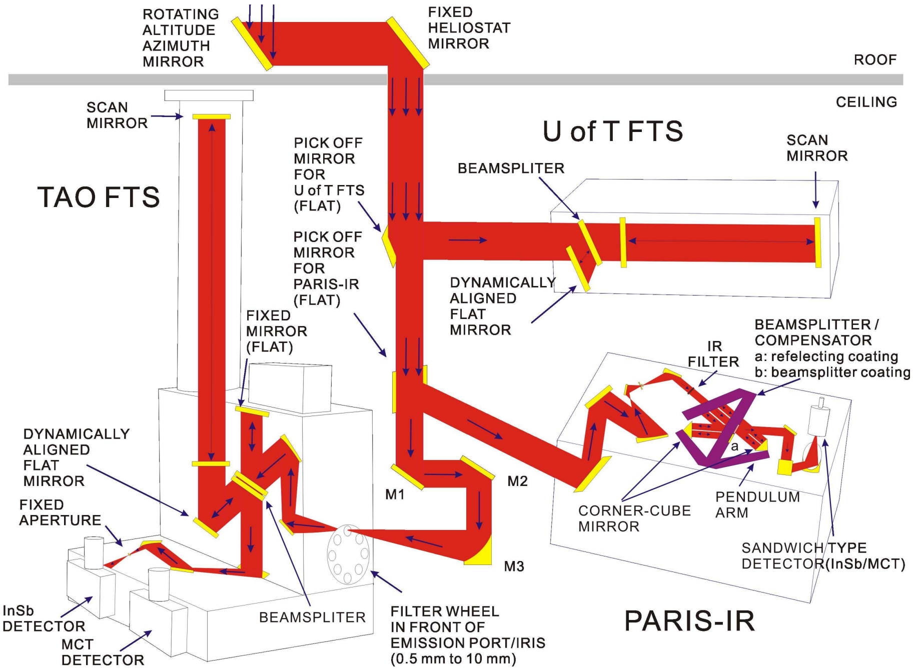

Figure 6.14: Experimental configuration of the TAO-FTS, U of T FTS, and PARIS-IR for the focused intercomparison. (Figure courtesy of D. Fu).

For consistency, the same four gases were retrieved from the same microwindows used in the extended intercomparison campaign (see Table 6.2). The only difference between the retrieval procedures for the three instruments is that the PARIS-IR retrievals were performed on a 29-layer grid, whereas the TAO and U of T FTS retrievals were performed on the standard 38-layer grid. The 29-layer grid is is standard for PARIS-IR retrievals as the reduced number of fitting points in the spectra decreases the vertical resolution [Fu

Table 6.4: Instrument parameters from the ground-based, focused FTS intercomparison campaign.

Parameters	PARIS-IR	U of T FTS	TAO-FTS
Maximum OPD (cm)	25	50	250
Time per scan (s)	20	50	300
Spectral Range (cm^{-1})	750–4400	1200–5000	F3 (2400–3100)
Measurement Period	24 Aug.–2 Sept.	26 May–12 Sept.	Year-round

et al., 2007]. By eliminating atmospheric condition differences between measurements, eliminating differences in line parameter characterization and minimizing the differences in the retrieval methods, the bulk of the discrepancies can now be attributed to differences in instrument line shapes and instrument resolution.

6.2.3 Influence of Instrument Line Shape

The importance of considering the influence of an individual instrument line shape for ground-based comparisons has been previously addressed [Griffith et al., 2003] and is particularly important in this case because of the pronounced differences in the resolution of the three instruments. Information about the ILS can be incorporated in the forward model by using tabular inputs to describe the effective apodization and phase error as a function of OPD, or by using polynomial coefficients to describe Effective Apodization Parameters (EAP) and Effective PHaSe error parameters (EPHS). For either of these two cases, a measurement made by each of the three spectrometers must be analysed to determine the values of these empirical parameters. This can be done under controlled conditions using calibrated gas cells [Coffey et al., 1998] and an independent retrieval algorithm designed to determine ILS information. This was done for the TAO-FTS and the U of T FTS with LINEFIT version 9.0, while PARIS-IR ILS information was determined with LINEFIT version 11.0 [Hase et al., 1999]. The difference between the results for the ILS for the two versions is negligible. To calculate the ILS, the U of T FTS and TAO-FTS measured blackbody radiation in the 2300-2700 cm^{-1} spectral region through a 2-cm long, 2.5-cm diameter HBr cell filled to 2 hPa. PARIS-IR measured blackbody radiation in the 2400-2800-cm^{-1} region through a 10-cm long, 5.0-cm diameter N_2O cell filled to 14.7 hPa. LINEFIT produces tabular modulation efficiency and phase error results as a function of OPD, which can be incorporated into the SFIT2 forward model. These parameters are shown for each instrument in Figure 6.15.

Inherent in this technique is the assumption that the ILS measured under these controlled conditions is identical to the ILS throughout the duration of all atmospheric measurements. This may be largely true over a few months for ground-based measurements, however, it will not generally be true for balloon-based measurements due to diurnal temperature variation and altitude gradients in both atmospheric temperature and pressure. Because of this, we may wish to calculate the ILS for each spectrum individually. Without a permanent gas cell in the optical path of each spectrometer during solar measurements (which none of these instruments possess), a method for retrieving ILS information from the solar spectrum itself is necessary. SFIT2 provides a solution for this with an option that allows for the retrieval of EAP and EPHS polynomial coefficients as part of the state vector. Third-order polynomial coefficients for both the EPHS and EAP parameters were retrieved for all three instruments. In the following sections, “ILS input” refers to the tabular LINEFIT results that were used as an input to SFIT2 (i.e. the black curves in Figure 6.15). The EAP and EPHS parameters retrieved by SFIT2 are referred to as “polynomial EPHS/EAP retrieved” ILS information (i.e. the blue curves in Figure 6.15). EPHS and EAP values for both the U of T FTS and PARIS-IR changed by $< 10\%$ (2σ) over the four days of measurements. When neither the LINEFIT tabular nor SFIT2 polynomial ILS information is included in a retrieval, an ideal ILS is assumed

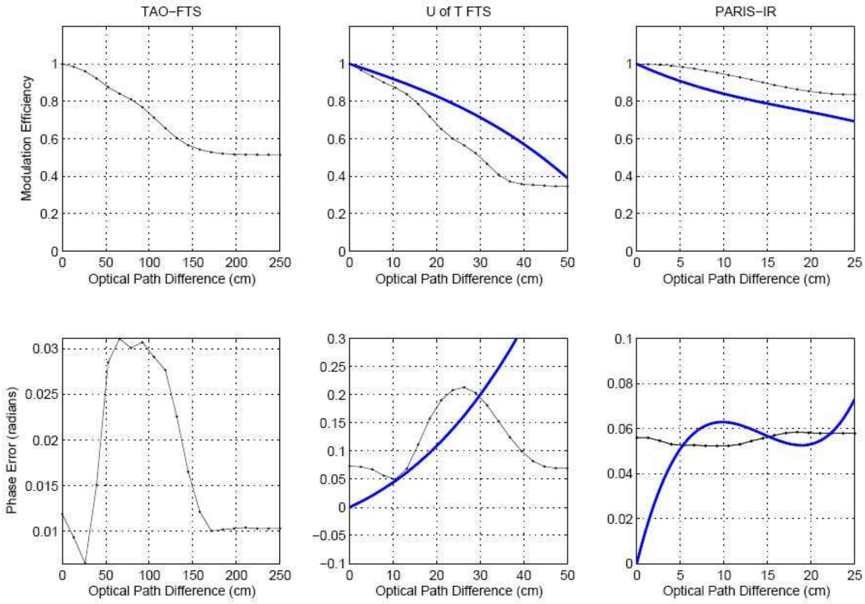

Figure 6.15: Modulation efficiency and phase error for the TAO-FTS (left), U of T FTS (centre), and PARIS-IR (right) measured during the focused intercomparison campaign. The black curves with dots were determined from gas cell measurements analysed using LINEFIT v.9.0 and v.11.0 [Hase et al., 1999]. The blue curves represent the calculated EAP and EPHS parameters derived from SFIT2 fits. The monotonic decrease in modulation efficiency observed by all instruments indicates that the intensity of the interferogram signal decreases with OPD, as expected. (Figure courtesy of D. Wunch).

in SFIT2, and this is referred to as the “standard retrieval”. The TAO-FTS regularly retrieves a simple phase parameter (SPHS) from SFIT2. SPHS is a single-parameter description of the asymmetry of a spectral line, and is included in all three retrieval types (ILS input, PHS/EAP retrieved and the standard retrieval).

The U of T FTS and PARIS-IR instruments retrieve EPHS and EAP information somewhat differently. The method employed for the U of T FTS spectra retrieves third-order polynomial EPHS and EAP parameters from the same microwindow as the retrieved species (that is, only one retrieval is necessary for each molecule). The method employed for the PARIS-IR data, however, retrieves third-order polynomial EPHS and EAP parameters from a spectral range that includes two N_2O lines in the 2806.1-2808.1 cm^{-1} microwindow, using *a priori* values from LINEFIT. The daily mean of these values is then used for all spectra when retrieving the other species (EAP and EPHS parameters can also be retrieved from each spectrum, but daily means were used for efficiency). This method was attempted for the U of T FTS data, but was found to be less successful than directly retrieving the parameters from the same microwindow. It is suspected that the success of the second, dedicated microwindow for retrieving the ILS parameters for the PARIS-IR instrument may be due, in part, to the lower degrees of freedom for signal obtained from the PARIS-IR spectra. Instead of retrieving a VMR profile and EPHS and EAP information from a given microwindow with limited information, extra ILS information is provided from the same spectrum, but in a different microwindow.

It has been noted by Griffith et al. [2003] that the stratospheric species (O_3 and HCl), which have narrow absorption lines, are highly sensitive to ILS distortions, while pressure-broadened tropospheric species (N_2O and CH_4) are less affected. This result has been confirmed here for the low-resolution instruments by comparing columns obtained when retrieving the EAP and EPHS using SFIT2 with columns retrieved when using LINEFIT results as inputs to SFIT2. The total column amounts were retrieved by SFIT2 for data recorded on September 2nd for three test runs. The first test run retrieved EPHS and EAP parameters ("PHS/EAP retrieved") from the microwindow itself in the U of T FTS case, and the broad N_2O microwindow in the PARIS-IR case. The second test run used tabular LINEFIT inputs ("ILS input") obtained from gas cell measurements. The third test run used only SPHS ILS information ("standard retrieval"). No significant differences in retrieved column amounts between the three ILS cases were seen for the TAO-FTS. Therefore, for comparison purposes, TAO-FTS data is considered to be closest to the truth.

For the U of T FTS, the best ozone column comparisons were generated with the ILS input run (see Figure 6.16). For O_3 in the 3040 cm^{-1} microwindow, the ILS input run is only slightly closer to the TAO-FTS mean values (by ≈0.4%) than the EPHS/EAP retrieval and both are more than 20% higher than the values from the standard run. The spectral fits from the EPHS/EAP retrieved and ILS input cases also show smaller residuals (the details of all spectral fits can be found in Wunch et al. [2007]). The PARIS-IR results are similar; retrieving EPHS/EAP parameters improved the agreement in the column amounts by ≈6% over the standard retrieval and the spectral fits are better for the EPHS/EAP retrieval and the ILS input cases than for the standard retrieval. Similar results are found for ozone in the 2775 cm^{-1} microwindow. The TAO-FTS total column values for these two ozone microwindows are significantly different, and this is caused by the altitude at which the respective averaging kernels for the microwindows are sensitive to the atmosphere (see Section 6.1.5).

The sensitivity of the U of T FTS HCl retrieval to the ILS is also high, as illustrated in Figure 6.16, with the EPHS/EAP retrieved run being closer (by ≈1%) to the TAO-FTS columns than the ILS input run. The difference in HCl columns between the EPHS/EAP retrieved and standard retrievals for the PARIS-IR instrument is ≈4.3%, with the standard retrieval mean closer to the TAO-FTS retrieved values. Residuals from the spectral fits for both the U of T FTS and PARIS-IR show, as for O_3, that the EPHS/EAP retrieval and ILS input cases are smaller than for the standard retrieval.

The U of T FTS N_2O retrieval is much less sensitive to the ILS (see Figure 6.16), although the EPHS/EAP retrieved values are closer to the TAO-FTS values than those

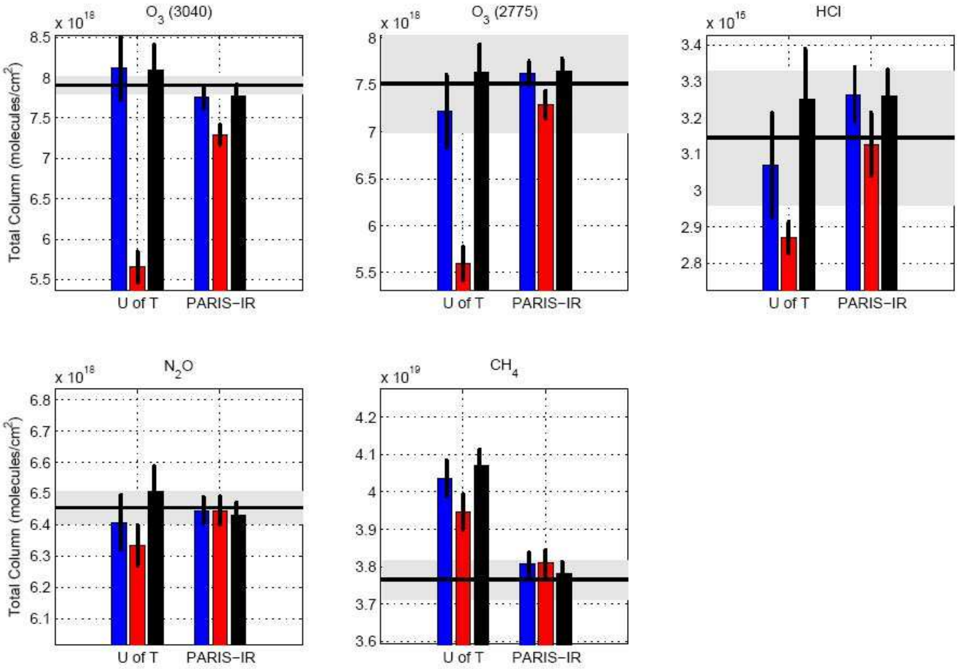

Figure 6.16: Mean columns from data recorded on 2 September 2005, using the EPHS/EAP retrieval (blue), the standard retrieval (red) and the ILS input retrieval (black). The thick black horizontal line indicates the TAO-FTS column means on the same day and the grey shading represents the standard deviation of the TAO-FTS retrieved values. The error bars indicate the standard deviation of the retrieved values. (Figure courtesy of D. Wunch).

from the standard retrieval. The sensitivity of the PARIS-IR retrieval to the ILS in the EPHS/EAP retrieved case is also quite low. There is only a ≈0.4% difference between the EPHS/EAP and standard cases. The residuals from the spectral fits (not shown) for both the U of T FTS and PARIS-IR instruments show only slightly better results for the EPHS/EAP retrieval and ILS input cases than for the standard retrieval.

The sensitivity of the U of T FTS CH_4 retrievals to the ILS is also lower than that found for O_3 and HCl. Retrieving the EPHS and EAP parameters for the U of T FTS data produces poorer comparisons with the TAO-FTS data, because it induces oscillations in the profile. There is systematic structure in the residuals from the CH_4 spectral fits for all three retrieval cases for both PARIS-IR and the U of T FTS. The TAO-FTS residuals also show systematic structure, pointing to a possible problem with the methane spectroscopy (see discussion in Section 6.1.4). The sensitivity of the PARIS-IR retrieval of CH_4 to the ILS is very low, with only ≈0.6% difference between the EPHS/EAP retrieved and standard retrieval scenarios.

In general, the U of T FTS ILS is poorer than that of PARIS-IR (central and right panels of Figure 6.15). Accordingly, the difference in total columns retrieved by the U of T FTS for the EPHS/EAP retrieved case and the standard retrieval will be exaggerated for the stratospheric species, which are most sensitive to ILS distortions. Nevertheless, using either the EPHS/EAP retrieved or the ILS input cases for both lower resolution instruments results in reasonable agreement with the TAO-FTS. From these results, it was determined that the EPHS/EAP retrieved scenario should be used to derive columns of O_3, HCl and N_2O for the U of T FTS, while the standard retrieval is used for CH_4. For PARIS-IR, the EPHS/EAP retrieved case is used for O_3 and HCl, and the standard retrieval is used for N_2O and CH_4. Since the TAO-FTS line shape is significantly narrower than both the stratospheric and tropospheric absorption lines, it is much less sensitive to instrument line shape distortions, and the standard retrieval is always used. Retrieving the EPHS and EAP parameters for the TAO-FTS causes small changes ($< 1\%$) in total columns retrieved.

6.2.4 Influence of Instrument Resolution

As the resolution of an instrument affects the number of spectral points that describe a microwindow, this, as well as the signal-to-noise ratio of the spectrum, limits the total degrees of freedom for signal in a given retrieval (see Section 5.4). There must, then, be a limiting resolution below which it is not possible to retrieve information about the atmosphere from a particular microwindow. This limit must be determined in order to ensure that the results from each of the respective instruments are valid.

The initial approach was to truncate the TAO-FTS interferograms to lower resolutions so that results derived from these lower-resolution TAO-FTS spectra could be directly compared with those of the U of T FTS and PARIS-IR spectra. However, the value of these results is limited because, as the OPD is decreased, both the SNR and the ILS improve significantly, so much so that the resulting spectra do not possess SNRs or ILSs that are comparable with those of the PARIS-IR or the U of T FTS spectra. With simulated spectra, however, the SNR and ILS can be constrained to more reasonable values for the lower-resolution instruments. For this reason, simulated spectra were used for the following sensitivity studies but, it should be noted, the truncated TAO-FTS results are consistent with the results from the simulated spectra.

To simulate the effect of resolution on total column amounts, an ensemble of 16 spectra was simulated for each of 12 cm, 25 cm, 50 cm, 100 cm, 150 cm, 200 cm and 250 cm maximum OPD, using the SZA values from the 1 September measurements. The signal-to-noise ratio was set to 250 for each of the simulated spectra (see Table 6.5), and all four molecules were retrieved using the same *a priori* values and ZPT profile as the data from September 1st. The "true" profile used to generate the spectra was a perturbation of the *a priori* profile of less than 20% at all altitudes. Identical phase and effective apodization errors were applied to each interferogram, for each resolution, with values similar to those of the TAO instrument.

In Figures 6.17-6.21, the retrieved column amounts of O_3, HCl, N_2O and CH_4 are shown

Table 6.5: Spectral parameters from the ground-based, focused FTS intercomparison campaign. The signal-to-noise ratio is the mean value determined from the noise in the residual of the spectral fit.

Target Gas	O_3	O_3	HCl	N_2O	CH_4
(Microwindow)	(3040)	(2775)	(2925)	(2482)	(2859)
TAO-FTS SNR	200	400	680	460	420
U of T FTS SNR	360	900	760	600	350
PARIS-IR SNR	150	100	100	130	130
TAO-FTS d_s	2.4	2.1	3.1	4.2	4.0
U of T FTS d_s	1.32	1.35	1.23	2.85	2.68
PARIS-IR d_s	1.04	0.72	0.66	2.31	2.38

with 2σ error bars as a function of the optical path difference, respectively. For ozone in the 3040 cm^{-1} microwindow (Figure 6.17), there is less than 0.3% difference in column amounts retrieved at 250 cm OPD between the standard and EPHS/EAP retrieved cases. The EPHS/EAP retrieved case changes less than the standard retrieval between the different OPD values, and retrieves columns that are closer to the truth at the lowest OPDs. The results are within 2% of the truth for all OPDs for the EPHS/EAP retrieved case and differ by more than 2% from the truth for the 50 cm OPD and 12 cm OPD standard retrieval. From this, it can be expected that results from the lower-resolution instruments should agree with the TAO-FTS in this microwindow if EPHS and EAP parameters are retrieved.

O_3 retrieved from the 2775 cm^{-1} microwindow is shown in Figure 6.18. At 250 cm OPD, the columns differ by less than 0.8% from the truth, obtained by either the standard retrieval or the EPHS/EAP retrieved case. The column average for the standard retrieval

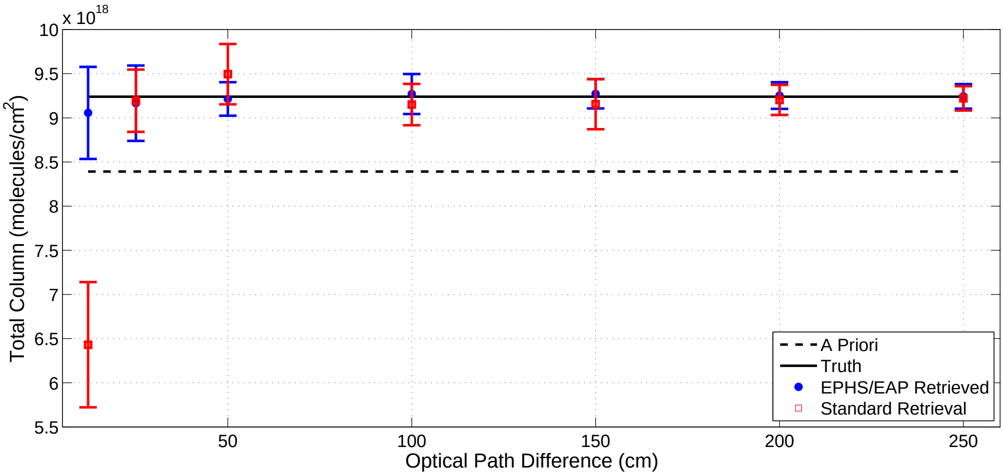

Figure 6.17: Simulated retrievals of ozone columns in the 3040 cm^{-1} microwindow as a function of OPD (assumed SNR = 250). Mean column amounts are shown with the 2σ standard deviation error bars derived from the ensemble of the two sets of retrievals: one that retrieves third-order polynomial coefficients for the EPHS and EAP functions from the microwindow itself (blue circles, labelled as "EPHS/EAP retrieved"), and one that does not retrieve coefficients (red squares, labelled as "standard retrieval"). The *a priori* column value is shown as a black dotted line and the "truth" is shown as a black solid line, where "truth" is the column amount that was used to generate the model spectra.

begins to decrease significantly below 100 cm OPD, with the column mean over the ensemble differing by $< 8\%$ from the truth at 50 cm OPD. The EPHS/EAP retrieved case has a difference of 2.7% at 25 cm OPD, whereas the standard retrieval gives a mean that is 18.9% smaller than the true value at 25 cm OPD. It may be concluded, then, that there should be good agreement for ozone in the 2775 cm^{-1} microwindow for lower-resolution instruments if they retrieve EPHS/EAP parameters and have an OPD of at least 25 cm.

For HCl (see Figure 6.19), the difference in retrieved columns between the standard re-

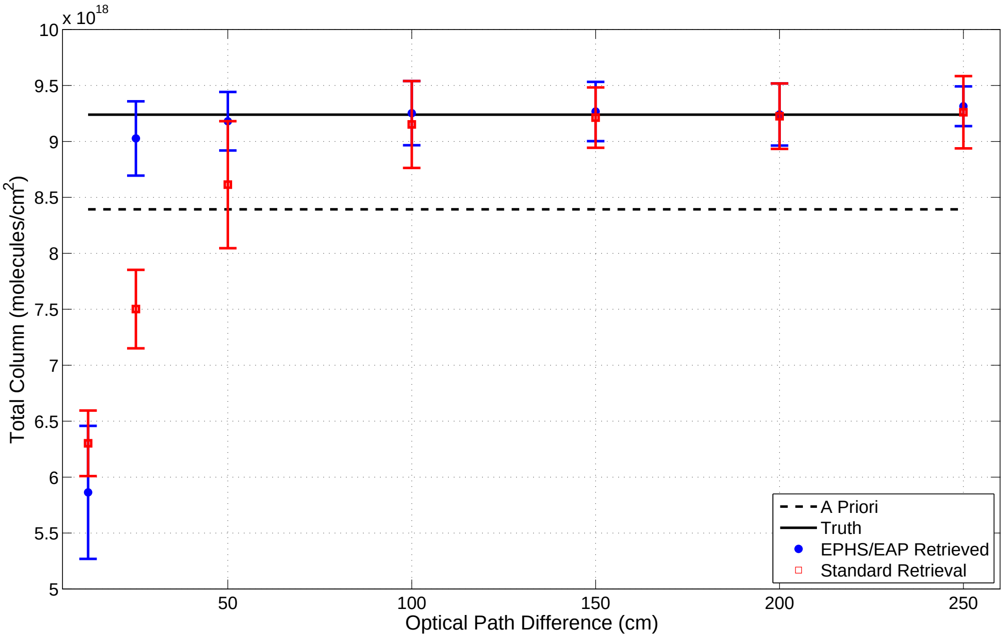

Figure 6.18: Same as Figure 6.17 but for simulations of ozone in the 2775 cm^{-1} microwindow.

trieval at 250 cm OPD and the truth is 0.27% and between the EPHS/EAP retrieved case at 250 cm OPD and the truth is 0.36%. The column amounts are within 1% of the truth until 50 cm OPD for the standard retrieval, and 25 cm OPD for the EPHS/EAP retrieved case. At and below 50 cm OPD, the percent difference from the truth increases in both cases, with the EPHS/EAP retrieved case showing significantly better agreement than the standard case. Therefore, there should be reasonable agreement for HCl between the higher and lower resolution instruments if EPHS and EAP parameters are retrieved.

For N_2O (see Figure 6.20), the difference between the columns retrieved with the standard retrieval at 250 cm OPD and the truth is ≈0.5%, and the difference in columns between the EPHS/EAP retrieval at 250 cm OPD and the truth is ≈0.02%. The N_2O

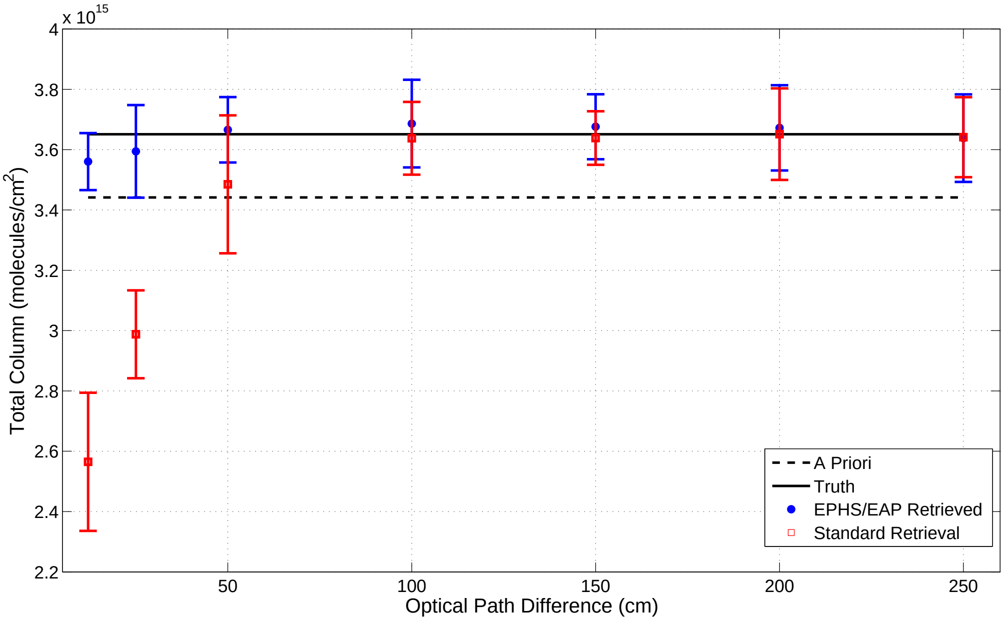

Figure 6.19: Same as Figure 6.17 but for simulations of HCl.

columns show good agreement with the truth ($< 1\%$) for all OPDs for the EPHS/EAP retrieved case, and good agreement with the truth for all OPDs at or larger than 100 cm for the standard retrieval. Below 100 cm OPD, the standard retrieval stays within $\approx$2% of the truth, and does not have the decrease that the stratospheric species show. It is expected, then, that all three instruments should have good agreement for N_2O if they perform either retrieval, but better results may be obtained from the lower-resolution instruments if they retrieve EPHS and EAP parameters.

For CH_4 (see Figure 6.21), the difference between columns retrieved using the standard retrieval at 250 cm OPD and the truth is $\approx$0.34%, and the difference in columns between the EPHS/EAP retrieval at 250 cm OPD and the truth is $\approx$0.22%. The CH_4 columns show good agreement with the truth ($< 1\%$) for all OPDs for the EPHS/EAP retrieved

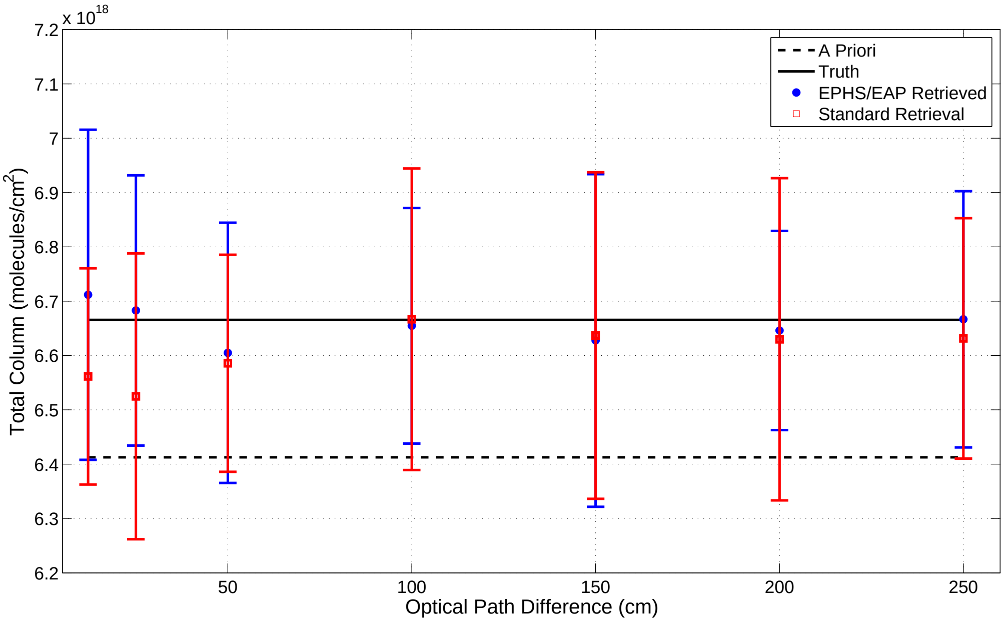

Figure 6.20: Same as Figure 6.17 but for simulations of N_2O.

case, except for 100 cm OPD, where the percent difference from the truth is ≈1.05%. There is good agreement with the truth for all OPDs for the standard retrieval, except for 25 cm OPD where the difference is ≈2.35%. Again, as for N_2O, the two retrieval cases stay within ≈2.5% of the truth, and do not show a significant decrease at smaller OPD. Consequently, all three instruments should have good agreement for CH_4 if they perform either retrieval. These findings corroborate the results from the extended intercomparison in Section 6.1.4.

6.2.5 Results from the Focused Intercomparison

These measurements took place on four days over a nine-day period in late August and early September 2005. Because of the relatively stable chemistry and dynamics of the

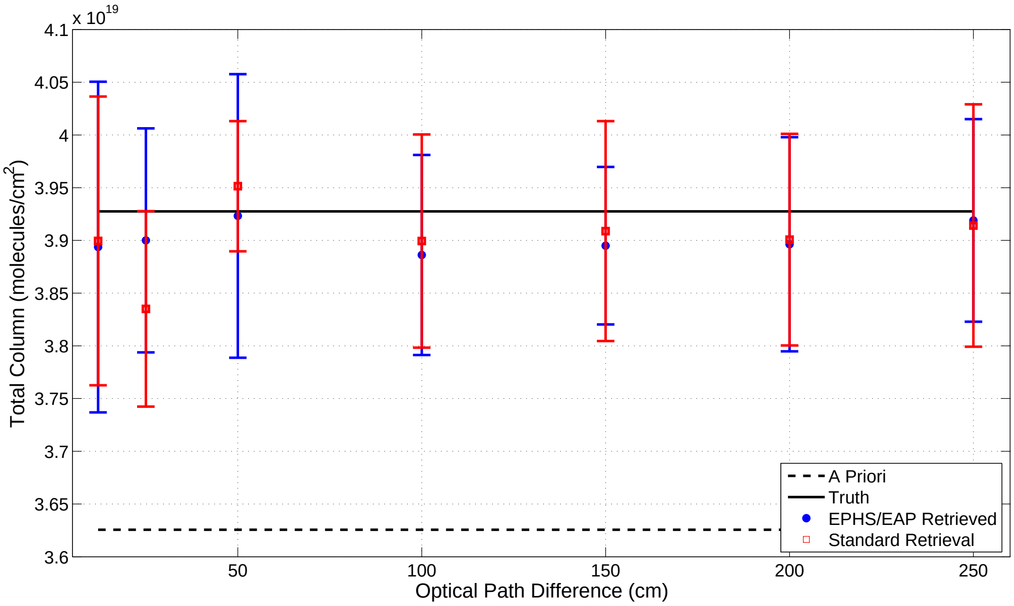

Figure 6.21: Same as Figure 6.17 but for simulations of CH_4.

atmosphere during that time [Wunch et al., 2005], we do not expect any significant trends in the column amounts of any of these molecules. Coincident observations made by all three instruments are plotted against each other in Figures 6.22-6.26. The total column errors in the figures consist of state space parameter interference error, retrieval noise, and smoothing error added in quadrature (see Section 5.3).

Total O_3 columns retrieved from the 3040 cm^{-1} microwindow show that there is a persistent bias between the TAO-FTS and U of T FTS (see Figure 6.22). As was found in the extended intercomparison, the U of T FTS consistently retrieves higher ozone columns than those of the TAO-FTS (on average, 3.3% higher). Conversely, PARIS-IR has better agreement with TAO-FTS total column O_3, averaging a difference of less than 1%, with a potential low bias for higher column values. The retrievals between the U of T FTS and PARIS-IR are significantly different (at the 95% confidence level) with an average

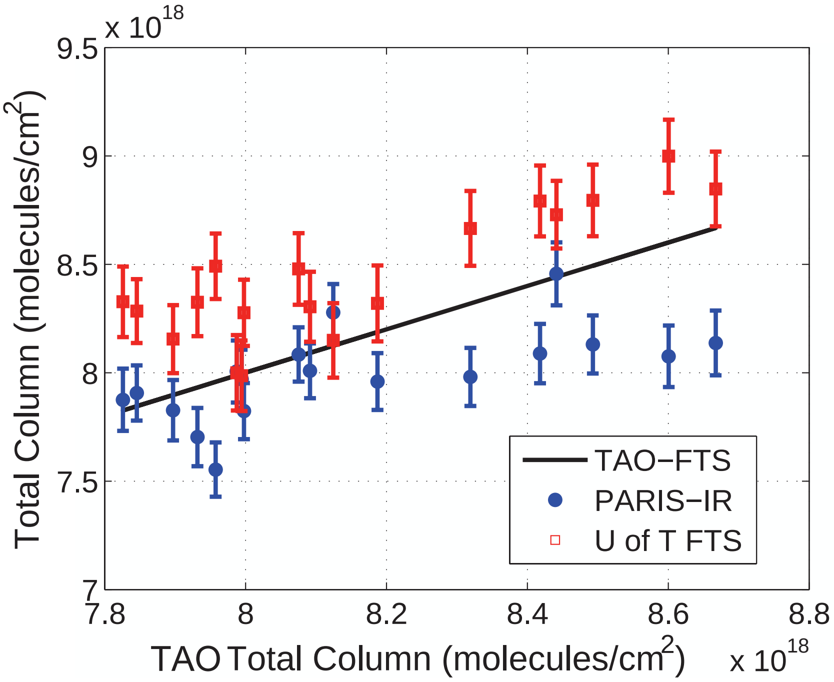

Figure 6.22: Ozone total columns retrieved from the 3040 cm^{-1} microwindow, co-added to 20-minute integration times so as to be consistent with that of the TAO-FTS. Columns from all three instruments are plotted against the coincident TAO columns, with PARIS-IR denoted by blue circles, the U of T FTS denoted by red squares, and the TAO-FTS denoted by a black 1:1 line (TAO vs TAO). Error bars represent state space parameter interference error, retrieval noise, and smoothing error added in quadrature.

difference of 4.3%. The results are summarized in Table 6.6.

O$_3$ columns retrieved from the 2775 cm^{-1} microwindow are in better agreement, reflecting the difference in altitude sensitivity of the two microwindows. The qualitative agreement between all three instruments is shown to be good (see Figure 6.23). In the extended intercomparison, the U of T FTS exhibited slightly higher total columns than those of the TAO-FTS. This trend is not readily apparent in the focused intercomparison, with

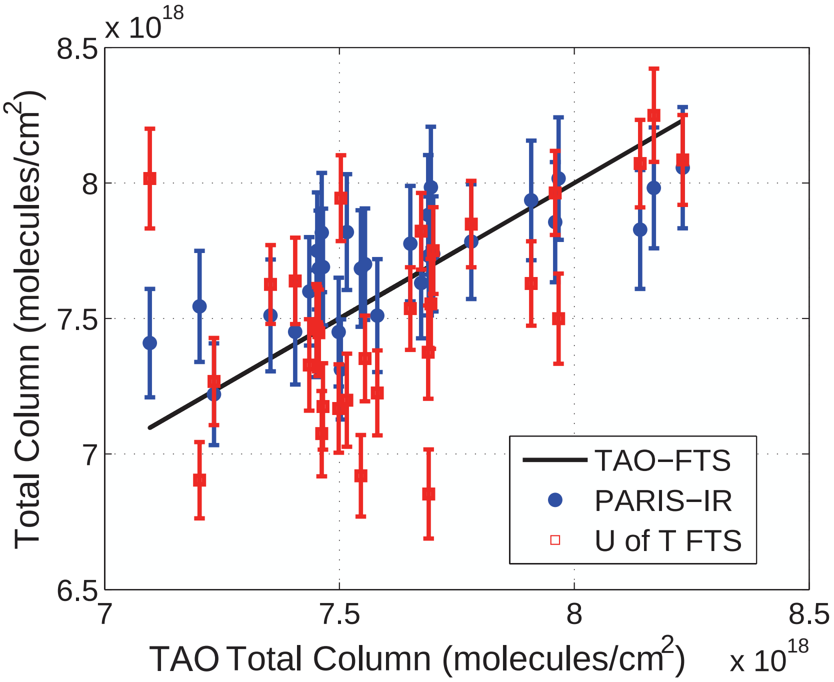

Figure 6.23: Same as Figure 6.22 but for ozone retrieved from the 2775 cm^{-1} microwindow.

the mean difference being only 0.7%. The TAO-FTS and PARIS-IR coincident columns also agree well with a mean difference of 1.2%. As well, the U of T FTS and PARIS-IR also show good agreement with only 2.8% difference.

The HCl coincident total columns also exhibit good quantitative agreement (see Figure 6.24). Values retrieved from PARIS-IR appear to exhibit a slight high bias compared to both of the other instruments. The average difference between PARIS-IR and TAO-FTS columns is 4.5% and that of PARIS-IR and the U of T FTS is 2.6%. The U of T FTS columns do not appear to be overly biased above or below those of the TAO-FTS. This is the opposite trend than that which was observed in the extended intercomparison, in which the TAO-FTS columns were markedly higher. The average differences, however,

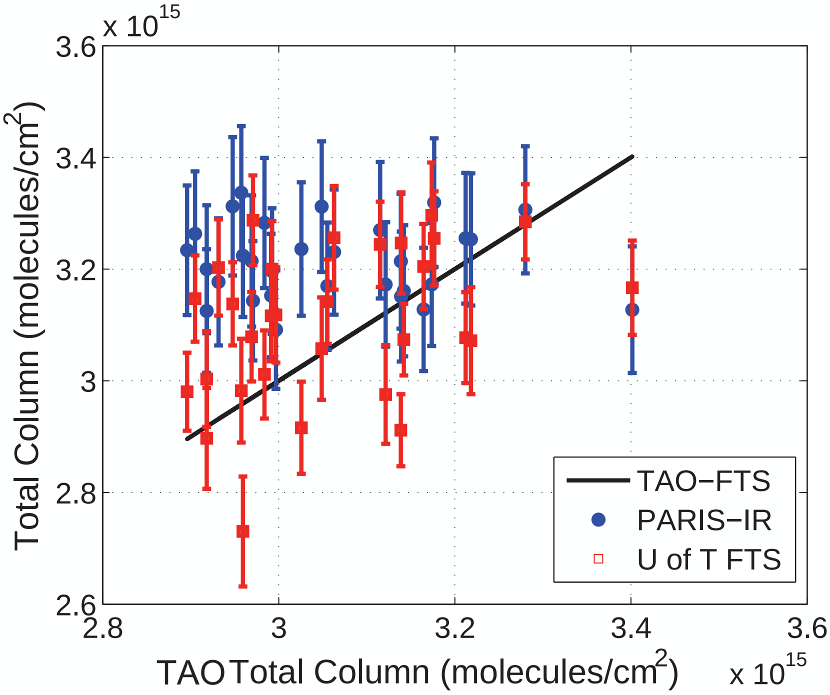

Figure 6.24: Same as Figure 6.22 but for HCl retrievals.

are still similar, with the focused intercomparison median difference being 1.7% and the extended intercomparison mean difference being 2.2%.

N_2O coincident total columns are shown in Figure 6.25. In the extended intercomparison, it was found that there was no discernible trend in the TAO-FTS and U of T FTS coincident columns. This same result can be seen for all three instruments in the focused comparison as most values agree to within the combined error. The mean difference between the TAO-FTS and the U of T FTS and between that TAO-FTS and PARIS-IR was only 0.4% for each (consistent with the average difference in the extended intercomparison). The mean difference between the PARIS-IR columns and the U of T FTS columns was 0.8%. The close agreement of these columns indicates that N_2O is retrieved by fine and coarse resolution FTS instruments with comparable precision from the ground.

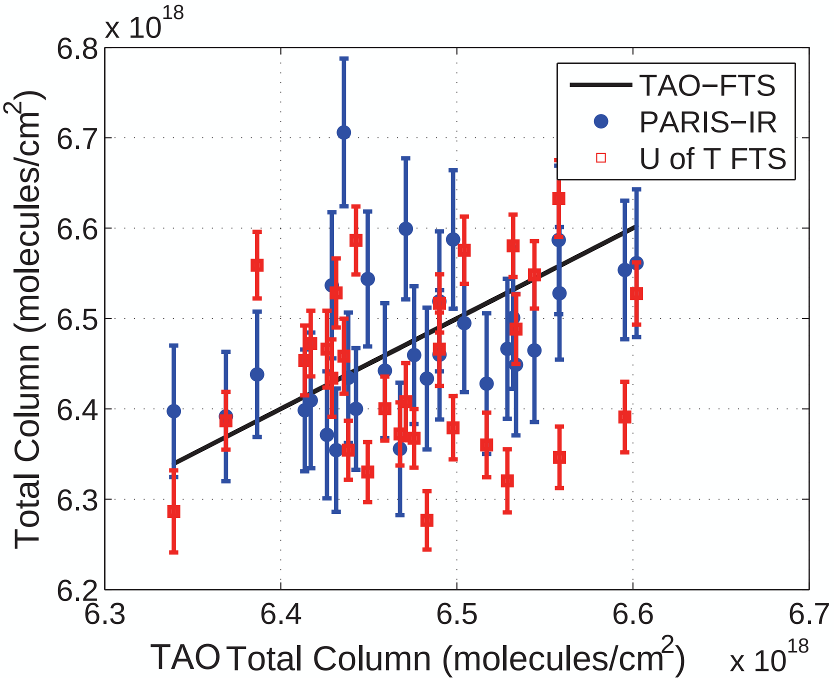

Figure 6.25: Same as Figure 6.22 but for N_2O retrievals.

Coincident total column CH_4 values from each instrument are shown in Figure 6.26. As was noted in the extended intercomparison, agreement between CH_4 columns is potentially limited by errors in the spectroscopic parameterization of the infrared line signatures, specifically the lack of accurate air-broadening coefficients and temperature dependencies, which has been noted by Rothman et al. [2005], Brown et al. [2003] and Worden et al. [2004]. This appears to result in the U of T FTS having consistently elevated retrieved columns over those of PARIS-IR, with a mean difference of 1.7 %. The mean difference between the TAO-FTS and PARIS-IR is only 0.5% with no detectable trend outside of the error bars.

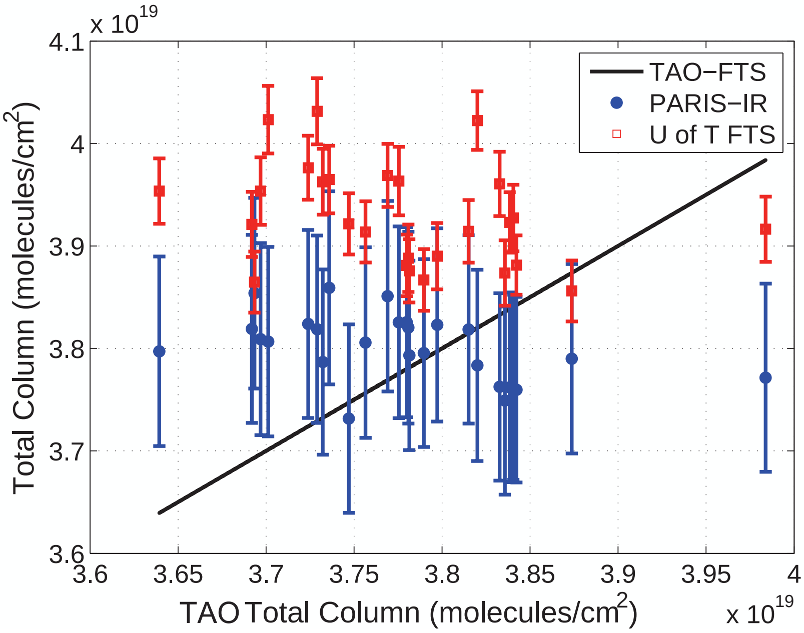

Figure 6.26: Same as Figure 6.22 but for CH_4 retrievals.

6.2.6 Summary of Focused Ground-Based Intercomparison

Total column amounts of O_3, HCl, N_2O and CH_4 were retrieved from PARIS-IR, the U of T FTS and the TAO-FTS. Measurements were averaged during coincident 20-min periods and the total column amounts retrieved from these averaged spectra were compared directly. The results, summarized in Table 6.6, show that the lower-resolution instruments can measure total columns of all species to within 4.5% of the TAO-FTS, and generally to much less than this. There is no discernable trend in the agreement between instruments, nor in the statistical results. The largest errors are obtained for the stratospheric species, and these errors can be attributed to the averaging kernels of the lower-resolution instruments [Wunch et al., 2007]. As with the extended intercomparison, the agreement for N_2O is very good, but there are significant differences for CH_4, possibly due to uncertainties in the spectroscopic parameters. The agreement between the TAO-FTS and the U of T FTS is slightly better in the focused intercomparison for most of the species. This may be due to the fact that only measurements that were obtained at solar zenith angles of greater than 40° were used in the comparison (for details of this comparison, see Wunch et al. [2007]).

Table 6.6: Mean total column differences calculated between the instruments (see Wunch et al. [2007] for details). Bold-faced values are significantly different at the 95% confidence level as derived from the t-test.

Target Gas and Micro-window (cm^{-1})	PARIS-IR vs TAO-FTS	U of T FTS vs TAO-FTS	U of T FTS vs PARIS-IR
O_3 - 3040	0.9	**3.3**	**4.3**
O_3 - 2775	1.2	0.7	2.8
HCl - 2925	**4.5**	1.7	**2.6**
N_2O - 2482	0.4	0.4	0.8
CH_4 - 2859	0.5	**2.3**	**1.7**

The agreement is worse than that found in the most recent high-resolution FTS intercomparison by Meier et al. [2005]. These results may give an upper bound on the ability to measure total column amounts of these species by lower-resolution instruments.

The results here confirm what was demonstrated in the extended intercomparison. The differences in the stratospheric species can be partially attributed to the lower sensitivity of the averaging kernels of the lower-resolution instruments to the stratosphere and the consequent increased reliance on the *a priori* in that region (for example figures, see Wunch et al. [2007]). It is therefore particularly important to choose appropriate microwindows and perform sufficient retrieval characterization of the lower-resolution instruments, to ensure optimal sensitivity.

Retrieving ILS EPHS and EAP parameters from SFIT2 significantly improves the column comparisons of the stratospheric species for the lower-resolution instruments over retrievals performed assuming an ideal ILS (see Figure 6.16). The ILS information is less important for the pressure-broadened tropospheric species. Also, retrieving the SFIT2 EPHS and EAP parameters as part of the state vector can replace the LINEFIT ILS information for balloon-based measurements when retrieving the ILS from a gas cell is not feasible.

Chapter 7

Satellite-Based Data Validation

Cross-validation of ground-based atmospheric data products with coincident satellite observations provides a rigorous method of characterizing instrument precision and bias. For comparisons of this nature, care needs to be taken to ensure that sampling homogeneity is maintained. This is done in two ways: the first accounts for the differences between the two observing systems and relies on the averaging kernels to characterize the differences in the sensitivity of the measurements, and the second ensures that the spatial and temporal sampling differences are adequately minimized so as to facilitate a reasonable comparison. To date, most comparisons of this nature have consisted of compiling the TAO-FTS observations with many other ground-based observations so as to best validate the satellite-based data products. Although these contributions do not explicitly scrutinize the nominal operations of the TAO-FTS they do provide insight into how well the TAO-FTS is performing relative to other ground-based instruments in the NDACC. Section 7.1 provides an overview of TAO validation activities related to the SCanning Imaging Absorption spectroMeter for Atmospheric CHartographY (SCIAMACHY) and the Atmospheric Chemistry Experiment Fourier Transform Spectrometer (ACE-FTS), while Section 7.2 provides a more detailed description of comparisons with the Optical Spectrograph and InfraRed Imager System (OSIRIS).

7.1 Comparisons with SCIAMACHY and ACE

SCIAMACHY was launched on board the European Space Agency's ENVISAT satellite in 2002 [Burrows et al., 1995]. SCIAMACHY measures a suite of trace gases both in the stratosphere and in the troposphere. These observations have been compared with total column measurements of CO, CH_4 and N_2O made at TAO as part of a study involving 11 different ground-based FTS sites [Dils et al., 2006]. The TAO-SCIAMACHY total column comparisons involved results from several different retrieval algorithms that were used to derive the SCIAMACHY products (see Table 7.1). The three algorithms included a Weighting Function Modified Differential Optical Absorption Spectrum (WFM-DOAS v0.5 and v0.4) method, an Iterative Maximum Likelihood Method (IMLM v6.3) and an Iterative Maximum A Posteriori Differential Optical Absorption Spectrum (IMAP-DOAS v1.1) method. Total columns of CO and CH_4 were retrieved from SCIAMACHY measurements using all three of these algorithms, while N_2O total columns were retrieved only with the WFM-DOAS algorithm. The results were compared with observations from 11 different ground-based FTS sites.

As these three retrieval algorithms were used to generate the SCIAMACHY data products, there are generally three comparisons to be made for each species compared. As well, there is a global range of comparisons determined from the 11 different FTS sites. The results are summarized in Table 7.1 with comparisons based on how well the TAO-FTS data agreed with SCIAMACHY and on how well all 11 ground-based FTS sites agreed with SCIAMACHY. The TAO % mean difference were determined for each species by comparing all coincident observations with results from all of the SCIAMACHY retrieval algorithms. The mean scatter was determined from the standard deviation of differences between the TAO measurements and all of the SCIAMACHY results for each species. The global % mean difference was determined from the average of the mean differences from each of the ground-based sites for each algorithm, for each species. Likewise, the global mean scatter is the standard deviation of differences between all of the ground-based measurements and all the SCIAMACHY results, for each species. The global range of differences represents the extreme % mean differences of the 11 sites compared (that is, the values from the sites with the lowest mean difference and the highest mean difference). The differences between TAO and SCIAMACHY were well within the range of differences observed by other instruments.

Table 7.1: Summary of (SCIAMACHY-TAO)/(TAO) comparisons. The first row indicates the % mean difference (with standard error of the mean) between TAO and SCIAMACHY determined for a specific gas, from each algorithm, as well as the scatter associated with the same comparison. The second row shows the same quantities calculated for the average of all 11 ground-based sites. The third row indicates the upper and lower extreme differences for each species. All values are from Dils et al. [2006].

	Total CO	Total CH_4	Total N_2O
TAO % Mean Diff.	-2.81±1.16	-3.12±0.22	3.74±0.23
Mean Scatter	27.6	2.71	9.68
Global % Mean Diff.	-5.98±0.97	-2.22±0.22	0.16±0.02
Mean Scatter	25.2	2.09	9.41
Global Range	-18.8±2.76 to	-9.99±0.38 to	-10.2±7.58 to
of Differences	58.6±27.2	-0.13±1.69	4.59±1.62

The Canadian ACE mission was launched onboard the SCISAT-1 research satellite in 2003. The mission consists of two instruments: the ACE-FTS and the Measurements of Aerosol Extinction in the Stratosphere and Troposphere Retrieved by Occultation instrument (MAESTRO) [McElroy et al., 2007]. The ACE-FTS is an infrared Fourier transform spectrometer that retrieves VMR profiles of more than 30 atmospheric constituents in the range 750-4400 cm^{-1} [Bernath, 2006]. Because SCISAT-1 is in a high-inclination, low-Earth orbit, the instruments can perform solar occultation measurements in tropical, mid-latitude, and polar regions.

The advantage of having measurements with highly-resolved altitude profiles is balanced by the limited global coverage caused by the solar occultation measurement technique. Due to the orbit of the satellite, there are approximately 30 opportunities for an occultation measurement each day. The primary geometric constraint on these opportunities is the beta angle. This is the angle between the satellite velocity vector and the vector connecting the Earth to the Sun. The two other limiting factors have to do with the capacity for downloading the data and scheduling. There must be a sufficient downlink to ground-stations for the recording and transferring of data, otherwise there is insufficient memory space to accommodate more measurements. Also, the scheduled cycle that is used for calibrating and maintaining the instruments on board the satellite can sometimes interfere with occultation opportunities.

When temporal constraints are considered for comparisons with a ground-based instrument, the number of coincident observations is inevitably small. Furthermore, because both the TAO-FTS and the ACE-FTS measure clear-sky infrared radiation, any cloud contamination interferes with tropospheric measurements. This results in there being only 35 coincident ACE occultations with TAO observations from January 2004 through December 2006. With this limited number of observations, calculations involving monthly means, or virtual coincidences are not possible. Essentially, this is a direct consequence of the orbital geometry of the ACE-FTS and the mid-latitude location of TAO.

Even though the comparison dataset is small, TAO has still been involved in a number of ACE comparison activities. TAO-FTS observations were first used to help validate ACE-

FTS v1.0 stratospheric HCl [Mahieu et al., 2005]. ACE-FTS data have also been used in conjunction with scientific process studies at TAO and Eureka [Wiacek et al., 2006]. Trace gas columns retrieved at TAO have been more extensively used for validating the latest version of ACE-FTS data (v2.2 + updates) and ACE-MAESTRO data (v1.2) and have included CO [Clerbaux et al., 2008], CH_4 [Mazière et al., 2008], O_3 [Dupuy et al., 2008], NO, NO_2 [Kerzenmacher et al., 2008], HCl [Mahieu et al., 2008], and N_2O [Strong et al., 2008]. A summary of the results of these comparisons is given in Table 7.2.

The results from the comparisons with the ACE-FTS show that TAO-FTS observations are in good agreement with ACE (within 12% or better) with the exception of CO and NO which each have a bias of about 25%. However, when the values for these two gases are compared with the performance of the rest of the ground-based FTS observations (column 2 in Table 7.2), it can be seen that the TAO observations are in the middle of the bounds. The only outlying comparison appears to be for CH_4, which is consistent with the poor comparisons seen in the ground-based validation of the TAO-FTS data (see Chapter 6).

To date, there has been one exclusively dedicated comparison between the TAO-FTS and a satellite-based instrument. Stratospheric gases were cross-validated with observations by the Optical Spectrograph and InfraRed Imager System (OSIRIS) instrument. The temporal and spatial sampling of the two instruments provided an unprecedented level of coincidence between data products. The details of this cross-validation work are given below but the originally published work may be found in Taylor et al. [2007].

Table 7.2: Summary of TAO-ACE partial column comparisons. The first column indicates mean TAO % differences for each species and standard deviation. The second column indicates the upper and lower difference bounds (with standard deviation) for each species, that is, the minimum and maximum difference of all the ground-based FTS sites involved in the comparison. The CO comparisons used two different smoothing techniques to compare the data products, as such, there is a range of values. All values are from Clerbaux et al. [2008], Mazière et al. [2008], Dupuy et al. [2008], Kerzenmacher et al. [2008], Mahieu et al. [2008], Strong et al. [2008].

	TAO % Mean Diff.	Global Range
ACE-FTS CO	24.5±11.2 to 33.7±23.0	13.1±6.9 to 40.4±29.5
ACE-FTS O_3	1.7±5.6	-9.9±6.5 to 6.3±1.9
ACE-MAESTRO O_3	-5.2±6.0	-8.7±4.7 to -0.5±10.8
ACE-FTS CH_4	-12.1±2.2	-12.1±2.2 to 9.8±3.5
ACE-FTS HCl	6.20±13.0	-5.68±16.9 to 15.45±19.3
ACE-FTS N_2O	-5.5±7.3	-18.6±29.6 to 3.8±2.4
ACE-FTS NO_2	1.1±17.4	-9.3±15.1 to 25.6±29.1
ACE-MAESTRO NO_2	-5.0±20.4	1.4±18.5 to 25.6±29.1
ACE-FTS NO	-25.7±32.0	-14.5±16.1 to -67.5±17.4

7.2 Comparisons with OSIRIS

In the middle stratosphere (25-40 km), catalytic destruction by NO_x (NO and NO_2) dominates [Crutzen, 1970, 1971, WMO, 2007]. In addition to this direct role, NO_x is coupled to the hydrogen, chlorine, and bromine families and may form longer-lived "reservoir" species (for details, refer to Brasseur and Solomon [2005]). Until 1997, mid-latitude O_3 in this region of the atmosphere was decreasing by about 6% per decade, while it decreased by as much as 10-15% from 1979 to the 1990s [WMO, 2007]. The rate of decrease has since levelled off, while total column NO_2 is increasing by 5.7-6.2% per decade [Liley et al., 2000, WMO, 2007]. In order to make accurate predictions about future concentrations of stratospheric O_3, measurements of O_3 and NO_2 must be at least as precise as these trend estimates. According to the requirements established for the Integrated Global Observing Strategy , lower stratospheric O_3 observations should be accurate to within 5% of the truth with a threshold of 20%, while lower stratospheric NO_2 observations should be accurate to within 15% of the truth with a threshold of 40% [IGOS, 2004] (where "threshold" defines the minimium precision necessary to be useful" and "accurate" defines the preferred precision).

The TAO NO_2 fits were performed on the $\nu_1 + \nu_3$ vibrational-rotational band in a microwindow from 2914.59 to 2914.70 cm^{-1}, which was first investigated by Camy-Peyret et al. [1983]. NO_2 has been previously measured with ground-based FTIR spectroscopy [Flaud et al., 1983, 1988, Mazière et al., 1998, Lambert et al., 2004, Sussmann et al., 2005, for example] and has been characterized at TAO. As per all nominal retrievals at TAO, a volume mixing ratio profile was retrieved, with the trace gas of interest represented on a 38-layer altitude grid in the state space. Spectroscopically interfering species (in this case, CH_4 and H_2O) were considered by determining the scaling factors which result in the best overall spectral fit when applied to the entire *a priori* profile of each interfering gas. The *a priori* profile was constructed from a 15-year climatology of HALogen Occultation Experiment (HALOE) data (v.19) between 19-44 km [Russell et al., 1994], with the remainder of the profile constructed from Michelson Interferometer for Passive Atmospheric Sounding (MIPAS) mid-latitude daytime reference climatology profiles (v.3.0) [Carli et al., 2004]. The *a priori* error estimates used here were set to 40% between 10-55 km and tapered to 10% outside of this region (for a detailed description of these NO_2 retrievals, refer to Wiacek [2006]). The retrievals resulted in a mean total column degrees of freedom for signal of 1.6, with the sensitivity concentrated primarily in the stratosphere.

O_3 measurements recorded by ground-based infrared Fourier transform spectroscopy have been previously used to validate similar measurements from satellites [Mazière et al., 2002, Griesfeller et al., 2005, for example]. The chosen microwindow was used in previous ground-based intercomparison exercises and was useful for identifying differences in retrievals (see Section 6.1). It was composed of multiple band passes in the the $2\nu_1 + \nu_2$ band: 2775.68-2776.30 cm^{-1}, 2778.85-2779.20 cm^{-1}, and 2781.57-2782.06 cm^{-1}. These three band passes were fitted simultaneously with interfering species CH_4, H_2O, HDO, CO_2, HCl, and N_2O so as to achieve the best global fit. This resulted in a mean total column degrees of freedom for signal of 2.1. As with NO_2, all of these retrievals were performed on a 38-layer altitude grid using an *a priori* profile constructed from HALOE and MIPAS climatologies. The *a priori* covariance matrix was set to 20% over the entire altitude range.

7.2.1 The Optical Spectrograph and Infrared Imager System

OSIRIS [Llewellyn et al., 2004] is one of two instruments that were launched on board the Odin satellite in February 2001 [Nordh et al., 2003]. This Canadian instrument is designed to record atmospheric extinction spectra in the ultraviolet-visible from limb-scattered sunlight. This technique allows for both global coverage and relatively high vertical resolution, yielding vertical profiles of trace gas concentrations from approximately 12-50 km altitude [von Savigny et al., 2003, Haley et al., 2004]. OSIRIS NO_2 and O_3 data sets have been validated with coincident satellite and sonde observations [Petelina et al., 2004, von Savigny et al., 2005, Brohede et al., 2007]. These data have, in turn, served as the calibrated "truth" for validating other atmospheric measurements [Petelina et al., 2005].

The Odin satellite is in a Sun-synchronous orbit at 600 km with the ascending node at 18h Local Solar Time and carries two instruments dedicated to two mission goals; OSIRIS exclusively carries out aeronomy studies, while the SubMillimetre Radiometer (SMR) [Frisk et al., 2003] records both astronomical and aeronomical observations. The Optical Spectrograph (OS) uses a grating spectrometer and a charge coupled device to record spectra of Rayleigh-scattered sunlight along the limb within the wavelength range 280-800 nm with 1 nm resolution [Llewellyn et al., 2004]. This provides vertical profile concentrations of several atmospheric trace gases, including O_3 and NO_2, as well as BrO, OClO and aerosols. A complete stratospheric scan requires about 85 seconds and hemispheric coverage is obtained through most of the year, with global coverage at the equinoxes. Because Odin is a two-discipline satellite, measurement time is divided such that the stratospheric observation mode happens one out of every three days [Murtagh et al., 2002].

NO_2 profiles were retrieved from the OSIRIS limb-scattered sunlight measurements using two different techniques. The first technique utilized a Differential Optical Absorption Spectroscopy (DOAS) algorithm with a maximum *a posteriori* estimator [Haley et al., 2004]. The fitted spectral microwindow ranged from 435 to 451 nm, with O_3 and O_4 fitted as interfering species. These measurements nominally cover a tangent height altitude range of 10-70 km with regular extensions up to 100 km altitude and a vertical resolution of roughly 2 km. A previous version of Level 2 data retrieved with this algorithm compared well with observations from other satellite platforms [Brohede et al., 2007]. Version 3.0 of the OSIRIS-DOAS NO_2 data set has been used in this study [Haley and Brohede, 2007]. The second technique was developed at the University of Saskatchewan and uses retrieval algorithms based upon a Multiplicative Algebraic Reconstruction Technique (MART) [Degenstein et al., 2006]. This algorithm uses a maximum likelihood expectation estimator over a narrower wavelength region, while simultaneously fitting aerosol concentrations.

The OSIRIS O_3 retrievals were also carried out using two different techniques. The first used the so-called Triplet Algorithm (version 3.0) to retrieve O_3 vertical profiles from the Chappuis absorption band [Flittner et al., 2000, von Savigny et al., 2003, Haley and Brohede, 2007]. This technique used the ratio of limb radiances at three different wavelengths (602.0 nm, 540.2 nm, and 663.9 nm) with Optimal Estimation to determine the altitude distribution of O_3. The second technique used the same MART retrieval that was used for NO_2 retrievals (version 2.0) [Degenstein et al., 2006]. The O_3 MART retrieval not only relied on the Chappuis absorption band, but also included measurements from the Huggins band. This should provide greater sensitivity to ozone at higher altitudes (although, for consistency, the same altitude regions will be compared for all retrievals). As with NO_2, these measurements had a vertical resolution of roughly 2 km.

This intercomparison provides the first statistical ground-truthing of OSIRIS observations using the latest version (v3.0) of O_3 and NO_2 observations by OSIRIS [Haley and Brohede, 2007] with measurements from the TAO-FTS. It also provides the first comparison with retrievals made by the OSIRIS MART algorithm. The coincident data that has been recorded at TAO for more than four years provides an opportunity not only to investigate simple observation biases, but also to statistically investigate issues related to temporal coincidence. The effects of comparing an infrared observing system with a UV-visible instrument are also addressed by comparing differing retrieval techniques.

7.2.2 Stratospheric NO_2 Cross-Validation

As has been used in previous OSIRIS validation studies [Petelina et al., 2005], the spatial coincidence selection criterion was chosen to be within ±5° latitude and ±10° longitude of TAO (that is, all coincidences are within $\approx \pm 700$ km of TAO). Other comparisons of ground-based NO_2 observations with satellite observations utilize spatial coincidence criteria of 750 km [Wetzel et al., 2007]. This definition was chosen for this study so as to maximize the number of comparable observations.

The high degree of spatial coverage of OSIRIS resulted in 904 spatially coincident observations between May 2002 and December 2006. Throughout this same time period, the TAO-FTS recorded 567 measurements. However, due to the orbit of Odin, OSIRIS observations are limited in the winter hemisphere, effectively restricting coincidence to March through October. This large number of spatially coincident measurements reduces sampling problems that often inhibit rigorous statistical comparisons from being made between two differing observation platforms. However, it is important to note that the short lifetime of NO_2 necessitates a strict temporal coincidence criterion for comparing individual measurements.

Following the approach first proposed at the Zugspitze Ground-Truthing Facility by Sussmann et al. [2005], the TAO NO_2 columns were corrected using "virtual coincidences". Previous corrections for NO_2 temporal coincidence have been made with photochemical box models [McLinden et al., 2000, for example], but the errors associated with this technique are difficult to estimate [Roscoe et al., 2001]. The virtual coincidence technique relies on the fact that there is no significant seasonal dependence in the daytime rate of increase of NO_2 at mid-latitudes. The annual average daytime rate of increase of 1.02×10^{14} molecules/cm^2/hour found at Zugspitze (47.42°N, 10.98°E) should be representative of that of Toronto (43.66°N, 79.40°W). Furthermore, error estimates can be made by using the difference in time between coincident measurements.

For each day of individual measurements recorded in Toronto, the NO_2 daily growth rate is used for extrapolating concentrations to coincide with the time of the OSIRIS overpass. By fitting a straight line with a constant slope of 1.02×10^{14} (*i.e.*, only allowing the vertical offset for this trend line to be fit) to the TAO NO_2 columns, these "virtual coincidences" can be defined (an example is shown in Figure 7.1). Since the error in the daytime rate of increase is 0.06×10^{14} molecules/cm^2/hour [Sussmann et al., 2005], this value can simply be multiplied by the number of hours separating the measurements to yield an error estimate. To further mitigate temporal sampling problems, the data were sorted into monthly bins and monthly mean statistics were calculated from each instrument's data. Only months in which each instrument had recorded more than five measurements were used for comparison (see Figure 7.2).

To ensure that the peak stratospheric concentrations were captured for the comparison, partial columns were integrated between 16-50 km, yielding 1.4 degrees of freedom for signal. Since the TAO-FTS retrieves vertical information with a coarser vertical resolution than OSIRIS, the TAO-FTS averaging kernels (see Figure 7.3) were used for smoothing and integrating the OSIRIS profiles into partial columns. Equation 5.10 is used to do this, but here $\mathbf{x}$ is the original OSIRIS profile and $\hat{\mathbf{x}}$ is the smoothed OSIRIS profile. For details of this technique, refer to Rodgers and Connor [2003].

Figure 7.4 shows the monthly mean timeseries of all three NO_2 data products. Although the individual monthly means display close agreement, it is necessary to consider long-

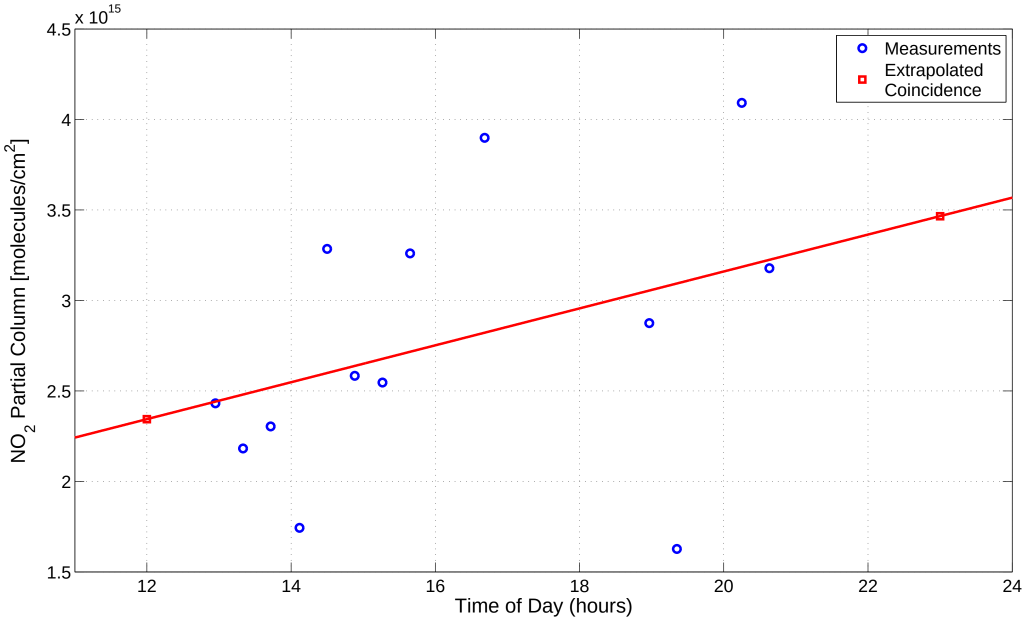

Figure 7.1: "Virtual coincidence" correction of NO_2 partial columns measured at TAO on 1 Sept. 2005 (shown as blue circles). The slope was fixed for each day at 1.02 $\times 10^{14}$ molecules/cm^2/hr and only the vertical offset was fitted to the columns (shown as the red solid line). The "coincidences" are extrapolated from the slope so as to coincide with the times of the OSIRIS overpass (shown as red squares).

term biases for data sets of this length. From the scatter plot shown in Figure 7.5, it may be seen that the OSIRIS-MART data and the TAO-FTS data have a high correlation (correlation coefficient, $R^2 = 0.89$) with some random differences. The weighted least-squares linear fit to the scatter plot shows a slope of 0.92, indicating that there is a multiplicative bias favouring the MART retrievals, that is, for larger column concentrations, the MART retrieval captures slightly elevated concentrations of NO_2 while for smaller column concentrations, the TAO-FTS shows relatively higher columns. Although no systematic bias is readily evident from the scatter plot, Figure 7.6 shows that

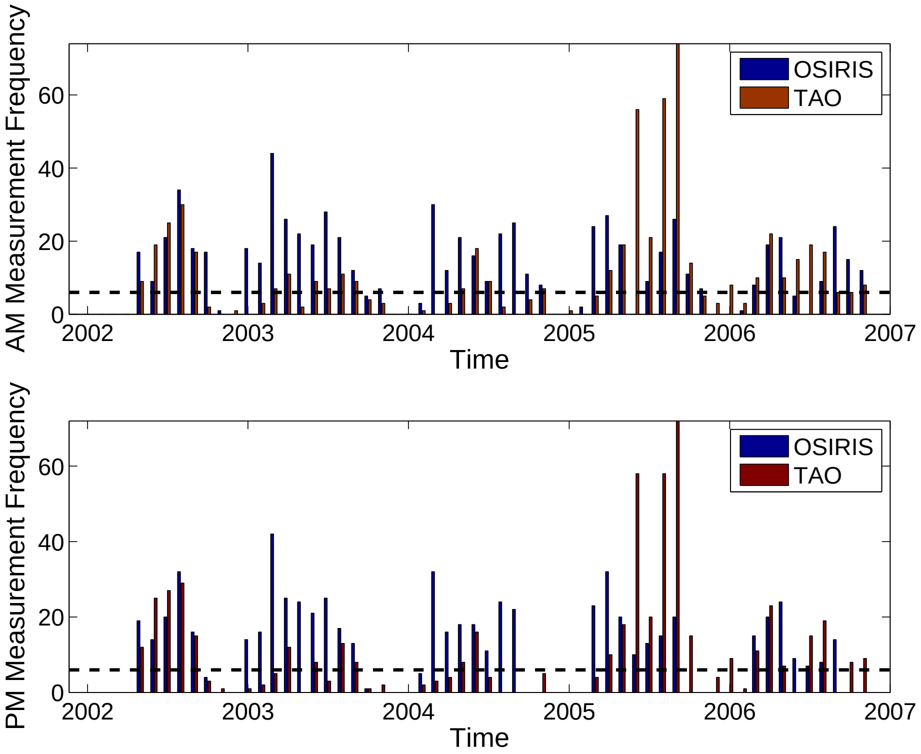

Figure 7.2: Monthly observation frequency of AM and PM measurements recorded by the TAO-FTS (red) and OSIRIS (blue) from May 2002 to December 2006. The dashed line represents the minimum statistical limit of five measurements; any month in which either instrument has fewer measurements is not used for this comparison.

the differences between the columns are evenly distributed, but slightly biased to higher MART columns, suggesting a systematic difference of approximately 10%.

Comparisons between the OSIRIS-DOAS retrievals and the TAO-FTS yield similar results (Figures 7.7 and 7.8). The data have a correlation coefficient of 0.85, and the linear fit to the scatter plot also shows a multiplicative bias that favours the OSIRIS columns (slope = 0.79). The histogram in Figure 7.8 shows that the OSIRIS-DOAS data exhibit,

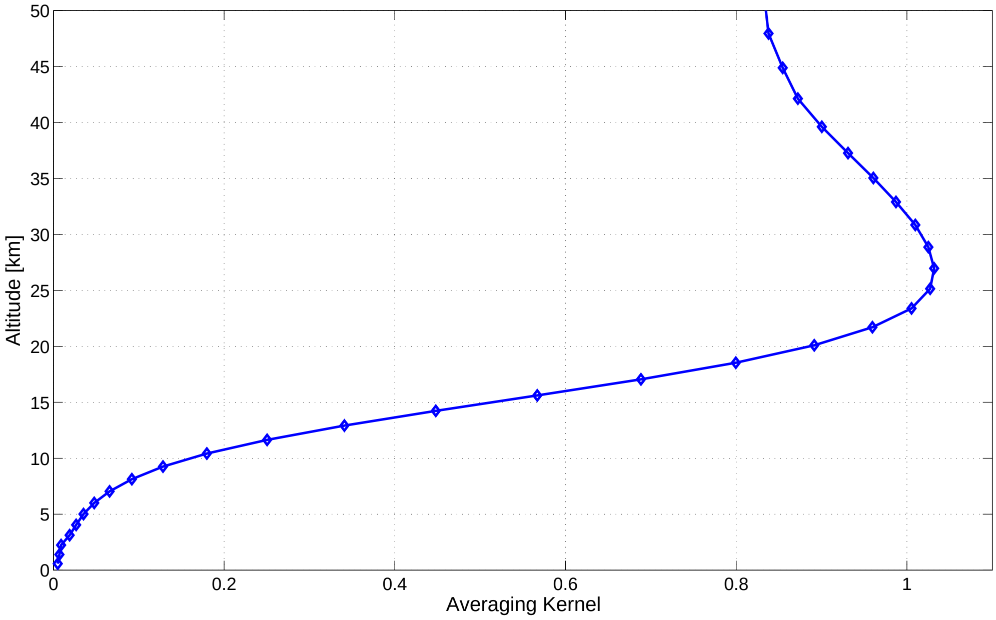

Figure 7.3: NO_2 partial column averaging kernel for the TAO-FTS. This represents the altitude sensitivity of the measurement to atmospheric volume mixing ratios between 16-50 km.

on average, a small systematic difference of 5% over that of the TAO monthly means.

The two OSIRIS retrieval techniques also show some differences (Figures 7.9 and 7.10). As should be expected of two differing retrievals from the same data, the correlation coefficient is high (0.93), but the scatter plot also shows a multiplicative bias. The linear fit to the scattered data has a slope of 0.87, indicating that the DOAS retrieval captures slightly higher monthly mean columns than those of the MART retrieval. Furthermore, the histogram shows that the DOAS retrievals have a systematic bias of approximately 5% over MART.

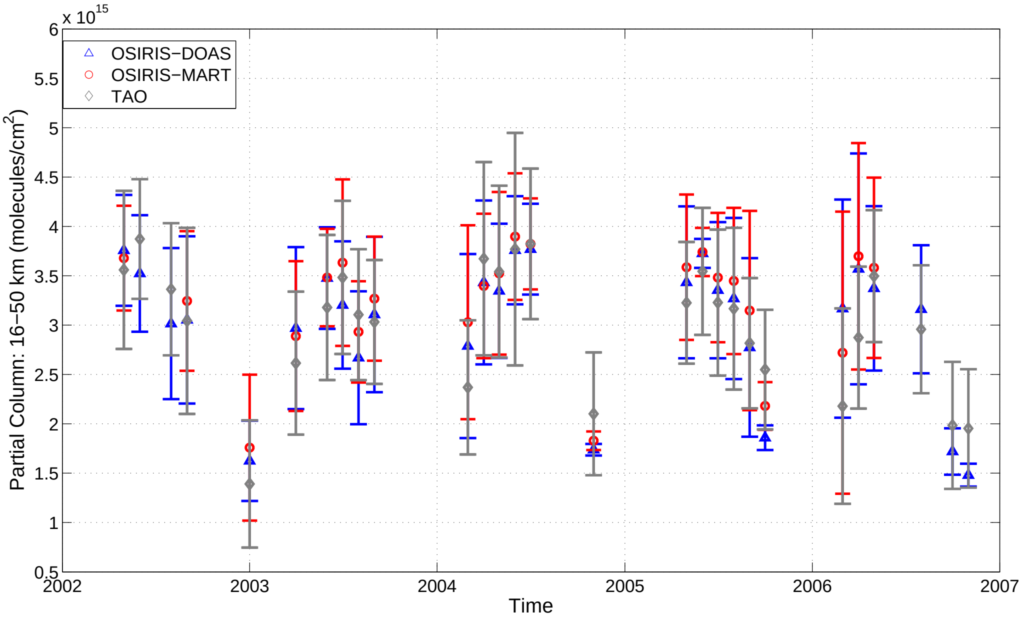

Figure 7.4: Timeseries of monthly mean NO_2 partial columns for each month in which there are more than five measurements. Blue triangles represent the DOAS-based retrievals from OSIRIS, red circles represent the MART-based retrievals from OSIRIS, and gray squares represent the values derived from the TAO-FTS. Error bars show one standard deviation.

Previous comparisons between NO_2 observations made in the UV-visible have shown that differences in absorption cross sections can generate as much as 5% systematic disagreement among columns [Vandaele et al., 2005]. In this comparison, DOAS and MART retrievals used UV-visible cross sections from Vandaele et al. [1998], while the TAO NO_2 retrievals used infrared parameters originally published by Perrin et al. [1998]. Since this comparison is obviously relying on differing spectroscopic parameterization between the infrared and UV-visible, it is unrealistic to expect that columns should agree to better than this 5% limit. The comparison between the two OSIRIS retrievals

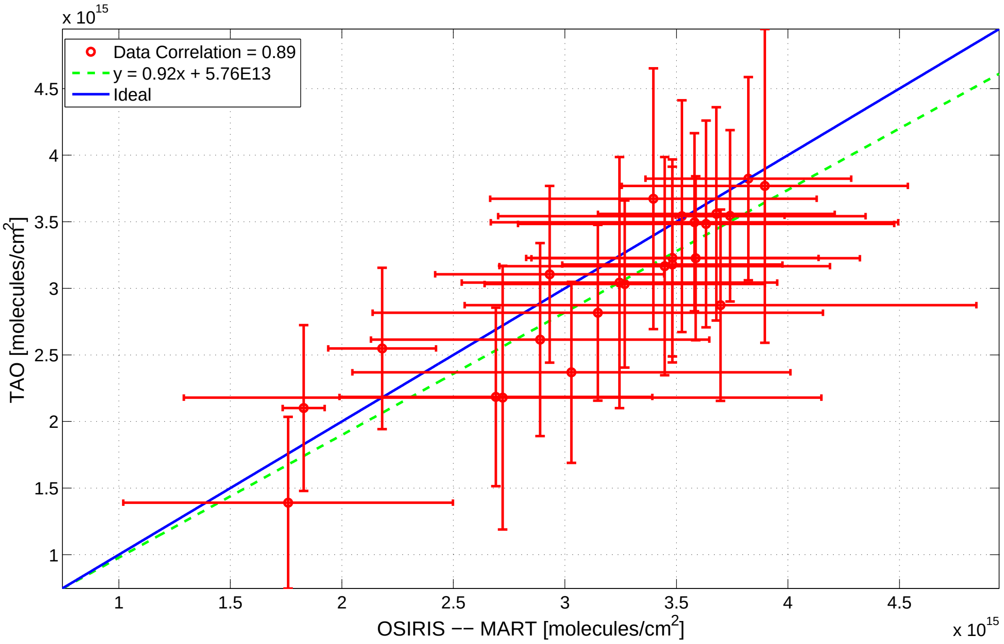

Figure 7.5: NO_2 monthly means derived from TAO-FTS observations plotted against monthly means derived from OSIRIS-MART retrievals. Error-bars represent one standard deviation. The solid line shows the 1:1 line and the dashed line shows a weighted-least-squares linear fit to the data.

reveal a general systematic difference evenly distributed around 5%. Similarly, the DOAS and TAO NO_2 differences are close to 5%. Only the MART−TAO difference shows a distribution around 5-10%, suggesting that these two data sets have a systematic bias that may be greater than any spectroscopically induced bias. As this is the first validation of products generated by the MART retrieval algorithm, it is possible that this systematic bias is a direct result of the retrieval. However, previous profile-based comparisons of OSIRIS NO_2 (version 2.4) with measurements from an infrared instrument (HALOE) that have shown that OSIRIS generally reports higher values above 35 km [Brohede et al., 2007], and the column discrepancy observed here may be a manifestation of this

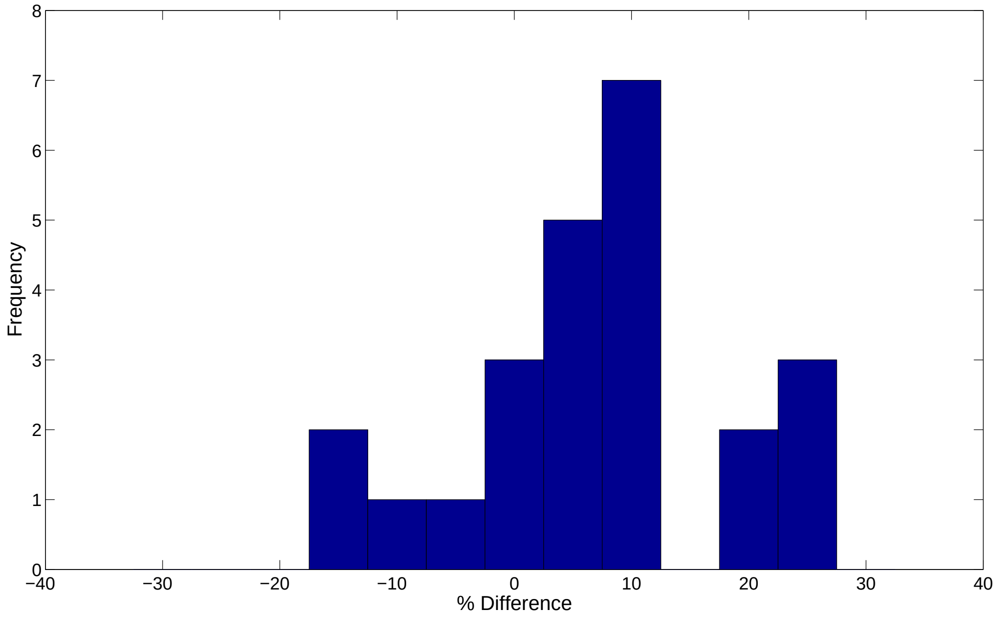

Figure 7.6: Histogram of the differences between NO_2 monthly mean partial columns: 100*2*(MART - TAO)/(MART + TAO).

difference.

7.2.3 Stratospheric O_3 Cross-Validation

The same temporal and spatial coincidence criteria were used for selecting OSIRIS O_3 measurements. This resulted in 904 spatially coincident OSIRIS observations and 651 TAO-FTS observations of O_3 between May 2002-December 2006. The data were sorted into monthly bins to facilitate monthly mean comparisons. Unlike NO_2, the distribution of temporal sampling within a month is not problematic, as the lifetime of O_3 at 30 km altitude is on the order of weeks to months at midlatitudes [Brasseur and Solomon, 2005]. Therefore, monthly mean values should be representative of the stratospheric O_3 concentration. However, to maintain consistency, the same minimum sample criterion of

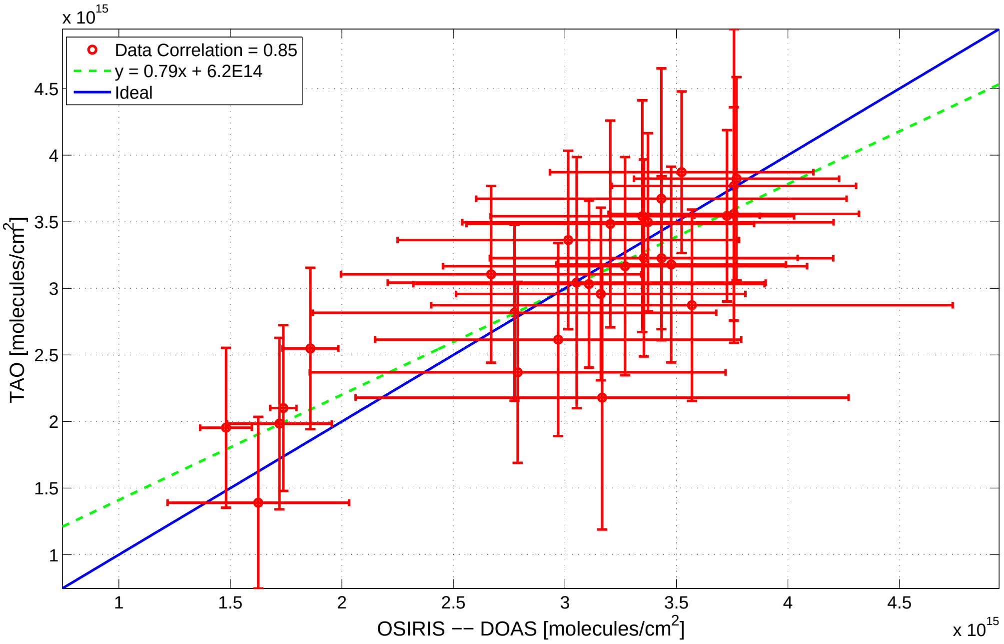

Figure 7.7: NO_2 monthly means derived from TAO-FTS observations plotted against monthly means derived from OSIRIS-DOAS retrievals. Error bars represent one standard deviation. The solid line shows the 1:1 line and the dashed line shows a weighted-least-squares linear fit to the data.

five measurements per instrument per month was implemented.

Figure 7.11 shows the complete timeseries of monthly mean O_3 partial columns produced by each of the three retrievals. With the exception of some obvious discrepancies at the beginning of 2003, most mean values agree to within 1σ. The relatively long lifetime of O_3 also acts to reduce the amount of scatter within a given month, resulting in smaller 1σ standard deviations than those of NO_2 (see Figure 7.4). Again, the apparent individual agreement for most months does not imply that there is a complete absence of bias between data sets.

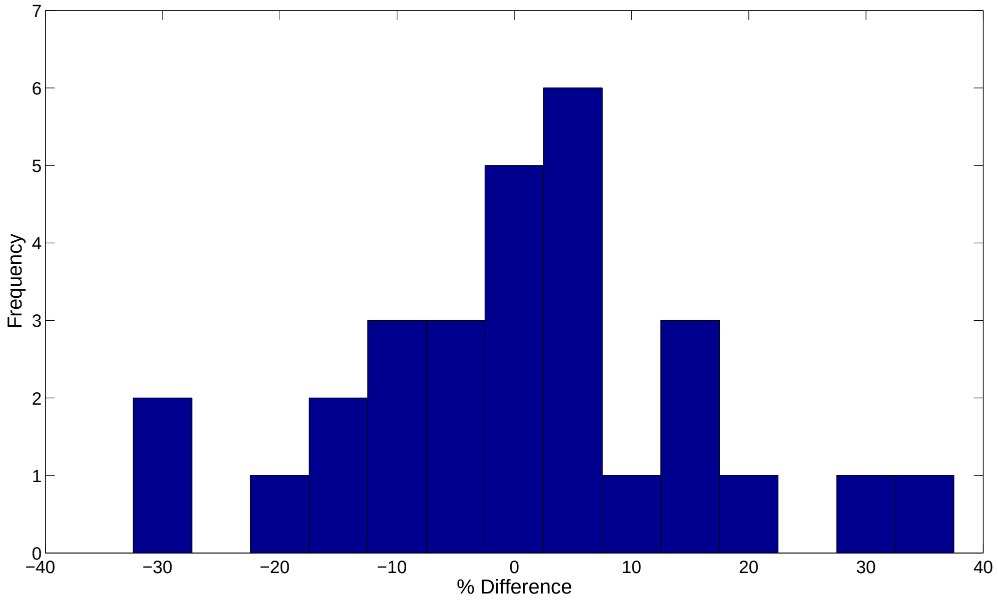

Figure 7.8: Histogram of the differences between NO_2 monthly mean partial columns: 100*2*(DOAS - TAO)/(DOAS + TAO).

The OSIRIS-MART O_3 retrievals are compared with the TAO-FTS O_3 data set in Figure 7.13. To minimize the errors arising from the differences in altitude sensitivity of the two observing systems, the OSIRIS profiles were smoothed with the TAO-FTS O_3 averaging kernels and integrated into partial columns from 16-50 km altitude (see Figure 7.12). The TAO retrievals show good correlations with the MART monthly means ($R^2 = 0.84$), however, the linear fit to the scatter-plotted data has a slope much less than 1 (0.55). This once again indicates that the MART retrievals have a relative multiplicative bias that results in generally capturing higher O_3 monthly mean values for months in which the concentration is higher, and the TAO-FTS retrievals show mainly higher values from months in which the O_3 concentration is lower. However, the histograms indicate that

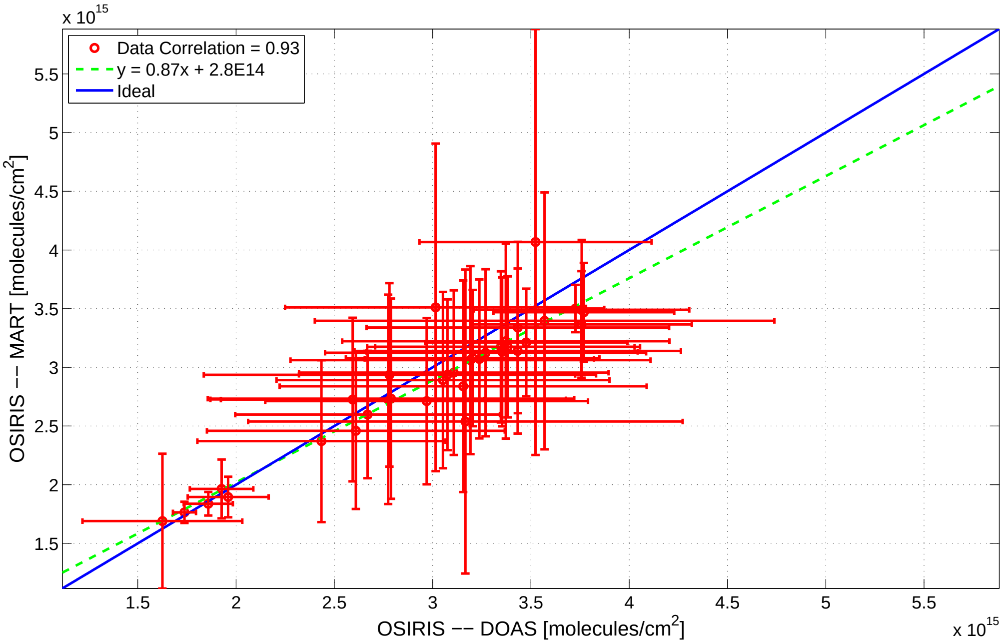

Figure 7.9: NO_2 monthly means derived from OSIRIS-MART observations plotted against monthly means derived from OSIRIS-DOAS retrievals. Error bars represent one standard deviation. The solid line shows the 1:1 line and the dashed line shows a weighted-least-squares linear fit to the data.

the systematic differences between the data sets are less conclusive. Comparing the TAO monthly means with those of the MART retrievals (Figure 7.14) shows that the MART data, in general, are skewed to retrieve 5% higher values. One difference is as large as 20%.

Making these same comparisons with the OSIRIS-Triplet retrievals shows slightly different results. Figure 7.15 shows the scatter plot between the TAO and OSIRIS-Triplet monthly means. Once again, the data show a strong correlation ($R^2 = 0.82$) and the slope of the linear fit is less than 1 (0.73). This suggests that the Triplet-based O_3 means have a multiplicative bias that is similar to that of the MART-based means (albeit not

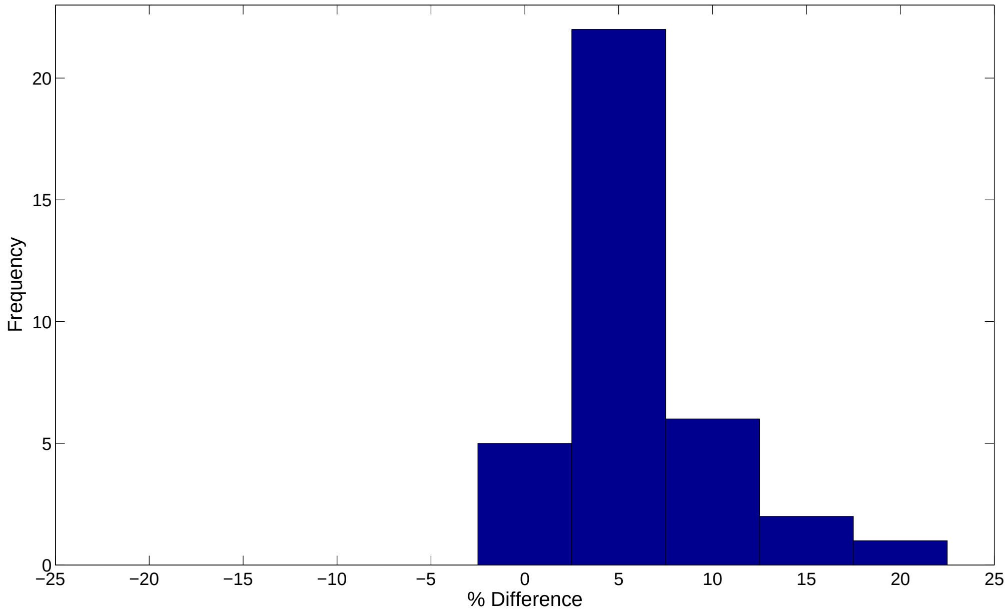

Figure 7.10: Histogram of the differences between NO_2 monthly mean partial columns: 100*2*(DOAS - MART)/(DOAS + MART).

as large). However, a systematic bias is not suggested by the histogram (Figure 7.16). The mean comparison shows a distribution of differences centred around 0% while there is a small number of outlying higher concentrations recorded by OSIRIS.

Comparing the two OSIRIS retrieval techniques also identifies a bias (Figures 7.17 and 7.18). There are both systematic biases and multiplicative biases that favour the MART-based retrieval. From the scatter plots shown in Figure 7.17, the slope of the linear fit is 1.3, illustrating a clear multiplicative bias of higher monthly means from the MART data. These same data values are systematically 5% greater than those derived from the Triplet-based retrieval. A similar systematic bias of 5% was seen between the two OSIRIS NO_2 retrievals.

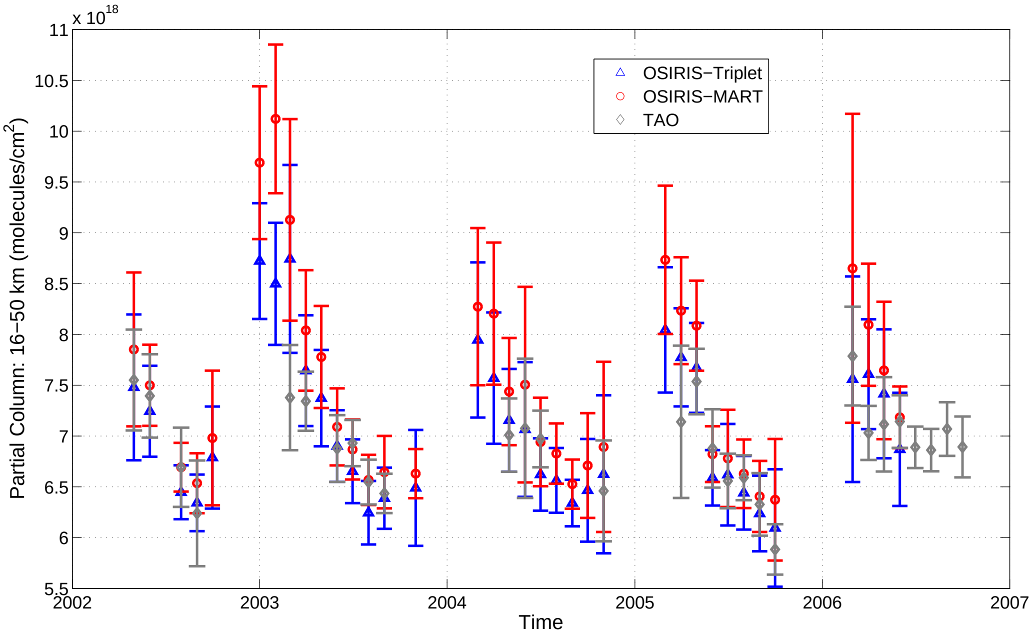

Figure 7.11: Timeseries of monthly mean O_3 partial columns for each month in which there are more than five measurements. Blue triangles represent the DOAS-based retrievals from OSIRIS, red circles represent the MART-based retrievals from OSIRIS, and gray squares represent the values derived from the TAO-FTS. Error bars show one standard deviation.

Previous comparisons of ground-based O_3 measurements by infrared FTSs with those of the UV-visible SCIAMACHY instrument on ENVISAT have been shown to disagree significantly in the stratosphere, with the FTS values consistently lower than those of the satellite [Palm et al., 2005]. For both OSIRIS retrievals, all O_3 cross-sections were taken from Bogumil et al. [2003], while the HITRAN 2004 infrared line parameters were based on original work by Mikhailenko et al. [2002] and de Backer-Barilly et al. [2003]. Validation of the ACE-FTS (v1.0) satellite instrument has included comparisons of O_3

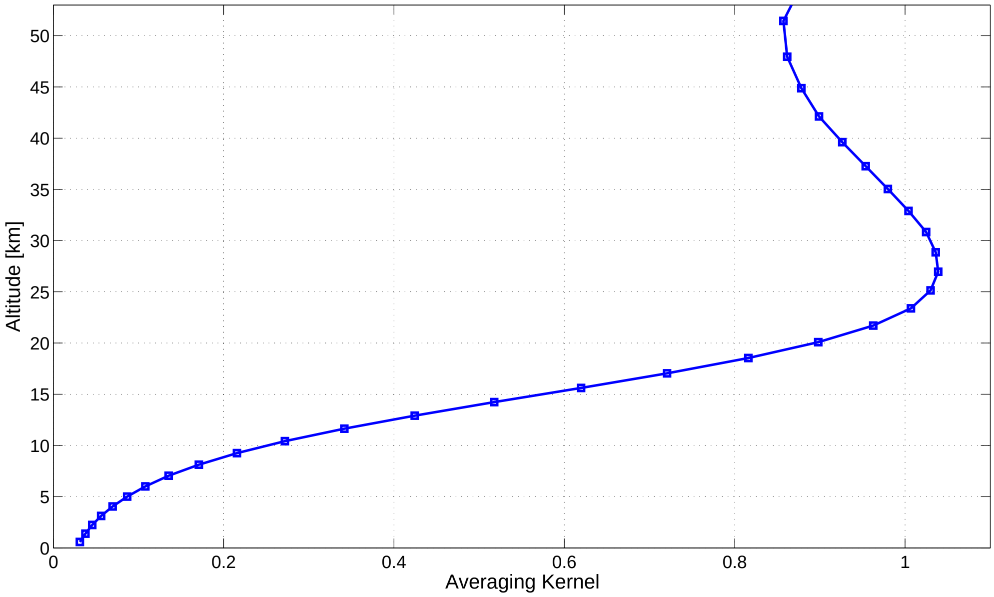

Figure 7.12: O_3 partial column averaging kernel for the TAO-FTS. This represents the altitude sensitivity of the measurement to atmospheric volume mixing ratios between 16-50 km.

profiles derived from infrared measurements with profiles from OSIRIS retrieved using the previous version of the Triplet algorithm [Petelina et al., 2005]. This comparison showed that OSIRIS retrieved values that were as much as +30% greater than those of ACE at some altitudes. Previous UV-visible satellite comparisons have also shown that OSIRIS regularly underestimates O_3 above 40 km [von Savigny et al., 2005]. The MART comparisons do not seem to replicate this underestimation at higher altitudes (possibly due to the inclusion of the Huggins band in the retrieval algorithm). Although integration into partial columns should reduce differences arising from altitude sensitivity, the TAO comparisons appear to be consistent with these previously identified differences.

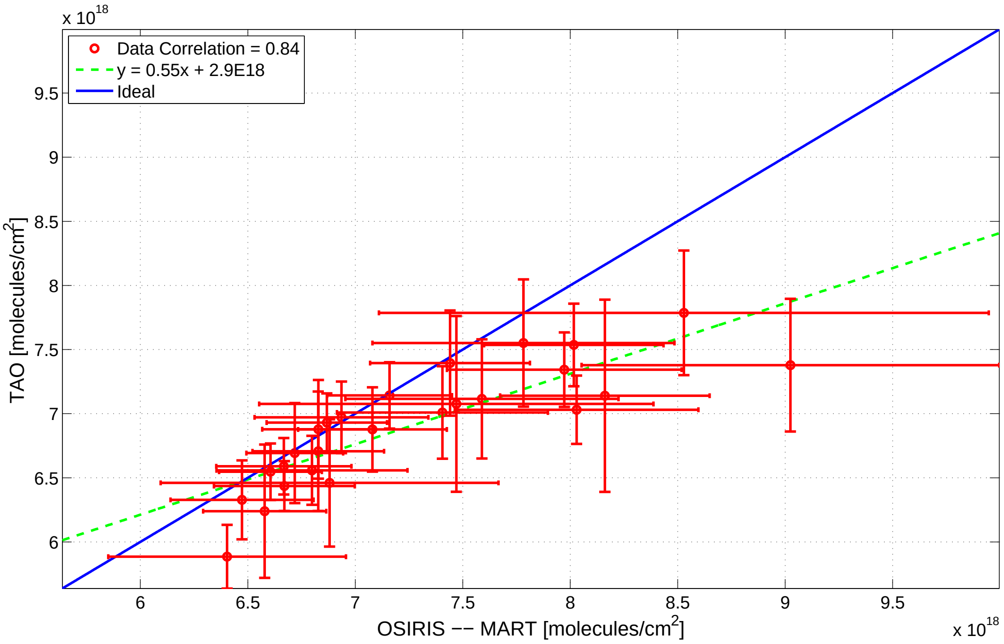

Figure 7.13: O_3 monthly means derived from TAO-FTS observations plotted against monthly means derived from OSIRIS-MART retrievals. Error bars represent one standard deviation. The solid line shows the 1:1 line and the dashed line shows a weighted-least-squares linear fit to the data.

7.2.4 Summary of TAO-OSIRIS Comparisons

Stratospheric NO_2 and O_3 columns measured by OSIRIS from May 2002 to December 2006 were compared with measurements by the TAO-FTS. NO_2 profiles were retrieved from OSIRIS UV-visible limb-scatter measurements using both DOAS and MART retrieval algorithms. OSIRIS O_3 profiles were derived from the MART algorithm as well as with the Triplet retrieval method. The TAO-FTS partial columns were retrieved with the SFIT2 optimal estimation algorithm. All coincidences were confined to be within 700 km of the TAO-FTS, with measurements sorted into monthly bins to derive mean partial column concentrations from 16-50 km. The results are summarized in Table 7.3.

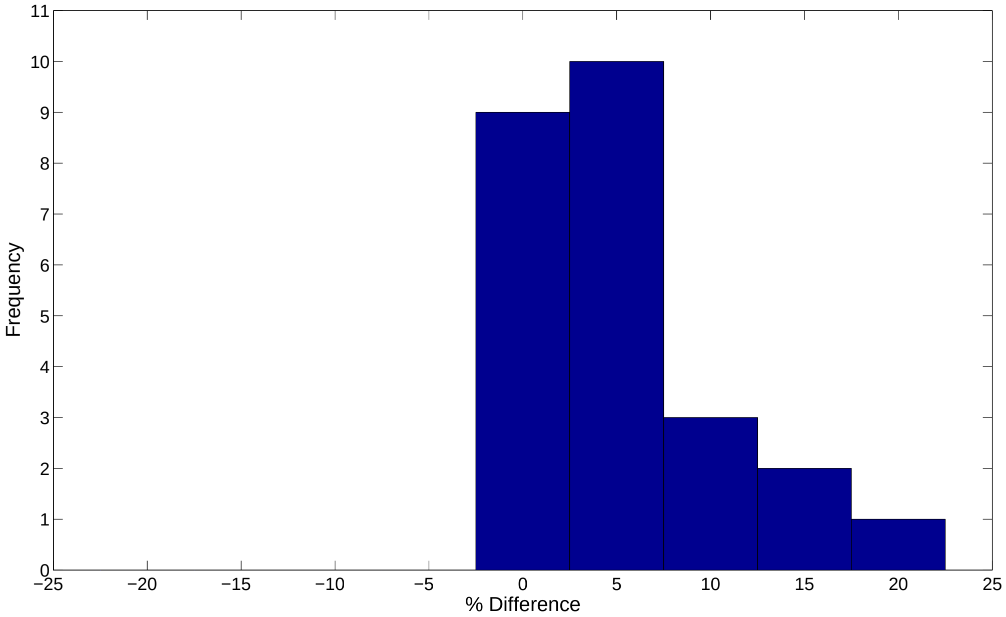

Figure 7.14: Histogram of the differences between O_3 monthly mean partial columns: 100*2*(MART - TAO)/(MART + TAO).

The NO_2 comparisons used coincident data spanning 59 months (see Figure 7.2 for details). All three comparisons showed a high degree of correlation, with R^2 values ranging from 0.85 to 0.93 and had a mean difference that ranged from +3.1% for OSIRIS-MART vs. TAO down to +0.1% for OSIRIS-DOAS vs. TAO. The standard deviations of these differences were less than 6.0%. Of the two OSIRIS retrievals, the DOAS retreival showed a systematic bias of +5% relative to the MART retrieval. The agreement between OSIRIS-MART and TAO and OSIRIS-DOAS and TAO are as good as or better than previous NO_2 column comparisons between infrared and UV-visible instruments.

The O_3 coincident comparisons spanned 58 months and also displayed well-correlated

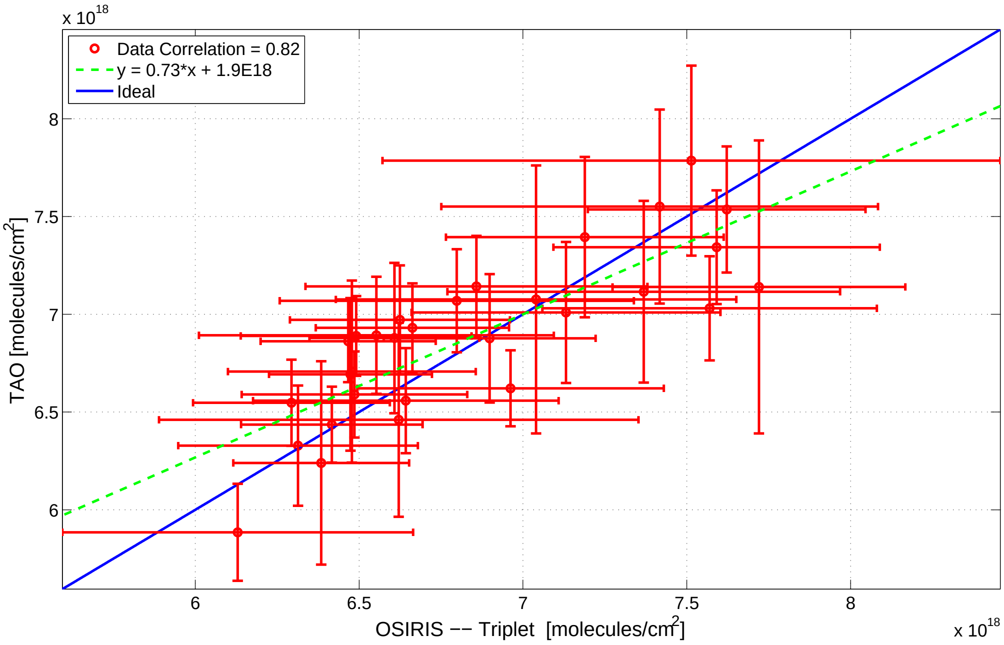

Figure 7.15: O_3 monthly means derived from TAO-FTS observations plotted against monthly means derived from OSIRIS-Triplet retrievals. Error bars represent one standard deviation. The solid line shows the 1:1 line and the dashed line shows a weighted-least-squares linear fit to the data.

monthly means (R^2 = 0.82-0.97). The mean differences were +2.5%, -0.3%, and -2.6% for MART−TAO, Triplet−TAO, and Triplet−MART, respectively, with standard deviations all less than 2.8%. The apparent high bias for the OSIRIS-MART values may be generated by the higher altitude sensitivity caused by the inclusion of the Huggins band in the MART retrievals. There were definite multiplicative biases between the data sets; results from both OSIRIS algorithms indicated a multiplicative bias relative to TAO with the OSIRIS-MART results exhibiting a multiplicative bias over the OSIRIS-Triplet results.

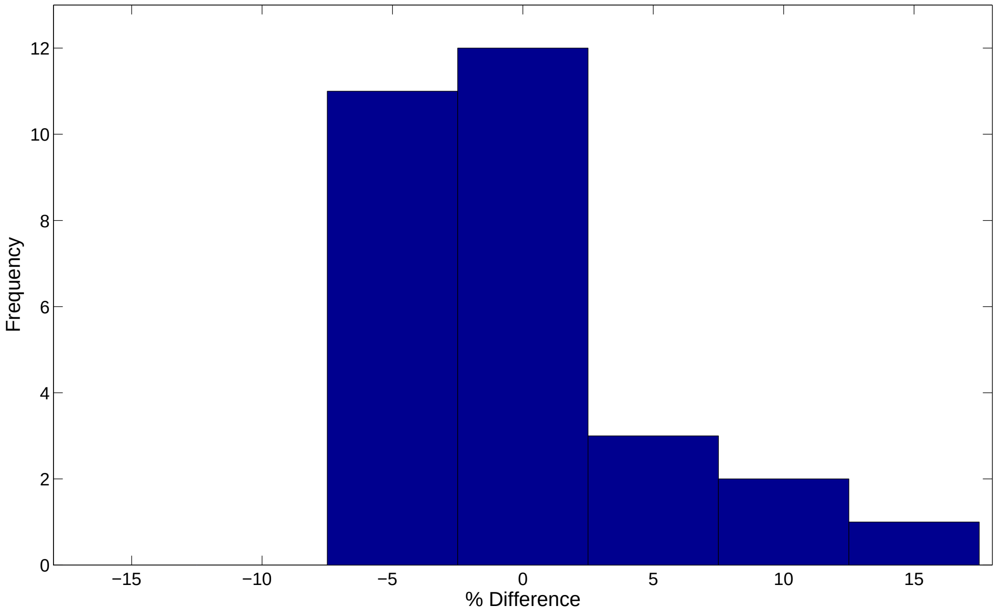

Figure 7.16: Histogram of the differences between O_3 monthly mean partial columns: 100*2*(Trip. - TAO)/(Trip. + TAO).

These two latest versions of OSIRIS retrievals for both O_3 and NO_2 have been shown to agree well with observations from a ground-based Fourier transform spectrometer in Toronto. The OSIRIS observations provide global coverage and are of value for the continued monitoring of stratospheric O_3 chemistry.

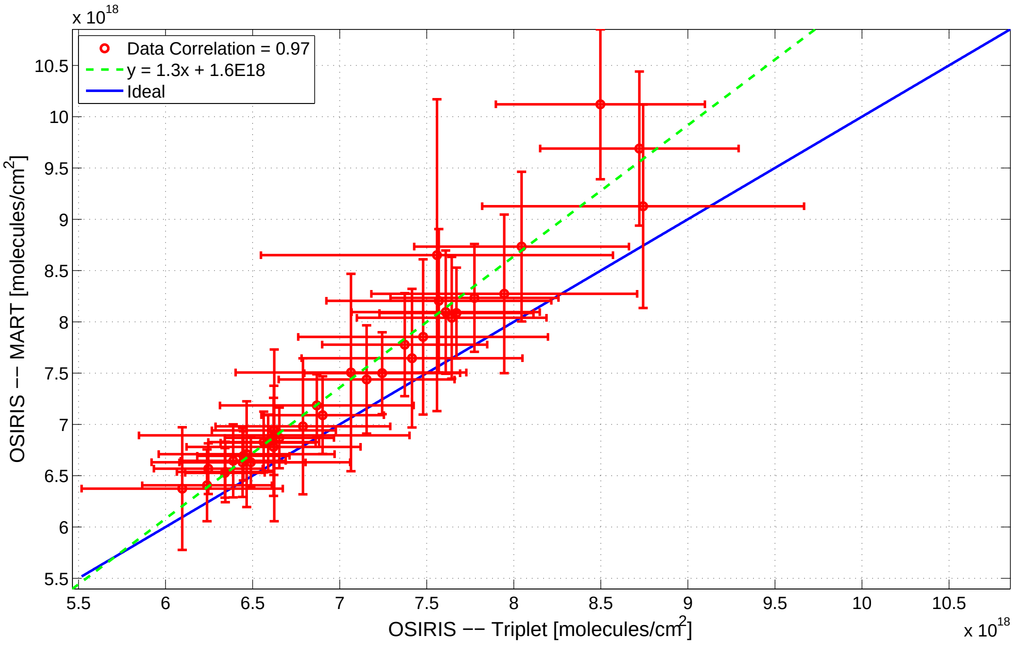

Figure 7.17: O_3 monthly means derived from OSIRIS-Triplet observations plotted against monthly means derived from OSIRIS-MART retrievals. Error bars represent one standard deviation. The solid line shows the 1:1 line and the dashed line shows a weighted-least-squares linear fit to the data.

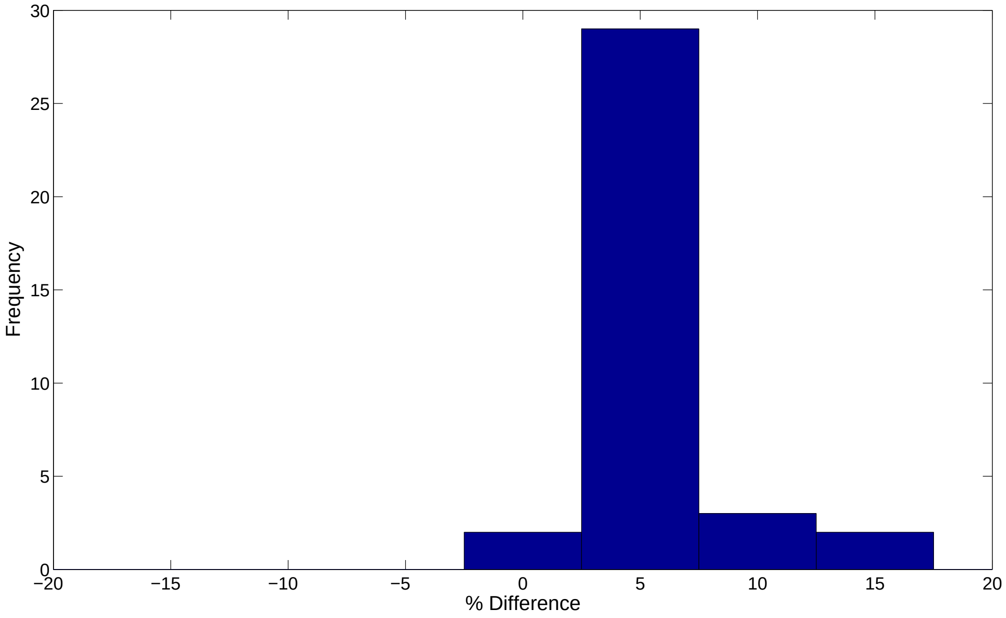

Figure 7.18: Histogram of the differences between O_3 monthly mean partial columns: 100*2*(Triplet - MART)/(Triplet + MART).

Table 7.3: Statistics of OSIRIS−TAO monthly mean column amounts. The comparison denoted in the first column gives the two retrieval methods being compared (the first minus the second). The second column gives the number of months compared: n. The third column gives the calculated correlation coefficient: R^2. The fourth column gives the mean percent difference in monthly mean columns: $\overline{\delta}$. The fifth column gives the standard deviation of the mean percent difference in monthly mean columns: σ_δ. The sixth column gives the calculated slope of the linear weighted-least-squares fit to the scatter plots of the first retrieval versus the second retrieval. The seventh column gives the value of the strongest statistical mode present in the histogram of the percent differences.

Comparison	n	R^2	$\overline{\delta}$ (%)	σ_δ (%)	slope	mode (%)
NO_2 (MART−TAO)	22	0.89	+3.1	1.7	0.92	+10
NO_2 (DOAS−TAO)	29	0.85	+0.1	6.0	0.79	+5
NO_2 (DOAS−MART)	36	0.93	+1.9	3.6	0.87	+5
O_3 (MART−TAO)	25	0.84	+2.5	2.8	0.55	+5
O_3 (Trip.−TAO)	29	0.82	-0.3	2.0	0.73	0
O_3 (Trip.−MART)	36	0.97	-2.6	2.0	1.3	+5

Chapter 8

Model-Based Validation

Because measurements of many tropospheric gases, particularly NMVOCs, are so limited, the option that provides the best opportunity for comprehensive tropospheric cross-validation of TAO data is atmospheric modelling. For this reason, measurements of two important tropospheric trace gases made by the TAO-FTS were compared with fields simulated by the GEOS-Chem Chemical Transport Model (CTM). The two compounds compared were CO, an important criteria pollutant and ground-level ozone precursor (see Section 2.3), and ethane (C_2H_6), an anthropogenically produced NMVOC that is not regularly monitored but is expected to increase considerably in the next 50 years (see Table 2.1).

Timeseries of CO and C_2H_6 have been previously reported by NDACC sites in New Zealand [Rinsland et al., 1998], the United States [Rinsland et al., 1999], Switzerland [Rinsland et al., 2000], Australia [Rinsland et al., 2001], Japan [Zhao et al., 2002], the Atlantic Ocean [Velazco et al., 2005], and in the European FTS UFTIR network (Time-series of Upper Free Troposphere Observations from a European Ground-based FTIR Network) [Gardiner et al., 2007]. As many of these sites have been operating for over 10 years, their data can provide insight into the trends associated with these tropospheric species. The results reported in the studies undertaken at these locations do not support consistent global conclusions about trends, but it is suggested that concentrations of tropospheric CO and C_2H_6 may be decreasing in the midlatitude northern hemisphere [Gardiner et al., 2007] (see Figures 8.1 and 8.2) with no significant long-term changes seen elsewhere [Rinsland et al., 2002b]. As the TAO-FTS is a relatively new site, there is not yet enough data to conduct such a trend analysis. As such, the work shown here is a preliminary comparison of one year of measurements with model data (2005). It should be noted that this validation study was designed to identify and understand potential sources of disagreement between the measurements and the model rather than address scientific concerns associated with changes in long-term concentrations.

Before comparisons are made between the model output and the TAO-FTS observations, it is useful to describe the current monitoring standards and air quality observation network near TAO.

8.1 Measurements of Pollutants in Toronto

In an attempt to address pollutant-related health concerns in Canada, the criteria pollutants defined by Health Canada (see Section 2.3) are regularly monitored and publicly disseminated by means of an Air Quality Index (AQI) and, more recently, an Air Quality Health Index (AQHI) [Ontario Ministry of the Environment, 2007]. The AQI represents the air quality based on the single highest concentration of the five criteria pollutants (O_3, NO_x, CO, SO_2, and PM). If the highest concentration is above a particular threshold, then the air quality is declared as *good*, *poor*, etc. This scheme is used because it is a rapid way to identify pollution events, as it is uncommon for any one pollutant to be elevated while the other four are not. Based on the AQI and the meteorological conditions, 2-day air quality forecasts and potential smog alerts are issued by the Province of

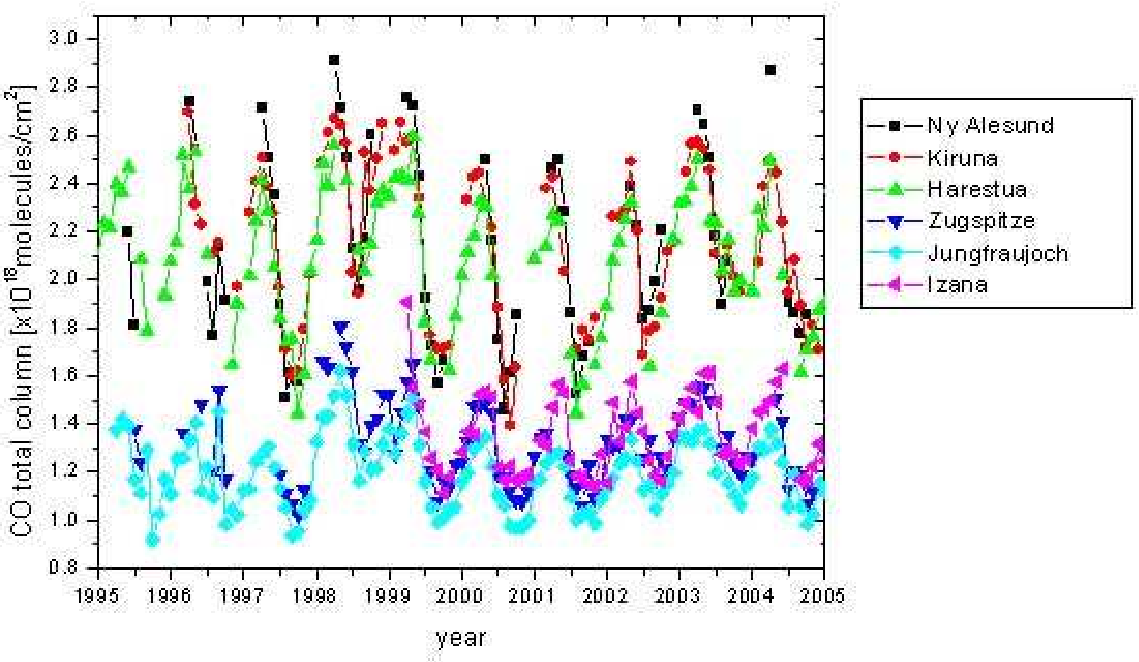

Figure 8.1: Timeseries of CO total columns measured by ground-based FTS sites in Europe. Measurements are shown from Ny Ålesund (black), Kiruna (red), Harestua (green), Zugspitze (blue), Jungfraujoch (cyan), and Izaña (pink), (courtesy of UFTIR group; Principal Investigator: M de Mazière; http://www.nilu.no/uftir/).

Ontario [Ontario Ministry of the Environment, 2007]. However, by using this threshold approach, the cumulative effects of having multiple elevated pollutants is not considered – the same warning is issued for a day in which there are elevated levels of only one pollutant as when there are elevated levels of all pollutants. These scenarios obviously have different health impacts and should be interpreted accordingly.

The Air Quality Health Index (AQHI) is a pilot program that is currently run in the City of Toronto, and in the Province of British Columbia [Ontario Ministry of the Environment, 2007]. The AQHI attempts to address the cumulative health effects of having

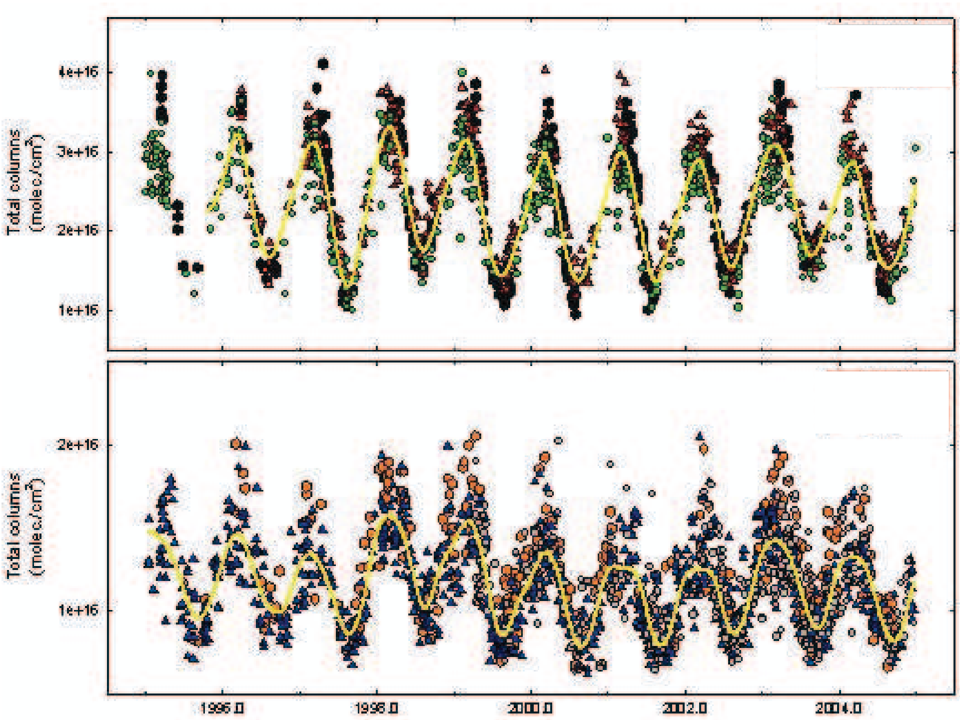

Figure 8.2: Top: Timeseries of C_2H_6 total columns observed by ground-based FTS sites in Europe. Top: measurements from Ny Ålesund (red circles), Kiruna (triangles), and Harestua (green circles). Bottom: measurements from Zugspitze (orange circles), Jungfraujoch (triangles), and Izaña (green circles), (courtesy of UFTIR group; Principal Investigator: M de Mazière; http://www.nilu.no/uftir/).

multiple pollutants elevated simultaneously. However, it does so only by incorporating observations of O_3, NO_2, and PM. Based on these three pollutants, a public announcement of *low health risk*, *high health risk*, etc. is issued.

Although these monitoring and public awareness programs are important initial steps toward understanding the magnitude of air quality problems in Toronto, they do not present a solution. Current municipal policies are directed at reducing "smog-causing pollutants" by 20% of 2004 levels [Toronto Environment Office, 2007]. This is an appreciable reduction target, however, smog-causing pollutants are only considered to be the aforementioned five species. Furthermore, the uncertainty associated with the effects of climate change causes air quality forecast model predictions to be limited and, therefore, inhibits the ability to adequately plan for future changes. In order to address these concerns, observations in Toronto of a suite of smog-causing pollutants must be considered in conjunction with models to develop a better understanding of how concentrations are changing and how the interdependence of their relationships is affected by these changes.

In the province of Ontario, concentrations of the five criteria pollutants (GLO, PM, NO_2, SO_2, and CO) are monitored at 38 different ground-level observation sites. Over the past 36 years of monitoring, concentrations of NO_2, CO, and SO_2 have all decreased, however, concentrations of GLO and PM still exceed ambient air quality reference levels [Ontario Ministry of the Environment, 2007]. From 2002-2006, Ontario smog advisories have been issued, on average, 27.2 days/year, with a maximum of 53 days in 2005.

Smog is primarily a suspended combination of GLO, CO, SO_2, and aerosols (such as PM) (see Section 2.3). The generation of these species requires the presence of other, precursor, gases, such as nitrogen oxides and VOCs. VOCs consist of many different carbonaceous compounds, of which CO, C_2H_6, CH_4, and hydrogen cyanide (HCN) are the most abundant indicators/precursors of pollution [Penkett et al., 2003]. As GLO is the primary component of smog (see Section 2.3), reducing the concentration of GLO should directly lower the number of smog events. To achieve this goal, the Canada Wide Standard for GLO was chosen to be 65 ppb over an 8-hour average by 2010 [Ontario Ministry of the Environment, 2004]. The average ground-level ozone concentration recorded in Toronto over 2004-2006 was 75 ppb [Ontario Ministry of the Environment, 2007].

One of the 38 monitoring sites is located in downtown Toronto, approximately 1 km from

TAO. Daily mean surface CO levels recorded at this location in 2005 are shown in Figure 8.3. There were 53 days in 2005 in which air quality advisories were issued (indicated by the black vertical lines in the figure). It may be seen that, on some of these days, there were definitely enhanced concentrations of CO which precipitated the advisory. However, there are other days on which advisories were issued where the surface CO concentrations were relatively low (*e.g.*, end of July). On these days, one or more of the other criteria pollutants must have exceeded the predetermined advisory levels. Of importance to note is that there are several days, particularly in the winter, where the surface CO concentrations were in the *extremely poor* range and yet no advisory was issued. This indicates that there is, potentially, a flaw in either the monitoring reporting system or the forecast model used to issue advisories. The observation capabilities of the TAO-FTS, combined with more powerful chemical transport models (such as GEOS-Chem), can help determine the current shortcomings of the Toronto air quality monitoring system.

This comparison will focus on TAO-FTS tropospheric partial columns of CO and C_2H_6. The retrieval parameters are summarized in Table 8.1. Both gases were retrieved from three spectral band passes that were simultaneously fitted to provide VMR altitude profiles. These profiles were then integrated into total and partial columns as needed. The mean total degrees of freedom for signal for the total column CO and C_2H_6 retrieved in 2005 were 3.1 and 2.6, respectively. This implies that, if desired, the retrieved CO profile can be integrated into three separate partial columns, while the C_2H_6 can be integrated into at least 2, on average.

8.2 GEOS-Chem Chemical Transport Model

The GEOS-Chem Model is a three-dimensional Chemical Transport Model (CTM) of global atmospheric composition driven by assimilated meteorological fields [Bey et al.,

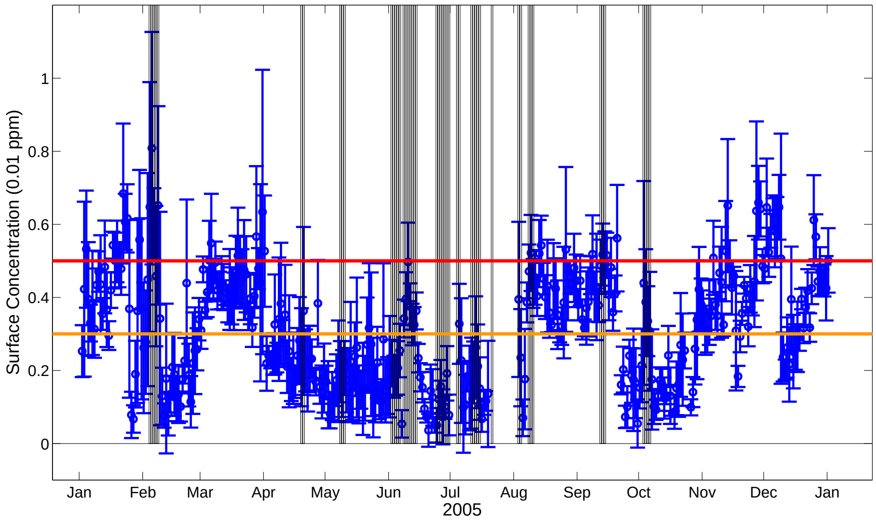

Figure 8.3: 2005 Daily mean surface CO concentrations observed by the Air Quality Ontario observing network site in downtown Toronto. Error bars represent 1 standard deviation, the orange line (30 ppm) represents the level above which CO concentrations are considered *poor*, the red line (50 ppm) represents the level above which CO concentrations are considered *extremely poor*, and the black vertical lines denote days upon which an air quality advisory was publicly issued. (Data obtained from `http://www.airqualityontario.ca/`).

2001]. The GEOS-4 (Goddard Earth Observing System version 4) assimilated fields are provided by NASA's Global Modelling Assimilation Office (GMAO). Emissions of pollutants, such as CO and C_2H_6, are specified in the model with emission inventories. In this version of the model, C_2H_6 emissions are based on the work of Xiao et al. [2004] which estimate a global inventory of ≈13.5 Tg/yr. Ethane emissions in the continental US are distributed according to the Environmental Protection Agency's National Emissions Inventory (EPA NEI-99) and are ≈2.2 Tg/yr, a factor of 3.5 higher than the assumed estimate of 0.6 Tg/yr [United States Department of Energy, 2005]. Global CO anthro-

Table 8.1: Spectral microwindows used for the retrieval of C_2H_6 and CO, as well as interfering species that were fitted simultaneously, the mean SNR, and mean total column degrees of freedom for signal (d_s). Both species were retrieved by globally fitting multiple bandpasses.

Target Gas	Microwindow(s) (cm^{-1})	Interfering Gases	2005 Mean SNR	2005 Mean Total d_s
C_2H_6	2976.60-2977.10	H_2O, CH_4, O_3, H_2CO	240	2.6
	2996.70-2997.10	H_2O, CH_4, O_3, H_2CO		
	3000.10-3000.60	H_2O, CH_4, O_3, H_2CO		
CO	2057.68-2058.00	O_3, CO_2, OCS	200	3.1
	2069.56-2069.76	O_3, CO_2, OCS		
	2157.51-2159.14	O_3, N_2O, H_2O		

pogenic emissions budgets are described by Duncan et al. [2007] and contain source values of ≈1000 Tg distributed about the US according to EPA NEI-99.

All results shown here were generated by the GEOS-Chem version 7-02-04 model. The horizontal resolution is 4° latitude by 5° longitude over the entire globe, with the data being taken from the grid box that encompasses Toronto (40-44°N by 77.5-82.5°W). The data are reported on a 30-vertical-layer grid with 12 layers below 10 km and 5 layers below 2 km altitude. All chemical fields are reported for each grid box every six hours. The simulation is spun up for 12 months to effectively remove the initial chemical climatology conditions.

It is important to note that GEOS-Chem is a global chemical transport model and, therefore, does not have the spatial resolution necessary for an air quality forecast model.

Figure 8.4 shows how the same surface observations of CO in 2005 from Figure 8.3 compare with the GEOS-Chem output for the Toronto-area grid box. It can be seen that some of the CO elevations are qualitatively well correlated (such as in Jan-Feb and Nov-Dec) but, overall, the magnitudes are poorly estimated and there are observed enhancements that are not captured by the model. This is almost certainly due to the fact that GEOS-Chem is a global model that represents average values of species over large regions; it is unlikely that the model will be able to simulate the CO concentrations that are localized to the boundary layer in downtown Toronto. For this reason, it is not beneficial to compare surface observations with GEOS-Chem estimates.

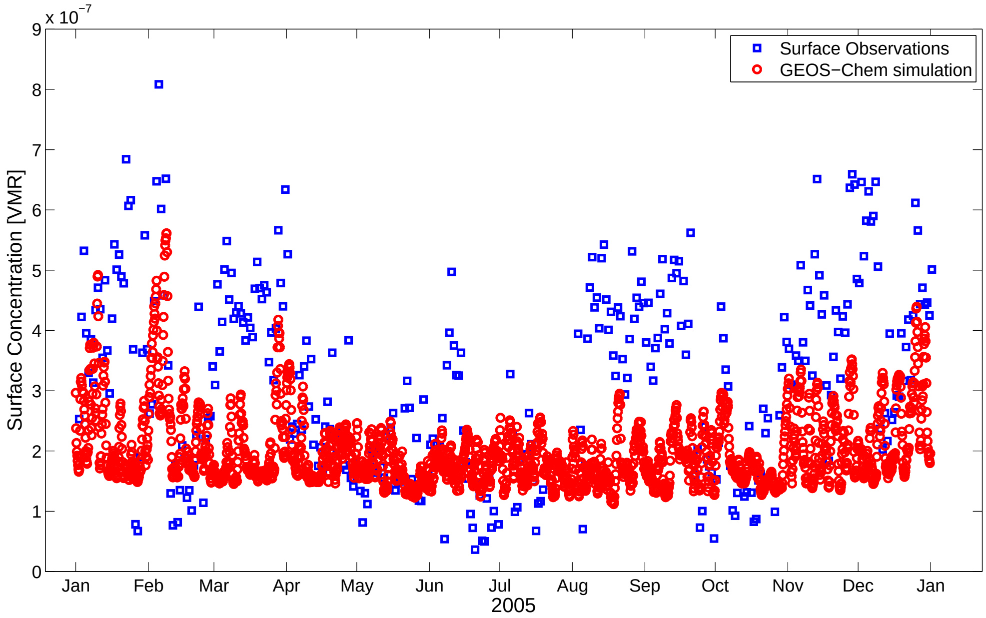

Figure 8.4: Daily mean surface CO concentrations observed by the Air Quality Ontario monitoring network site in downtown Toronto in 2005 (blue squares) compared with like daily means generated by GEOS-Chem (red circles). The GEOS-Chem values are from the lowest layer output for the grid-box encompassing Toronto (974.07 hPa).

8.3 Tropospheric C_2H_6 Cross-Validation

Although the coarse horizontal resolution of GEOS-Chem promotes some smearing of trace gas concentrations, it does have well-resolved vertical resolution, which provides profile information into the boundary layer. Even though measurements by the TAO-FTS occur with changing solar zenith angle and rely upon integration over altitude profiles, the location of TAO ensures that there is limited horizontal smearing over the course of the 20-minute measurement time. Figures 8.5 and 8.6 show the extent of horizontal smearing that occurs at different altitudes: for the tropospheric values, it can be seen that this is very small. However, the TAO-FTS tropospheric retrievals do not contain the same level of vertical sensitivity as GEOS-Chem, therefore it is necessary to smooth the GEOS-Chem profiles with the TAO averaging kernels in the same fashion as was used in Section 7.2.2. That is, Equation 5.10 is used, but here $\mathbf{x}$ is the GEOS-Chem output profile and $\hat{\mathbf{x}}$ is the smoothed GEOS-Chem profile. For details of this technique, refer to Rodgers and Connor [2003]. Figure 8.7 shows a sample C_2H_6 profile over Toronto output from the GEOS-Chem model and the resulting profile that is generated by smoothing with the TAO-FTS C_2H_6 *a priori* profile and averaging kernel. The complete ensemble of all C_2H_6 profiles generated by GEOS-Chem and smoothed are shown in Figure 8.8. It can be seen that the smoothing causes a slight decrease in the low altitude sensitivity of the model but, overall, the profiles are not significantly different ($\approx 1\%$ on average in the 3-12 km partial column).

As was seen in Figure 8.4, the model's ability to capture localized boundary layer enhancements is limited. So, even though the smoothed model profiles indicate that there is some low altitude sensitivity, any local enhancement that is captured by the TAO observations is unlikely to be properly represented in the model. To avoid this problem, tropospheric partial columns were integrated between 3 and 12 km altitude. The mean total degrees of freedom for signal of TAO C_2H_6 columns retrieved in this altitude range

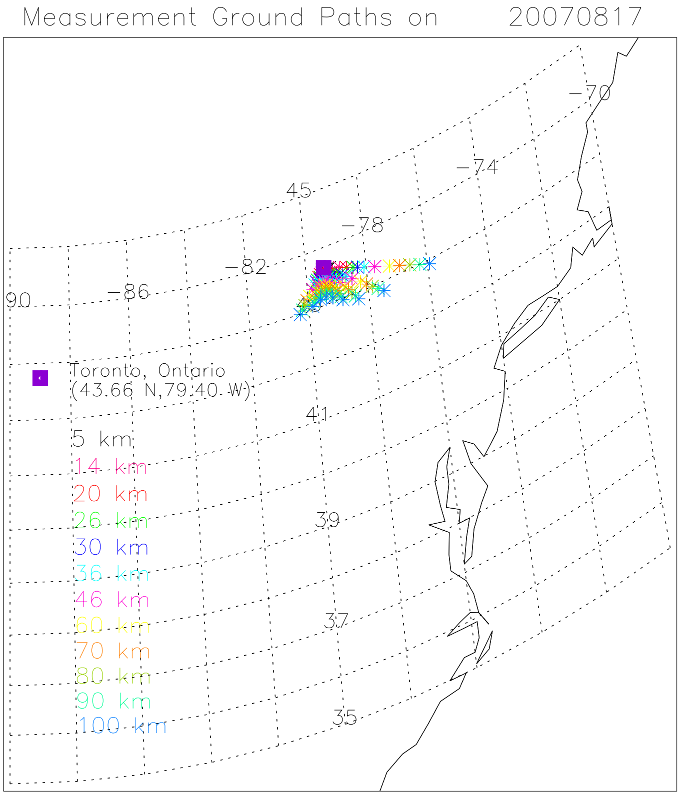

Figure 8.5: Typical horizontal measurement smearing that occurs during an observation in the summer by the TAO-FTS. Differing colours represent different altitudes along the line-of-sight during a 20-minute observation. This example was calculated for 17 August 2007 using geometric assumptions. (Figure courtesy of F. Kolonjari).

is 2.4. The same quality control techniques that were applied to retrieved quantities archived with the NDACC were applied here (see Section 5.5). The complete time series of measured 3-12 km partial column C_2H_6 is shown in Figure 8.9.

It can be seen from the TAO-FTS tropospheric columns that there is a pronounced seasonal cycle linked to the calendar year. Because removal of C_2H_6 from the troposphere is primarily due to reaction with OH radicals, the average global C_2H_6 lifetime is approximately two months [Rudolph and Ehhalt, 1981]. Although it is released at the surface,

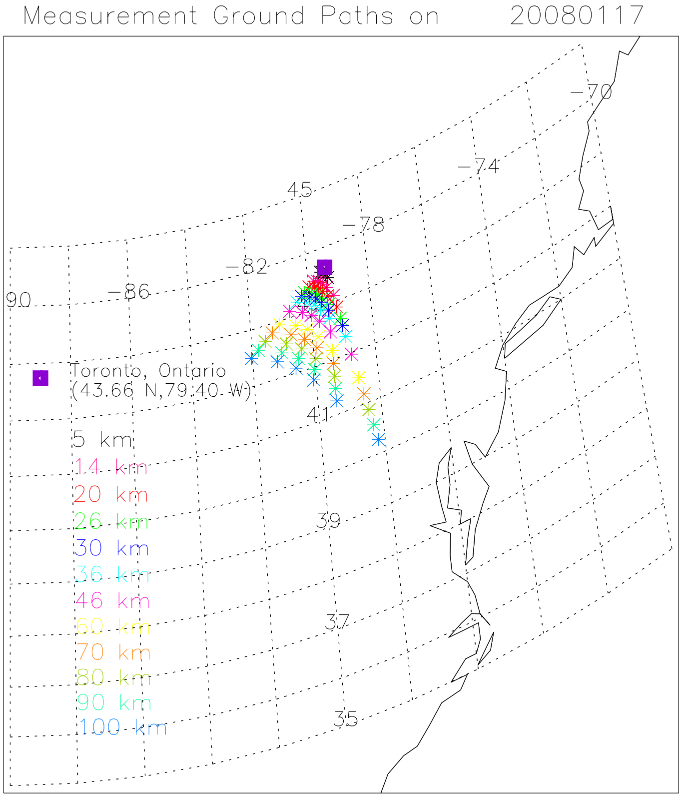

Figure 8.6: Same as Figure 8.5 but representative of winter observing conditions. This example was calculated for 17 January 2008 using geometric assumptions. (Figure courtesy of F. Kolonjari).

principally by natural gas leaks in the northern hemisphere and biomass burning in the tropics [Rudolph, 1995], variations in these sources are not normally strong enough to perturb this seasonal cycle.

Daily mean tropospheric columns of C_2H_6 retrieved from the TAO-FTS and output from GEOS-Chem in 2005 are shown in Figure 8.10. From the figure, it may be seen that the data have significant differences. During late summer/early fall, C_2H_6 levels are at their seasonal minimum and the agreement between the two data sets is best. However, during the springtime seasonal maximum, GEOS-Chem appears to have columns that are ele-

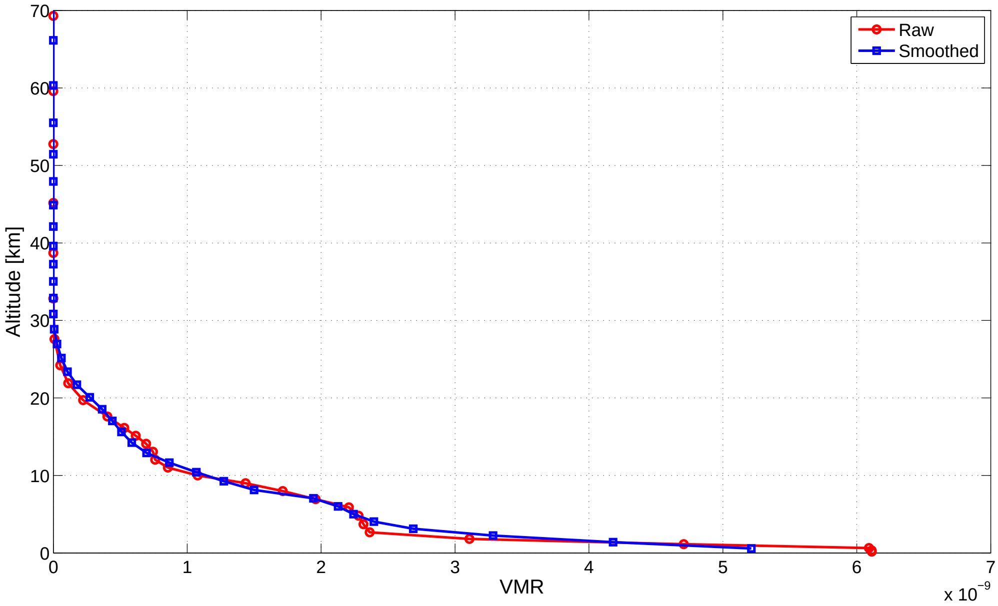

Figure 8.7: Sample C_2H_6 profile over Toronto generated by the GEOS-Chem model (red) and the same C_2H_6 profile smoothed with the TAO-FTS averaging kernel and *a priori* profile (blue). VMR is expressed in parts per volume.

vated by ≈ 30% over those of the TAO-FTS. It is possible that this is merely a sampling artefact and the limited number of TAO-FTS observations near the seasonal maximum does not adequately capture the expected elevation. The other possibility is that the apparent high bias of the model is a systematic feature that is due to mis-representation of the atmosphere over Toronto. Before this question can be adequately answered, it is necessary to compare the CO data.

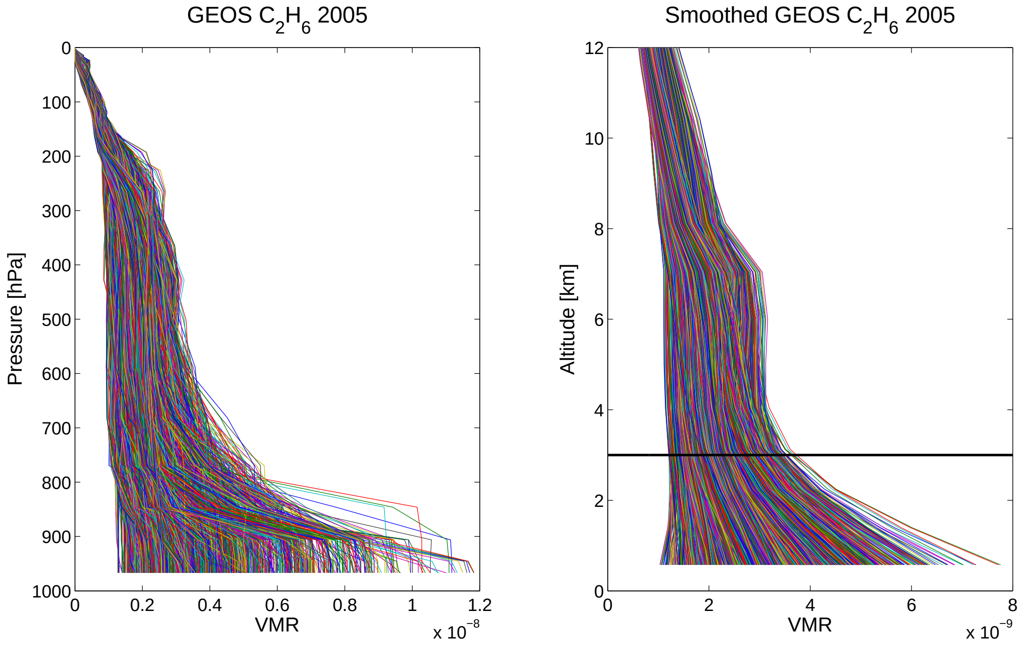

Figure 8.8: All C_2H_6 profiles over Toronto generated by the GEOS-Chem model in 2005. The raw profiles output from the model are shown on the left panel, while the right panel shows the same profiles after smoothing with the TAO-FTS averaging kernel and *a priori* profile. The black, horizontal line at 3-km altitude represents the lower boundary of the partial column calculation. VMR is expressed in parts per volume.

8.4 Tropospheric CO Cross-Validation

Similarly to C_2H_6, CO is produced primarily though biomass burning, fossil fuel combustion, and oxidation of other hydrocarbons [Logan et al., 1981]. It also has OH as a primary sink and, consequently, has a similar lifetime of approximately two months [Crutzen and Zimmermann, 1991]. However, there is a slight difference in the seasonal cycle of CO because there can be significant contributions from both local and long-range-transported CO plumes. As a result, the seasonal cycle can be perturbed by these enhancements.

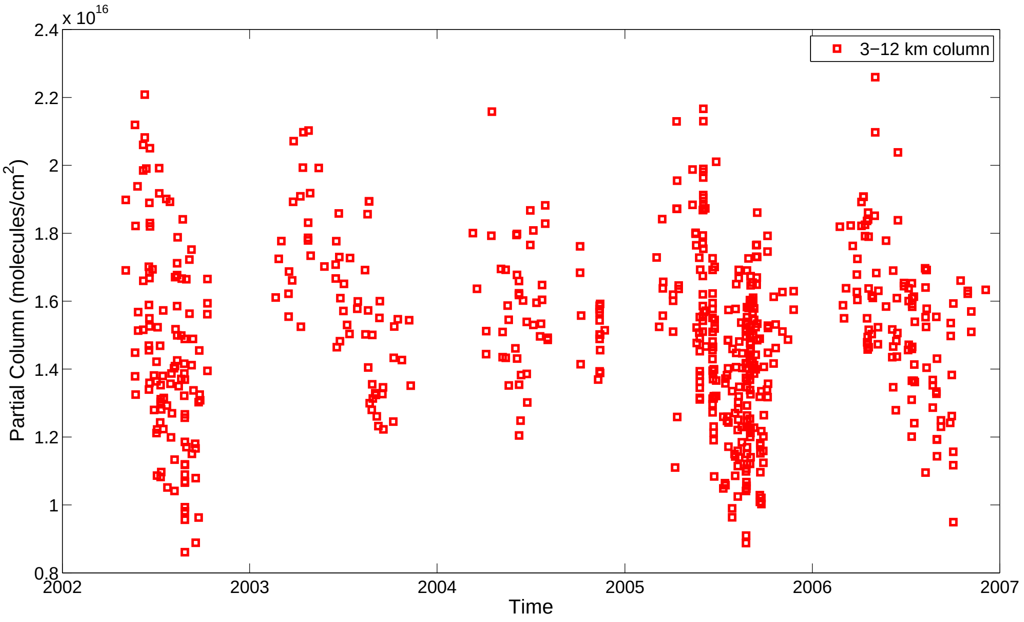

Figure 8.9: Timeseries of C_2H_6 3-12 km partial column retrievals from the TAO-FTS. The median partial column error is $\approx$ 1.3% and is composed of state space parameter interference error and retrieval noise added together in quadrature. For clarity, the error bars are not shown.

As with C_2H_6, all CO VMR profiles generated by GEOS-Chem were smoothed with the TAO-FTS averaging kernels and *a priori* profile. Figure 8.11 shows all of the GEOS-Chem CO profiles before and after smoothing. An example profile before and after smoothing is shown in Figure 8.12. The smoothing process significantly reduces the amount of information in the profile at low altitudes, but for the 3-12 km range over which the partial column is calculated, the differences are not significant ($<$ 5% for all cases). The mean total degrees of freedom for signal in this partial column was 3.0 and the standard quality control techniques used at TAO were applied to all of the data (see Section 5.5).

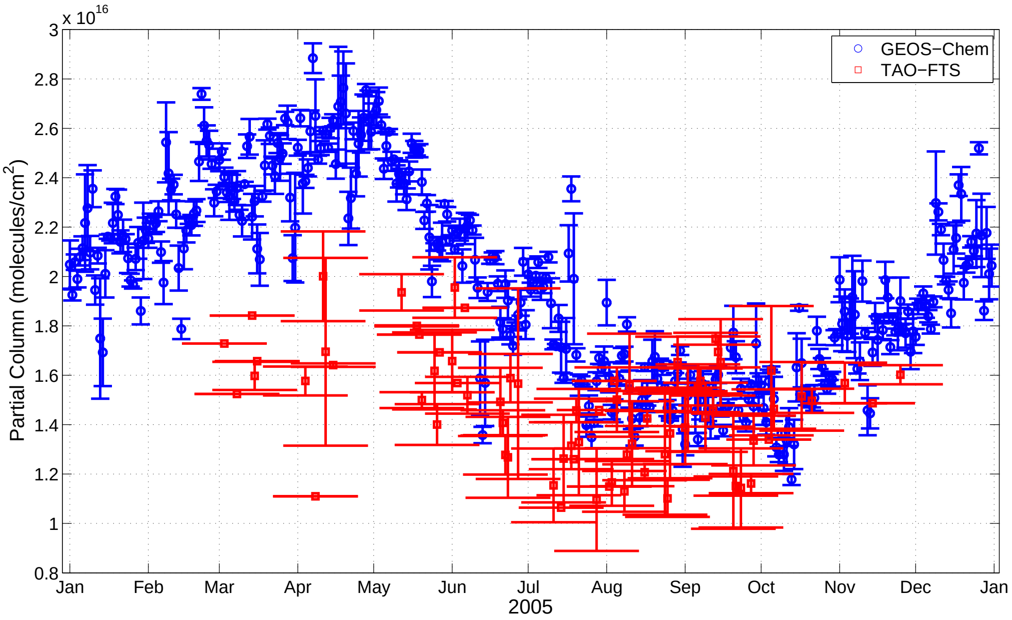

Figure 8.10: Timeseries of C_2H_6 3-12 km partial column daily means retrieved from the TAO-FTS (red) and the GEOS-Chem model (blue). Error bars represent 1 standard deviation (for the days upon which there is only one measurement, the error bars are set to 0).

Similarly to C_2H_6, CO exhibits a seasonal cycle over Toronto, with a springtime maximum and late summer/fall minimum (see Figure 8.13). It should be noted that since CO is retrieved from the region of the spectrum that is covered by Filter 2 measurements (see Table 4.1), the TAO-FTS CO data density is much less than that of C_2H_6. This also inhibits the ability to make direct daily mean comparisons with a significant number of measurements. Nonetheless, comparison with the GEOS-Chem model should provide insight into how well CO concentrations over Toronto are understood.

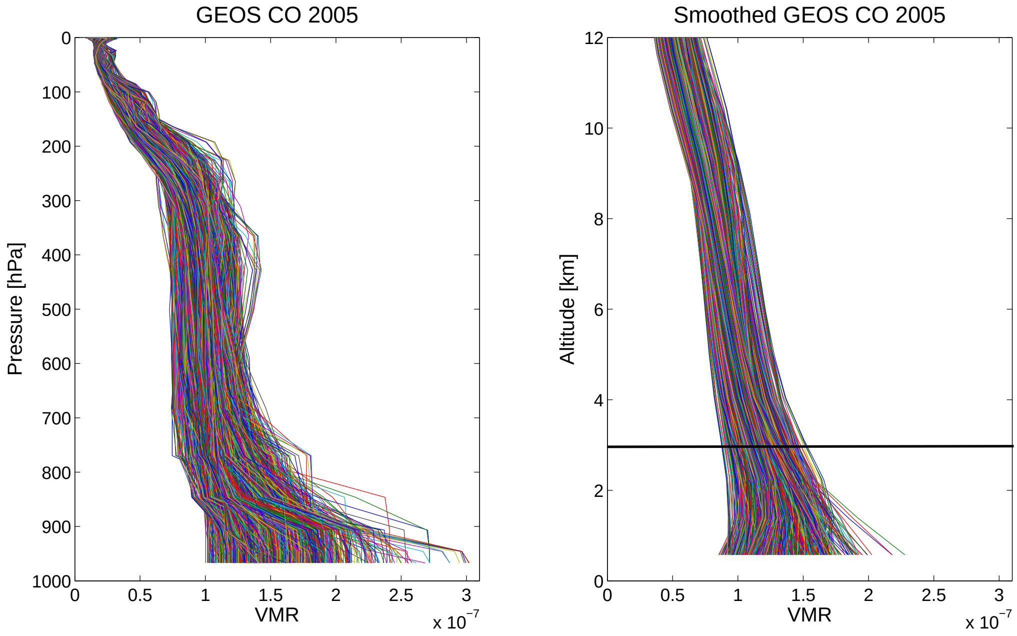

Figure 8.11: All CO profiles over Toronto generated by the GEOS-Chem model in 2005. The raw profiles output from the model are shown on the left, while the right shows the same profiles after smoothing with the TAO-FTS averaging kernel and *a priori* profile. The black, horizontal line at 3 km altitude represents the lower boundary of the partial column calculation. VMR is expressed in parts per volume.

Figure 8.14 shows the 3-12 km integrated partial columns of CO derived from TAO-FTS observations and GEOS-Chem simulations in 2005. The apparent GEOS-Chem column overestimation that was present in the C_2H_6 data is also present here. However, the CO tropospheric columns do not appear to agree as well as those of C_2H_6 during the seasonal minimum, rather, the CO columns exhibit a high bias of the GEOS-Chem data throughout the entire season. The agreement in the daily means again appears to be worse during the seasonal maximum, potentially indicating that the root cause of this discrepancy is the same for both species.

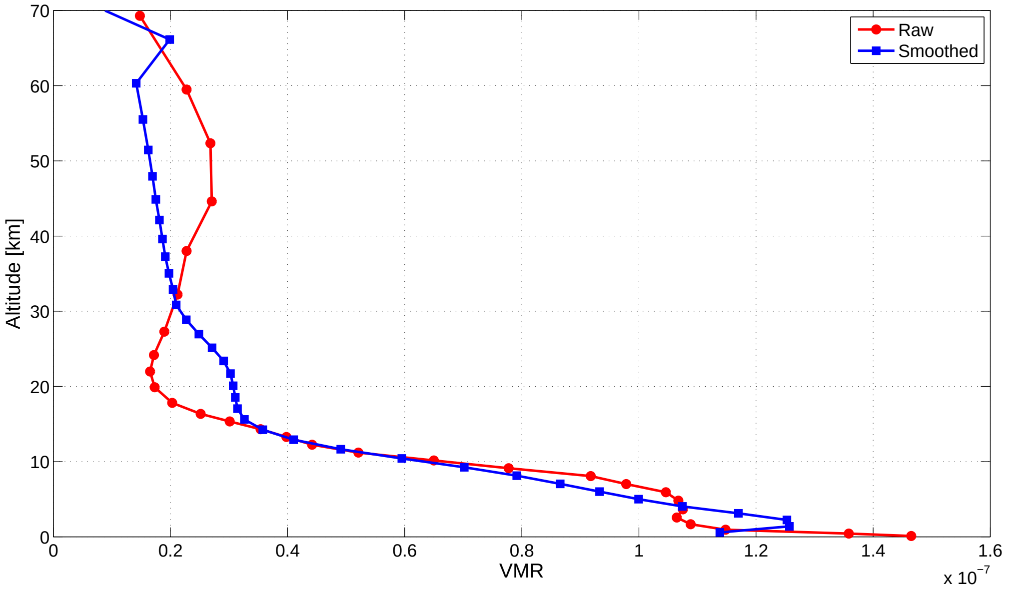

Figure 8.12: Sample CO profile over Toronto generated by the GEOS-Chem model (red) and the same CO profile smoothed with the TAO-FTS averaging kernel and *a priori* profile (blue). VMR is expressed in parts per volume.

Because the CO 3-12 km columns are sensitive to emissions, it is possible that the emission inventories prescribed in the model are overestimating the values observed by the TAO-FTS. There are four potential causes for this in the model: 1. Asian emissions are overestimated and there is an increase caused by transport of pollutants, 2. local North American emissions are overestimated and contributions from regionally local sources are forcing the columns to be higher in the model, 3. a combination of both of these effects, or 4. the concentrations of OH that control the CO chemistry in the model may be incorrect.

Recent work by Hudman et al. [2008] has compared the GEOS-Chem CO fields with North American observations from the ICARTT (International Consortium for Atmo-

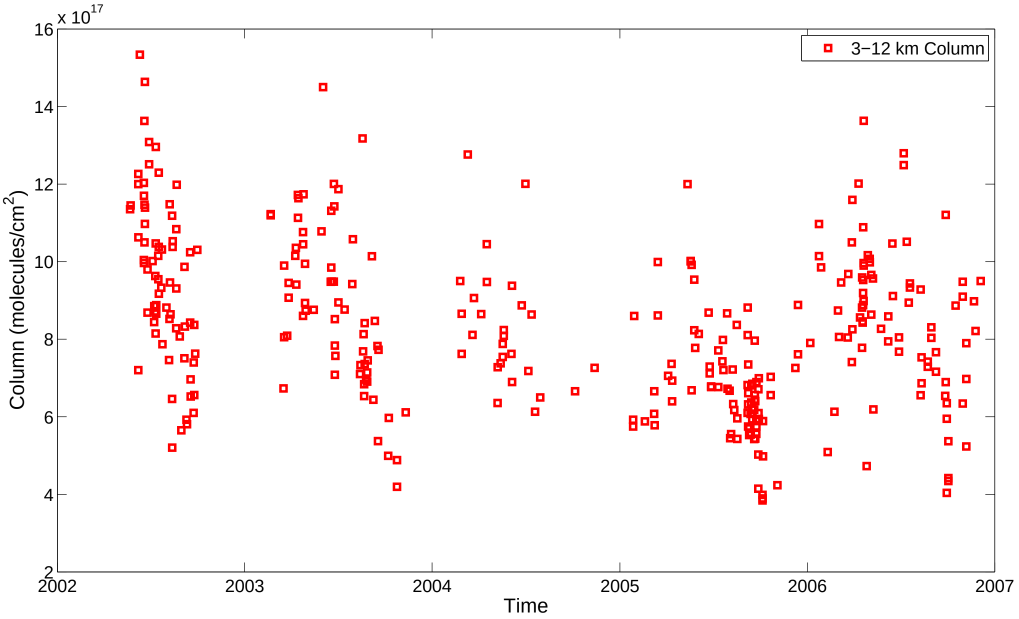

Figure 8.13: Timeseries of CO 3-12 km partial column retrievals from the TAO-FTS. The median partial column error is less than 1% and is composed of state space parameter interference error and retrieval noise added together in quadrature. For clarity, the error bars are not shown.

spheric Research on Transport and Transformation) aircraft campaign [Fehsenfeld et al., 2006]. By comparing ICARTT observations with GEOS-Chem output generated using the same anthropogenic CO emission inventories that were used here (EPA NEI-99), it was found that the CO emissions should have been inventoried 60% lower. A new GEOS-Chem simulation was generated with the CO emission inventory modified to reflect this North American reduction (see Figure 8.15).

Although this change in the CO emission inventory results in slightly better agreement with the TAO-FTS retrieved partial columns, the data still do not agree. In order to

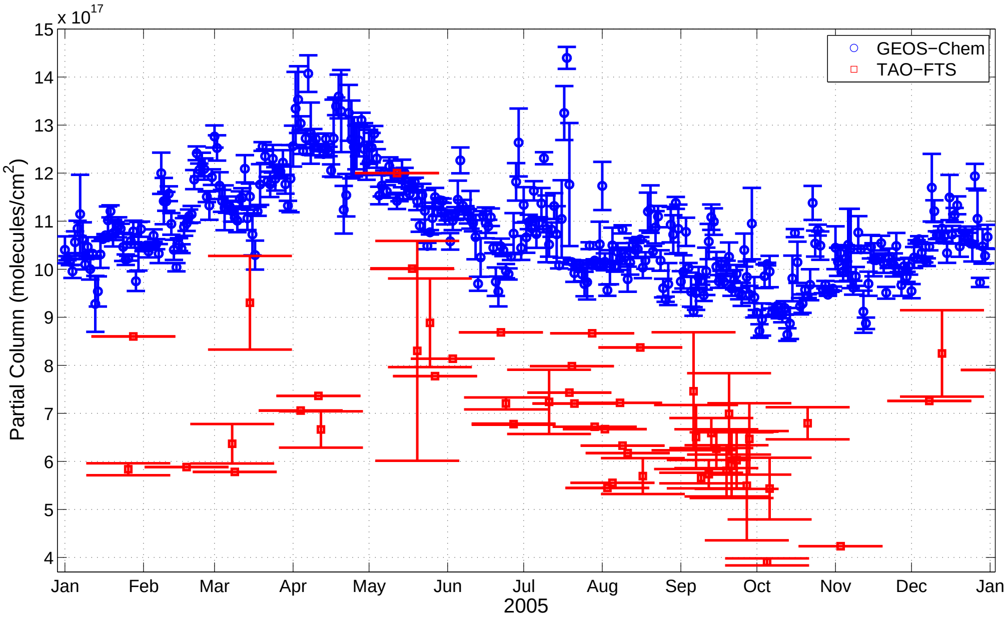

Figure 8.14: Timeseries of CO 3-12 km partial column daily means retrieved from the TAO-FTS (red) and the GEOS-Chem model (blue). Error bars represent 1 standard deviation (for the days upon which there is only one measurement, the error bars are set to 0).

properly ameliorate these differences, comparisons will need to be made over extended time periods and further model simulations will be required. Other tropospheric trace gases observed at TAO, such as hydrogen cyanide (HCN) and acetylene (C_2H_2), will also help characterize the level of agreement with the GEOS-Chem modelled tropospheric species.

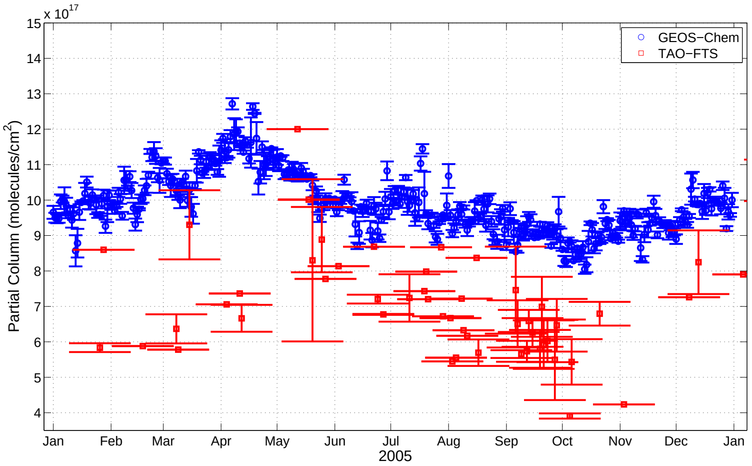

Figure 8.15: Timeseries of CO 3-12 km partial column daily means retrieved from the TAO-FTS (red) and the GEOS-Chem model with a North American emission reduction of 60% (blue). Error bars represent 1 standard deviation (for the days upon which there is only one measurement, the error bars are set to 0).

8.5 Summary and Future Work on Model-Based Validation of Tropospheric Gases

This preliminary comparison showed that the GEOS-Chem simulated C_2H_6 tropospheric partial columns were $\approx$ 30% greater than those observed by the TAO-FTS. Results from Xiao et al. [In Press] show that global C_2H_6 emissions in GEOS-Chem are slightly overestimated in the emissions inventories used here and should be reduced from $\approx$13.5 Tg/yr to $\approx$13.0 Tg/yr. However, they also note that North American estimates of C_2H_6 emissions are underestimated and should be increased. This suggests that changing the North American emissions inventory would only increase the discrepancy between the TAO-FTS observations and the GEOS-Chem output.

Initial comparisons between GEOS-Chem simulated tropospheric CO partial columns and those observed by the TAO-FTS indicated that the model was estimating ≈ 35% more than was observed. By following the work of Hudman et al. [2008], the North American anthropogenic CO emissoins inventory was reduced by 60% and the GEOS-Chem CO estimates over Toronto were uniformly reduced. However, the reduced partial columns were still ≈ 25% greater than those observed by the TAO-FTS. Hudman et al. [2008] also notes that biogenic emission estimates are now greater than those of anthropogenic emissions which is likely further be contributing to this discrepancy.

Since the parameterization of local North American emissions of CO and C_2H_6 have recently been investigated for the model output shown here, it is unlikely that local sources are completely responsible for the lack of agreement in the data. This suggests that Asian sources and/or transport of emissions are more responsible for the apparent elevation of columns. It is also possible that the discrepancy is entirely due to representation error arising from the coarse horizontal resolution of the model simulation. The 4° by 5° grid box encompassing Toronto also includes many other sources of emissions in Southern Ontario and North Eastern United States. The smearing of these values over Toronto may result in the apparent elevations that have been seen here.

To better diagnose these supposed causes of disagreement, future simulations with GEOS-Chem are planned with finer horizontal resolution (2° by 2.5° and/or 1° by 1° over Toronto). The results from these simulations will better represent the true state of the atmosphere over Toronto. It is also known that pollutants emitted from the same sources should have correlated concentrations [Xiao et al., 2004]. Thus far, the TAO data have not exhibited strong correlations, but with an extended set of GEOS-Chem output, it will be possible to better interpret the correlations that are present in the TAO data. By incorporating other tropospheric trace gases into the analysis, it will also be possible to distinguish anomalous events that contribute to observational enhancements not captured by the model, such as forest fires. By combining these different simulations with the TAO-FTS observations, a better understanding of how tropospheric chemical composition is controlled above Toronto can be attained.

Chapter 9

Conclusions

9.1 Summary of Results

Measurements that can be used to address scientific concerns in the areas of atmospheric climate change, tropospheric air quality, and stratospheric ozone depletion have been extensively assessed at the Toronto Atmospheric Observatory. The TAO-FTS has been operationally recording data under clear sky conditions since May 2002. In May 2004, the TAO was designated a complementary station of the NDACC, an international consortium of ground-based atmospheric observatories. Over the past five years, the TAO-FTS has averaged approximately 85 days of observations per year, which is consistent with other NDACC FTS instruments.

One part of TAO's NDACC obligations is to publicly store partial and total columns of several primary species retrieved from the FTS observations in the NDACC archive. This allows long-term observations of species that are important for climate change to ultimately be analysed for statistically significant long-term trends. Although the TAO-FTS hasn't been operational long enough to provide such insight, the data are being archived regularly. The most recent archiving took place in Fall 2007, and included all quality-controlled, retrieved values of HCl, HF, N_2O, NO_2, NO, O_3, and CH_4 in 2005 and 2006. This not only ensures that the TAO-FTS is adhering to an international standard of measurements and analysis, it also provides the framework for developing operational standards.

As part of assessing the quality of the data recorded by the TAO-FTS, this project has sought to perform cross-validation of species that are scientifically pertinent to climate change, air quality, and stratospheric ozone depletion. This has been done through side-by-side comparisons with two ground-based instruments, comparisons between the TAO-FTS and three satellite-based instruments, and comparisons with a chemical transport model.

Ground-based instrument intercomparisons at TAO took place in two campaigns: an extended campaign between the TAO-FTS and the U of T FTS in the Summer of 2005, and a focused campaign between the TAO-FTS, the U of T FTS, and PARIS-IR over a two-week period in August-September 2005. In both campaigns, simultaneous measurements of O_3, HCl, N_2O, and CH_4 were recorded by all the instruments. In the extended campaign, comparisons between the retrievals of stratospheric species (O_3 and HCl) do not show a consistent multiplicative bias between instruments. O_3 retrievals in two microwindows showed that the lower-resolution observations by the U of T FTS were more sensitive to changes in the lower atmosphere, although this had little impact on the total column comparison. For both microwindows, the U of T FTS had a fitted multiplicative bias of 0.89±0.03 and 0.78±0.03 times that of the TAO-FTS for the 3040 cm^{-1} and 2775 cm^{-1} microwindows, respectively. The median column differences (UofT - TAO) were 2.7±3.7% and -1.7±3.7% for the 3040 cm^{-1} and 2775 cm^{-1} microwindows, respectively. The TAO-FTS observations were 5 to 25% more sensitive to HCl concentrations than the U of T FTS, resulting in a total column multiplicative bias ratio of 1.18±0.05.

The resulting median difference in HCl column measurements was 2.2±4.8%. Compared to the tropospheric retrievals, the stratospheric species showed qualitatively less scatter from the linear fit and were better correlated. The difference in multiplicative bias between the two instruments arises from the lack of sensitivity to pressure broadening for HCl (as well as for O_3) by the U of T FTS, resulting in narrower spectroscopic features that are not easily captured by lower-resolution instruments. The tropospheric species did not allow for as detailed a comparison as the stratospheric gases. The median total column differences were 3.7±2.5% and 0.36±1.8% for CH_4 and N_2O, respectively. The pressure-induced line broadening of these tropospheric species generates broader spectroscopic features that were captured by both the low- and high-resolution instruments. A campaign of longer duration, albeit unpractical, would better capture the seasonal variation of the tropospheric gases and allow for better comparison of the scatter-plotted data. This highlights the need to be aware of instrument biases in total column measurements arising from lower-resolution infrared observations and their averaging kernels.

For the focused intercomparison, measurements were averaged during coincident 20-minute periods and the total column amounts retrieved from these averaged spectra were directly compared. The results showed that the lower-resolution instruments can measure total columns of O_3, HCl, N_2O, and CH_4 species to better than 4.5% of the TAO-FTS. There was no discernable trend in the agreement between instruments. The largest errors were obtained for the stratospheric species, and these errors can be attributed to the averaging kernels of the lower-resolution instruments, as was found in the extended intercomparison. The agreement for N_2O was very good, but there were significant differences for CH_4, possibly due to uncertainties in the spectroscopic parameters. The agreement between the TAO-FTS and the U of T FTS is slightly better than in the focused intercomparison for most of the species. This may be due to the fact that only measurements that were obtained at solar zenith angles of greater than 40° were used in the comparison. It was also found that retrieving ILS EPHS and EAP parameters from SFIT2 significantly improved the column comparisons of the stratospheric species for the lower-resolution instruments over retrievals performed assuming an ideal ILS. As expected, the ILS information was less important for the pressure-broadened tropospheric species.

The satellite-based validation at TAO focused on comparing the timeseries of stratospheric NO_2 and O_3 columns measured by the OSIRIS satellite instrument from May 2002-December 2006. NO_2 profiles were retrieved from OSIRIS UV-visible limb-scatter measurements using both DOAS and MART retrieval algorithms. OSIRIS O_3 profiles were derived from the MART algorithm as well as with the Triplet retrieval method. All coincidences were confined to be within ±5° latitude and ±10° longitude of TAO, with like measurements sorted into monthly bins to derive mean partial column concentrations from 16-50 km.

The NO_2 comparisons used coincident data spanning 59 months. All three comparisons showed a high degree of correlation, ranging from R^2 = 0.85-0.93 and had a mean difference that ranged from 3% for OSIRIS-MART vs. TAO down to nearly 0% for OSIRIS-DOAS vs. TAO. The standard deviations of these differences were less than 6%. Of the two OSIRIS retrievals, the DOAS retrieval showed a marked systematic bias of 5% greater than the MART retrieval. The agreement between OSIRIS-MART and TAO and OSIRIS-DOAS and TAO are as good as or better than previous NO_2 column comparisons between infrared and UV-visible instruments. The O_3 coincident comparisons spanned 58 months and also displayed well-correlated monthly means (R^2 = 0.82-0.97). The mean differences were +2.5%, -0.3%, and -2.6% for MART−TAO, Triplet−TAO, and Triplet−MART, respectively, with standard deviations all less than 3%. The apparent high bias for the OSIRIS-MART values may be generated by the higher altitude sensitivity caused by the inclusion of the Huggins band in the MART retrievals. There were definite multiplicative biases between some data sets (OSIRIS-MART and TAO), as well as systematic differences.

The results from the comparisons with the ACE-FTS show that TAO-FTS observations are within 12%, or better, of those of ACE with the exception of CO and NO which each have an average bias of about 25%. However, when the values for these two gases are compared with the performance of the rest of the ground-based FTS observations, it can be seen that the TAO observations are in the middle of the bounds. The only marginally outlying comparison appears to be for CH_4, which is consistent with the poor comparisons seen in the ground-based validation of the TAO-FTS data. SCIAMACHY comparisons demonstrated that TAO agreed well with like observations of CO, CH_4, and N_2O with average total column differences less than 10% in all comparison cases.

Due to the inherent difficulty associated with validating tropospheric observations with satellite instruments, the GEOS-Chem chemical transport model was used to simulate concentrations of CO and C_2H_6 in the troposphere above Toronto. The simulated C_2H_6 3-12 km tropospheric partial columns were $\approx$ 30% greater than those observed by the TAO-FTS in 2005. Recent work has suggested that GEOS-Chem may actually be underestimating North American emissions, which would only indicate an increase in the discrepancy between the TAO-FTS observations and the model output. Initial comparisons between GEOS-Chem simulated 3-12 km tropospheric CO partial columns and those observed by the TAO-FTS in 2005 indicated that the model was estimating $\approx$ 35% more than was observed. After adjusting the North American anthropogenic CO emissions inventory in the model, the GEOS-Chem CO estimates over Toronto were uniformly reduced. However, the reduced partial columns were still $\approx$ 25% greater than those observed by the TAO-FTS. Continued comparisons between the TAO-FTS observations and the model estimates are necessary if these differences are to be understood.

9.2 Future Work

Although this project has demonstrated that the results from the TAO-FTS are reliable, there are still more scientifically interesting questions that can be addressed with these data.

Comparisons with the OSIRIS instrument have demonstrated that a multi-year timeseries of stratospheric measurements at TAO is trustworthy. In the future, the TAO data set will only get larger and thus provide enough measurements to draw conclusions about statistically significant trends in the column concentrations of these species. Furthermore, these trends can also be calculated at other NDACC locations and the global distribution of these growth rates can provide insight into questions surrounding stratospheric ozone depletion/recovery and atmospheric climate change. In this context of future validation, these timeseries are also valuable for calibrating/validating future satellite observations.

The same approach of utilizing global comparisons between multiple NDACC sites can also be applied to tropospheric species. This can aid in answering questions surrounding agreement with the GEOS-Chem CTM. Model representation error for an urban area such as Toronto could be significant and through comparisons with observations at other "cleaner" sites, a better understanding of the causes of disagreement can be attained. By utilizing observations from affiliated NDACC sites in Japan and the US, the impact of North American and Asian emission inventories can also be characterized. These questions can also be extended to encompass larger data sets of tropospheric pollutants observed in other years.

Other questions endemic to the GEOS-Chem comparison can be addressed though specific model simulations. Issues related to chemical concentrations of OH and CO over Toronto can be solved by generating a "CO-only" run which controls CO entirely through OH chemistry. Simulations with higher horizontal resolution over Toronto can also address coarse representation concerns. As well, further modifications to emission inventories can help distinguish the effects of North American vs Asian contributions to pollution over Toronto.

In addition to the questions which directly stem from the work done in this project, there are other observations and data analysis techniques that can be explored at TAO. Many questions related to tropospheric pollution can be addressed through the optimization of retrievals of other molecular species, such as acetylene, ethylene, formaldehyde, etc. Further work can also be done to explore the potential for retrieving other stratospheric and tropospheric gases related to ozone depletion and climate change (*e.g.*, CFCs, HCFCs, etc.).

Finally, for the purposes of continuity, arrangements for the long-term maintenance of the TAO-FTS must be made so as to ensure that high-quality infrared spectra are recorded. These measurements must be archived at TAO and, ultimately, the retrieved columns must be archived in the NDACC database. Because new retrieval software is always in development, it will also be necessary to implement new analysis routines that can incorporate the latest updates in SFIT2 (or, if necessary, new retrieval algorithms altogether). For consistency, the re-analysis of previously archived results will be necessary for re-submission to the NDACC database. As well, updates to instrument hardware, operating software, and heliostat control software should be regularly implemented as the system ages.

Appendix A

The retrieval methodology applied to measurements made by the TAO-FTS was initially developed by Wiacek [2006]. These retrieval parameters were chosen specifically for generating data products for archival in the NDACC database. The 2005-2006 TAO-FTS retrieval results that were submitted to the NDACC database were shown in Section 5.5. For completeness, details of microwindow parameters, fits, and averaging kernels of the retrievals for all seven species are shown below. A more thorough discussion of why these parameters were chosen can be found in Wiacek [2006].

Table A.1: Spectral microwindows used for the retrieval of each trace gas as well as interfering species that were fitted simultaneously for the 2005-2006 NDACC archival. CH_4 was globally fitted with three simultaneous band-passes.

Target Gas	Microwindow(s) (cm^{-1})	Interfering Gases
HCl	2925.80-2926.00	CH_4, NO_2, O_3
HF	4038.77-4039.13	H_2O, HDO, CH_4
N_2O	2481.30-2482.60	CO_2, CH_4, O_3
NO_2	2914.59-2914.71	CH_4, H_2O
NO	1899.88-1900.15	CO_2
O_3	3045.10-3045.35	H_2O, CH_4
CH_4	2650.85-2651.25	HDO
	2666.95-2667.35	HDO
	2673.90-2674.41	HDO

Table A.2: Parameterization of *a priori* error covariance and typical measurement error covariance (expressed as SNR) used in the retrieval of gases for the 2005-2006 NDACC archival.

Target Gas	*A Priori* Covariance	Typical SNR
HCl	40% tapering to 10% outside stratosphere; Gaussian correlated, HWHM=4km; 0-100 km	≈ 650
HF	50% tapering to 10% outside stratosphere; Gaussian correlated, HWHM=4km; 0-100 km	≈ 250
N_2O	20% all levels Gaussian correlated, HWHM=4km; 0-15 km	≈ 400
NO_2	40% tapering to 10% outside stratosphere; Gaussian correlated, HWHM=4km; 0-100 km	≈ 900
NO	40% tapering to 10% outside stratosphere; Gaussian correlated, HWHM=4km; 0-100 km	≈ 125
O_3	30% all levels Gaussian correlated, HWHM=4km; 0-100 km	≈ 300
CH_4	20% all levels Gaussian correlated, HWHM=4km; 0-15 km	≈ 600

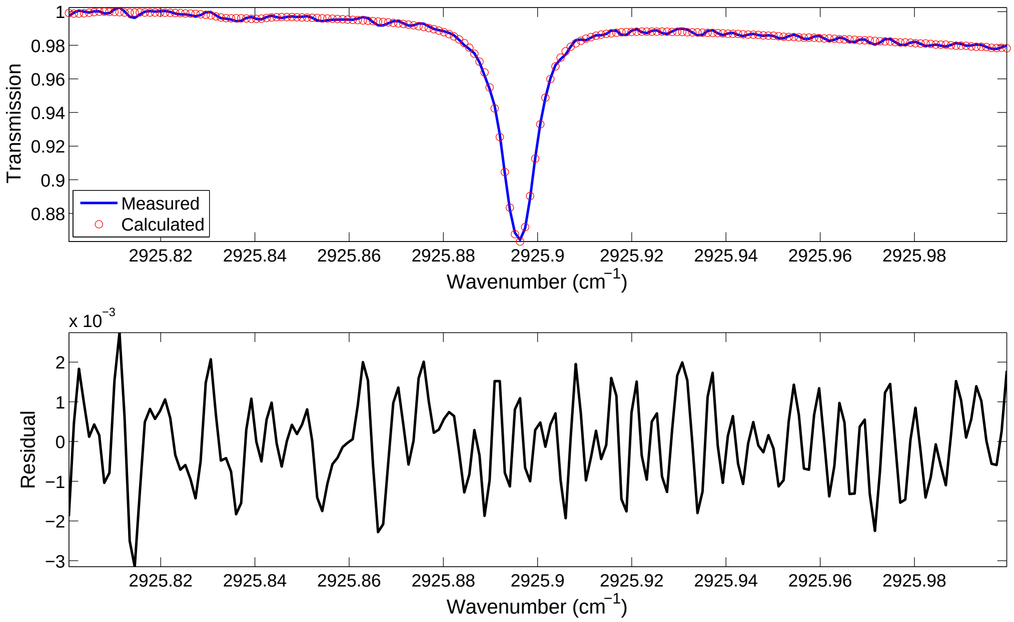

Figure A.1: Fit and residual for the HCl infrared absorption spectral microwindow in the 2925 cm^{-1} region (Filter 3) from an observation taken on 10 Aug 2005. The observed spectrum is shown in blue and the forward modelled values are shown in red.

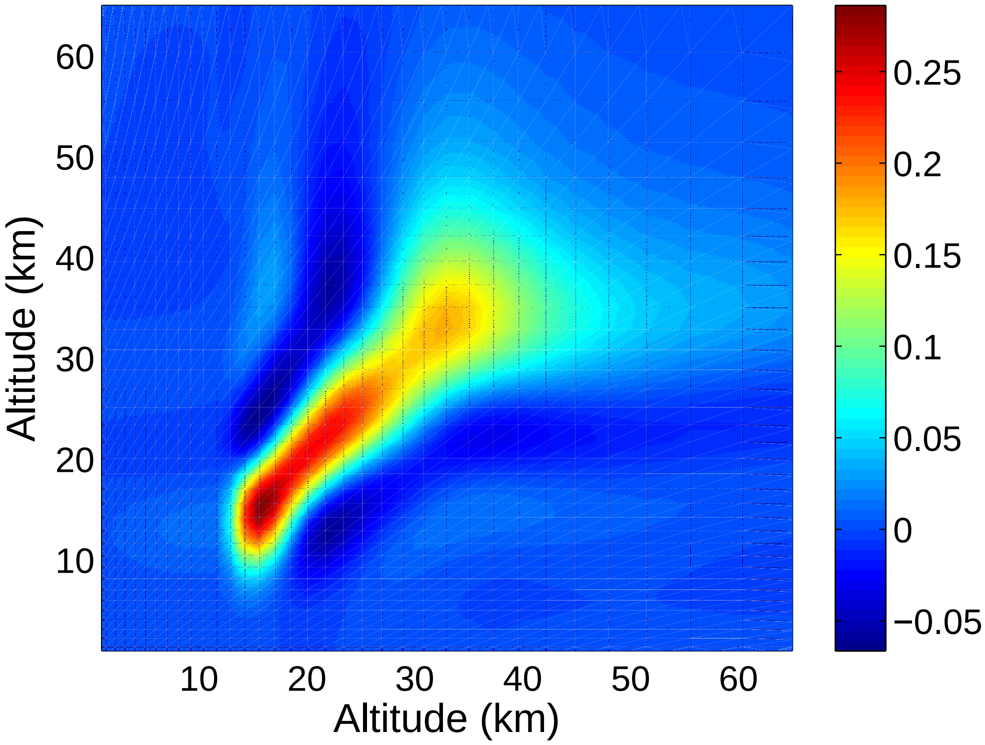

Figure A.2: Averaging kernel matrix calculated for the HCl infrared absorption spectral microwindow shown in Figure A.1.

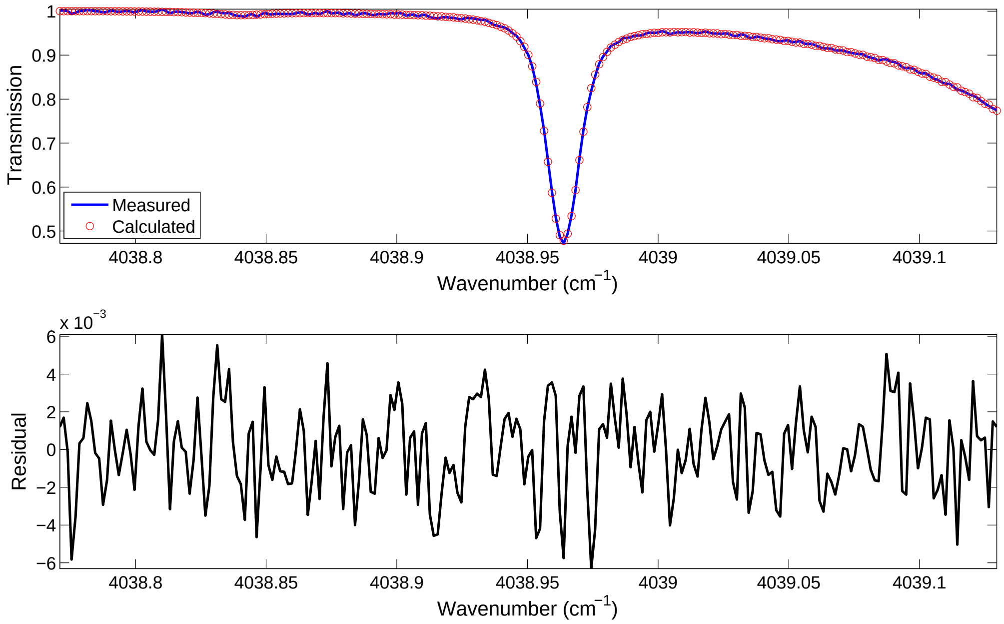

Figure A.3: Fit and residual for the HF infrared absorption spectral microwindow in the 4039 cm^{-1} region (Filter 1) from an observation taken on 6 Jan 2006. The observed spectrum is shown in blue and the forward modelled values are shown in red.

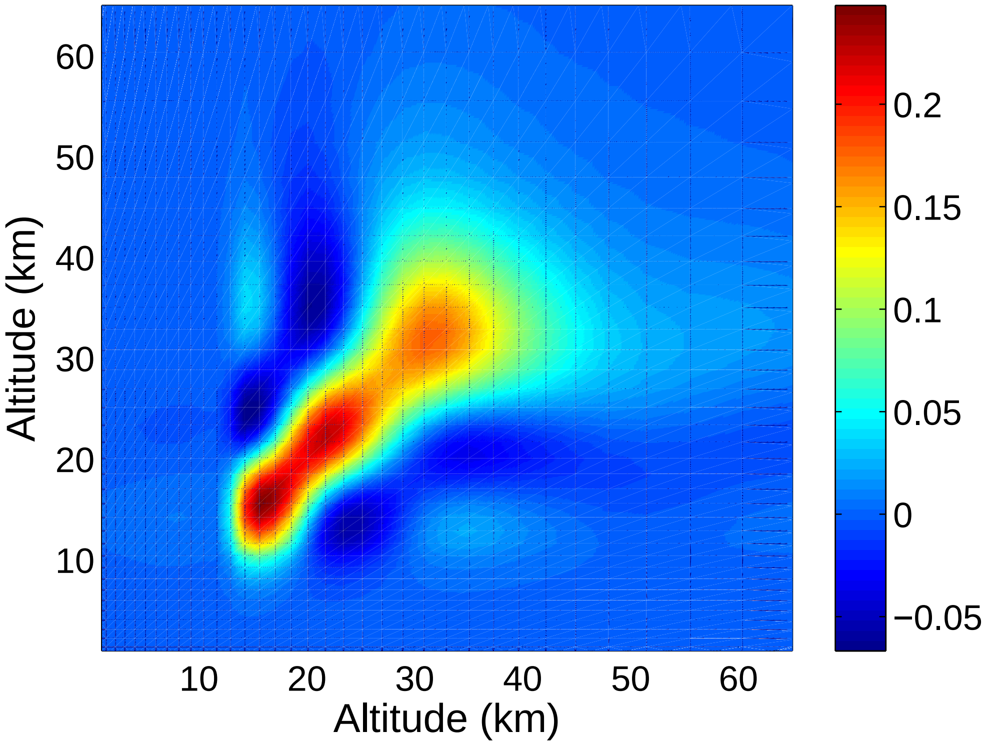

Figure A.4: Averaging kernel matrix calculated for the HF infrared absorption spectral microwindow shown in Figure A.3.

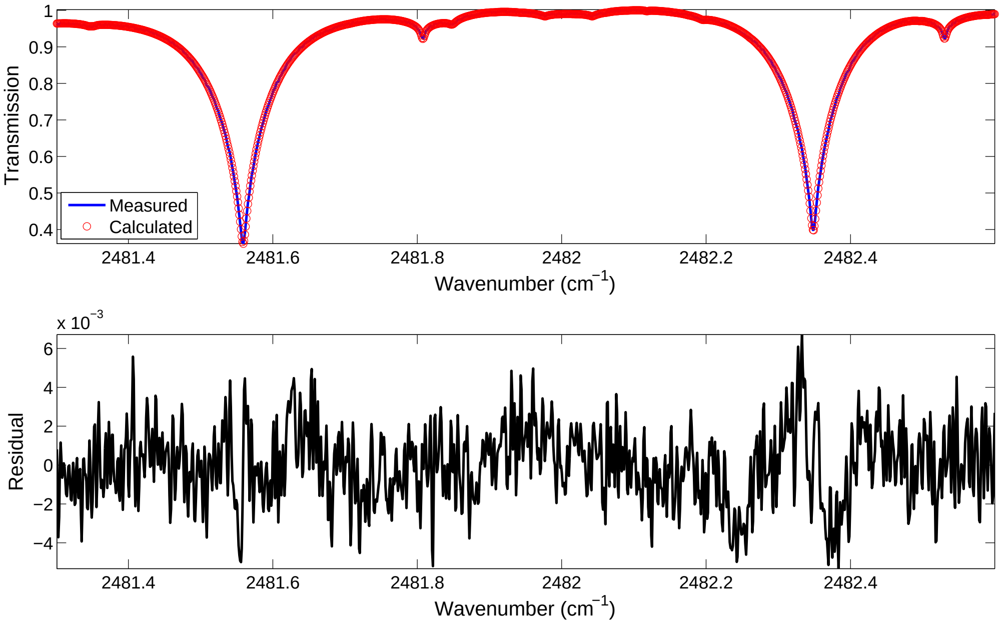

Figure A.5: Fit and residual for the N_2O infrared absorption spectral microwindow in the 2482 cm^{-1} region (Filter 3) from an observation taken on 6 Nov 2006. The observed spectrum is shown in blue and the forward modelled values are shown in red.

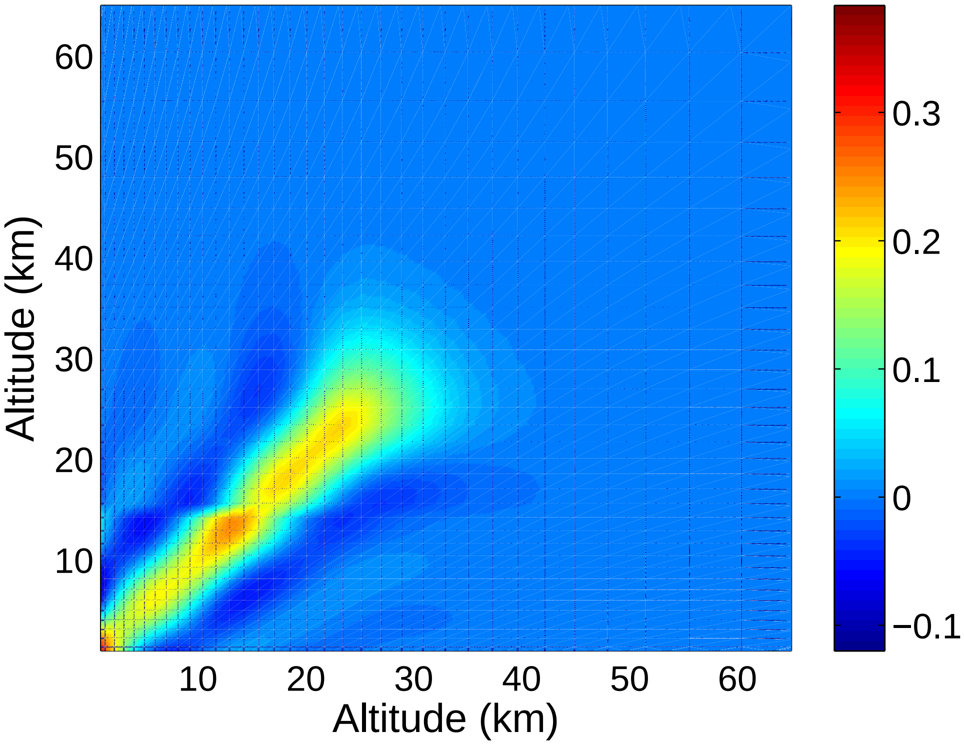

Figure A.6: Typical averaging kernel matrix calculated for the N_2O infrared absorption spectral microwindow shown in Figure A.5.

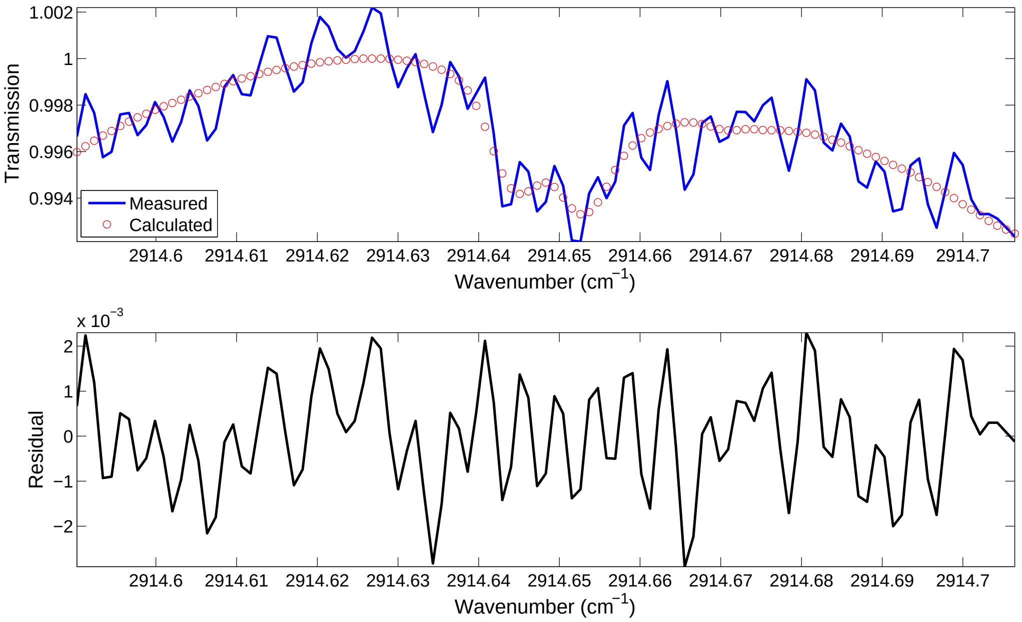

Figure A.7: Typical fit and residual for the NO_2 infrared absorption spectral microwindow in the 2914 cm^{-1} region (Filter 3) from an observation taken on 26 Jan 2006. The observed spectrum is shown in blue and the forward modelled values are shown in red.

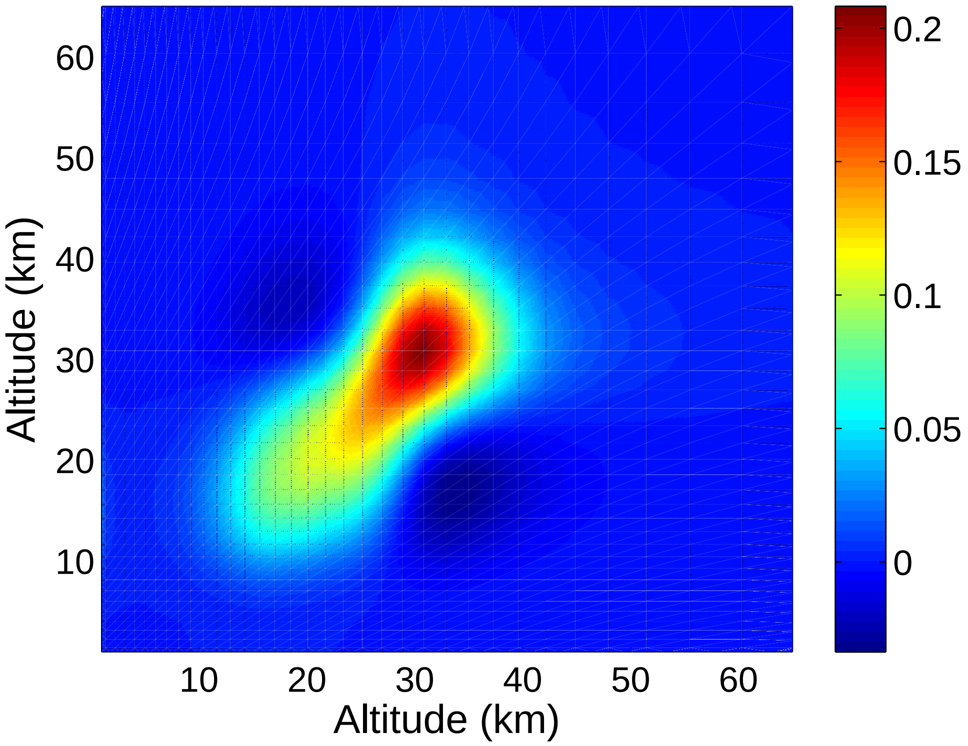

Figure A.8: Typical averaging kernel matrix calculated for the NO_2 infrared absorption spectral microwindow shown in Figure A.7.

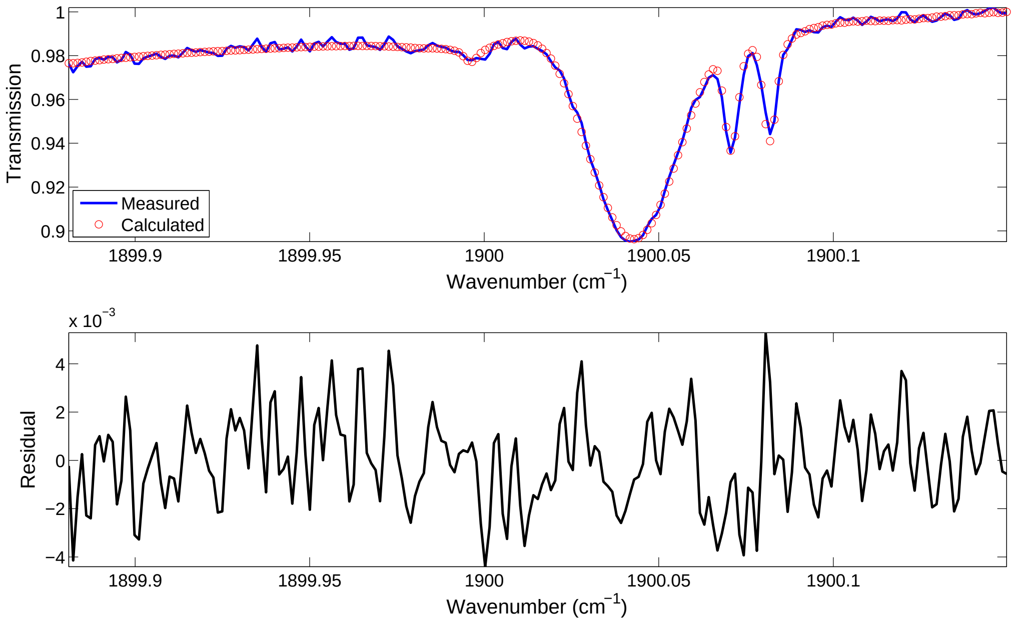

Figure A.9: Typical fit and residual for the NO infrared absorption spectral microwindow in the 1900 cm^{-1} region (Filter 5) from an observation taken on 31 Aug 2006. The observed spectrum is shown in blue and the forward modelled values are shown in red.

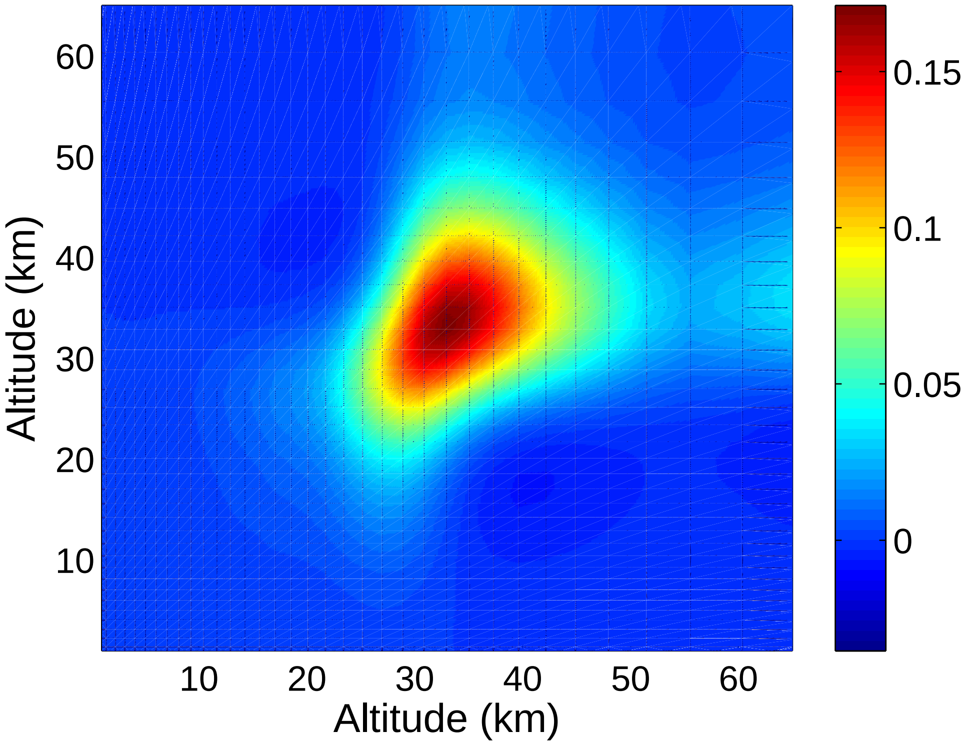

Figure A.10: Typical averaging kernel matrix calculated for the NO infrared absorption spectral microwindow shown in Figure A.9.

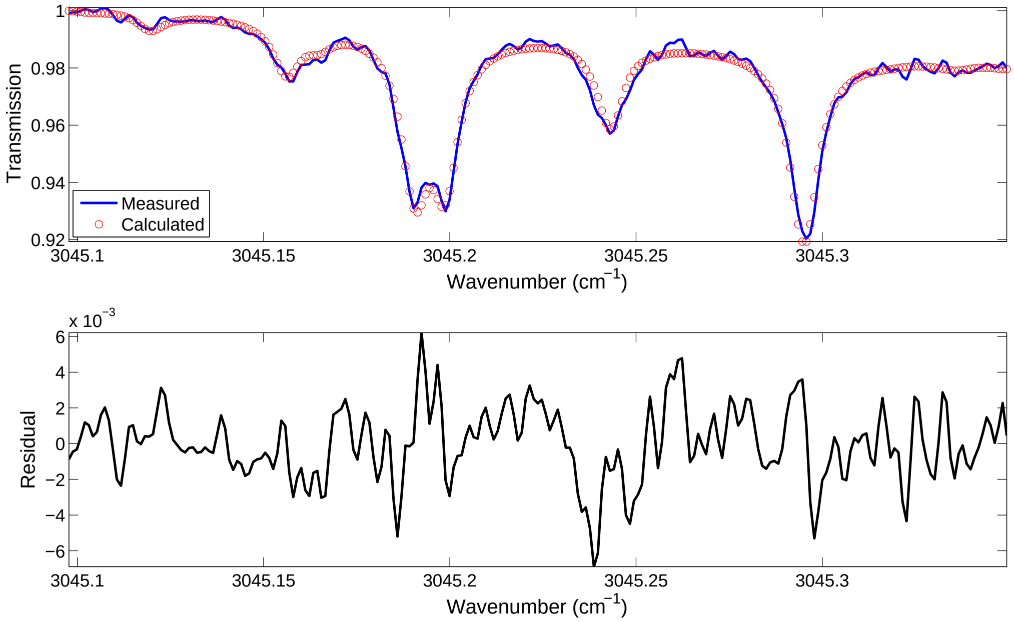

Figure A.11: Typical fit and residual for the O_3 infrared absorption spectral microwindow in the 3045 cm^{-1} region (Filter 3) from an observation taken on 14 June 2006. The observed spectrum is shown in blue and the forward modelled values are shown in red.

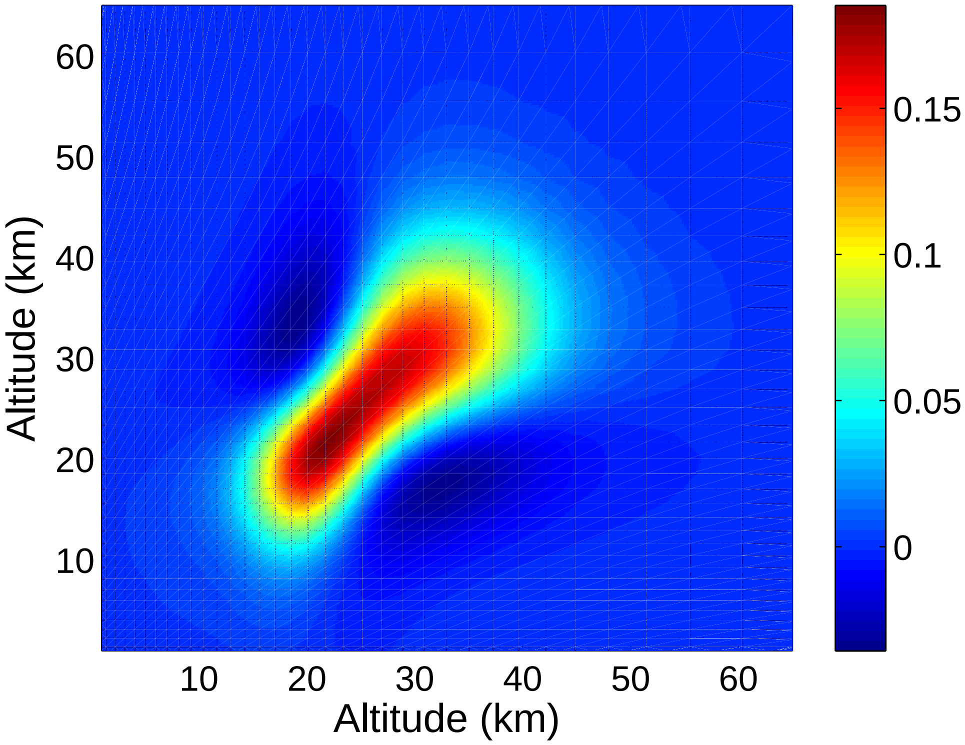

Figure A.12: Typical averaging kernel matrix calculated for the O_3 infrared absorption spectral microwindow shown in Figure A.11.

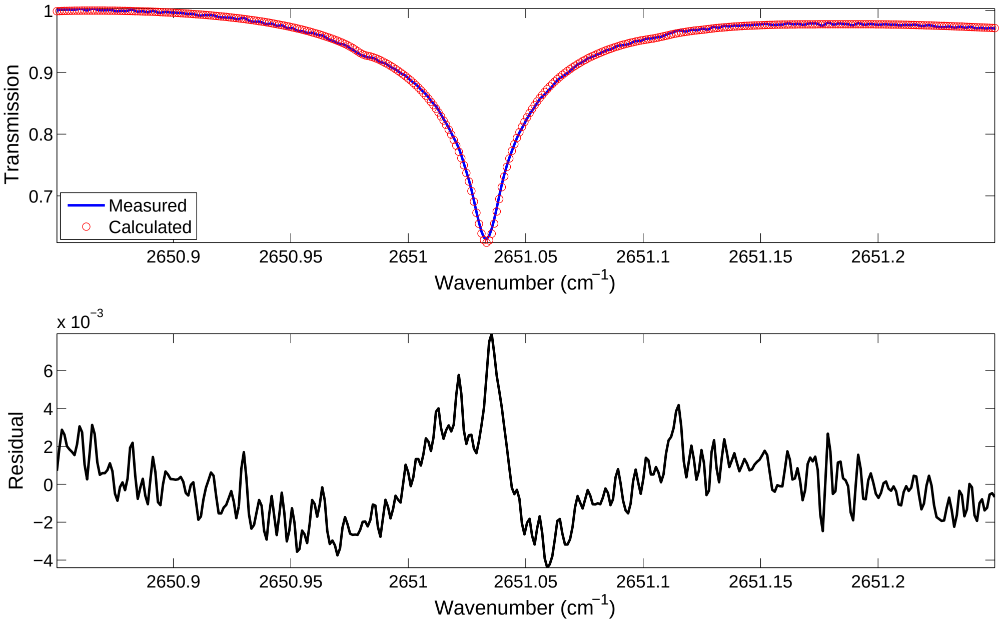

Figure A.13: Typical fit and residual for the CH_4 infrared absorption spectral microwindow in the 2651 cm^{-1} region (Filter 3) from an observation taken on 24 Nov 2006. The observed spectrum is shown in blue and the forward modelled values are shown in red.

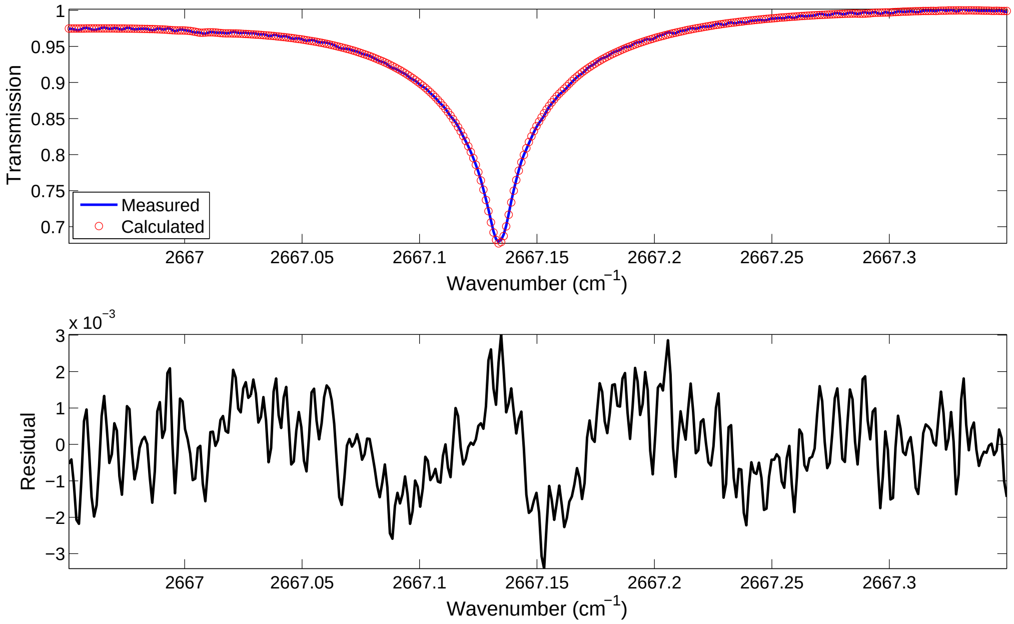

Figure A.14: Typical fit and residual for the CH_4 infrared absorption spectral microwindow in the 2667 cm^{-1} region (Filter 3) from an observation taken on 24 Nov 2006. The observed spectrum is shown in blue and the forward modelled values are shown in red.

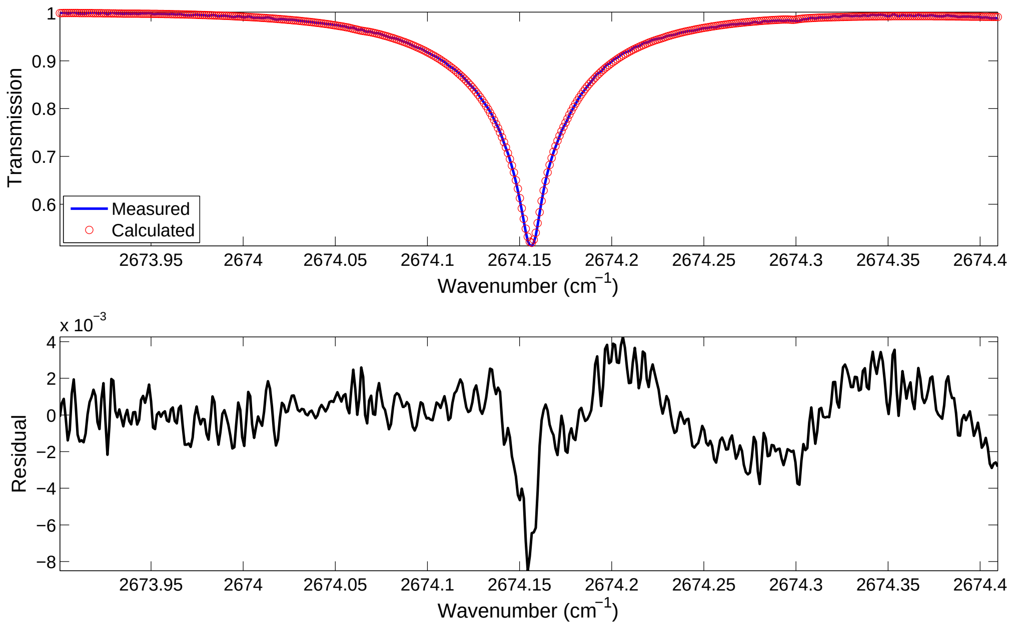

Figure A.15: Typical fit and residual for the CH_4 infrared absorption spectral microwindow in the 2674 cm^{-1} region (Filter 3) from an observation taken on 24 Nov 2006. The observed spectrum is shown in blue and the forward modelled values are shown in red.

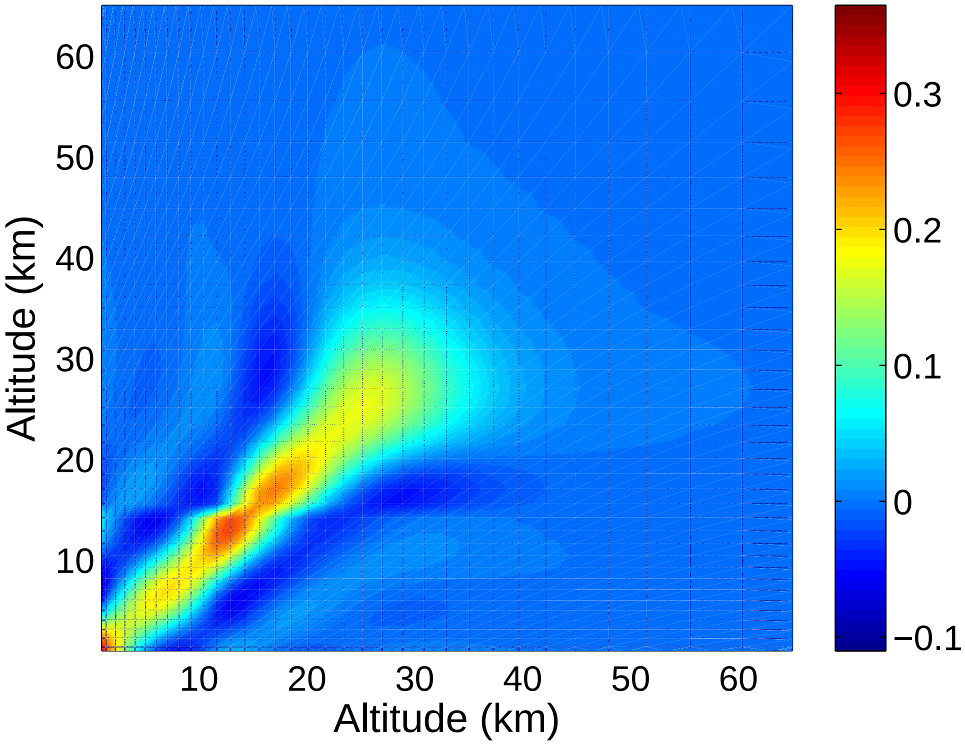

Figure A.16: Typical averaging kernel matrix calculated for all three CH_4 infrared absorption spectral microwindows shown in Figures A.13–A.15.

Bibliography

S Arrhenius. On the influence of carbonic acid in the air upon the temperature of the ground. *Philosophical Magazine and Journal of Science*, 41:237–276, 1896.

CN Banwell. *Fundamentals of Molecular Spectroscopy.* McGraw-Hill, 3rd edition, 1983.

B Barret, M De Mazière, and P Demoulin. Retrieval and characterization of ozone profiles from solar infrared spectra at the Jungfraujoch. *J. Geophys. Res.*, 107: doi:10.1029/2001JD001298, 2002.

MR Bassford, K Strong, CA McLinden, and CT McElroy. Ground-based measurements of ozone and NO2 during MANTRA 1998 using a new zenith-sky spectrometer. *Atmos.-Ocean*, 43:325–335, 2005.

T Bayes. An essay towards solving a problem in the doctrine of chances. *Phil. Trans. R. Soc. Lond.*, 53:370–418, 1763.

RJ Bell. *Introductory Fourier Transform Spectroscopy.* Academic Press, 1972.

P Bergamaschi, M Krol, F Dentener, A Vermeulen, F Meinhardt, R Graul, M Ramonet, W Peters, and EJ Dlugokencky. Inverse modelling of national and european CH4 emissions using the atmospheric zoom model TM5. *Atmos. Chem. Phys.*, 5:2431–2460, 2005.

P Bernath. *Spectra of Atoms and Molecules.* Oxford University Press, 2nd edition, 2005.

PF Bernath. Atmospheric chemistry experiment (ACE): Analytical chemistry from orbit. *Trends Anal. Chem.*, 25:647–654, 2006.

PF Bernath, CT McElroy, MC Abrams, CD Boone, M Butler, C Camy-Peyret, M Carleer, C Clerbaux, PF Coheur, R Colin, P DeCola, M De Mazière, JR Drummond, D Dufour, WFJ Evans, H Fast, D Fussen, K Gilbert, DE Jennings, EJ Llewellyn, RP Lowe, E Mahieu, JC McConnel, M McHugh, SD McLeod, R Michaud, C Midwinter, R Nassar, F Nichitiu, C Nowlan, CP Rinsland, YJ Rochon, N Rowlands, K Semeniuk, P Simon, R Skelton, JJ Sloan, MA Soucy, K Strong, P Tremblay, D Turnbull, KA Walker, I Walkty, DA Wardle, V Wehrle, R Zander, and Zou J. Atmospheric Chemistry Experiment (ACE): Mission overview. *Geophys. Res. Lett.*, 32:doi:10.1029/2005GL022386, 2005.

G Bernhard, CR Booth, JC Ehramjian, and SE Nichol. UV climatology at McMurdo Station, Antarctica, based on version 2 data of the National Science Foundations Ultraviolet Radiation Monitoring Network. *J. Geophys. Res.*, 111:doi:10.1029/2005JD005857, 2006.

I Bey, DJ Jacob, RM Yantosca, JA Logan, B Field, AM Fiore, Q Li, H Liu, LJ Mickley, and M Schultz. Global modeling of tropospheric chemistry with assimilated meteorology: Model description and evaluation. *J. Geophys. Res.*, 106:23073–23096, 2001.

D Blake and F Rowland. Continuing worldwide increase in tropospheric methane, 1978 to 1987. *Science*, 239:1129–1131, 1988.

K Bogumil, J Orphal, T Homann, S Voigt, P Spietz, OC Fleischmann, A Vogel, M Hartmann, H Kromminga, H Bovensmann, J Frerick, and JP Burrows. Measurements of molecular absorption spectra with the SCIAMACHY pre-flight model: instrument characterization and reference data for atmospheric remote-sensing in the $230-2380$ nm region. *J. Photochem. Photobiol. A: Chem.*, 157:167–184, 2003.

P Bouguer. *Essai d'Optique sur la gradation de la Lumiere*. Jombert; Paris, 1729.

G Brasseur and S Solomon. *Aeronomy of the Middle Atmosphere*. Springer-Verlag, 3rd edition, 2005.

GP Brasseur, P Artaxo, LA Barrie, RJ Delmas, I Gallbally, WM Hao, RC Harriss, ISA Isaksen, DJ Jacob, CE Kolb, M Prather, H Rodhe, D Schwela, W Steffen, and DJ Wuebbles. An integrated view of the causes and impacts of atmospheric changes. In GP Brasseur, RG Prinn, and AAP Pszenny, editors, *Atmospheric Chemistry in a changing world: An integration and synthesis of a decade of tropospheric chemistry research*. Springer-Verlag, 2003.

SM Brohede, CS Haley, CA McLinden, CE Sioris, DP Murtagh, SV Petelina, EJ Llewellyn, A Bazureau, F Goutail, CE Randall, JD Lumpe, G Taha, LW Thomasson, and LL Gordley. Validation of Odin/OSIRIS stratospheric NO_2 profiles. *J. Geophys. Res.*, 112:doi:10.1029/2006JDO07586, 2007.

L Brown, DC Benner, J Champion, V Devi, L Fejard, R Gamache, T Gabard, J Hilico, B Lavorel, M Loete, G Mellau, A Nikitin, A Pine, A Predoi-Cross, C Rinsland, O Robert, R Sams, M Smith, S Tashkun, and V Tyuterevk. Methane line parameters in HITRAN. *J. Quant. Spectros. Radiat. Transfer*, 82:219–238, 2003.

JP Burrows, E Hölzle, APH Goede, H Visser, and W Fricke. SCIAMACHY - SCanning Imaging Absorption spectroMeter for Atmospheric CHartographY. *Acta Astronautica*, 35:445–451, 1995.

Y Calisesi, VT Soebijanta, and R van Oss. Regridding of remote soundings: Formulation and application to ozone profile comparison. *J. Geophys. Res.*, 110: doi:10.1029/2005JD006122, 2005.

C Camy-Peyret, JM Flaud, J Laurent, and GM Stokes. First infrared measurement of atmospheric NO_2 from the ground. *Geophys. Res. Lett.*, 10:35–38, 1983.

Cancer Care Ontario. Cancer fact: Skin cancer is the most common cancer. Technical report, Toronto, Canada, 2005.

B Carli, D Alpaslan, M Carlotti, E Castelli, S Ceccherini, BM Dinelli, A Dudhia, JM Flaud, M Hoepfner, V Jay, L Magnani, H Oelhaf, V Payne, C Piccolo, M Prosperi, P Raspollini, J Remedios, M Ridolfi, and R Spang. First results of MIPAS/ENVISAT with operational level 2 code. *Adv. Space Res.*, 33:1012–1019, 2004.

J Chamberlain. *Fourier Transform Infrared Spectrometry.* John Wiley & Sons, 1979.

S Chapman. On ozone and atomic oxygen in the upper atmosphere. *Philos. Mag.*, 10: 369–383, 1930.

C Clerbaux, M George, S Turquety, KA Walker, B Barret, P Bernath, C Boone, T Borsdorff, JP Cammas, V Catoire, M Coffey, P-F Coheur, M Deeter, M De Mazière, J Drummond, P Duchatelet, E Dupuy, R de Zafra, F Eddounia, DP Edwards, L Emmons, B Funke, J Gille, DWT Griffith, J Hannigan, F Hase, M Höpfner, N Jones, A Kagawa, Y Kasai, I Kramer, E Le Flochmoën, NJ Livesey, M López-Puertas, M Luo, E Mahieu, D Murtagh, P Nédélec, A Pazmino, H Pumphrey, P Ricaud, CP Rinsland, C Robert, M Schneider, C Senten, G Stiller, A Strandberg, K Strong, R Sussmann, V Thouret, J Urban, and A Wiacek. CO measurements from the ACE-FTS satellite instrument: data analysis and validation using ground-based, airborne and spaceborne observations. *Atmos. Chem. Phys.*, 8:2569–2594, 2008.

MT Coffey, A Goldman, JW Hannigan, WG Mankin, WG Schoenfeld, CP Rinsland, C Bernardo, and DWT Griffith. Improved vibration-rotation (0-1) HBr line parameters for validating high resolution infrared atmospheric spectra measurements. *J. Quant. Spectros. Radiat. Transfer*, 60:863–867, 1998.

J Connes. Domaine d'utilization de la méthod par transformée de fourier. *J. Physique et le Radium*, 19:197–208, 1958.

P Connes. Astronomical Fourier spectroscopy. *Ann. Rev. Astron. Astrophys.*, 8:209–230, 1970.

P Connes. Fourier's three. *Mikrochim. Acta.*, 3:337–352, 1987.

JW Cooley and JW Tukey. An algorithm for the machine calculation of complex Fourier series. *Mathematics Computation*, 19:297–301, 1965.

PJ Crutzen. The influence of nitrogen oxides on the atmospheric ozone content. *Q. J. R. Meteorol. Soc.*, 96:320–325, 1970.

PJ Crutzen. Ozone production rates in an oxygen-hydrogen-nitrogen oxide atmosphere. *J. Geophys. Res.*, 76:7311–7327, 1971.

PJ Crutzen and PH Zimmermann. The changing photochemistry in the troposphere. *Tellus*, 43:136–151, 1991.

SP Davis, MC Abrams, and JW Brault. *Fourier Transform Spectrometry.* Academic Press, 2001.

MR de Backer-Barilly, A Barbe, and VG Tyuterev. Infrared spectrum of $^{16}O^{18}O^{16}O$ in the 5 micron range: Positions, intensities, and atmospheric applications. *Atmos. Oceanic Opt.*, 16:183–188, 2003.

DA Degenstein, AE Bourassa, CZ Roth, ND Lloyd, and EJ Llewellyn. Retrieval of vertical profiles with limb scattered sunlight measurements made by OSIRIS, a Multiplicative Algebraic Reconstruction Technique (MART) approach. In *American Geophysical Union - Fall Meeting*, San Francisco, United States, December 2006.

B Dils, M De Mazière, T Blumenstock, M Buchwitz, R de Beek, P Demoulin, P Duchatelet, H Fast, C Frankenberg, A Gloudemans, D Griffith, N Jones, T Kerzenmacher, I Kramer, E Mahieu, J Mellqvist, RL Mittermeier, J Notholt, CP Rinsland, H Schrijver, D Smale, A Strandberg, AG Straume, W Stremme, K Strong, R Sussmann, JR Taylor, M van den Broek, T Wagner, T Warneke, A Wiacek, and S Wood. Comparisons between SCIAMACHY and ground-based FTIR data for total columns of CO, CH4, CO2 and N2O. *Atmos. Chem. Phys.*, 6:1953–1976, 2006.

EJ Dlugokencky, S Houweling, L Bruhwiler, KA Masarie, PM Lang, JB Miller, and PP Tans. Atmospheric methane levels off: Temporary pause or a new steady-state? *Geophys. Res. Lett.*, 30:doi:10.1029/2003GL018126, 2003.

GMB Dobson. Origin and distribution of polyatomic molecules in the atmosphere. *Proc. Roy. Soc. London A*, 236:187–193, 1956.

BN Duncan, JA Logan, I Bey, IA Megretskaia, RM Yantosca, PC Novelli, NB Jones, and CP Rinsland. Global budget of CO, 1988–1997: Source estimates and validation with a global model. *J. Geophys. Res.*, 112:doi:10.1029/2007JD008459, 2007.

G Dunn. *Statistical evaluation of measurement errors: design and analysis of reliability studies*. Arnold, 2nd edition, 2004.

E Dupuy, KA Walker, J Kar, CD Boone, CT McElroy, PF Bernath, JR Drummond, R Skelton, SD McLeod, RC Hughes, CR Nowlan, DG Dufour, J Zou, F Nichitiu, K Strong, RM Bevilacqua, T Blumenstock, GE Bodeker, T Borsdorff, AE Bourassa, IS Boyd, A Bracher, C Brogniez, JP Burrows, V Catoire, S Ceccherini, S Chabrillat, T Christensen, MT Coffey, U Cortesi, J Davies, C de Clercq, DA Degenstein, M De Mazière, P Demoulin, J Dodion, B Firanski, H Fischer, G Forbes, L Froidevaux, D Fussen, P Gérard, J Granville, D Griffith, CS Haley, JW Hannigan, M Höpfner, JJ Jin, A Jones, NB Jones, K Jucks, A Kagawa, Y Kasai, TE Kerzenmacher, A Kleinböhl, AR Klekociuk, I Kramer, H Küllmann, J Kuttippurath, E Kyrölä, J-C Lambert, NJ Livesey, EJ Llewellyn, ND Lloyd, E Mahieu, GL Manney, BT Marshall, JC McConnell, MP McCormick, IS McDermid, M McHugh, CA McLinden, J Mellqvist, K Mizutani, Y Murayama, DP Murtagh, H Oelhaf, A Parrish, SV Petelina, C Piccolo, CE Randall, C Robert, C Roth, JM Russell III, C Senten, T Steck, A Strandberg, KB Strawbridge, R Sussmann, DPJ Swart, DW Tarasick, JR Taylor, C Tétard, LW Thomason, AM Thompson, MB Tully, J Urban, F Vanhellemont, T von Clarmann, P von der Gathen, C von Savigny, JW Waters, JC Witte, M Wolff, and JM Zawodny. Validation of ozone measurements from the Atmospheric Chemistry Experiment (ACE). *Atmos. Chem. Phys. Discuss.*, 8:2513–2656, 2008.

K Emanuel. Increasing destructiveness of tropical cyclones over the past 30 years. *Nature*, 436:686–688, 2005.

United States Environmental Protection Agency EPA. Smog: Who does it hurt? – what you need to know about ozone and your health. Technical report, Washington, United States, 1999.

MD Erickson. Gas chromatography/Fourier transform infrared spectroscopy applications. *Appl. Spectrosc. Rev.*, 15:261–298, 1979.

FC Fehsenfeld, G Ancellet, TS Bates, AH Goldstein, RM Hardesty, R Honrath, KS Law, AC Lewis, R Leaitch, S McKeen, J Meagher, DD Parrish, AAP Pszenny, PB Russell, H Schlager, J Seinfeld, R Talbot, and R Zbinden. International Consortium for Atmospheric Research on Transport and Transformation (ICARTT): North America to Europeoverview of the 2004 summer field study. *J. Geophys. Res.*, 111: doi:10.1029/2006JD007829, 2006.

PB Fellgett. *The Multiplex Advantage.* PhD thesis, University of Cambridge, 1951.

JM Flaud, C Camy-Peyret, JW Brault, CP Rinsland, and D Cariolle. Nighttime and daytime variation of atmospheric NO_2 from ground-based infrared measurements. *Geophys. Res. Lett.*, 15:261–264, 1988.

JM Flaud, C Camy-Peyret, D Cariolle, J Laurent, and GM Stokes. Daytime variation of atmospheric NO_2 from groundbased infrared measurements. *Geophys. Res. Lett.*, 10: 1104–1107, 1983.

DE Flittner, PK Bhartia, and BM Herman. O_3 profiles retrieved from limb scattered measurements: Theory. *Geophys. Res. Lett.*, 27:2061–2064, 2000.

P Friedlingstein, JL Dufresne, PM Cox, and P Rayner. How positive is the feedback between climate change and the carbon cycle? *Tellus*, 55:692–700, 2003.

U Frisk, M Hagström, J Ala-Laurinaho, S Andersson, J-C Berges, J-P Chabaud, M Dahlgren, A Emrich, H-G Florén, G Florin, M Fredrixon, T Gaier, R Haas, T Hirvonen, Å Hjalmarsson, B Jakobsson, P Jukkala, PS Kildal, E Kollberg, J Lassing, A Lecacheux, P Lehikoinen, A Lehto, J Mallat, C Marty, D Michet, J Narbonne, M Nexon, M Olberg, AOH Olofsson, G Olofsson, A Origné, M Petersson, P Piironen, R Pons, D Pouliquen, I Ristorcelli, C Rosolen, G Rouaix, AV Räisänen, G Serra, F Sjöberg, L Stenmark, S Torchinsky, J Tuovinen, C Ullberg, E Vinterhav, N Wadefalk, H Zirath, P Zimmermann, and R Zimmermann. The Odin satellite I. Radiometer design and test. *Astron. Astrophys.*, 402:L27–L34 10.1051/0004–6361:20030335, 2003.

D Fu, KA Walker, RL Mittermeier, K Strong, K Sung, H Fast, PF Bernath, CD Boone, WH Daffer, P Fogal, F Kolonjari, P Loewen, GL Manney, and O Mikhailov. Simultaneous atmospheric measurements using two fourier transform infrared spectrometers at the Polar Environment Atmospheric Research Laboratory during spring 2006, and comparisons with the Atmospheric Chemistry Experiment-Fourier Transform Spectrometer. *Atmos. Chem. Phys. Discuss.*, 8:5305–5358, 2008.

D Fu, KA Walker, K Sung, CD Boone, MA Soucy, and PF Bernath. The portable atmospheric research interferometric spectrometer for the infrared, PARIS-IR. *J. Quant. Spectros. Radiat. Transfer*, 103:362–370, 2007.

WO Gallery, FX Kneizys, and SA Clough. Air mass computer program for atmospheric transmittance/radiance calculation: FSCATM. Environmental research paper ERP-828=AFGL-TR-83-0065, Air Force Geophysical Laboratory, Hanscom Air Force Base, MA, USA, 1983.

T Gardiner, A Forbes, P Woods, M De Mazière, C Vigouroux, E Mahieu, P Demoulin, V Velazco, J Notholt, T Blumenstock, F Hase, I Kramer, R Sussman, W Stremme, J Mellqvist, A Strandberg, K Ellingsen, and M Gauss. Method for evaluating trends in greenhouse gases from ground-based remote FTIR measurements over Europe. *Atmos. Chem. Phys. Discuss.*, 7:15781–15803, 2007.

A Goldman, FJ Murcray, RD Blatherwick, and DG Murcray. Quantification of HCl from high-resolution, ground-based, infrared solar spectra in the 3000 cm^{-1} region. *J. Quant. Spectros. Radiat. Transfer*, 36:385–387, 1986.

A Goldman, C Paton-Walsh, W Bell, GC Toon, J-F Blavier, B Sen, MT Coffey, JW Hannigan, and WG Mankin. Network for the Detection of Stratospheric Change Fourier transform infrared intercomparison at Table Mountain Facility, November 1996. *J. Geophys. Res.*, 104:30481–30503, 1999.

A Griesfeller, J Griesfeller, F Hase, T Blumenstock, and H Nakajima. Comparison of ILAS-ii data with ground-based FTIR measurements of O3, HNO3, N2O, and CH4 over Kiruna, Sweden. In *American Geophysical Union - Fall Meeting*, San Fransisco, United States, December 2005.

DWT Griffith, NB Jones, B McNamara, C Paton-Walsh, W Bell, and C Bernardo. Intercomparison of NDSC ground-based solar FTIR measurements of atmospheric gases at Lauder, New Zealand. *J. Atmos. Oceanic Technol.*, 20:1138–1153, 2003.

PR Griffiths and JA de Haseth. *Fourier Transform Spectrometry.* John Wiley & Sons, 1986.

CS Haley and SM Brohede. Status of the Odin/OSIRIS stratospheric O_3 and NO_2 data products. *Can. J. Phys.*, 85:1177–1194, 2007.

CS Haley, SM Brohede, CE Sioris, E Griffioen, DP Murtagh, IC McDade, P Eriksson, EJ Llewellyn, A Bazureau, and F Goutail. Retrieval of stratospheric O_3 and NO_2 profiles from Odin Optical Spectrograph and InfraRed Imager System (OSIRIS) limb-scattered sunlight measurements. *J. Geophys. Res.*, 109:doi:10.1029/2004JD004588, 2004.

F Hase, T Blumenstock, and C Paton-Walsh. Analysis of the instrumental line shape of high-resolution fourier transform IR spectrometers with gas cell measurements and new retrieval software. *Appl. Opt.*, 38:3417–3422, 1999.

F Hase, JW Hannigan, MT Coffey, A Goldman, M Höpfner, NB Jones, CP Rinsland, and SW Wood. Intercomparison of retrieval codes used for the analysis of high-resolution, ground-based FTIR measurements. *J. Quant. Spectros. Radiat. Transfer*, 87:25–52, 2004.

Health Canada. Smog and your health. Technical report, Ottawa, Canada, 2003.

W Heisenberg. Ueber den anschaulichen inhalt der quantentheoretischen kinematic and mechanik. *Zeitschrift für Physik*, 43:172–198, 1927. (English translation in Wheeler and Zurek, 1983, pp 62-84).

G Herzberg. *Molecular Spectra and Molecular Structure I: Spectra of Diatomic Molecules.* Van Nostrand Reinhold Company, 2nd edition, 1950.

PV Hobbs. *Introduction to Atmospheric Chemistry.* Cambridge University Press, 2000.

J Houghton. *The Physics of Atmospheres.* Cambridge University Press, 3rd edition, 2002.

X Huang and Y Ling Yung. A common misunderstanding about the Voigt line profile. *J. Atmos. Sci.*, 61:1630–1632, 2004.

RC Hudman, LT Murray, DJ Jacob, DB Millet, S Turquety, S Wu, DR Blake, AH Goldstein, J Holloway, and GW Sachse. Biogenic versus anthropogenic sources of CO in the United States. *Geophys. Res. Lett.*, 35:doi:10.1029/2007GL032393, 2008.

BG Hunt. The need for a modified photochemical theory of the ozonosphere. *J. Atmos. Sci.*, 23:88–95, 1966.

Integrated Global Observing Strategy IGOS. The changing atmosphere: An integrated global atmospheric chemistry observation theme for the IGOS partnership – GAW report no. 159. Technical report, Geneva, Switzerland, 2004.

Intergovernmental Panel On Climate Change IPCC. *Climate Change 1995: The Science of Climate Change. Contribution of Working Group I to the Second Assessment of the Intergovernmental Panel on Climate Change.* Cambridge University Press, 1995.

Intergovernmental Panel On Climate Change IPCC. *Climate Change 2001: The Scientific Basis. Contribution of Working Group I to the Third Assessment Report of the Intergovernmental Panel on Climate Change.* Cambridge University Press, 2001.

Intergovernmental Panel On Climate Change IPCC. *Climate Change 2007: The Physical Science Basis. Contribution of Working Group I to the Fourth Assessment Report of the Intergovernmental Panel on Climate Change.* Cambridge University Press, 2007.

Intergovernmental Panel On Climate Change Technology & Economic Assessment Panel IPCC/TEAP. *Safeguarding the Ozone Layer and the Global Climate System: Issues Related to Hydrofluorocarbons and Perfluorocarbons.* Cambridge University Press, 2005.

D Jacob. *Introduction to Atmospheric Chemistry.* Princeton University Press, 1999.

P Jacquinot and C Dufour. Conditions optiques demploi des cellules photoélectriques dans les spectrographes et les interféromètres. *J. Rech. CNRS (Paris)*, 6:91, 1948.

J Kauppinen and J Partanen. *Fourier Transforms in Spectroscopy.* Wiley-VCH, 2001.

CD Keeling and TP Whorf. Atmospheric CO2 records from sites in the SIO air sampling network. In *Trends: A Compendium of Data on Global Change.* Carbon Dioxide Information Analysis Center, Oak Ridge National Laboratory, US Department of Energy, 2005.

JB Kerr, CT McElroy, DI Wardle, RA Olafson, and WFJ Evans. The automated Brewer spectrophotometer. In CS Zerefos and A Ghazi, editors, *Atmospheric Ozone*, pages 396–401. Reidel, Dordrecht, The Netherlands, 1985.

T Kerzenmacher, MA Wolff, K Strong, E Dupuy, KA Walker, LK Amekudzi, RL Batchelor, PF Bernath, G Berthet, T Blumenstock, CD Boone, K Bramstedt, C Brogniez, S Brohede, JP Burrows, V Catoire, J Dodion, JR Drummond, DG Dufour, B Funke, D Fussen, F Goutail, DWT Griffith, CS Haley, F Hendrick, M Höpfner, N Huret, N Jones, J Kar, I Kramer, EJ Llewellyn, M López-Puertas, G Manney, CT McElroy, CA McLinden, S Melo, S Mikuteit, D Murtagh, F Nichitiu, J Notholt, C Nowlan, C Piccolo, J-P Pommereau, C Randall, A Richter, M Schneider, O Schrems, M Silicani, GP Stiller, JR Taylor, C Tétard, M Toohey, F Vanhellemont, T Warneke, JM Zawodny, and J Zou. Validation of NO_2 and NO from the Atmospheric Chemistry Experiment (ACE). *Atmos. Chem. Phys. Discuss.*, 8:3027–3142, 2008.

TE Kerzenmacher, KA Walker, K Strong, R Berman, PF Bernath, CD Boone, JR Drummond, H Fast, A Fraser, K MacQuarrie, C Midwinter, K Sung, CT McElroy, RL Mittermeier, J Walker, and H Wu. Measurements of O3, NO2 and temperature during the 2004 Canadian Arctic ACE validation campaign. *Geophys. Res. Lett.*, 32: doi:10.1029/2005GL023032, 2005.

S Kreidenweis, G Tyndall, M Barth, FJ Dentener, J Lelieveld, and M Mozurkewich. Aerosols and clouds. In GP Brasseur, JJ Orlando, and GS Tyndall, editors, *Atmospheric Chemistry and Global Change.* Oxford University Press, 1999.

MJ Kurylo and RJ Zander. The NDSC - its status after ten years of operation. In *Proc. of the 19th Quadrennial Ozone Symposium*, 2000.

JC Lambert, T Blumenstock, F Boersma, A Bracher, M De Mazière, P Demoulin, I De Smedt, H Eskes, M Gil, F Goutail, J Granville, F Hendrick, DV Ionov, PV Johnston, I Kostadinov, K Kreher, E Kyrö, R Martin, A Meier, E Navarro-Comas, A Petritoli, JP Pommereau, A Richter, HK Roscoe, C Sioris, R Sussmann, M Van Roozendael, T Wagner, S Wood, and M Yela. Geophysical validation of SCIAMACHY NO_2 vertical columns: overview of early 2004 results. In *Proceedings of ACVE-2 Workshop*, Frascati, Italy, May 2004.

JB Liley, PV Johnston, RL McKenzie, AJ Thomas, and IS Boyd. Stratospheric NO2 variations from a long time series at Lauder, New Zealand. *J. Geophys. Res.*, 105: 11633–11640, 2000.

KN Liou. *An Introduction to Atmospheric Radiation*. Academic Press, 2nd edition, 2002.

EJ Llewellyn, ND Lloyd, DA Degenstein, RL Gattinger, SV Petelina, AE Bourassa, JT Wiensz, EV Ivanov, IC McDade, BH Solheim, JC McConnell, CS Haley, C von Savigny, CE Sioris, CA McLinden, E Griffioen, J Kaminski, WFJ Evans, E Puckrin, K Strong, V Wehrle, RH Hum, DJW Kendall, J Matsushita, DP Murtagh, S Brohede, J Stegman, G Witt, G Barnes, WF Payne, L Pich, K Smith, G Warshaw, DL Deslauniers, P Marchand, EH Richardson, RA King, I Wevers, W McCreath, E Kyrölä, L Oikarinen, GW Leppelmeier, H Auvinen, G Mégie, A Hauchecorne, F Lefèvre, J de la Nöe, P Ricaud, U Frisk, F Sjoberg, F von Schéele, and L Nordh. The OSIRIS instrument on the Odin spacecraft. *Can. J. Phys.*, 82:411–422, 2004.

JA Logan, MJ Prather, SC Wofsy, and MB McElroy. Tropospheric chemistry: A global perspective. *J. Geophys. Res.*, 86:7210–7254, 1981.

HA Lorentz. The absorption and emission of lines of gaseous bodies. In *HA Lorentz Collected Papers (The Hague, 1934-1939)*, volume 3, pages 215–238. 1906.

E Mahieu, P Duchatelet, P Demoulin, KA Walker, E Dupuy, L Froidevaux, C Randall, V Catoire, K Strong, CD Boone, PF Bernath, J-F Blavier, T Blumenstock, M Coffey, M De Mazière, D Griffith, J Hannigan, F Hase, N Jones, KW Jucks, A Kagawa, Y Kasai, Y Mebarki, S Mikuteit, R Nassar, J Notholt, CP Rinsland, C Robert, O Schrems, C Senten, D Smale, JR Taylor, C Ttard, GC Toon, T Warneke, SW Wood, R Zander, and C Servais. Validation of ACE-FTS v2.2 measurements of HCl, HF, CCl_3F and CCl_2F_2 using space-, balloon-and ground-based instrument observations. *Atmos. Chem. Phys. Discuss.*, 8:3431–3495, 2008.

E Mahieu, R Zander, P Duchatelet, JW Hannigan, MT Coffey, S Mikuteit, F Hase, T Blumenstock, A Wiacek, K Strong, JR Taylor, R Mittermeier, H Fast, CD Boone, SD McLeod, KA Walker, PF Bernath, and CP Rinsland. Comparisons between ACE-FTS and ground-based measurements of stratospheric HCl and $ClONO_2$ loadings at northern latitudes. *Geophys. Res. Lett.*, 32:doi:10.1029/2005GL022396, 2005.

G Marland, TA Boden, and RJ Andres. Global, regional, and national CO2 emissions. In *Trends: A Compendium of Data on Global Change.* Carbon Dioxide Information Analysis Center, Oak Ridge National Laboratory, US Department of Energy, 2006.

M De Mazière, B Barret, C Vigouroux, T Blumenstock, F Hase, I Kramer, C Camy-Peyret, P Chelin, T Gardiner, M Coleman, P Woods, K Ellingsen, M Gauss, I Isaksen, E Mahieu, P Demoulin, P Duchatelet, J Mellqvist, A Strandberg, V Velazco, A Schulz, J Notholt, R Sussmann, W Stremme, and A Rockmann. Ground-based FTIR measurements of O3- and climate-related gases in the free troposphere and lower stratosphere. In *Quadrenial Ozone Symposium*, Kos, Greece, June 2004.

M De Mazière, T Coosemans, B Barret, T Blumenstock, A Griesfeller, P Demoulin, H Fast, D Griffith, N Jones, E Mahieu, J Mellqvist, RL Mittermeier, J Notholt, C Rinsland, A Schulz, D Smale, A Strandberg, R Sussmann, S Wood, and M Buchwitz. Validation of ENVISAT-1 level-2 products related to lower atmosphere O_3 and NO_y chemistry by a FTIR quasi-global network. In *Proceedings of Envisat Validation Workshop*, Frascati, Italy, December 2002.

M De Mazière, M Van Roozendael, C Hermans, P C Simon, P Demoulin, G Roland, and R Zander. Quantitative evaluation of the post-Mount Pinatubo NO_2 reduction and recovery, based on 10 years of Fourier transform infrared and UV-visible spectroscopic measurements at Jungfraujoch. *J. Geophys. Res.*, 103:doi:10.1029/97JD03362, 1998.

M De Mazière, C Vigouroux, PF Bernath, P Baron, T Blumenstock, C Boone, C Brogniez, V Catoire, M Coffey, P Duchatelet, D Griffith, J Hannigan, Y Kasai, I Kramer, N Jones, E Mahieu, GL Manney, C Piccolo, C Randall, C Robert, C Senten, K Strong, JR Taylor, C Tétard, KA Walker, and S Wood. Validation of ACE-FTS v2.2 methane profiles from the upper troposphere to lower mesosphere. *Atmos. Chem. Phys.*, 8: 2421–2435, 2008.

CT McElroy. A spectroradiometer for the measurement of direct and scattered solar spectral irradiance from on-board the NASA ER-2 high-altitude research aircraft. *Geophys. Res. Lett.*, 22:1361–1364, 1995.

CT McElroy, CR Nowlan, JR Drummond, PF Bernath, DV Barton, DG Dufour, C Midwinter, RB Hall, A Ogyu, A Ullberg, DI Wardle, J Kar, J Zou, F Nichitiu, CD Boone, KA Walker, and N Rowlands. The ACE-MAESTRO instrument on SCISAT: description, performance, and preliminary results. *Appl. Opt.*, 46:4341–4356, 2007.

CA McLinden, SC Olsen, B Hannegan, O Wild, MJ Prather, and J Sundet. Stratospheric ozone in 3-D models: A simple chemistry and the cross-tropopause flux. *J. Geophys. Res.*, 105:14653–14665, 2000.

A Meier, A Goldman, PS Manning, TM Stephen, CP Rinsland, NB Jones, and SW Wood. Improvements to air mass calculations for ground-based infrared measurements. *J. Quant. Spectros. Radiat. Transfer*, 83:109–113, 2004.

A Meier, C Paton-Walsh, W Bell, T Blumenstock, F Hase, A Goldman, Å Steen, R Kift, P Woods, and Y Kondo. Evidence of reduced measurement uncertainties from an FTIR instrument intercomparison at Kiruna, Sweden. *J. Quant. Spectros. Radiat. Transfer*, 96:75–84, 2005.

SML Melo, E Farahani, K Strong, MR Bassford, and KE Preston. NO_2 vertical profiles retrieved from ground-based measurements during spring 1999 in the Canadian Arctic. *Adv. Space Res.*, 34:786–792, 2004.

L Mertz. Auxiliary computation for Fourier spectrometry. *Infrared Phys.*, 7:17–23, 1967.

AA Michelson. The relative motion of the earth and the luminiferous ether. *Amer. J. Sci.*, 34:333–345, 1887.

G Mie. Beiträge zur optik trüber medien, speziell kolloidaler metallösungen. *Ann. Phys.*, 330:377–445, 1908.

S Mikhailenko, A Barbe, and VG Tyuterev. Extended analysis of line positions and intensities of ozone bands in the $2900-3400$ cm^{-1} region. *J. Mol. Spec.*, 215:29–41, 2002.

MJ Molina and LT Molina. Megacities and atmospheric pollution. *J. Air Waste Manage. Assoc.*, 54:644–680, 2004.

MJ Molina and FS Rowland. Stratospheric sink for chlorofluoromethanes: chlorine atom catalysed destruction of ozone. *Nature*, 249:810–812, 1974.

MJ Molina, TL Tso, LT Molina, and FCY Wang. Antarctic stratospheric chemistry of chlorine nitrate, hydrogen chloride, and ice: Release of active chlorine. *Science*, 238: 1253–1257, 1987.

PM Morse. Diatomic molecules according to the wave mechanics II: Vibrational levels. *Phys. Rev.*, 34:57–64, 1929.

D Murtagh, U Frisk, F Merino, M Ridal, A Jonsson, J Stegman, G Witt, P Eriksson, C Jiménez, G Megie, J de la Noë, P Ricaud, P Baron, JR Pardo, A Hauchcorne, EJ Llewellyn, DA Degenstein, RL Gattinger, ND Lloyd, WFJ Evans, IC McDade, CS Haley, C Sioris, C von Savigny, BH Solheim, JC McConnell, K Strong, EH Richardson, GW Leppelmeier, E Kyrölä, H Auvinen, and L Oikarinen. An overview of the Odin atmospheric mission. *Can. J. Phys.*, 80:309–319, 2002.

M Neubergera, D Rabczenkob, and H Moshammera. Extended effects of air pollution on cardiopulmonary mortality in Vienna. *Atmos. Env.*, 41: doi:10.1016/j.atmosenv.2007.07.013, 2007.

HL Nordh, F von Scheele, U Frisk, K Ahola, RS Booth, PJ Encrenaz, A Hjalmarson, D Kendall, E Kyrola, and S Kwok. The Odin orbital observatory. *Astron. Astrophys.*, 402:L21–L26, 2003.

Ontario Ministry of the Environment. Ontario's clean air action plan: Protecting environmental and human health in Ontario. Technical report, Toronto, Canada, 2004.

Ontario Ministry of the Environment. Air quality in Ontario - 2006 report. Technical report, Toronto, Canada, 2007.

JC Orr, VJ Fabry, O Aumont, L Bopp, SC Doney, RA Feely, A Gnanadesikan, N Gruber, A Ishida, F Joos, RM Key, K Lindsay, E Maier-Reimer, R Matear, P Monfray, A Mouchet, RG Najjar, GK P, KB Rodgers, CL Sabine, JL Sarmiento, R Schlitzer, RD Slater, IJ Totterdell, MF Weirig, Y Yamanaka, and A Yool. Anthropogenic ocean acidification over the twenty-first century and its impact on calcifying organisms. *Nature*, 437:681–686, 2005.

M Palm, C von Savigny, T Warneke, V Velazco, J Notholt, K Künzi, J Burrows, and O Schrems. Intercomparison of O_3 profiles observed by SCIAMACHY, ground based microwave and FTIR instruments. *Atmos. Chem. Phys. Diss.*, 5:911–936, 2005.

ML Parry, C Rosenzweig, A Iglesias, M Livermore, and G Fischer. Effects of climate change on global food production under SRES emissions and socio-economic scenarios. *Global. Environ. Chang.*, 14:53–67, 2004.

C Paton-Walsh, W Bell, T Gardiner, N Swann, P Woods, J Notholt, H Schutt, B Galle, W Arlander, and J Mellqvist. An uncertainty budget for ground-based Fourier transform infrared column measurements of HCl, HF, N_2O, and HNO_3 deduced from results of side-by-side instrument comparisons. *J. Geophys. Res.*, 102:8867–8873, 1997.

SA Penkett, KS Law, T Cox, and P Kasibhatla. Atmospheric photooxidants. In GP Brasseur, RG Prinn, and AAP Pszenny, editors, *Atmospheric Chemistry in a changing world: An integration and synthesis of a decade of tropospheric chemistry research*. Springer-Verlag, 2003.

A Perrin, J-M Flaud, A Goldman, C Camy-Peyret, WJ Lafferty, P Arcas, and CP Rinsland. NO_2 and SO_2 line parameters: 1996 HITRAN update and new results. *J. Quant. Spectros. Radiat. Transfer*, 60:839–850, 1998.

FH Perrin. Whose absorption law? *J. Opt. Soc. Am.*, 38:72–74, 1948.

SV Petelina, EJ Llewellyn, DA Degenstein, ND Lloyd, RL Gattinger, CS Haley, C von Savigny, E Griffioen, IC McDade, WFJ Evans, DP Murtagh, and J de la Noe. Comparison of the Odin/OSIRIS stratospheric ozone profiles with coincident POAM III and ozonesonde measurements. *Geophys. Res. Lett.*, 31:doi:10.1029/2003GL019299, 2004.

SV Petelina, EJ Llewellyn, KA Walker, DA Degenstein, CD Boone, PF Bernath, CS Haley, C von Savigny, ND Lloyd, and RL Gattinger. Validation of ACE-FTS stratospheric ozone profiles against Odin/OSIRIS measurements. *Geophys. Res. Lett.*, 32: doi:10.1029/2005GL022377, 2005.

RT Pierrehumbert. Warming the world. *Nature*, 432:677, 2004.

A Pinkus and S Zafrany. *Fourier Series and Integral Transforms.* Cambridge University Press, 1999.

M Planck. Ueber irreversible strahlungsvorgänge. *Ann. Physik*, 311:818–831, 1901. (English translation provided by the Smithsonian/NASA Astrophysics Data System).

JP Pommereau and F Goutail. O_3 and NO_2 ground-based measurements by visible spectrometry during Arctic winter and spring 1988. *Geophys. Res. Lett.*, 15:891–894, 1988.

NS Pougatchev, CP Rinsland, and BJ Connor. Infrared measurements of the ozone vertical distribution above Kitt Peak. *J. Geophys. Res.*, 100:16689–16697, 1995.

L Rayleigh. On the light from the sky, its polarization and colour. *Phil. Mag.*, 41: 107–120,274–279, 1871.

CP Rinsland, A Goldman, E Mahieu, R Zander, J Notholt, NB Jones, DWT Griffith, TM Stephen, and LS Chiou. Ground-based infrared spectroscopic measurements of carbonyl sulfide: Free tropospheric trends from a 24-year time series of solar absorption measurements. *J. Geophys. Res.*, 107:doi:10.1029/2002JD002522, 2002a.

CP Rinsland, A Goldman, FJ Murcray, TM Stephen, NS Pougatchev, J Fishman, SJ David, RD Blatherwick, PC Novelli, NB Jones, and B Connor. Infrared solar spectroscopic measurements of free tropospheric CO, C_2H_6 and HCN above Mauna Loa, Hawaii: Seasonal variations and evidence for enhanced emissions from the southeast Asian tropical fires of 1997-1998. *J. Geophys. Res.*, 104:18667–18680, 1999.

CP Rinsland, NB Jones, BJ Connor, JA Logan, N Pougatchev, A Goldman, FJ Murcray, TM Stephen, AS Pine, R Zander, E Mahieu, and P Demoulin. Northern and southern hemisphere ground-based infrared spectroscopic measurements of tropospheric carbon monoxide and ethane. *J. Geophys. Res.*, 103:28197–28217, 1998.

CP Rinsland, NB Jones, BJ Connor, SW Wood, A Goldman, TM Stephen, FJ Murcray, LS Chiou, R Zander, and E Mahieu. Multiyear infrared solar spectroscopic measurements of HCN, CO, C_2H_6, and C_2H_2 tropospheric columns above Lauder, New Zealand (45°S latitude). *J. Geophys. Res.*, 107:10.1029/2001JD001150, 2002b.

CP Rinsland, E Mahieu, R Zander, P Demoulin, J Forrer, and B Buchmann. Free tropospheric CO, C_2H_6 and HCN above central Europe: Recent measurements from the Jungfraujoch station including the detection of elevated columns during 1998. *J. Geophys. Res.*, 105:24235–24259, 2000.

CP Rinsland, E Mahieu, R Zander, NB Jones, MP Chipperfield, A Goldman, J Anderson, JM Russell III, P Demoulin, J Notholt, GC Toon, J-F Blavier, B Sen, R Sussmann, SW Wood, A Meier, DWT Griffith, LS Chiou, FJ Murcray, TM Stephen, F Hase, S Mikuteit, A Schulz, and T Blumenstock. Long-term trends of inorganic chlorine from ground-based infrared solar spectra: Past increases and evidence for stabilization. *J. Geophys. Res.*, 108:doi:10.1029/2002JD003001, 2003.

CP Rinsland, A Meier, DWT Griffith, and LS Chiou. Ground-based measurements of tropospheric CO, C_2H_6, and HCN from Australia at 34°S latitude during 1997-1998. *J. Geophys. Res.*, 106:20913–20924, 2001.

CP Rinsland, MAH Smith, PL Rinsland, A Goldman, JW Brault, and Stokes GM.

Ground-based infrared spectroscopic measurements of atmospheric hydrogen cyanide. *J. Geophys. Res.*, 87:11119–11125, 1982.

C Rodgers. *Inverse Methods for Atmospheric Sounding: Theory and Practice.* World Scientific, 2000.

C Rodgers and BJ Connor. Intercomparison of remote sounding instruments. *J. Geophys. Res.*, 108:doi:10.1029/2002JD002299, 2003.

TL Root, JT Price, KR Hall, SH Schneider, C Rosenzweig, and JA Pounds. Fingerprints of global warming on wild animals and plants. *Nature*, 421:57–60, 2003.

HK Roscoe, AJ Charlton, DJ Fish, and JGT Hill. Improvements to the accuracy of measurements of NO_2 by zenith-sky visible spectrometers II: Errors in zero using a more complete chemical model. *J. Quant. Spectros. Radiat. Transfer*, 68:337–349, 2001.

LS Rothman, D Jacquemart, A Barbe, DC Benner, M Birk, LR Brown, MR Carleer, C Chackerian Jr, K Chance, V Dana, VM Devic, J-M Flaud, RR Gamache, A Goldman J-M Hartmann, KW Jucks, AG Maki, J-Y Mandin, ST Massie, J Orphal, A Perrin, CP Rinsland, MAH Smith, J Tennyson, RN Tolchenov, RA Tothe, JV Auwera, P Varanasi, and G Wagner. The HITRAN 2004 molecular spectroscopic database. *J. Quant. Spectros. Radiat. Transfer*, 96:139–204, 2005.

J Rudolph. The tropospheric distribution and budget of ethane. *J. Geophys. Res.*, 100: 11369–11382, 1995.

J Rudolph and DH Ehhalt. Measurements of C2-C5 hydrocarbons over the north Atlantic. *J. Geophys. Res.*, 86:11959–11964, 1981.

JM Russell, LL Gordley, LE Deaver, RE Thompson, and JH Park. An overview of the halogen occultation experiment (HALOE) and preliminary results. *Adv. Space Res.*, 14:9–13, 1994.

M Schneider, T Blumenstock, MP Chipperfield, F Hase, W Kouker, T Reddmann, R Ruhnke, E Cuevas, and H Fischer. Subtropical trace gas profiles determined by ground-based FTIR spectroscopy at Izaña (28°N, 16°W): Five-year record, error analysis, and comparison with 3-D CTMs. *Atmos. Chem. Phys.*, 5:153–167, 2005a.

M Schneider, T Blumenstock, F Hase, M Höpfner, E Cuevas, A Redondas, and JM Sancho. Ozone profiles and total column amounts derived at Izanã, Tenerife Island, from FTIR solar absorption spectra, and its validation by an intercomparison to ECC-sonde and Brewer spectrometer measurements. *J. Quant. Spectros. Radiat. Transfer*, 91:245–274, 2005b.

K Schwarzschild. Diffusion and absorption in the sun's atmosphere. *Sitzungsberichte der Königlichen Preussichen Akademie der Wissenschaften*, pages 1183–1200, 1914. English Translation in Menzel, 1966.

H Slaper, GJM Velders, JS Daniel, FR de Gruijl, and JC van der Leun. Estimates of ozone depletion and skin cancer incidence to examine the Vienna Convention achievements. *Nature*, 384:256–258, 1996.

DM Stieb, S Judek, and RT Burnett. Meta-analysis of timeseries studies of air pollution and mortality: effects of gases and particles and the influence of cause of death, age and season. *J. Air Waste Manage. Assoc.*, 52:470–484, 2002.

K Strong, G Bailak, D Barton, MR Bassford, RD Blatherwick, S Brown, D Chartrand, J Davies, JR Drummond, PF Fogal, E Forsberg, R Hall, A Jofre, J Kaminski, J Kosters, C Laurin, JC McConnell, CT McElroy, CA McLinden, SML Melo, K Menzies, C Midwinter, FJ Murcray, C Nowlan, RJ Olson, BM Quine, Y Rochon, V Savastiouk, B Solheim, D Sommerfeldt, A Ullberg, S Werchohlad, H Wu, and D Wunch. MANTRA – a balloon mission to study the odd-nitrogen budget of the stratosphere. *Atmos.-Ocean*, 43:289–299, 2005.

K Strong, MA Wolff, TE Kerzenmacher, KA Walker, PF Bernath, T Blumenstock, C Boone, V Catoire, M Coffey, M De Mazière, P Demoulin, P Duchatelet, E Dupuy, J Hannigan, M Höpfner, N Glatthor, DWT Griffith, JJ Jin, N Jones, K Jucks, H Kuellmann, J Kuttippurath, A Lambert, E Mahieu, JC McConnell, J Mellqvist, S Mikuteit, DP Murtagh, J Notholt, C Piccolo, C Robert, M Schneider, O Schrems, K Semeniuk, C Senten, GP Stiller, A Strandberg, JR Taylor, C Tétard, M Toohey, J Urban, T Warneke, and S Wood. Validation of ACE-FTS N_2O measurements. *Atmos. Chem. Phys. Discuss.*, 8:3597–3663, 2008.

K Sung, R Skelton, KA Walker, CD Boone, D Fu, and PF Bernath. N_2O and O_3 arctic column amounts from PARIS-IR observations: Retrievals, characterization and error analysis. *J. Quant. Spectros. Radiat. Transfer*, 107:385–406, 2007.

R Sussmann, W Stremme, JP Burrows, A Richter, W Seiler, and M Rettinger. Stratospheric and tropospheric NO_2 variability on the diurnal and annual scale: a combined retrieval from ENVISAT/SCIAMACHY and solar FTIR at the permanent groundtruthing facility Zugspitze/Garmisch. *Atmos. Chem. Phys.*, 5:2657–2677, 2005.

DW Tarasick, VE Fioletov, DI Wardle, JB Kerr, LJB McArthur, and CA McLinden. Climatology and trends of surface UV radiation. *Atmos.-Ocean*, 41:121–138, 2003.

JR Taylor. Instrument characterization of a Fourier transform spectrometer at the Toronto Atmospheric Observatory. Master's thesis, University of Toronto, 2003.

JR Taylor, K Strong, CA McLinden, DA Degenstein, and CS Haley. Comparison of OSIRIS stratospheric NO_2 and O_3 measurements with ground-based Fourier transform spectrometer measurements at the Toronto Atmospheric Observatory. *Can. J. Phys.*, 85:1301–1316, 2007.

JR Taylor, D Wunch, C Midwinter, A Wiacek, JR Drummond, and K Strong. An extended intercomparison of simultaneous ground-based Fourier transform spectrometer measurements at the Toronto Atmospheric Observatory. *J. Quant. Spectros. Radiat. Transfer*, 109:2244–2260, 2008.

C Tebaldi and DB Lobell. Towards probabilistic projections of climate change impacts on global crop yields. *Geophys. Res. Lett.*, 35:doi:10.1029/2008GL033423, 2008.

AM Thompson. The oxidizing capacity of the atmosphere: Probable past and future changes. *Science*, 256:1157–1165, 1992.

TM Thompson, JH Butler, BC Daube, GS Dutton, JW Elkins, BD Hall, DF Hurst, DB King, ES Kline, BG LaFleur, J Lind, S Lovitz, DJ Mondeel, SA Montzka, FL Moore, JD Nance, JL Neu, PA Romashkin, A Scheffer, and WJ Snible. Halocarbons and other atmospheric trace species. In RC Schnell, A-M Buggle, and RM Rosson, editors, *Climate Monitoring and Diagnostics Laboratory, Summary Report No. 27*. Natioanl Oceanic and Atmospheric Administration Climate Diagnostics and Monitoring Laboratory, 2004.

Toronto Environment Office. Climate change, clean air and sustainable energy action plan: Moving from framework to action Phase 1. Technical report, Toronto, Canada, 2007.

Toronto Public Health. Air pollution burden of illness in Toronto: 2004 summary. Technical report, Toronto, Canada, 2004.

United States Department of Energy. Emissions of greenhouse gases in the united states, report of Energy Information Administration (EIA). Technical report, Washington, United States, 2005.

AC Vandaele, C Fayt, F Hendrick, C Hermans, F Humbled, M Van Roozendael, M Gil, M. Navarro, O Puentedura, M Yela, G Braathen, K Stebel, K Tørnkvist, P Johnston, K Kreher, F Goutail, A Mieville, J-P Pommereau, S Khaikine, A Richter, H Oetjen, F Wittrock, S Bugarski, U Frieß, K Pfeilsticker, R Sinreich, T Wagner, G Corlett, and R Leigh. An intercomparison campaign of ground-based UV-visible measurements of NO_2, BrO, and OClO slant columns: Methods of analysis and results for NO_2. *J. Geophys. Res.*, 110:doi:10.1029/2004JD005423, 2005.

AC Vandaele, C Hermans, PC Simon, M Carleer, R Colin, S Fally, MF Merienne, A Jenouvrier, and B Coquart. Measurements of the NO_2 absorption cross-section from 42 000 cm^{-1} to 10 000 cm^{-1} (238-1000 nm) at 220 K and 294 K. *J. Quant. Spectros. Radiat. Transfer*, 59:171–184, 1998.

V Velazco, J Notholt, T Warneke, M Lawrence, H Bremer, J Drummond, A Schulz, J Krieg, and O Schrems. Latitude and altitude variability of carbon monoxide in the atlantic detected from ship-borne Fourier transform spectrometry, model, and satellite data. *J. Geophys. Res.*, 110:doi:10.1029/2004JD005351, 2005.

T von Clarmann. Validation of remotely sensed profiles of atmospheric state variables: Strategies and terminology. *Atmos. Chem. Phys.*, 6:4311–4320, 2006.

T von Clarmann and U Grabowski. Elimination of hidden a priori information from remotely sensed profile data. *Atmos. Chem. Phys.*, 7:397–408, 2007.

C von Savigny, CS Haley, CE Sioris, IC McDade, EJ Llewellyn, D Degenstein WFJ Evans, RL Gattinger, E Griffioen, E Kyrölä, ND Lloyd, JC McConnell, CA McLinden, G Mégie, DP Murtagh, B Solheim, and K Strong. Stratospheric ozone profiles retrieved from limb scattered sunlight radiance spectra measured by the OSIRIS instrument on the Odin satellite. *Geophys. Res. Lett.*, 30:1755–1758 doi:10.1029/2002GL016401, 2003.

C von Savigny, IC McDade, E Griffioen, CS Haley, CE Sioris, and EJ Llewellyn. Sensitivity studies and first validation of stratospheric ozone profile retrievals from

Odin/OSIRIS observations of limb-scattered solar radiation. *Can. J. Phys.*, 83:957–972, 2005.

L Wallace and W Livingston. Spectroscopic observations of atmospheric trace gases over Kitt Peak. I - carbon dioxide and methane from 1979 to 1985. *J. Geophys. Res.*, 95: 9823–9827, 1990a.

L Wallace and W Livingston. Spectroscopic observations of atmospheric trace gases over Kitt Peak. II - nitrous oxide and carbon monoxide from 1979 to 1985. *J. Geophys. Res.*, 95:16383–16390, 1990b.

G Wetzel, A Bracher, B Funke, F Goutail, F Hendrick, JC Lambert, S Mikuteit, C Piccolo, M Pirre, A Bazureau, C Belotti, T Blumenstock, M De Mazière, H Fischer, N Huret, D Ionov, M López-Puertas, G Maucher, H Oelhaf, JP Pommereau, R Ruhnke, M Sinnhuber, G Stiller, M Van Roozendael, and G Zhang. Validation of MIPAS-ENVISAT NO_2 operational data. *Atmos. Chem. Phys.*, 7:3261–3284, 2007.

World Health Organization WHO. *Climate change and human health: RISKS AND RESPONSES*. World Health Organization, 2003.

World Health Organization WHO. Health aspects of air pollution – results from the WHO project “systematic review of health aspects of air pollution in Europe”. Technical report, Copenhagen, Denmark, 2004.

World Health Organization WHO. WHO air quality guidelines for particulate matter, ozone, nitrogen dioxide and sulfur dioxide – global update 2005. Technical report, Geneva, Switzerland, 2005.

A Wiacek. *First trace gas measurements using fourier transform infrared solar absorption spectroscopy at the University of Toronto Atmospheric Observatory*. PhD thesis, University of Toronto, 2006.

A Wiacek, NB Jones, K Strong, JR Taylor, RL Mittermeier, and H Fast. First detection of meso-thermospheric nitric oxide NO by ground-based FTIR solar absorption spectroscopy. *Geophys. Res. Lett.*, 33:doi:10.1029/2005GL024897, 2006.

A Wiacek, JR Taylor, K Strong, R Saari, TE Kerzenmacher, N Jones, and DWT Griffith. Ground-based solar absorption FTIR spectroscopy: a novel optical design instrument at a new NDSC complementary station, characterization of retrievals and first results. *J. Atmos. Oceanic Technol.*, 24:432–448, 2007.

World Meteorological Organization WMO. Scientific assessment of ozone depletion: 2006, global ozone research and monitoring project – report no. 50. Technical report, Geneva, Switzerland, 2007.

J Worden, SS Kulawik, MW Shephard, SA Clough, H Worden, K Bowman, and A Goldman. Predicted errors of tropospheric emission spectrometer nadir retrievals from spectral window selection. *J. Geophys. Res.*, 109:doi:10.1029/2004JD004522, 2004.

S Wu, LJ Mickley, DJ Jacob, D Rind, and DG Streets. Effects of 2000-2050 global change on ozone air quality in the United States. *J. Geophys. Res.*, 113: doi:10.1029/2007JD008917, 2008.

D Wunch, C Midwinter, JR Drummond, CT McElroy, and AF Bagès. The University of Toronto's balloon borne Fourier transform spectrometer. *Rev. Sci. Inst.*, 77: doi:10.1063/1.2338289, 2006.

D Wunch, JR Taylor, D Fu, P Bernath, JR Drummond, C Midwinter, K Strong, and KA Walker. Simultaneous ground-based observations of O_3, HCl, N_2O and CH_4 over Toronto, Canada by three Fourier transform spectrometers with different resolutions. *Atmos. Chem. Phys.*, 7:1275–1292, 2007.

D Wunch, MP Tingley, TG Shepherd, JR Drummond, GWK Moore, and K Strong.

Climatology and predictability of the late summer stratospheric zonal wind turnaround over Vanscoy, Saskatchewan. *Atmos.-Ocean*, 43:301–313, 2005.

YP Xiao, DJ Jacob, JA Logan, RC Hudman, RM Yantosca, and DR Blake. The global budget of ethane and regional constraints on U.S. sources. *J. Geophys. Res.*, In Press.

YP Xiao, DJ Jacob, JS Wang, JA Logan, PI Palmer, P Suntharalingam, RM Yantosca, GW Sachse, DR Blake, and DG Streets. Constraints on Asian and European sources of methane from CH4-C2H6-CO correlations in Asian outflow. *J. Geophys. Res.*, 109: doi:10.1029/2003JD004475, 2004.

D York, N Evensen, M López Martínez, and J de Basabe Delgado. Unified equations for the slope, intercept, and standard errors of the best straight line. *Am. J. Phys.*, 72: 367–375, 2004.

R Zander, P Demoulin, DH Ehhalt, and U Schmidt. Secular increase of the vertical column abundance of methane derived from IR solar spectra recorded at the Jungfraujoch station. *J. Geophys. Res.*, 94:11029–11039, 1989.

R Zander, DH Ehhalt, CP Rinsland, U Schmidt, E Mahieu, J Rudolph, P Demoulin, G Roland, L Delbouille, and AJ Sauval. Secular trend and seasonal variability of the column abundance of N_2O above the Jungfraujoch station determined from IR solar spectra. *J. Geophys. Res.*, 99:16745–16756, 1994.

A Zanobetti and J Schwartz. Air pollution and emergency admissions in Boston, MA. *J. Epidemiol. Community Health*, 60:890–895, 2006.

Y Zhao, K Strong, Y Kondo, M Koike, Y Matsumi, H Irie, CP Rinsland, NB Jones, K Suzuki, H Nakajima, H Nakane, and I Murata. Spectroscopic measurements of tropospheric CO, C_2H_6, C_2H_2, and HCN in northern Japan. *J. Geophys. Res.*, 107: doi:10.1029/2001JD000748, 2002.